University of Alberta

Magnetotransport and magnetoresistive anisotropy in perovskite manganites

by

Mehmet Egilmez

A thesis submitted to the Faculty of Graduate Studies and Research
in partial fulfillment of the requirements for the degree of

Doctor of Philosophy

Department of Physics

©Mehmet Egilmez
Fall 2009
Edmonton, Alberta

Permission is hereby granted to the University of Alberta Libraries to reproduce single copies of this thesis and to lend or sell such copies for private, scholarly or scientific research purposes only. Where the thesis is converted to, or otherwise made available in digital form, the University of Alberta will advise potential users of the thesis of these terms.

The author reserves all other publication and other rights in association with the copyright in the thesis and, except as herein before provided, neither the thesis nor any substantial portion thereof may be printed or otherwise reproduced in any material form whatsoever without the author's prior written permission.

Library and Archives Canada

Published Heritage Branch

395 Wellington Street
Ottawa ON K1A 0N4
Canada

Bibliothèque et Archives Canada

Direction du Patrimoine de l'édition

395, rue Wellington
Ottawa ON K1A 0N4
Canada

Your file *Votre référence*
ISBN: 978-0-494-51223-4
Our file *Notre référence*

NOTICE:
The author has granted a non-exclusive license allowing Library and Archives Canada to reproduce, publish, archive, preserve, conserve, communicate to the public by telecommunication or on the Internet, loan, distribute and sell theses worldwide, for commercial or non-commercial purposes, in microform, paper, electronic and/or any other formats.

The author retains copyright ownership and moral rights in this thesis. Neither the thesis nor substantial extracts from it may be printed or otherwise reproduced without the author's permission.

AVIS:
L'auteur a accordé une licence non exclusive permettant à la Bibliothèque et Archives Canada de reproduire, publier, archiver, sauvegarder, conserver, transmettre au public par télécommunication ou par l'Internet, prêter, distribuer et vendre des thèses partout dans le monde, à des fins commerciales ou autres, sur support microforme, papier, électronique et/ou autres formats.

L'auteur conserve la propriété du droit d'auteur et des droits moraux qui protège cette thèse. Ni la thèse ni des extraits substantiels de celle-ci ne doivent être imprimés ou autrement reproduits sans son autorisation.

In compliance with the Canadian Privacy Act some supporting forms may have been removed from this thesis.

While these forms may be included in the document page count, their removal does not represent any loss of content from the thesis.

Conformément à la loi canadienne sur la protection de la vie privée, quelques formulaires secondaires ont été enlevés de cette thèse.

Bien que ces formulaires aient inclus dans la pagination, il n'y aura aucun contenu manquant.

Canada

Examining Committee

Jan Alexander Jung, Physics

Kim H. Chow, Physics

Frances Fenrich, Physics

Vadim Kravchinsky, Physics

Thomas Etsell, Chemical and materials engineering

A. S. Alexandrov, Physics, Loughborough University, UK

Abstract

We have investigated several topics in the area of manganites including oxygen disorder, grain boundaries, low field magnetoresistance, magnetoresistive anisotropy and magnetic properties. Studied materials were in the form of polycrystalline samples and epitaxial thin films. The studied compounds were $Sm_{1-x}Sr_xMnO_3$ (SSMO) and $La_{1-x}Ca_xMnO_3$ (LCMO).

1. We have studied the effects of oxygen disorder and grain boundary disorder in SSMO system close to half ($x \approx 0.5$) hole doping level. The temperature dependencies of resistivity and magnetoresistance were measured as a function of the vacuum annealing time. We observed a logarithmic increase of the resistivity as a function of vacuum annealing time. We have shown that an increasing grain boundary disorder softens the magnetic phase transition from a first order phase transition into a second order transition. Furthermore, the peaks in the resistivity and specific heat are broadened and there is an increase in the charge-carrier scattering rates in the metallic state. On the other hand, the polaronic hopping activation energies in the insulating state changed slightly as a function of grain boundary disorder. The origin of these phenomena is discussed. Magnetoresistive anisotropy has been studied as a function of the grain size. Results showed a strong grain size dependence of anisotropic electrical transport in granular samples of manganites.

2. We investigated the anisotropic magnetoresistance (AMR) in ultrathin LCMO manganite films grown on various substrates. It was found that depending on the strain state, the AMR in some of these systems exceeds 100% and can even change sign. These changes are very dramatic when compared to the few percent change in AMR in conventional ferromagnets. The mechanism behind these changes in the AMR is discussed. We have studied the effects of strain on resistive peak broadening with a simple percolation model. We have shown that strain associated with a lattice mismatched substrate in thin films can

cause new electronic behavior, not found in bulk materials or thicker films of the same chemical composition. Resistivity of the ultra thin films exhibit strong relaxation effects when measured as a function of time in a constant magnetic field.

Preface

The research presented in this thesis was carried out in the Department of Physics at the University of Alberta under the supervision of Professor Jan Alexander Jung from September 2004 to March 2009.

Unless otherwise stated, the material presented is based on my own work. No part of this thesis has been or is being submitted for any other qualification at this or any other university.

Most of the work presented here based on the following articles:

1. "Effects of correlated disorder on the magneto-transport in colossal magnetoresistance manganites"
   M. Egilmez, Z. Salman, KH Chow, J Jung, *PSS-Rapid Research Letters*, 4, 94 (2009)

2. "The anisotropic magnetoresistance in epitaxial thin films and polycrystalline samples of $La_{0.65}Ca_{0.35}MnO_3$"
   M. Egilmez, Rongchao Ma, KH Chow, J Jung . *Journal of Applied Physics*, 105, 07D706 (2009).

3. "Correlation of structural phase transition and electrical transport properties of manganite films on $SrTiO_3$"
   M. Egilmez, MM Saber, I. Fan, KH Chow, J Jung *Physical Review B*, 78 172405 (2008).

4. "Dramatic strain induced modification of the low field anisotropic magnetoresistance in manganite films "
   M. Egilmez, MM Saber, AI Mansour, Rongchao Ma, KH Chow, J Jung *Applied Physics Letters*, 93, 182505 (2008).

5. " Softening of the First-order magnetic phase transition and magneto-transport properties of $Sm_{0.55}Sr_{0.45}MnO_3$ manganite"

M. Egilmez, Z. Salman, A. I. Mansour, K.H. Chow, and J. Jung *Journal of Applied Physics*, 104 093915 (2008).

6. "Oxygen-isotope exchange and cation disorder effects on magneto-transport properties of $(Sm_{1-y}Gd_y)_{0.55}Sr_{0.45}MnO_3$"
   M. Egilmez, I. Isaac, D.D. Lawrie, K.H. Chow, and J. Jung *Journal of Materials Chemistry*, 18 5796 (2008).
   **The data of this paper was mostly collected by Dr.Franck, Dr. Isaac and Dr. Jung from University of Alberta.*

7. "Percolative model of the effect of disorder on the resistive peak broadening in $La_{2/3}Ca_{1/3}MnO_3$ near the metal-insulator transition"
   M. Egilmez, K.H. Chow, and J. Jung, *Applied Physics Letters*, 92, 162515 (2008).

8. "Metal-insulator transition, specific heat, and grain-boundary-induced disorder in $Sm_{0.55}Sr_{0.45}MnO_3$"
   M. Egilmez, K.H. Chow, J. Jung, I. Fan, A.I. Mansour, and Z. Salman, *Applied Physics Letters*, 92, 132505 (2008).

9. "Lattice-strain control of magneto-resistivity and magneto-resistive anisotropy induced by ion-beam-milling in $La_{0.65}Ca_{0.35}MnO_3$ films near the metal-insulator transition"
   M. Egilmez, A.I. Mansour, M.M. Saber, K.H. Chow, and J. Jung, *Applied Physics Letters*, 92, 022501 (2008)

10. "Magnetoresistive anisotropy and magnetoresistivity in strained $La_{0.65}Ca_{0.35}MnO_3$ films near the metal insulator transition"
    M. Egilmez, R. Patterson, K.H. Chow, and J. Jung, *Applied Physics Letters*, 90, 232506 (2007).

11. "Quench-disorder-controlled magnetoresistance in $Sm_{0.55}Sr_{0.45}MnO_3$"
    M. Egilmez, K.H. Chow, J. Jung, and Z. Salman *Applied Physics Letters*, 90,

162508 (2007).

12. "Oxygen-redistribution-induced disorder and magneto-transport properties of $Sm_{0.55}Sr_{0.45}MnO_3$ manganites"
M. Egilmez, K.H. Chow, and J. Jung, *Applied Physics Letters*, 89, 062511 (2006).

See Chapter 1 for the full list of publication of the author.

ACKNOWLEDGEMENT

I would like to express my deep thanks and appreciation to my supervisor Dr. Jan Jung for his great continuous support, guidance and friendship during the course of the research and preparation of this thesis. I am really impressed by his deep insight in research and his excellent personality. The amount of time and effort that he devoted to help me in my research were indispensable. I have benefitted from his wide range of knowledge almost in everything from superconductivity and magnetism to history and archeology. I really enjoyed the time spent with him.

Another special thank you goes to Dr. Kim Chow. His deep physics knowledge and his valuable suggestions (perhaps from different point of view which I have never thought of) always impressed me. I enjoyed his friendship and I would say it was a pleasure to work with him.

I would like to express my thanks to the members of my committee Professors Vadim Kravchinsky, Frances Fenrich, Thomas Etsell from University of Alberta and Professor A. Sasha Alexandrov from Loughborough University for their comments and suggestions on my research and thesis.

I would like to express special thanks to Dr. Maher Abdelhadi and Rob Paterson for their assistance in the experimental set up and the data acquisition programme. I am also grateful to Dr. Zaher Salman of University of Oxford for some of the magnetization measurement. The experimental part of this research required the assistance of several people, I would like to thank Mr. D. Mullin, Mr Greg Popowich and Mr. T. Walford for their valuable technical support when needed.

I am also grateful to my dear coffee break friends Fabio Mezzacapo and to Faruk Uygul for their friendship. I am also grateful to my lab. colleagues in no particular order; Isaac Fan, Ahmad Mansour, Rongchao Ma and Mohammed Elsayed for their contributions during the course of the thesis.

I wish like to thank University of Alberta, Department of Physics and Dr. Jung for financial support trough Golden Bell Jar, Andrew Stewart, Dissertation fellowship awards and research and teaching assistantships.

Finally, none of this would be possible without the constant love and support of Handan and my parents.

Abbreviations

1. MR: Magnetoresistance
2. CMR: Colossal magnetoresistance
3. GMR: Giant magnetoresistance
4. AMR: Anisotropic magnetoresistance
5. TMR: Tunneling magnetoresistance
6. TAMR: Tunneling anisotropic magnetoresistance

Contents

1 Overview **1**

1.1 List of Publications 5

2 Introduction **12**

2.0.1 Motivations 13

2.1 Phase diagrams 16

2.1.1 $La_{1-x}Ca_xMnO_3$ 16

2.1.2 $Sm_{1-x}Sr_xMnO_3$ 22

3 Basic properties and theoretical understanding of manganites **28**

3.1 Introduction 28

3.2 Crystal field effect and Jahn Teller distortions 29

3.3 Double exchange model 33

3.4 Simple realistic model for manganites 36

3.4.1 Coulombic terms 37

3.4.2 Heisenberg term 37

3.4.3 The electron-phonon coupling 38

3.4.4 One orbital model 41

3.4.5 $J_H = \infty$ limit 42

3.4.6 Jahn-Teller phononic and Coulombic models (Two-orbital model) 42

3.4.7 Main results from theoretical phase separation models of manganites 43

3.4.8 Phase separation caused by the influence of disorder on first-order transitions . . . 49
3.4.9 Resistivity of manganites in the mixed phase regime . . . 51
3.5 Carrier density collapse and colossal magnetoresistance in doped manganites . . . 54
3.5.1 Ferromagnetic transition in doped manganites . . . 55

4 Experimental set-up and procedure **66**
4.1 Sample preparation . . . 66
4.1.1 Polycrystalline (Bulk) samples . . . 66
4.1.2 Oxygen stoichiometry in bulk samples . . . 67
4.1.3 Thin film growth . . . 68
4.2 Sample characterization . . . 70
4.2.1 Resistivity measurement . . . 73
4.2.2 Magnetization measurements . . . 76
4.2.3 Structural characterizations . . . 76

5 Oxygen redistribution induced disorder and magneto-transport properties of $Sm_{0.55}Sr_{0.45}MnO_3$ manganites **78**
5.1 Introduction . . . 78
5.2 The resistivity of $Sm_{1-x}Sr_xMnO_3$ system . . . 80
5.3 Vacuum annealing induced Oxygen disorder in $Sm_{0.55}Sr_{0.45}MnO_3$ . . . 82
5.4 Discussion and summary . . . 86

6 Disorder induced softening of the first-order magnetic phase transition and grain size dependent properties of $Sm_{0.55}Sr_{0.45}MnO_3$ manganite **94**
6.1 Introduction . . . 94
6.2 Sample preparation and structural properties . . . 96
6.3 Magnetic properties . . . 101
6.4 Specific heat and entropy . . . 108

6.5 Electrical transport 113
6.6 Summary and conclusions 117

7 Grain size dependence of the magnetoresistive anisotropy in polycrystalline $Sm_{0.55}Sr_{0.45}MnO_3$ 125
7.1 Introduction 125
7.2 Results and discussion 127
7.3 Summary and conclusions 135

8 Magnetotransport and magnetoresistive anisotropy in $Sm_{0.55}Sr_{0.45}MnO_3/Nd_{0.55}Sr_{0.45}MnO_3$ bilayers 138
8.1 Introduction 138
8.2 Results and discussion 141
8.3 Summary and conclusions 146

9 Magnetoresistive anisotropy and magneto-resistivity in strained $La_{0.65}Ca_{0.35}MnO_3$ films near the metal-insulator transition 149
9.1 Introduction 149
9.2 Results and discussion 151
9.3 Summary and conclusions 158

10 Dramatic strain induced modification of the low field anisotropic magneto-resistance in ultra-thin manganite films 161
10.1 Introduction 161
10.2 Results and discussion 163
10.3 Summary and conclusions 169

11 Lattice-strain control of magneto-resistivity and magneto-resistive anisotropy induced by ion-beam-milling in $La_{0.65}Ca_{0.35}MnO_3$ films near the metal-insulator transition 173
11.1 Introduction 173

11.2 Results and discussion 176
11.3 Summary and conclusions 182

12 Percolative model of the effect of disorder on the resistive peak broadening in $La_{2/3}Ca_{1/3}MnO_3$ near the metal-insulator transition 185
12.1 Introduction 185
12.2 Results and discussion 187
12.3 Summary and conclusions 194

13 Strain induced meta stable phases in $La_{0.65}Ca_{0.35}MnO_3$ films 197
13.1 Introduction 197
13.2 Results and discussions 198
13.3 Summary and conclusions 205

14 Summary and future work on manganites 208
14.1 Future work 213
14.1.1 Correlation between the structural phase transition and the electrical transport properties of manganite films on $SrTiO_3$. 213
14.1.2 Oxygen-isotope exchange and quenched disorder effects on magnetotransport properties of $(Sm_{1-y}Gd_y)_{0.55}Sr_{0.45}MnO_3$ 215
14.1.3 Magnetotransport in $Nd_{0.55}Sr_{0.45}MnO_3$ films 217
14.1.4 Magnetic tunnel junctions with MgO tunnel barrier 217

List of Tables

6.1 Parameters that describe SSMO(T_a): ϵ is the magnitude of the micro-strain obtained from a W-H analysis, GS1 and GS2 corresponds to the grain size obtained from SEM and W-H analysis, T_{MIT} is the metal-insulator transition temperature, T_c is the Curie temperature. 100

6.2 Parameters that describe SSMO(T_a): T_{MIT} is the metal-insulator transition temperature, T_c is the Curie temperature, ρ_0 is the residual resistivity, ρ_2 is the electron-electron scattering coefficient, ρ_5 is the electron-phonon scattering coefficient, b is the polaronic coefficient, Δ is the bipolaron binding energy, and δC_p is the full width at half maximum of the specific heat peak. 101

7.1 Parameters that describe the properties of the SSMO samples: T_p is the metal insulator transition temperature (MIT), ρ_p is the resistivity at the MIT, D is the grain size 132

12.1 Parameters that describe LCMO crystal and films: t is the film thickness, T_p is the metal-insulator transition temperature, ρ_0 is the residual resistivity, ρ_2 and ρ_5 are the electron-electron scattering and the electron-phonon scattering coefficients, respectively, b is the polaronic coefficient, Δ is the bipolaron binding energy, and Γ is the width of the Gaussian distribution. The fitting parameters errors are around 1%. IM corresponds to ion milled. 186

List of Figures

2.1 An illustrative representation of the Colossal Magnetoresistance effect in (a) $(Sm)_{0.55}Sr_{0.45}MnO_3$ (b) $(Sm_{0.5}Gd_{0.5})_{0.55}Sr_{0.45}MnO_3$. T_M corresponds to metal insulator transition temperature. Figure is reproduced from Egilmez *et al.*[5] 14

2.2 The magnetization, resistivity, and magnetoresistance of $La_{1-x}Ca_xMnO_3$ (x=0.25), as a function of temperature at various magnetic fields. The inset is ρ at low temperatures. Reproduced from Schiffer *et al.*[7] . . . 17

2.3 Phase diagram of $La_{1-x}Ca_xMnO_3$, constructed from measurements of macroscopic quantities such as the resistivity and magnetic susceptibility, reproduced from Cheong and Hwang.[11] FM: Ferromagnetic Metal, FI: Ferromagnetic Insulator, AF: Antiferromagnetism, CAF: Canted AF, and CO: Charge/Orbital Ordering. FI and/or CAF could be a spatially inhomogeneous states with FM and AF coexistence. . . 18

2.4 The charge and orbital ordering configurations for $La_{1-x}Ca_xMnO_3$ with x=0, 1/2, and 2/3.Open circles are Mn^{4+} and the lobes show the orbital ordering of the e_g-electrons of Mn^{3+}. Figure reproduced from Cheong and Hwang.[11] 20

2.5 Temperature dependence of the electrical resistivity for $Sm_{1-x}Sr_xMnO_3$ crystals. Arrows indicate Curie temperatures, up triangle is indicative of the Neel temperature. Figure reproduced from Ivanov *et al.*[19] . . 21

2.6 Phase diagram of $Sm_{1-x}Sr_xMnO_3$ crystals. The phases are denoted by: P/I: paramagnetic insulator, CAF/I: canted AF insulator, F'/I: possible inhomogeneous or canted F insulator, F/M: F metal, LCO/I: local charge ordering insulator, AF1/I: antiferromagnetic (A-type) insulator, AF2/I: antiferromagnetic (C-type) insulator, WF/I: weak F insulator. Cross points are taken from Martin *et al.*[22], all other pointsthis work, linesguide for the eyes. Figure reproduced from Ivanov *et al.*[19] . . . 23

2.7 The electronic phase diagram of $Sm_{1-x}Sr_xMnO_3$ $0.30<x<0.60$. The ferromagnetic metal, the A-type antiferromagnetic state and the charge/orbital-ordered insulator are denoted as FM, AF (A-type) and CO/OOI, respectively. The transition temperatures from (to) the FM, AF, and CO/OOI are denoted as open (closed) squares, triangles, and circles, respectively. Figure reproduced from Tomioka *et al.*[23] 24

3.1 The angular distribution of the s, p and d orbitals. d_{z^2} orbital is sometimes refereed as $d_{z^2-r^2}$ 30

3.2 Crystal field splitting of five-fold degenerate atomic $3d$ levels in to lower t_{2g} and higher e_g levels. Jahn-Teller distortion of MnO_6 octahedron further lifts each degeneracy as shown in the figure. Figure is reproduced from Tokura.[3] 32

3.3 Schematic features of the double exchange mechanism. 34

3.4 Schematic features of the double exchange mechanism. Representation of the hopping exchange integral. 35

3.5 MnO_6 octahedron at site **i**. The labeling for oxygen ions is shown. . . 40

3.6 Phase diagram of the two-orbital model for manganites in 1D and T=0 including JT phonons, obtained with MC techniques.[10] S-F labels a spin-FM configuration; O-F, O-AF, and O-D denote a state where the orbital degrees of freedom are ordered uniformly, staggered, or disordered, respectively; PS indicates a phase separated state, and AF is an anti-FM state. Hund coupling is J_H=8 and Heisenberg coupling between localized classical spins is J=0.05, both in units of the hopping among the same orbitals. Meaning of the dashed line is a bordering some realistic limit for simulations when compared with the experiments and explained in more detail original citation.[16] 46

3.7 Qualitative representation of a macroscopic phase-separated state (A) as well as possible CI states stabilized by extended Coulomb interactions, such as spherical droplets (B) or stripes (C). Diameter of droplets and stripes are expected to be microscopic, but realistic calculations are still lacking. 48

3.8 Top panel: Phase diagram results for different disorder levels (W) for details see book by Dagotto.[8] Bottom panel: experimental phase diagram for $RE_{0.55}Sr_{0.45}MnO_3$.[9] Note that with the presence of finite disorder simulations will reproduce the experimental data more convincingly. 50

3.9 (a) Schematic representation of the mixed-phase state near percolation. The arrows indicate conduction either through the insulating or metallic regions depending on temperature. (b) Two resistances in parallel model for Mn-oxides. The (schematic) plot for the effective resistance R_{eff} vs. T arises from the parallel connection of metallic (percolative) R_M^{per} and insulating R_I resistances.[27] Right panel: Net resistivity ρ_{dc} of the 100×100 random resistor network used in the a and b, but with a metallic fraction p changing with temperature. Representative values of p are indicated. Results averaged over 40 resistance configurations are shown.[27] 52

3.10 A schematic diagram of free-polaron (P) and polaron bound-pair (BP) densities of states at temperatures below and above T_c for up-spin (↑) and down-spin (↓) moments. The pairs (BP) break below T_c if the exchange J_{pd} S between p-hole polarons and Mn d^4 local spins exceeds the pair binding energy Δ, as in the case shown. The exchange interaction of polarons with the localized spins sets in below T_c; the spin-up polaron sub-band sinks abruptly below the bipolaron band, causing the break-up of the immobile bipolarons (left-hand panel). A sudden drop (collapse) of the density of the current carriers (polarons) in the vicinity of the ferromagnetic transition is the cause of a large peak in resistivity and colossal magnetoresistance. 58

3.11 Polaron density n/x and magnetization as a function of temperature $t = 2k_BT/J_{pd}S$ in a doped charge-transfer insulator near (a) the first order, $\delta = \Delta/J_{pd}S$=0.5, and (b) second order, δ= 0.25, phase transitions (doping $x = 0.25$). Inset: The critical value of the relative binding energy of polaron pairs δ separating the regions of the first and second order phase transitions. 59

3.12 Inverse polaron density for different magnetic fields, $\delta = \Delta/J_{pd}S$=0.5, doping x 0.25. Note that the transition is a strong first order, and becomes continuous only when the external magnetic field exceeds some critical value. Inset: Schematic of polaron (P) and bipolaron (BP) densities of states at temperatures below and above T_c for up (↑) and down (↓) spin moments. The pairs (BP) break below Tc if exchange $J_{pd}S$ exceeds the pair binding energy Δ. 60

3.13 Resistivity of $La_{0.75}Ca_{0.25}MnO_3$ calculated within the present theory for the pair binding energy Δ= 900 K, and polaron exchange with the localized Mn^{3+} spins $J_{pd}S$= 2250 K (a), compared with experiment [30] on panel (b). Note an extreme sensitivity of the theoretical resistivity to external magnetic field (a), observed experimentally (b) for the doped manganite. 61

4.1 A picture from sputtering system during an epitaxial manganite film deposition 69

4.2 A picture of resistivity measurement unit 71

4.3 Magnetic field and current configurations applied during the measurements of resistivity of manganite thin films. 74

5.1 Temperature dependence of resistivity of SSMO for 0.40< x <0.50. . 81

5.2 The resistivity at the Metal insulator transition temperature and the metal insulator transition temperature for SSMO for different vacuum anneal conditions. The lines are guide for eye. 83

5.3 Temperature dependence of resistivity of $Sm_{0.55}Sr_{0.45}MnO_3$ for different annealing times at 325°C in vacuum. 85

5.4 The change in T_p (metal insulator transition temperature) with an increasing annealing time. The line is a guide to the eye. 86

5.5 Temperature dependence of resistivity ρ/ρ_{max} of $Sm_{0.55}Sr_{0.45}MnO_3$ normalized to the maximum magnitude of resistivity ρ_{max} and to T_p. The curves are plotted for different annealing times at 325°C in vacuum. The inset shows the change in FWHM (full width at half maximum) of the resistive peak with an increasing annealing time. The line is a guide to the eye. 87

5.6 Dependence of (a) the magnitude of resistivity at the maximum ρ_{max} measured in a field of 0 T and 0.68 T, and (b) the magnitude of magnetoresistance at the maximum, MR_{max}, measured in a magnetic field of 0.68 T, on the annealing time at 325°C in vacuum. The lines are guides to the eye. 88

5.7 Dependence of the magnitude of resistivity at the maximum ρ_{max} measured in a field of 0 T and 0.68 T on the annealing time at $325°C$ in vacuum. In both 0 T and 0.68 T, ρ_{max} shows logarithmic dependence on the annealing time. The lines are the fits to the data. Similar behavior was observed in all $Sm_{0.55}Sr_{0.45}MnO_3$ samples studied. . . . 89

6.1 X-ray diffraction patterns of SSMO(T_a): (a) SSMO(1200) (b) SSMO(1300) (c) SSMO(1400) (d) SSMO(1500). The intensity of each pattern was normalized to the (200) peak intensity. 97

6.2 SEM surface micrographs of SSMO annealed at different temperatures T_a. 99

6.3 Williamson-Hall plots of SSMO(T_a) for different annealing temperatures. 100

6.4 Temperature dependence of the ZFC magnetization for SSMO(T_a) samples measured in a field of 0.025 T (figures (a)-(d)), and in a field of 0.75 T (figures (e)-(h)). 103

6.5 Temperature dependence of the ZFC (solid symbols) and FC (open symbols) magnetization measured in a field of 0.025 T for (a) SSMO(1200) (b) SSMO(1300) (c) SSMO(1400) (d) SSMO(1500). Temperature is normalized to T_c obtained from the minimum of the temperature dependence of dM/dT, which corresponds very closely to the onset of the increase in magnetization M. The arrows indicate the warming and cooling cycles. 104

6.6 Magnetic field dependence of magnetization of SSMO(T_a) for different annealing temperatures T_a: (a) SSMO(1200) (b) SSMO(1300) (c) SSMO(1400) (d) SSMO(1500). Arrows indicate an increasing or a decreasing applied field. 106

6.7 (a)-(d) H/M versus M^2 plotted for SSMO(T_a) samples for temperatures close to 130 K. The data were obtained from the field dependence of the magnetization. Note the positive sign of the slope d(H/M)/d(M^2) for SSMO(1200) and SSMO(1300) samples (the second-order phase transition) and the negative one for SSMO(1500) and SSMO(1400) samples (the first-order magnetic phase transition). 107

6.8 Temperature dependence of reduced magnetization(Magnetization normalized to its maximum in the M(T) curves) for all SSMO(T_a) samples. 108

6.9 Temperature dependence of the specific heat (C_p) for SSMO(T_a) samples. 109

6.10 Temperature dependence of the specific heat jump (ΔC_p) at the transition for SSMO(T_a) samples. 110

6.11 Temperature dependence of the entropy change (Δ S) at the vicinity of metal insulator transition. 111

6.12 Temperature dependence of the inverse magnetization measured in a field of 0.025 T for SSMO(T_a) samples. The straight dashed lines are the fits of the theoretical Curie-Weiss law to the high temperature data with the Curie constants of 2.49 and 2.57 (emu K)/T for SSMO(1200-1300) and SSMO(1400-1500) samples, respectively. 112

6.13 Temperature dependence of resistivity ρ measured in zero magnetic field for al samples. Solid lines are fits (see text). 114
6.14 Temperature dependence of resistivity ρ data far below the MIT. Solid lines are fits (see text). 116
6.15 Temperature dependence of the TCR measured at zero field for SSMO(T_a) samples. 116
6.16 Temperature dependence of resistivity ρ measured in zero magnetic field for SSMO(T_a) samples and temperature dependence of the magnetoresistivity MR measured in a field of 0.68 T for SSMO(T_a) samples. . 118
6.17 Dependence of resistivity on magnetic field measured at different temperatures for SSMO(T_a) samples. The resistivities are normalized to the value of zero field resistivity. The lines are guides to the eye. . . . 119

7.1 [Left panel] Temperature dependence of the resistivity for SSMO(T_a). For definitions of $\rho_\perp$ and $\rho_\parallel$ see text. Insets are SEM pictures for corresponding samples. [Right panel] The temperature dependence of magnetoresistance measured in a field of 6.8 kG for two different resistivity measurement configuration. For definitions of $MR_\perp$ and $MR_\parallel$ see text. 129
7.2 [Left panel] (Color online) Angular dependence of resistivity measured at 127 K in fields of 0.85, 2.10 and 6.80 kG for SSMO(T_a). The lines are fits to the theoretical expression (see text). [Right panel] Temperature dependence of the AMR measured in fields of 0.42, 0.85, 2.1, 3.4, 5.1 and 6.8 kG for SSMO(T_a). The lines are guides for the eye. 130

7.3 [Top panel] A schematic representation for the magnetotransport behavior of the manganite samples with grains. Here, circles represents individual grains, large arrow inside the circles corresponds to the internal magnetization direction within the grain. The region with small arrows around the individual grains stand for the grain-boundary (small arrows indicates the magnetization direction within the grain-boundary region). [Bottom panels] A schematic representation for the anisotropic magnetotransport behavior of the manganite samples with grains. Graphs represent the field dependence of the resistivity of SSMO(T_a) for $\rho_\perp$ and $\rho_\parallel$ configuration at 125 K. 131

8.1 [Top panel] Temperature dependence of the resistivity for SSMO grown on LAO and STO. [Bottom panel] Temperature dependence of the resistivity for NSMO buffered SSMO grown on LAO and STO. For definitions of $\rho_\perp$ and $\rho_\parallel$ see text. 140

8.2 The temperature dependence of magnetoresistance measured in a field of 6.8 kG for two different resistivity measurement configuration. For definitions of $MR_\perp$ and $MR_\parallel$ see text. 142

8.3 [Top panel] Angular dependence of resistivity measured at 100 K in different magnetic fields for NSMO buffered SSMO films. 143

8.4 Temperature dependence of the AMR measured in different fields for NSMO buffered SSMO films. The lines are guides for the eye. 144

9.1 Magnetic field and current configurations applied during the measurements of resistivity of LCMO thin films. 151

9.2 (a) Temperature dependence of the resistivity measured in a zero magnetic field for 10 nm and 1000 nm thick samples. Inset: Thickness dependences of the value of the peak resistivity and the temperature at which the peak resistivity occurs T_p. (b) Temperature dependence of the magneto-resistivity MR measured in a magnetic field of 0.68 T for 10 nm and 1000 nm samples. Inset: Thickness dependence of the MR. 152

9.3 (a) and (b) Temperature dependence of the magneto-resistive anisotropy AMR_1^{out} measured for 10 nm and 1000 nm thick LCMO films in a field of 0.21 T and 0.68 T, respectively. (c) and (d) Thickness dependence of the maximum values of the "out-of-plane" AMR_1^{out} and AMR_2^{out} for a field of 0.21 T and 0.68 T, respectively. (e) and (f) Thickness dependence of the maximum values of the "in-plane" AMR^{in} for a field of 0.21 T and 0.68 T, respectively. The lines are guides for the eye. . . . 154

9.4 (a) and (b) Magnetic field dependence of the resistivity measured for 10 nm and 1000 nm thick LCMO films, respectively, for different magnetic field-current configurations (see Fig. 9.1). The resistivities were measured at a temperature corresponding to the maximum AMR. They were normalized to the value of the zero-field resistivity. An increase followed by a decrease of the magnetic field shows negligible hysteretic effects. (c) and (d) The field dependence of the maximum values of the "out-of-plane" and the "in-plane" AMRs for 10 nm and 1000 nm thick films, respectively. The lines are guides for the eye. 155

10.1 Temperature dependence of the (a)-(b) Resistivity in zero field and temperature dependence of (c)-(d) Magnetoresistivity of LCMO/STO and LCMO/LAO samples in a field of 6800 Gauss. 163

10.2 (a)-(b) The angular dependence of the normalized resistivity at the AMR peak's maximum temperature measured in the 7 and 150 nm thick films. The solid lines are the fits to the data (see text); The corresponding polar plots of the angular dependence of the normalized resistivity at the AMR peak's maximum temperature, measured for different applied fields. 164

10.3 The angular dependence of the normalized resistivity at the AMR peak's maximum temperature measured in the 7 and 150 nm thick films. The solid lines are the fits to the data (see text); The corresponding polar plots of the angular dependence of the normalized resistivity at the AMR peak's maximum temperature, measured for different applied fields. 166

10.4 The angular dependence of the resistivity measured at 85 K in the 7 nm thick LCMO/LAO and LCMO/STO films; The corresponding dependence of the AMR on the applied field. 167

11.1 (a) Ion-beam-milling experimental set-up; (b) Temperature dependence of the resistivity in a zero magnetic field for the ion-beam-milled $La_{0.65}Ca_{0.35}MnO_3$ films of thicknesses between 10 and 650 nm; (c) Thickness dependence of the resistivity at the resistive peak; (d) Thickness dependence of the metal-insulator transition temperature (T_p). The lines are guides for the eye. 175

11.2 Magneto-resistivity (MR) measured in a magnetic field of 0.68 T for the ion-beam-milled films. (b) Thickness dependence of the maximum values of the MR. The lines are guides for the eye. 176

11.3 [(a)-(b)] Temperature dependence of the magneto-resistive anisotropy AMR^{out} for the ion-beam-milled films in a field of 0.21 and 0.68 T, respectively. Thickness dependence of the maximum value of the AMR^{out} [(c)-(d)], and the AMR^{in} [(e)-(f)] for the ion-beam-milled (both un-annealed and oxygen-annealed) films and the as-grown films in a field of 0.21 and 0.68 T, respectively. The lines are guides for the eye. . . . 179

11.4 Temperature dependence of the normalized resistivity [(a)-(b)], in a zero field measured for the 10 and 60 nm thick ion-beam-milled (both un-annealed and oxygen-annealed) films and the as-grown films. Temperature dependence of the magneto-resistivity (MR) [(c)-(d)] and the the magneto-resistive anisotropy AMR^{out} [(e)-(f)] of the 10 and 60 nm thick ion-beam-milled (both un-annealed and oxygen-annealed) films and the as-grown films in a field of 0.68 T. 180

12.1 (a) Temperature dependence of generic LCMO data. Solid lines indicate the extrapolated fits at low temperatures to a power law and at high temperatures to bi-polaronic hopping model. (b)-(e) Temperature dependence of resistivity ρ measured in zero magnetic field, and the temperature coefficient of resistance (TCR) for LCMO crystal and films. The resistivity data of single crystal sample was taken from the Tokura.[16] The shaded area marks the mixed metal-insulator state. . 188

12.2 Temperature dependence of the fraction ν of the metallic phase and the corresponding Gaussian distribution of transition temperatures in LCMO crystal and films. 189

12.3 Temperature dependence of resistivity ρ measured in zero magnetic field. The resistivity was normalized to that at the peak's maximum. The solid lines represent the fits to the data. 190

12.4 Temperature dependence of the reduced magnetization $M(T)/M_{max}$ and of the fraction ν of the metallic phase in a 650 nm thick film. . . 191

13.1 Temperature dependence of resistivity of LCMO/LAO for 7 nm, 9 nm, 15 nm and 150 nm samples. 198
13.2 The time dependence of resistivity measured in a constant field 0f 6.8 kG at 80 K for films of different thicknesses. 199
13.3 Aging effect for 7 nm and 150 nm LCMO/LAO films. 200
13.4 The temperature dependence of resistivity of 7 nm LCMO/LAO sample measured in zero field and field of 6.8 kG for different aging conditions. 201
13.5 Time dependence of resistivity measured in a constant field of 6.8 kG at different temperatures. 202
13.6 Temperature dependence of relaxation rate for all samples. The lines are guides for the eye. 203
13.7 (a) Temperature dependence of resistivity of 15 months aged $La_{0.65}Ca_{0.35}MnO_3$ sample, (b) temperature dependence of relaxation rate for all samples, (c)-(e) A qualitative description of the electronic phase separation in our samples. 204

14.1 (a) Temperature dependence of ΔTCR of LCMO films obtained by subtracting the background from the temperature dependence of TCR shown in Figure 1. (b) Temperature dependence of ΔTCR normalized to its maximum value. The lines are guides for the eye. 214
14.2 The field dependence of the isotope exchange exponent α_0 for different levels of quenched disorder. All σ^2 values (quench disorder) are in units of $\AA^2$. The lines are guides for the eye. 216
14.3 Temperature dependence of resistance of NSMO/LAO films for different post annealing conditions. 218
14.4 Angular dependence of resistance for 250 nm NSMO/STO film measured at 80 K for different magnetic fields. 219
14.5 Definition of tunnel magnetoresistance. 220
14.6 Bias voltage dependence of the tunneling current in LCMO/MgO/LCMO junctions for relatively low voltages. 221

14.7 Bias voltage dependence of the tunneling current in LCMO/MgO/LCMO junctions for relatively high voltages. 222
14.8 Bias voltage dependence of the TMR in LCMO/MgO/LCMO junctions for 3.4 and 6.8 kG. 223
14.9 Angular dependence of the tunneling current LCMO/MgO/LCMO junctions for different bias voltages in a constant field of 6.8 kG. At some certain angles the carriers starts to tunnel across the junction causing a discontinuities in the data. 224

Chapter 1

Overview

Over the last several decades, many materials exhibiting complex properties have been discovered, such as high temperature superconductors (cuprates) and Mn-based complex magnetic oxides (manganites). In particular, manganites such as $RE_{1-x}A_xMnO_3$ (RE and A are trivalent rare earth and divalent alkaline earth elements respectively) attract a great interest of the scientific community because of the rich physics which they exhibit: ferromagnet-antiferromagnet, charge-orderdisorder, and metalinsulator phase transitions, anomalous thermal lattice expansions, and particularly colossal magnetoresistance (CMR). Many of these interesting properties are result of close interplay of lattice, charge, and spin degrees of freedom.

Despite the fact that microscopic physics involved in manganites is not fully understood, the physical properties of manganites show extremes of functional behavior such as CMR. CMR has been the driving force in manganite research with the expectation of possible magnetoresistance based device applications. For potential applications the understanding of the basic properties and controlling the properties which are suitable for applications is essential. In order to contribute to the studies aimed at the understanding of these complex materials for potential applications such as magnetic read heads or sensors we have studied over 300 samples of manganites in the form of bulk and epitaxial thin films.[5]

The dissertation consists of 14 chapters.

Chapter 1 is the overview of the thesis; the content of the each individual chapter is briefly summarized here. The last part of this chapter lists the publications of the author.

In Chapter 2 we have given a brief history of the manganites along with their importance for the scientific community. This chapter also involves the main motivations of the thesis. We can summarize some of our motivations in addressing the following questions: i) What is the effect of the oxygen disorder on transport properties of manganites in the low magnetic field regime? ii) What is the effect of the grain-boundary induced disorder on transport properties and the magnetic phase transitions of manganites in the low magnetic field regime? iii) How could the low magnetic field anisotropic magnetoresistance be improved in manganite films? iv) How does the lattice disorder affect the low field anisotropic magnetoresistance in manganite films? In this chapter we also discuss the magnetic phase diagrams of the $La_{1-x}Ca_xMnO_3$ and $Sm_{1-x}Sr_xMnO_3$ systems, two important prototype examples of manganites studied in the dissertation.

In Chapter 3 we reviewed the main contributions to the theory of manganites. First part of the chapter is devoted to Jahn-Teller and Crystal Field effects. Then we will describe the phase separation scenario and finally we will review the Current Carrier Density Collapse (CCDC) theory.

In Chapter 4 we described our experimental set up and measurement techniques.

In Chapter 5 we have shown the effects of vacuum annealing and oxygen redistribution induced disorder on the magnetotransport of $Sm_{0.55}Sr_{45}MnO_3$ manganite near the metal-insulator transition. Oxygen redistribution in the sample was obtained by annealing at 325^o C in vacuum. The temperature dependencies of resistivity and magnetoresistance were measured as a function of the vacuum annealing time. We observed a dramatic increase in the magnitude of the resistivity peak at the metal-insulator transition and a reduction of its width after an initial short-time annealing, followed by a logarithmic increase of the resistivity with annealing time. In this chapter we also gave a brief compositional dependence of the temperature dependence of

the resistivity of the $Sm_{1-x}Sr_xMnO_3$ system.

In Chapter 6, the effects of the grain-boundary-induced lattice disorder on the resistivity, the magnetization, and the specific heat of a prototypical manganite $Sm_{0.55}Sr_{45}MnO_3$ near half doping were investigated at temperatures near the metal-insulator transition. An increasing lattice disorder softens the magnetic phase transition from a first order phase transition into a second order transition. Furthermore, the peaks in the resistivity and specific heat are broadened and there is an increase in the charge carrier scattering rates in the metallic state. On the other hand, the polaronic hopping activation energies in the insulating state changed slightly as a function of grain boundary disorder. The origin of these phenomena is discussed.

In Chapter 7, we have shown that polycrystalline $Sm_{0.55}Sr_{0.45}MnO_3$ samples exhibit large anisotropic magnetoresistance (AMR). The magnitude of the AMR strongly depends on the grain size of the samples. The AMR in the bulk samples exhibits sizeable low field and low temperature AMR which is in contrast to single crystal samples and epitaxial films. This suggests that the well established spin polarized transport model for understanding of low temperature and low field magnetoresistance in manganites is essentially anisotropic. Our results indicate that AMR in manganite samples could be tuned for large temperature ranges at low magnetic fields by controlling the crystallinity and defect structure.

In Chapter 8 we have shown that the SSMO films grown on the $LaAlO_3$ and $SrTiO_3$ substrates exhibit insulating behavior with negligible magnetoresistance effect in contrast to bulk samples of the same composition. On the other hand, when these films were buffered with a thin layer of $Nd_{0.55}Sr_{0.45}MnO_3$, a large low field magnetoresistance behavior along with the bulk like properties were observed. Our results suggest that low field magnetoresistance and magnetoresistive anisotropy could be improved dramatically in hetero-structured manganite films.

In Chapter 9, magnetotransport properties of strained $La_{0.65}Ca_{0.35}MnO_3$ (LCMO) thin films with thickness between 10 and 1000 nm were investigated at temperatures near the metal-insulator transition and in magnetic fields up to 0.7 Tesla. The reduc-

tion of the thin film thicknesses which in turn produces an increasing epitaxial lattice strain dramatically increases the in-plane magnetic anisotropy and the magnetoresistivity.

In Chapter 10, we investigated the anisotropic magnetoresistance (AMR) in ultrathin La-based manganite films grown on various substrates. It was found that depending on the strain state, the AMR in some of these systems exceeds 100% and can even change sign. These changes are very dramatic when compared to the few percent change in AMR in conventional ferromagnets. The mechanism behind these large changes in the AMR is discussed

In Chapter 11, the lattice-disorder-induced changes in the magnetoresistivity and the magnetoresistive anisotropy of epitaxial ion-beam-milled LCMO films were investigated. The results suggest that, for films less than 20 nm thick, an increase of the magnetoresistivity and a reduction in the magnetoresistive anisotropy of the ion-beam-milled films are governed mostly by the point defect induced deformation, in contrast to the as-grown films where an increase of both the magnetoresistivity and the magnetoresistive anisotropy is determined by the epitaxial strain.

In Chapter 12, the effect of the lattice disorder on the resistivity of $La_{1-x}Ca_xMnO_3$ (LCMO) near x=1/3 at the metal-insulator transition was studied by using a percolation model based on the CCDC theory. The percolation model was applied to calculate the temperature dependence of the resistivity ρ(T) of the mixed state, where metallic ferromagnetic and insulating paramagnetic clusters simultaneously exist. The temperature dependence of the fraction of the metallic phase was obtained by assuming a Gaussian distribution of random transition temperatures, whose width increases with an increasing lattice disorder. The resistivity ρ(T) calculated from the model reproduces well the experimental ones for LCMO crystals and disordered films.

In Chapter 13, we have shown that strain associated with a lattice mismatched substrate in the ultra thin films can cause new electronic behavior, not found in the bulk materials or the thicker films of the same chemical composition of LCMO. Resistivity of the ultra thin films exhibit strong relaxation effects when measured as a

function of time in a constant magnetic field. Moreover, the ultrathin films ages dramatically faster than the thicker counterparts causing an upturn in the temperature dependence of the resistivity at lower temperatures where material is supposed to be ferromagnetic metal.

Chapter 14 is a general summary of all chapters and we have shown some highlights of important results that we were not able to include to the dissertation in detailed way.

1.1 List of Publications

- "Effects of correlated disorder on the magneto-transport in colossal magnetoresistance manganites"
  M. Egilmez, Z. Salman, KH Chow, J Jung, *PSS-Rapid Research Letters*, 4, 94 (2009)

- "Correlation of structural phase transition and electrical transport properties of manganite films on $SrTiO_3$"
  M. Egilmez, MM Saber, I. Fan, KH Chow, J Jung Physical Review B, 78 172405 (2008).

- "Dramatic strain induced modification of the low field anisotropic magnetoresistance in manganite films "
  M. Egilmez, MM Saber, AI Mansour, Rongchao Ma, KH Chow, J Jung Applied Physics Letters, 93, 182505 (2008).

- "Influence of photoexcitation on the diamagnetic muonium states in Ge studied via their precession signatures"
  I Fan, KH Chow, B. Hitti, R. Scheuermann, AI Mansour, WA MacFarlane, BE. Schultz, M. Egilmez, J Jung, YG Celebi, HN Bani-Salameh, BR Carroll, JE Vernon, RL Lichti. Physical Review B, 78 153203 (2008).

- " Softening of the First-order magnetic phase transition and magneto-transport

properties of $Sm_{0.55}Sr_{0.45}MnO_3$ manganite"
M. Egilmez, Z. Salman, A. I. Mansour, K.H. Chow, and J. Jung Journal of Applied Physics, 104 093915 (2008).

- "Oxygen-isotope exchange and cation disorder effects on magneto-transport properties of $(Sm_{1-y}Gd_y)_{0.55}Sr_{0.45}MnO_3$"
M. Egilmez, I. Isaac, D.D. Lawrie, K.H. Chow, and J. Jung Journal of Materials Chemistry, 18 5796 (2008).

- "Percolative model of the effect of disorder on the resistive peak broadening in $La_{2/3}Ca_{1/3}MnO_3$ near the metal-insulator transition"
M. Egilmez, K.H. Chow, and J. Jung, Applied Physics Letters, 92, 162515 (2008).

- "Metal-insulator transition, specific heat, and grain-boundary-induced disorder in $Sm_{0.55}Sr_{0.45}MnO_3$"
M. Egilmez, K.H. Chow, J. Jung, I. Fan, A.I. Mansour, and Z. Salman, Applied Physics Letters, 92, 132505 (2008).

- "Lattice-strain control of magneto-resistivity and magneto-resistive anisotropy induced by ion-beam-milling in $La_{0.65}Ca_{0.35}MnO_3$ films near the metal-insulator transition"
M. Egilmez, A.I. Mansour, M.M. Saber, K.H. Chow, and J. Jung, Applied Physics Letters, 92, 022501 (2008)

- "Optically induced dynamics of muonium centers in Si studied via their precession signatures"
I. Fan, K.H. Chow, B. Hitti, R. Scheuermann, W.A. MacFarlane, A.I. Mansour, B.E. Schultz, M. Egilmez, J. Jung, and R.L. Lichti, Physical Review B, 77, 035203 (2008).

- "Magnetoresistive anisotropy and magnetoresistivity in strained $La_{0.65}Ca_{0.35}MnO_3$ films near the metal insulator transition"

M. Egilmez, R. Patterson, K.H. Chow, and J. Jung, Applied Physics Letters, 90, 232506 (2007).

- "Temperature dependence of the persistent critical current and instabilities in MgB_2 thin films"
  A.I. Mansour, M. Egilmez, I. Fan, K.H. Chow, J. Jung, E.M. Choi, H.S. Lee, S.I. Lee, and H. Darhmaoui Applied Physics Letters, 90, 162511 (2007).

- "Quench-disorder-controlled magnetoresistance in $Sm_{0.55}Sr_{0.45}MnO_3$"
  M. Egilmez, K.H. Chow, J. Jung, and Z. Salman Applied Physics Letters, 90, 162508 (2007).

- "Oxygen-redistribution-induced disorder and magneto-transport properties of $Sm_{0.55}Sr_{0.45}MnO_3$ manganites"
  M. Egilmez, K.H. Chow, and J. Jung, Applied Physics Letters, 89, 062511 (2006).

- "Electrical and mechanical properties of superconducting MgB_2/Mg metal matrix composites",
  M.Egilmez, L. Ozyuzer, M. Tanoglu, S. Okur, O. Kamer and Y. Oner, Supercond. Sci. Technol. 19, 359 (2006).

- "Onset of percolation and the temperature dependence of the persistent critical current in $YBa_2Cu_3O_{7-\delta}$ films",
  J. Jung, K.H. Chow, M. Egilmez, and A. Welsh, Applied Physics Letters, 87, 262506 (2005).

- "Local magnetic properties of $Y_{12}Co_5Bi$ and $Gd_{12}Co_5Bi$ studied by muSR"
  M. Egilmez, KH Chow, WA MacFarlane, A Mar, I Fan, AI Mansour , D Schick-Martin, J Jung, A. V. Tkachuk, B Hitti, D. Arseneau Journal of Applied Physics, 105 07A906 (2009)

- "The anisotropic magnetoresistance in epitaxial thin films and polycrystalline samples of $La_{0.65}Ca_{0.35}MnO_3$"

M. Egilmez, Rongchao Ma, KH Chow, J Jung . Journal of Applied Physics, 105 07D706 (2009)

- "Local magnetic properties of $(RE)_{12}Co_5Bi$ studied by muSR "
  M. Egilmez, I Fan, KH Chow, WA MacFarlane, AI Mansour, D Schick-Martin, J Jung, B Hitti, D Arseneau, A. V. Tkachuk, A Mar Physica B, 404 611 (2009)

- "Beta-NMR of a thin Pt film"
  I Fan, KH Chow, T. J Parolin, M. Egilmez, MD Hossain, J Jung, TA Keeler, RF Kiefl, SR Kreitzman, CDP Levy, R Ma, G. D Morris, MR Pearson, H. Saadaoui, Z Salman, M Smadella, Q Song, D Wang, M Xu, WA MacFarlane Physica B, 404 906 (2009)

- "Muonium dynamics in doped Si probed by photo-exited TF-MuSR measurements"
  I Fan, KH Chow, M. Egilmez, B Hitti, BR Carroll, JE Vernon, AI Mansour, R. Scheuermann, BE Shultz, WA MacFarlane, J Jung, RL Lichti Physica B, 404 852 (2009)

- "Spin Lattice Relaxation of 8Li in a Ferromagnetic EuO Epitaxial Thin Film"
  Q Song , KH Chow, M Egilmez, I Fan, MD Hossain, RF Kiefl, SR Kreitzman, CDP Levy, G.D.Morris, T.J.Parolin, M.R.Pearson, Z.Salman, H.Saadaoui, M.Smadella, D.Wang, N.J.C.Ingle, and W.A.MacFarlane Physica B, 404 619 (2009)

- "Surface Dependent Structural Phase Transition in SrTiO3 Observed with Spin Relaxation of ^{8}Li"
  M.Smadella, Z.Salman, K.H.Chow, M.Egilmez, I Fan, M. D. Hossain, R. F. Kiefl, C. D.P.Levy, W. A. MacFarlane, A. I. Mansour, G. D. Morris, T. J. Parolin, M. Pearson, H. Saadaoui, Q. Song, and D.Wang Physica B, 404 924 (2009)

- "A muSR search for the magnetism in the cluster compound Nb_6F_{15}"
  WA MacFarlane, D Schick-Martin, M Egilmez, I Fan, Q Song, KH Chow, S Cordier, C Perrin, SD Goren Physica B, 404 622 (2009)

- "Diamagnetic states in Germanium studied by the photo-exited TF-muSR measurements"
  I Fan, KH Chow, B Hitti, A.I. Mansour, R. Scheuermann, WA MacFarlane, BE Shultz, M. Egilmez, J Jung, YG Celebi, H-N Bani-Salameh, BR Carroll, JE Vernon, RL Lichti, Physica B, 404 849 (2009)

- "Local magnetism in $YbCrSb_3$, an anomalous member of the $RECrSb_3$ series"
  KH Chow, WA MacFarlane, Z Salman, I Fan, SJ Crerar, A Mar, M. Egilmez, J Jung, B Hitti, D Arseneau Physica B, 404 615 (2009)

- "Possible donor and acceptor energies for Mu in ZnSe"
  TJ Parolin, Z. Salman, J. Chakhalian, Q Song, KH Chow, GD Morris, M,Egilmez, I Fan, MD Hossain, TA Keeler, RF Kiefl, SR Kreitzman, CDP Levy, AI Mansour, RI Miller, MR Pearson, H. Saadaoui, M. Smadella, D Wang, M Xu, WA MacFarlane Physica B, 404 917 (2009)

- "Hyperfine fields in thin Pd films studied by Beta detected NMR"
  RL Lichti, BR Carroll, JE Vernon, H-N Bani-Salameh, KH Chow, I Fan, M. Egilmez, RC Vilao, JM Gil, HV Alberto, J Piroto Duarte, N Ayres DeCampos, SP Cottrell, SFC Cox, Physica B, 404 827 (2009)

- "The Spin lattice Relaxation of 8Li in simple metals"
  MD Hossain, H Saadaoui TJ Parolin, Q Song, D Wang, M Smadella, K.H.Chow, M. Egilmez, I Fan, RF Kiefl, CDP Levy, G.D Morris, M. Pearson, Z Salman,WA MacFarlane Physica B, 404 914 (2009)

- "Intrinsic nanoscale disorder and the physical properties of HTSC",
  Jung JA, Chow KH, Egilmez M, and Mansour AI, Journal of Superconductivity and Novel Magnetism, 20, 567-570 (2007).

- "Intrinsic nanoscale disorder in HTSC: Effect on the physical properties", Jung J, Chow KH, Egilmez M, and Mansour A, International Journal of Modern Physics B, 21, 3183-3189 (2007).

- "Properties of Reactive O_2 Ion beam sputtered TiO_2 on Si Wafers", S. Ulucan, G. Aygun, L. Ozyuzer, M. Egilmez, R. Turan, Journal of Optoelectronic and Advanced Materials 7, 297 (2005).

- "Microstructural And Electrical Characterization of Ti and Mg Doped Cu-Clad MgB_2 Superconducting Wires", S. Okur, M. Kalkanci, M. Yavas, M. Egilmez, L. Ozyuzer, Journal of Optoelectronic and Advanced Materials 7, 411 (2005).

- "Fabrication Of Superconducting MgB_2 From Boron Oxide (B_2O_3), and Its Microstructural and Electrical Characterization ", M. Yavas, S. Okur, M. Egilmez, M. Kalkanci, L. Ozyuzer, Journal of Optoelectronic and Advanced Materials 7, 407 (2005)

- "Electrical and Microstructural Properties of Superconducting MgB_2/Mg Composites", M. Egilmez, A. Gunel. S. Okur, M. Tanoglu and L. Ozyuzer, Key Engineering Materials, 264, 1197 (2004).

Bibliography

[1] M. Egilmez, R. Patterson, K.H. Chow, and J. Jung, *Applied Physics Letters*, 90, 232506 (2007).

Chapter 2

Introduction

Manganites such as $RE_{1-x}A_xMnO_3$ (RE and A are trivalent rare earth and divalent alkaline earth elements, respectively) are members of set of compounds where the effect of correlations among electrons play a crucial role. This broader framework is widely known as the area of the strongly correlated electrons.[1] At present, there is enormous amount of interest in the study of manganites. However, it is widely recognized that the first paper reporting results for manganites was presented in 1950 by Jonker and Van Santen.[2] In that original paper, La was substituted by Ca, Sr or Ba for polycrystalline samples of $LaMnO_3$. The main result was the appearance of ferromagnetism in those compounds. They also discovered that the resistance below the magnetic ordering temperature (Curie temperature, T_c) exhibits a positive thermal coefficient indicating metallic like behavior and negative gradient above T_c. This is called metal insulator transition (MIT) which brings a maximum resistance around T_c. Additionally, Jonker and Van Santen found that the manganites crystallize in a perovskite structure.[2]

Despite much progress, the implications of MIT behavior were only explored in 1993, when a reduction of resistance was observed in thin films of $La_{2/3}Ba_{1/3}MnO_3$ under application of a relatively small magnetic field.[3] This reduction was only 50% of the zero field resistance. A year later it proved to be possible to reduce the resistivity by several orders of magnitude.[4] The term colossal magnetoresistance (CMR)

was born. The new term is a superlative of giant magnetoresistance (GMR), which is observed in the resistance of ferromagnetic/non magnetic heterostructures by switching an external magnetic field. Giant magnetoresistance is caused by introducing interfaces in spin polarized conductors and it is restricted below T_c, whereas CMR is a intrinsic property which originated from magnetic ordering and usually confined to the vicinity of T_c or the metal insulator transition temperature T_M. Notice that GMR was one of the most successful inventions in the history of science; after less than a decade of their discovery GMR sensors dominated in the market of computer technology. Obviously, success of the GMR motivates the new studies on CMR materials.

2.0.1 Motivations

As we mentioned above, currently manganite research is a hot topic for experimental and theoretical condensed matter physicists aiming to improve our understanding of the behavior of electrons in crystals. There are three main reasons that make manganites an important area of research for scientists all around the world :

1. The first obvious reason is the unexpectedly large magnetotransport properties. Upon application of relatively small magnetic fields, the resistivity changes by several orders of magnitude, an effect that carries the name "Colossal Magnetoresistance "(CMR)". An illustrative representation of this effect is shown in Fig. 2.1 for $(Sm_{1-y}Gd_y)_{0.55}Sr_{0.45}MnO_3$. Note that the resistance change with field so called magnetoresistance in this case could reach up to 30000%. The magneto-resistance is defined as $-MR = [\rho(H) - \rho(0)/\rho(H)]$, where $\rho(H)$ and $\rho(0)$ are the resistivities in an applied field H and in a zero field, respectively.

2. A second motivation to study the manganites is contained in their rich phase diagram, exhibiting a variety of phases, with unusual spin, charge, lattice and orbital order. These four active degrees of freedom lead to a rich phenomenology and an overabundance of phases that have been identified experimentally using

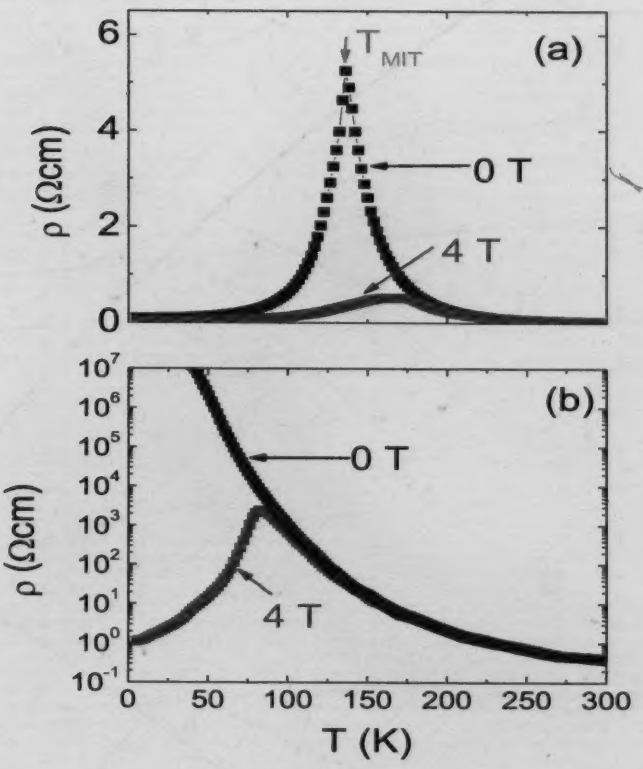

Figure 2.1: An illustrative representation of the Colossal Magnetoresistance effect in (a) $(Sm)_{0.55}Sr_{0.45}MnO_3$ (b) $(Sm_{0.5}Gd_{0.5})_{0.55}Sr_{0.45}MnO_3$. T_M corresponds to metal insulator transition temperature. Figure is reproduced from Egilmez *et al.*[5]

a variety of techniques. Phase competition at the boundary between these phases produces interesting phenomena like CMR.

3. The physics involved in manganites makes connection with physics unveiled in high temperature superconductors (HTS); evidence suggests that even in the best crystals available, manganites are intrinsically inhomogeneous. The states formed in these compounds are dominated by coexistence of competing phases. The study of in homogeneities in manganites will also likely lead to important information about similar phenomena found in other materials such as HTS.

Although my research program contains all the motivations mentioned above, it is mainly concentrated on electrical and magnetic properties of manganites with the objective of understanding the basic properties and controlling the properties which are suitable for applications. For this purpose, over 300 samples of manganites were studied during the course of this dissertation. In particular, dissertation addresses important issues in manganite physics namely: i) What is the effect of the oxygen disorder on transport properties of manganites in the low field regime? ii) What is the effect of the grain-boundary induced disorder on transport properties and the magnetic phase transitions of manganites in the low field regime? iii) How could the low field anisotropic magneto-resistance be improved in manganite films? iv) How does the lattice disorder affect the low field anisotropic magnetoresistance in manganite films? In order to address these questions we have studied $Sm_{1-x}Sr_xMnO_3$, $Nd_{1-x}Sr_xMnO_3$, $Gd_{1-x}Sr_xMnO_3$, $La_{1-x}Sr_x$ MnO_3 and $La_{1-x}Ca_xMnO_3$ types of manganites. However, the dissertation mostly consists of experimental results from the $La_{1-x}Ca_xMnO_3$ and $Sm_{1-x}Sr_xMnO_3$ systems, two intermediate bandwidth manganites: therefore in the coming sections of the chapter we will briefly discuss the magnetic phase diagram for these two important systems.

2.1 Phase diagrams

2.1.1 $La_{1-x}Ca_xMnO_3$

In this subsection, the magnetic phase diagram of $La_{1-x}Ca_xMnO_3$ will be discussed. This compound presents some characteristics of large bandwidth manganites, such as the presence of a robust ferromagnetic metallic phase. However, it also has features that indicate strong deviations from double-exchange behavior, including the existence of charge/orbital-ordered phases. For this reason, the manganite community consider that this compound should be labeled as of "intermediate bandwidth", to distinguish it from the truly low-bandwidth compound $Pr_{1-x}Ca_xMnO_3$ where a metallic ferromagnetic phase can only be stabilized by the application of magnetic fields.

$La_{1-x}Ca_xMnO_3$ has been analyzed since the early days of manganite studies[2, 6], but it is only recently that it has been systematically scrutinized as a function of hole density and temperature. In particular, it has been observed that $La_{1-x}Ca_xMnO_3$ has a large MR effect. For example, Fig. 2.2 reproduces results from Schiffer *et al.* at x=0.25 showing the magnetization and resistivity as a function of temperature, and the existence of a robust MR, larger than 80%.[7] The drop in ρ_{dc} with decreasing temperature and the peak in magnetoresistance are correlated with the ferromagnetic transition in the magnetization. The insulating behavior above the Curie temperature is very prominent and the explanation of its origin is among the most important issues to be addressed in theories of manganites. Below T_c the presence of ferromagnetism was tentatively attributed to the double-exchange mechanism, but further work reviewed especially phase separation scenario and (bi)polaronic models has actually revealed a far more complex structure with coexisting phases even in this metallic regime.[1, 8, 9] In fact, hints of this behavior may already be present in Fig. 2.2 which already reveals a MR effect as large as 30% well below T_c. In addition, it is also interesting to observe that hydrostatic pressure leads to large changes in resistivity comparable to those found using magnetic fields.

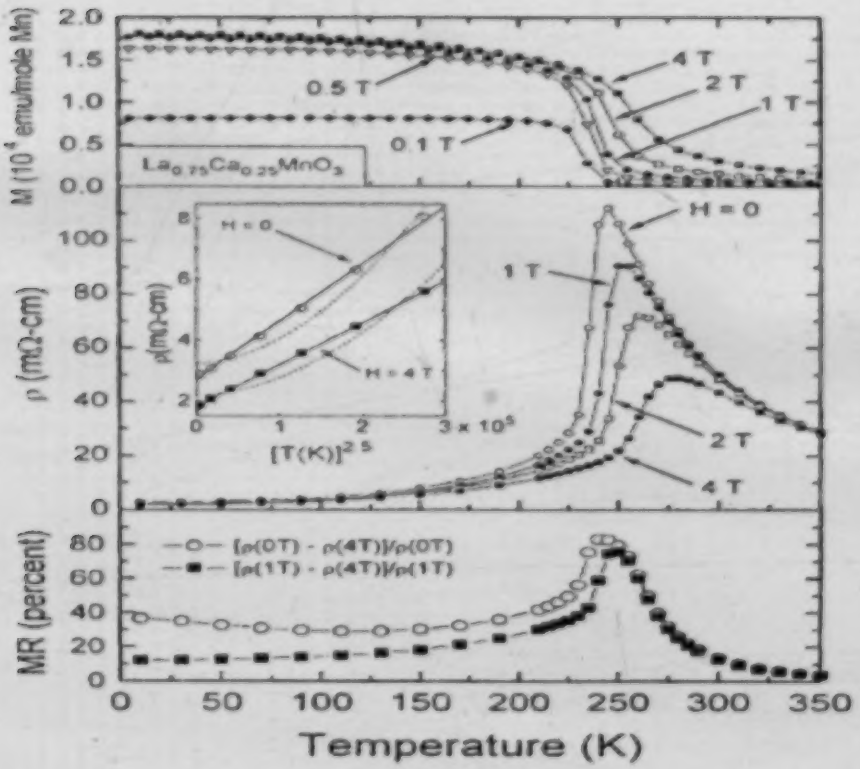

Figure 2.2: The magnetization, resistivity, and magnetoresistance of $La_{1-x}Ca_xMnO_3$ (x=0.25), as a function of temperature at various magnetic fields. The inset is ρ at low temperatures. Reproduced from Schiffer *et al.*[7]

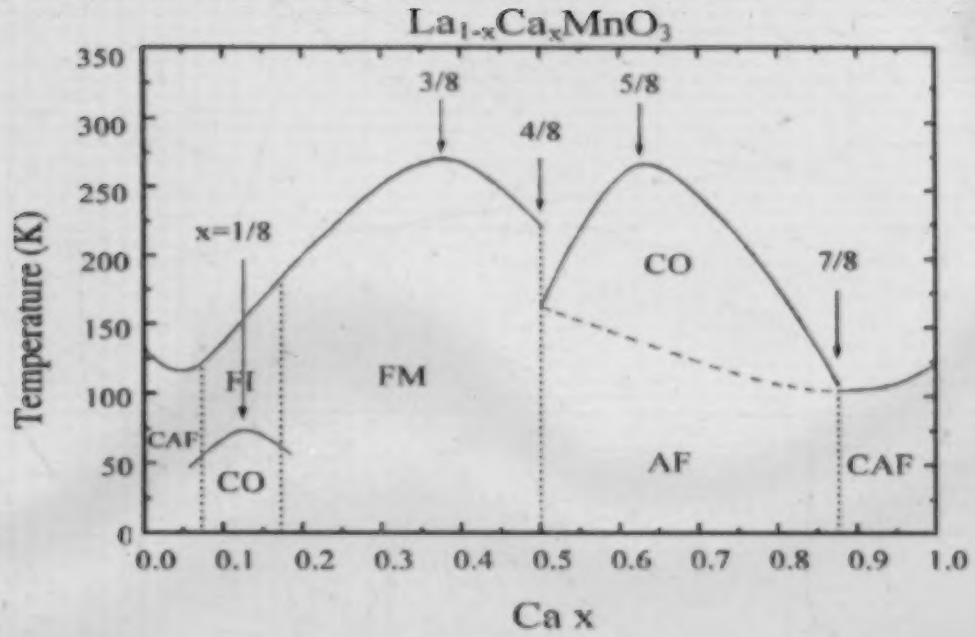

Figure 2.3: Phase diagram of $La_{1-x}Ca_xMnO_3$, constructed from measurements of macroscopic quantities such as the resistivity and magnetic susceptibility, reproduced from Cheong and Hwang.[11] FM: Ferromagnetic Metal, FI: Ferromagnetic Insulator, AF: Antiferromagnetism, CAF: Canted AF, and CO: Charge/Orbital Ordering. FI and/or CAF could be a spatially inhomogeneous states with FM and AF coexistence.

The qualitative features of Fig. 2.2 contribute to the understanding, at least in part, of the CMR effect found in thin films of this same compound.[4] In LCMO films it has been shown that, in addition to hole doping, or magnetic field, substrate induced strain also has significant impact on the physical properties of the films.[10]

The complete phase diagram of $La_{1-x}Ca_xMnO_3$, based on magnetization and resistivity measurements, is reproduced in Fig. 2.3, taken from Cheong and Hwang.[11] Note that the FM phase actually occupies just a fraction of the whole diagram, illustrating once again that DE does not provide a full understanding of the manganites. For instance, equally prominent are the charge ordered (CO) states between x=0.50

and 0.87. The CO state at x=0.50 was already described by Wollan and Koehler as a CE-state, and the characteristics at other densities are discussed below. In the regime of CO-states, studies by Ramirez et al. of the sound velocity, specific heat, and electron diffraction were attributed to strong electron-phonon coupling, in agreement with the predictions of Millis et al.[12, 13] The canted state at x close to 1 could be a mixed-phase state with coexisting FM-AF characteristics based on recent theoretical calculations by Dagotto's group. The low hole-density regime is quite unusual and nontrivial, and it appears to involve a charge-ordered phase, and a curious ferromagnetic insulator. Actually at x=0.10, there is no large Magnetoresistance effect using fields of 12 T, according to Fig. 6 of Ibarra and De Teresa.[14] The same reference shows that at x=0.65, well inside the charge-ordered state, a 12 T field is also not sufficient to destabilize the insulating state into a metallic one. Thus, to search for a large magnetoresistance effect, the density must be closer to that leading to the FM metallic regime.

In Fig. 2.3 note also the presence of well-defined features at commensurate carrier concentrations x=N/8 (N=1,3,4,5 and 7). The Curie temperature is maximized at x=3/8 according to Cheong and Hwang, contrary to the x=0.30 believed by many to be the most optimal density for ferromagnetism. Cheong and Hwang also remarked that in the large-bandwidth compound $La_{1-x}Sr_xMnO_3$ the Curie temperature is also maximized at the same x=3/8 concentration, implying that this phenomenon is universal. It is important to realize that within a simple one-orbital double-exchange model, as described later, the optimal density for ferromagnetism should be x=0.50. The fact that this is not observed is already indicative of the problems faced by a double-exchange description of manganites. Note also that Zhao *et al.* and *Franck et al.* found a giant oxygen isotope shift in T_c of about 20 K at x=0.2, showing the relevance of electron-phonon couplings in manganites.[5]

The charge-ordering temperature T_{CO} peaks at x=5/8 (the same occurs in (Bi, Ca)-based compounds), while at x=4/8=1/2 there is a sharp change from ferromagnetic to antiferromagnetic ground states. The whole phase diagram has a pronounced

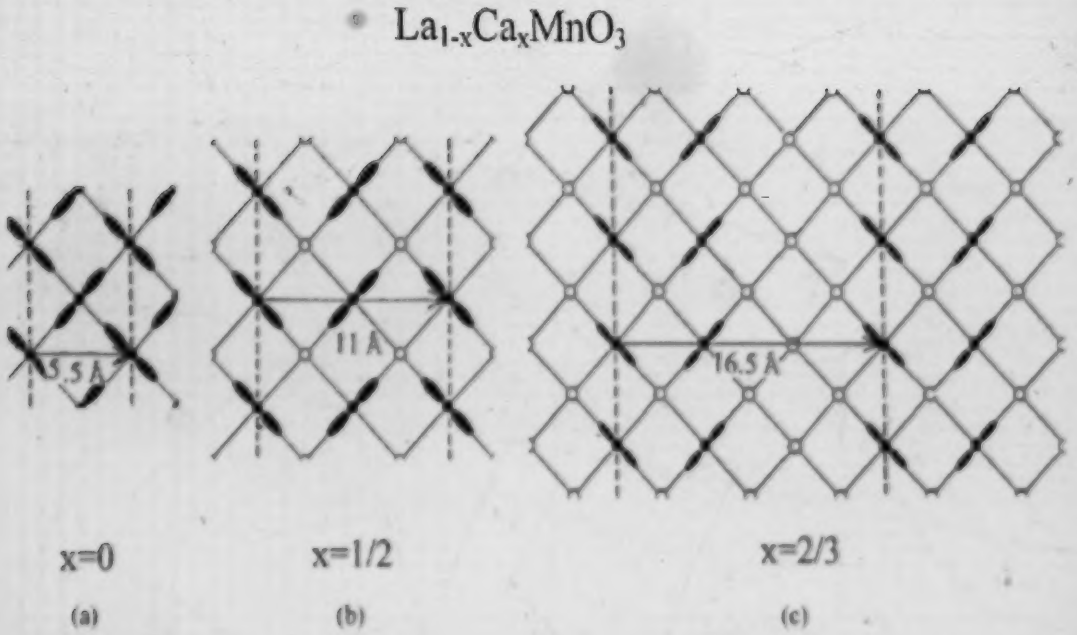

Figure 2.4: The charge and orbital ordering configurations for $La_{1-x}Ca_xMnO_3$ with x=0, 1/2, and 2/3.Open circles are Mn^{4+} and the lobes show the orbital ordering of the e_g-electrons of Mn^{3+}. Figure reproduced from Cheong and Hwang.[11]

electron-hole asymmetry, showing again that simple double-exchange models with only one orbital are not realistic. At x=1/8 the low-density charge-ordered state appears to have the largest strength, while on the other side at x=7/8 charge ordering disappears into a mixed FM-AF state. Finally, at x=0 the ground state is an A-type antiferromagnet (see also original citation.[15]) with ferromagnetic spin correlations on a plane and antiferromagnetism between planes, while at x=1 it is a G-type antiferromagnet (AF in all directions), both of them insulating.

Some of the arrangements that have been identified from Fig. 2.3 are shown in Fig. 2.4 reproduced from Cheong and Hwang.[11] At x=0, the A-type spin state is orbitally ordered as it appears in Fig. 2.4 (a). At x=0.5 the famous CE-type arrangement Fig. 2.4 (b) already found in early studies of manganites is certainly stabilized.

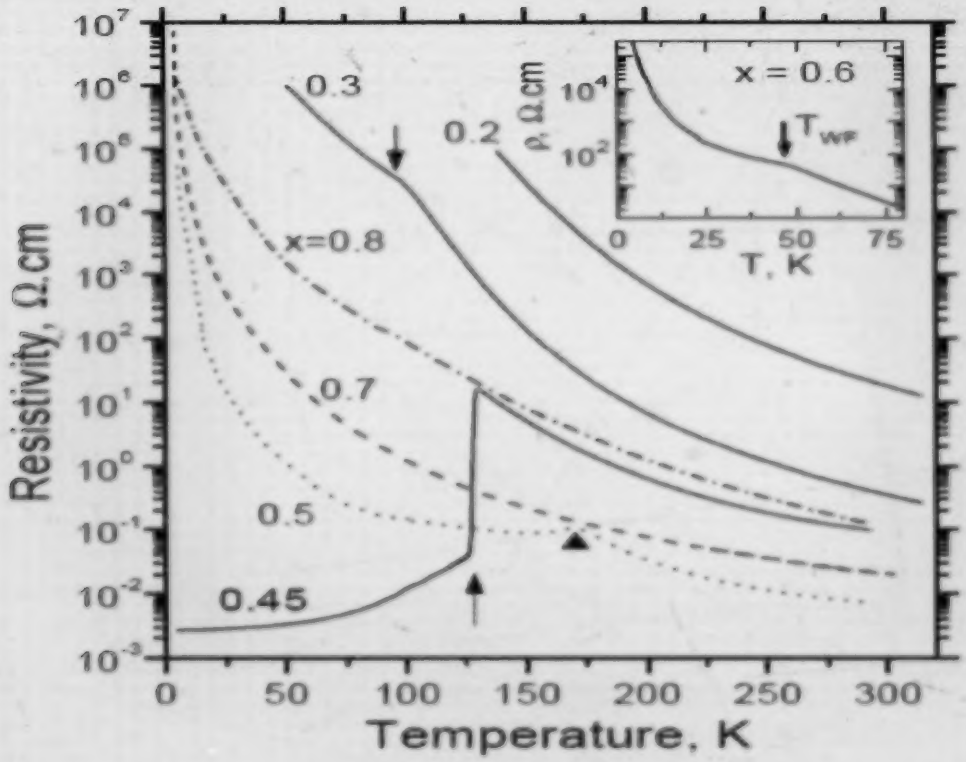

Figure 2.5: Temperature dependence of the electrical resistivity for $Sm_{1-x}Sr_xMnO_3$ crystals. Arrows indicate Curie temperatures, up triangle is indicative of the Neel temperature. Figure reproduced from Ivanov *et al.*[19]

This state has been observed experimentally using resonant X-ray scattering (see original citation.[16]). At x=2/3, and also x=3/4, a novel 'bi-stripea arrangement is found (see original citation[17]). The x=0.65 state is very stable upon the application of a magnetic field.[14] The origin of the term bi-stripe is obvious from Fig. 2.4 (c). However, theoretical work (see original citation[18]) has shown that it is more appropriate to visualize this arrangement as formed by FM zigzag chains running in the direction perpendicular to those of the charge stripes of Fig. 2.4(c).

2.1.2 $Sm_{1-x}Sr_xMnO_3$

$Sm_{1-x}Sr_xMnO_3$ (SSMO) exhibits a number of intriguing physical properties. For example, the inverse magnetization of this compound shows a clear deviation from the CurieWeiss law.[10] Its paramagnetic region above T_c is magnetically heterogeneous, as indicated by neutron diffraction and μSR experiments.[20] The magnetostriction measurements revealed that the magnetotransport properties of SSMO, compared to the other manganites, are extremely strain sensitive.[21] These properties suggest that the SSMO is very susceptible to the presence of any external stimuli including structural disorder, magnetic field, strain and so forth. The region in the phase diagram of the SSMO where the CMR effect could be observed accompanied with a metal insulator transition is relatively narrow ($0.3<x<0.52$).

Fig. 2.5 shows the temperature dependence of resistivity of SSMO. As it is clear from the figure the metal insulator transition is observed in SSMO around intermediate doping levels such as $0.3<x<0.52$. The complete phase diagram of the compound is given in Fig. 2.6. As it can be seen from the phase diagram SSMO exhibits a number of intriguing magnetic behaviors ranging from orbital-charge order to ferromagnetism. The $Sm_{0.55}Sr_{0.45}MnO_3$ manganite is of particular interest since this composition is bordering the charge/orbital order instability, being one of the most striking examples of manganites in which the multiphase competition has been comprehensively verified by experiment.[23] The phase diagram which shows where colossal magnetoresistance persists is reproduced after Tomioka *et al.* in Fig. 2.7. The multiphase coexistence is also clear in this phase diagram. However, there is a limited number of studies dedicated to this important composition. In the first part of the dissertation we will present our results on bulk samples of this important composition. Moreover, we made the thin films of this composition. This is particularly important since we are

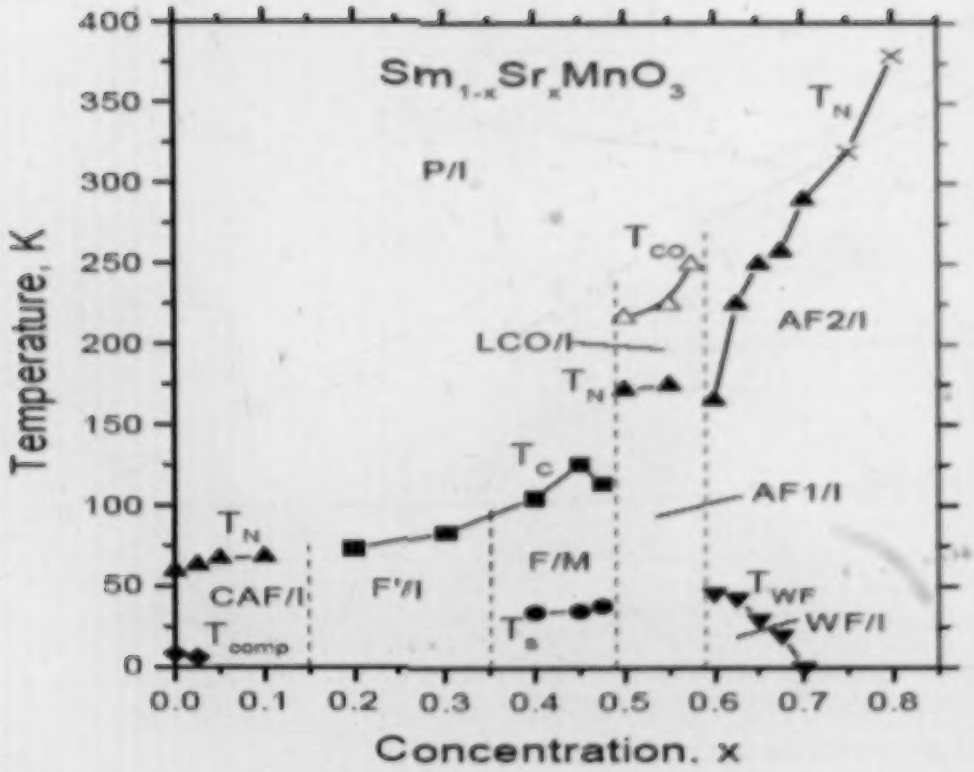

Figure 2.6: Phase diagram of $Sm_{1-x}Sr_xMnO_3$ crystals. The phases are denoted by: P/I: paramagnetic insulator, CAF/I: canted AF insulator, F'/I: possible inhomogeneous or canted F insulator, F/M: F metal, LCO/I: local charge ordering insulator, AF1/I: antiferromagnetic (A-type) insulator, AF2/I: antiferromagnetic (C-type) insulator, WF/I: weak F insulator. Cross points are taken from Martin *et al.*[22], all other pointsthis work, linesguide for the eyes. Figure reproduced from Ivanov *et al.*[19]

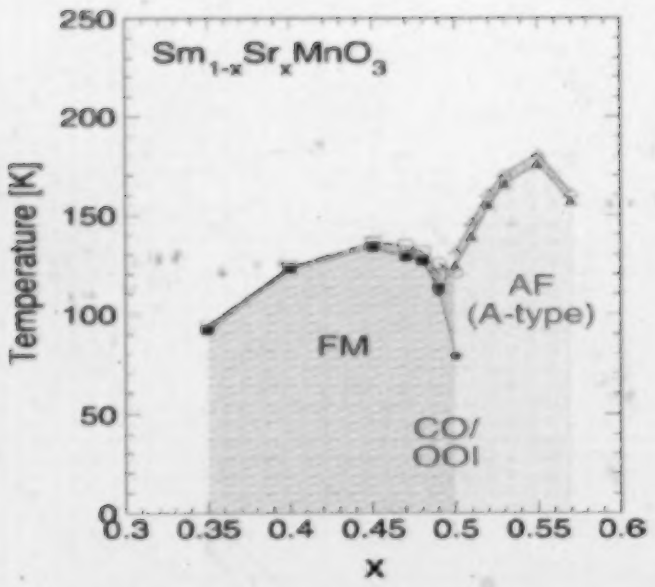

Figure 2.7: The electronic phase diagram of $Sm_{1-x}Sr_xMnO_3$ $0.30<x<0.60$. The ferromagnetic metal, the A-type antiferromagnetic state and the charge/orbital-ordered insulator are denoted as FM, AF (A-type) and CO/OOI, respectively. The transition temperatures from (to) the FM, AF, and CO/OOI are denoted as open (closed) squares, triangles, and circles, respectively. Figure reproduced from Tomioka *et al.*[23]

the first group to make SSMO films with bulk like physical properties.

Bibliography

[1] E. Dagotto, *Nanoscale Phase separation and Colossal Magneto-resistance*, 1st ed. (Springer, Berlin, 2002).

[2] J. H. Van Santen and G. H. Jonker, *Phyica*, **16**, 599 (1950). G. H. Jonker and J. H. Van Santen, *Phyica*, **16**, 337 (1950).

[3] R. Von Helmolt *et al.*, *Phys. Rev. Lett.*, **73**, 2331 (1993).

[4] S.Jin *et al.*, *Science* **264**, 413 (1994).

[5] M.Egilmez *et al.*, *Journal of materials chemistry*, **18**, 5796 (2008) and references therein.

[6] E. O. Wollan and W. C. Koehler, *Phys. Rev.*, **100**, 545 (1955).

[7] P. Schiffer *et al.*, *Phys. Rev. Lett.*, **75**, 3336 (1995).

[8] A. S. Alexandrov and A. M. Bratkovsky, *Phys. Rev. Lett.*, **82**, 141 (1999).

[9] A. S. Alexandrov, A. M. Bratkovsky, and V. V. Kabanov, *Phys. Rev. Lett.*, **96**, 117003 (2006).

[10] M Egilmez, KH Chow, J Jung, I Fan, AI Mansour, and Z Salman, *Applied Physics Letters*, **92**, 132505 (2008).

[11] S. W. Cheong *et al.*, ed. by Y. Tokura, *Colossal magneto-resistive oxides*, 1st ed. (Gordon and Breach, Amsterdam, 2000), p 237-280.

[12] A. P. Ramirez *et al.*, *Phys. Rev. Lett.*, **76**, 3188 (1996).

[13] A. J. Millis *et al.*, *Phys. Rev. Lett.*, **74**, 5144 (1995); A. J. Millis *et al.*, *Phys. Rev. Lett.*, **77**, 175 (1996)

[14] M.R. Ibarra *et al.*, *J. Magn. Magn. Mater.*, **177-181**, 846 (1998); M.R. Ibarra *et al.*, *Phys. Rev. B*, **57**, 7446 (1998).

[15] G. Matsumoto *et al.*, *J. Phys. Soc. Japan*, **29**, 606 (1970);G. Matsumoto *et al.*, *J. Phys. Soc. Japan*, **29**, 615 (1970).

[16] M. Zimmermann, C. S. Nelson, J. P. Hill, D. Gibbs, M. Blume, D. Casa, B. Keimer, Y. Murakami, C. C. Kao, C. Venkataraman, T. Bog, Y. Tomioka, and Y. Tokura , *Phys. Rev. B* **64**, 195133 (2001).

[17] S. Mori *et al.*, *Nature*, **392**, 473 (1998).

[18] T. Hotta *et al.*, *Phys. Rev. Lett.*, **84**, 2477 (2000).

[19] V. Yu. Ivanov *et al.*, *J. Magn. Magn. Mater.*, **258-259**, 535 (2003).

[20] J. M. Teresa, M. R. Ibarra, P. Algarabel, L. Morellan, B. Garacia-Landa, C. Marquina, C. Ritter, A. Maignan, C. Martin, B. Raveau, A. Kurbakov, and V. Trounov, *Phys. Rev. B* **65**, 100403 (2002).

[21] Y. Tokura, *Colossal magneto-resistive oxides*, 1st ed. (Gordon and Breach, Amsterdam, 2000).

[22] C. Martin *et al.*, *Phys. Rev. B* **60**, 12191 (1999).

[23] Y. Tomioka, H. Hiraka, Y. Endoh, and Y. Tokura, *Phys. Rev. B.* **74**, 104420 (2006).

Chapter 3

Basic properties and theoretical understanding of manganites

3.1 Introduction

Over the past decade, there has been significant interest in the understanding of the fascinating properties of manganites, such as the metal-insulator transition (MIT) and the colossal magnetoresistance (CMR) effect. According to the double-exchange (DE) model, the MIT and the CMR are a consequence of the DE mechanism combined with the Jahn-Teller electron-phonon interaction with d states, leading to the conclusion that the low and high temperature phases are a spin polarized ferromagnetic metal and a polaronic paramagnetic insulator, respectively. Tunneling experiments and Monte Carlo simulations suggest that the ground states of manganites tend to be intrinsically inhomogeneous due to strong tendencies toward phase separation, typically involving ferromagnetic metallic and antiferromagnetic charge and orbital ordered insulating domains. This implies that disorder is an important inherent element of the CMR effect. Indeed, it has been demonstrated in various experimental studies, that lattice disorder introduced into manganites through chemical substitutions, pressure, strain, and electric field induces dramatic changes in their ground state properties. More recently, the Current Carrier Density Collapse theory (CCDC), on the other

hand, postulates that the MIT and the CMR are caused by a magnetic breakup at T_c of heavy bi-polarons (which are formed by pairing of oxygen p holes in the paramagnetic phase).

In this chapter we will review the main contributions to the theory of manganites. The first part of the chapter is devoted to Jahn-Teller and Crystal Field effects. Then we will describe the phase separation scenarios and finally we will review the Current Carrier Density Collapse theory.

3.2 Crystal field effect and Jahn Teller distortions

The magnetic properties of many crystals containing rare earths can be deduced by considering the rare earth ions to be behaving as completely free ions without interacting with each other or their surroundings. However, for magnetic ions in certain crystals one can not ignore these kind of interactions such as manganites. To understand the effect of the local environment due to the crystal on the energy levels of an atom, it is necessary to first review the shapes of the atomic orbitals. The angular dependences of the electron density of the s, p and d orbitals are shown in Fig. 3.1. As seen from the Fig. 3.1 only s orbitals are spherically symmetric and the p and d-orbitals have a pronounced angular dependence.

The manganese (Mn) ion in the manganites is surrounded by the oxygen octahedron. The $3d$ orbitals on the Mn site placed in such an octahedron coordination are subject to the partial lifting of the degeneracy by the crystal field as shown in Fig. 3.2. The lower lying orbitals, t_{2g}, are d_{xy}, d_{yz} and d_{zx}, while the higher lying ones, e_g states, are $d_{x^2-y^2}$ and $d_{3z^2-r^2}$. The crystal field splitting between the t_{2g} and e_g state is about 1 eV. In the Mn^{3+} based compounds, the Mn site shows the electronic configuration of $t_{2g}^3\ e_g^1$ (total spin number S=2). All $3d$ electrons are subject to electron repulsion interaction or the electron correlation effect,and tend to localize in the "carrier undoped" or the mother all Mn^{3+} based compound, forming so called

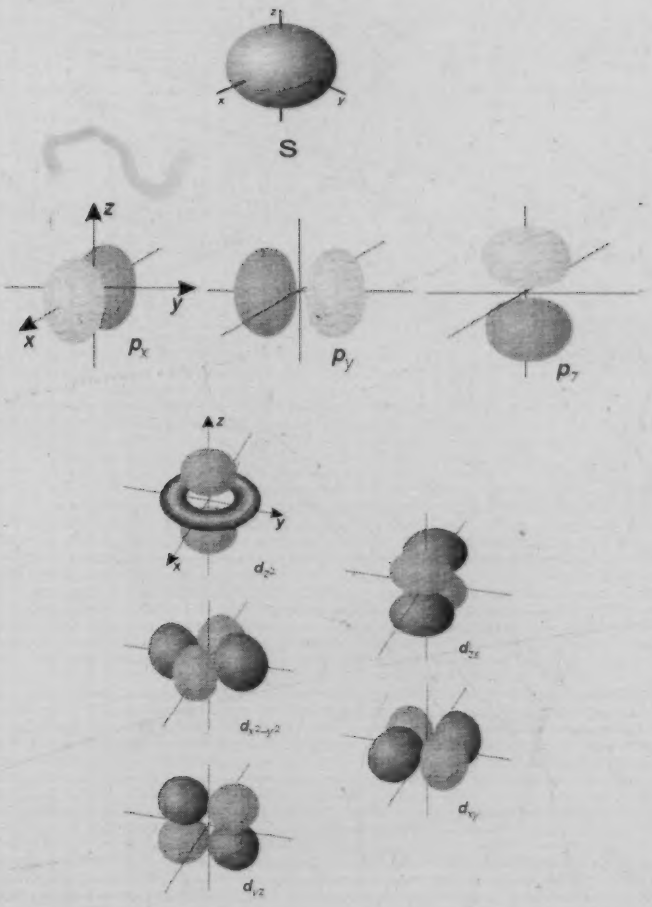

Figure 3.1: The angular distribution of the s, p and d orbitals. d_{z^2} orbital is sometimes refereed as $d_{z^2-r^2}$.

Mott insulator. However, the e_g electrons can be itinerant and hence play a role of conduction electrons, when electron vacancies or holes are created (doping with, Ca, Sr, Ba..) in the e_g orbital states of the crystal.[1, 3] The latter hole doping procedure corresponds to creation of mobile Mn^{4+} species on the Mn sites. By contrast, the t_{2g} electrons, less hybridized with $2p$ states and stabilized by the crystal field splitting, are viewed as always localized by the strong correlation effect and as forming the local spin (S=3/2) even in the metallic state.

There is a further possible splitting of the t_{2g} and e_g energy levels if manganese undergoes a Jahn-Teller distortion. Under such a distortion, both the t_{2g} and e_g sets of orbitals are split in energy, with the mean of each set remaining constant.[3] A schematic representation is shown in Fig. 3.2. The Jahn-Teller distortion is only energetically favorable if either of the t_{2g} or e_g sets is partially occupied. This only occurs for Mn^{3+} with its single e_g electron. In a Jahn-Teller distortion the Mn-O bond length is increased in the c direction and increased slightly in the a-b plane.

The Mn-O bonds (i.e. the bond angle or length) are mainly responsible for the electrical transport throughout the sample. In an octahedral environment, the orbitals in the Mn t_{2g} triplet (xy, yz and zx symmetries) have poor overlap with the oxygen $2p$ orbitals and are all strongly localized. However, the e_g orbitals ($d_{3z^2-r^2}$ and $d_{x^2-y^2}$ symmetries) are more diffusive and point towards the O $2p$ orbitals. The probability of overlap between a Mn e_g orbital and an O $2p$ orbital is sufficiently large for a hopping mechanism to be a possible method of conduction. The closer the Mn-O-Mn bonds are to being linear and the shorter the Mn-O distance, then the better the overlap between the relevant orbitals, and the higher the probability of hopping occurring. The length and angle of the Mn-O-Mn bonds is affected by the radii of the rare earth and alkaline element. When an e_g electron moves between adjacent Mn ions the Jahn-Teller induced lattice distortion moves with it. This coupling between the lattice distortion and the e_g electron is known as a polaron. As we will discuss later (see section current carrier density collapse model) in the paramagnetic state of

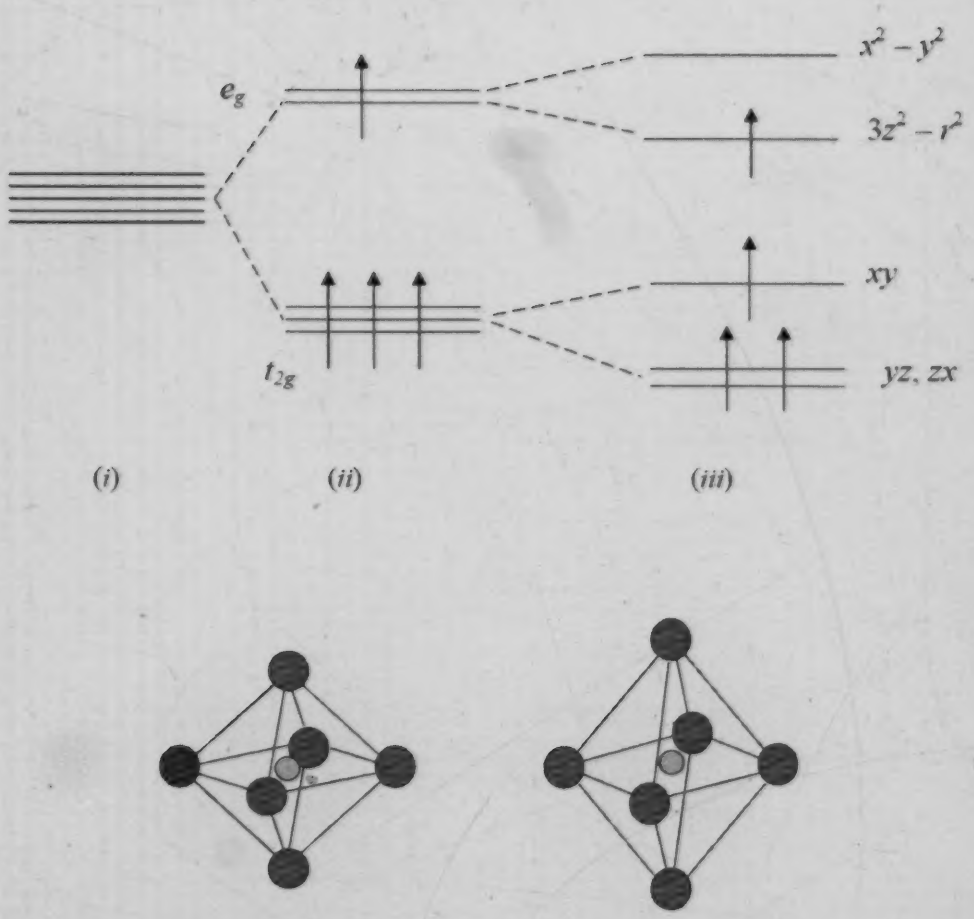

Figure 3.2: Crystal field splitting of five-fold degenerate atomic $3d$ levels in to lower t_{2g} and higher e_g levels. Jahn-Teller distortion of MnO_6 octahedron further lifts each degeneracy as shown in the figure. Figure is reproduced from Tokura.[3]

all manganites electrical conduction will be provided by polaronic hopping.

3.3 Double exchange model

The important consequence of the apparent separation into the spin and charge sectors in the $3d$ orbital states is the effective strong coupling between the e_g conduction electron spin (S=1/2) and t_{2g} localized electrons total spin (S=3/2). This on site ferromagnetic coupling is nothing but Hund's rule. The exchange energy J_H (Hund's rule coupling energy) is as large as 2-3 eV for the manganites and exceeds the inter-site hopping interaction.

This large Hund's energy only provides the hopping condition for an e_g electron which has same spin polarization of localized t_{2g} electrons, this is called double exchange interaction.[4] Basic mechanism in double exchange interaction is shown in Fig. 3.3. In terms of Anderson-Hasegawa relation, t_{ij}^0 defines the hopping interaction of the e_g electron between the neighboring sites, i and j.[5] In the case of strong coupling limit with $J_H/t_{ij} \longrightarrow \infty$, the effective hopping interaction t_{ij} can be expressed as:

$$t_{ij} = t_{ij}^0[cos(\theta_i/2)cos(\theta_j/2) + exp[i(\phi_i - \phi_j)]sin(\theta_i/2)sin(\theta_j/2)] \tag{3.1}$$

where the core spins are treated as purely classical object described by unit vectors at site i and j specified by polar angles θ_i, ϕ_i and θ_j, ϕ_j. By neglecting the Berry phase term $exp[i(\phi_i - \phi_j)]$ (see book by Tokura[3]), it leads to:

$$t_{ij} = t_{ij}^0 cos(\theta_{ij}/2) \tag{3.2}$$

In other words, the absolute magnitude of the effective hopping depends on the relative angle (θ_{ij}) between the neighboring spins as seen in Fig. 3.4. A very qual-

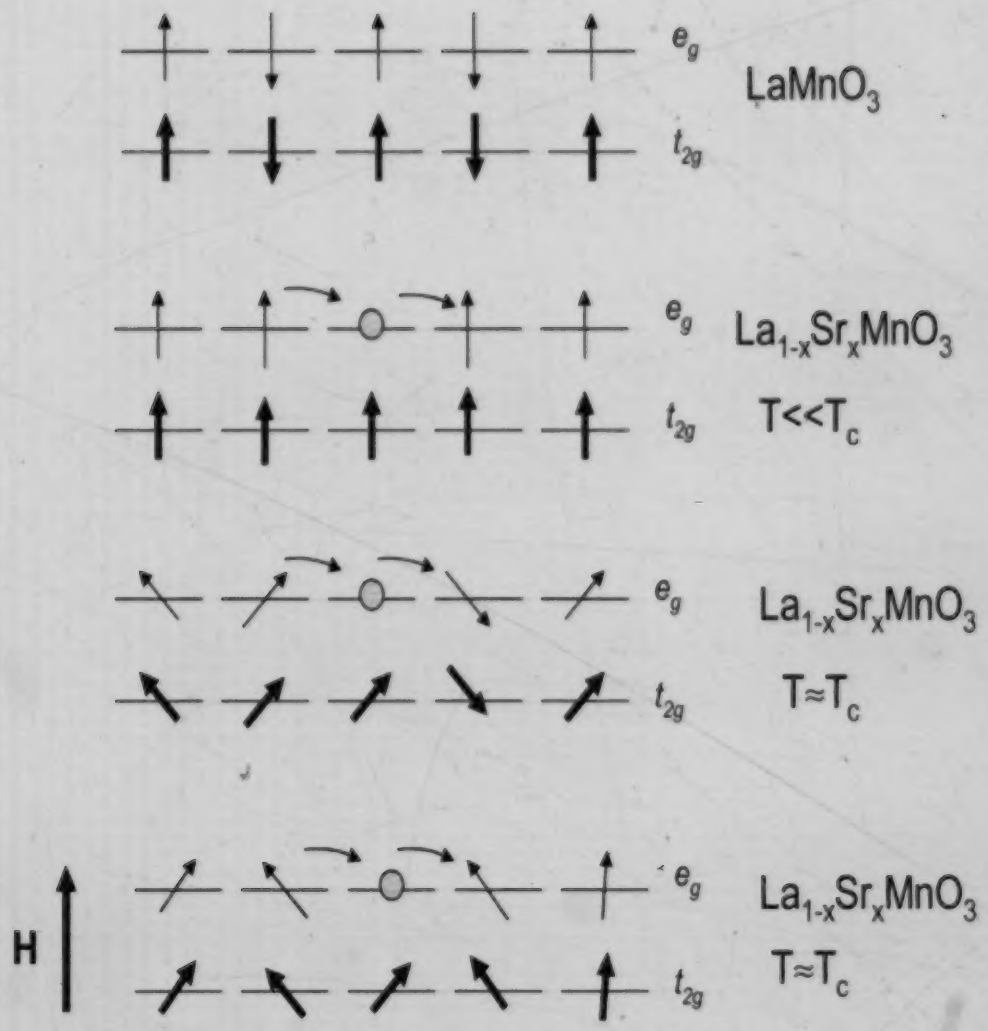

Figure 3.3: Schematic features of the double exchange mechanism.

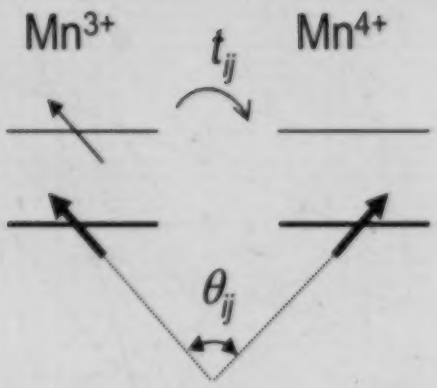

Figure 3.4: Schematic features of the double exchange mechanism. Representation of the hopping exchange integral.

itative picture of the double exchange scenario is plotted in Fig. 3.3.[3] This figure illustrates the mother compound which has a antiferromagnetic spin alignment between the neighboring manganese ions (top panel). By creating electron-vacancy sites (or hole doping) the e_g electron can hop depending on the relative configuration of the local spins. The ferromagnetic metallic state is stabilized by maximizing the kinetic energy of the conduction electrons (θ_{ij}=0, T$\ll T_c$). When temperature is raised up to near or above T_c, the configuration of spin is dynamically disordered and accordingly the effective hoping interaction is also subject to disorder and reduced on average. This would lead to the enhancement of the resistivity near and above T_c. Therefore, large magnetoresistance can be expected around T_c, since the local spins are easily aligned by an external field and hence the randomness of the e_g hopping interaction is reduced. This is the simplest explanation of the magnetoresistance observed for the manganites around T_c.

The magnetoresistance and spin polarization are more complicated in manganites and the double exchange scenario fails to explain some features of some manganites such as multiphase coexistence or insulating like optical conductivity.

In the following part of the chapter we will review important theoretical models which tend to explain the physics of manganites. These models could be summa-

rized in two main groups namely: Phase separation models based on Monte Carlo simulations[6] and polaronic conductivity based models[7] (i.e. Current carrier density collapse theory).

3.4 Simple realistic model for manganites

In general a Hamiltonian for manganites consists of five terms: (i) A kinetic energy term for e_g electrons, usually denoted by H_{kin} or T. The t_{2g} electrons are assumed to be localized, and only their spin degree of freedom is kept. In addition these spins are assumed to be classical.(ii) The Hund coupling between the e_g electrons and the t_{2g} spins. (iii) The anti-ferromagnetic Heisenberg exchange coupling between nearest neighbor spins, H_{AF}. To induce this term it is necessary to allow for the t_{2g} electrons to move between the nearest neighbor (super-exchange interaction). However, once the effective Heisenberg interaction is derived, the t_{2g} kinetic energy can be dropped. (iv) The coupling between the electrons and the Jahn-Teller distortions of the local MnO_6 octahedron, H_{el-ph}. The actual implementation can involve cooperative or non-cooperative phonons. The phonons are usually assumed to be classical. (v) The coulomb interaction among the e_g electrons, H_{el-el}. In this term, interactions beyond the on site terms should in principle be included, but often "screening" or "polarization" is involved to truncate the interaction to just the on site contribution. Then the total Hamiltonian could be written as:

$$H = H_{kin} + H_{Hund} + H_{AF} + H_{el-ph} + H_{el-el} \tag{3.3}$$

Simplifications to this Hamiltonian and its application to manganites could be found in detail in the book by Dagotto.[8] H_{kin} and H_{e-e} terms are straight forward and could be found in any quantum mechanics text book.[8] Lets now look in more detail to other terms especially their simplified version in the manganite case.

3.4.1 Coulombic terms

The complicated interactions contained in the Hamiltonian presented above are virtually impossible to handle accurately, even with many body techniques. Removal of the degeneracy in d-orbitals by crystal field splitting and the Jahn-Teller effect is a simplification in coulombic terms since the problem will deal with two orbitals (e_g and t_{2g}) rather than five orbitals. The e_g multiplet is higher in energy than the latter. The t_{2g} electrons at each site are not effected by hole doping. Their population remains constant and the well known Hund rule of atomic physics enforces alignment of the three t_{2g} spins into a S=3/2 state. Then the t_{2g} sector of the problem could be replaced by a localized spin at each manganese ion. Moreover, the value 3/2 for net spin is high enough that the use of "classical spins" could be regarded as a good approximation. In fact the spin the most quantum is 1/2, with only two allowed projections along the z-axis. As the spin magnitude grows, the magnitude of projections increases and the limit of a classical spin (with no restrictions on the z-axis projections) is approached. The only important interaction between the t_{2g} and e_g sectors can involve at most the spin, not the charge and it is contained in the Hund interaction of the multi orbital Hamiltonian which favors a ferromagnetic alignment. This phenomenological term is estimated to be:

$$H_{Hund} = -J_H \sum_i s_i Si \tag{3.4}$$

where $s_i = \sum_{\gamma\alpha\beta} c^{\dagger}_{i\alpha\gamma} \sigma_{\alpha\beta} c_{i\beta\gamma}$ is the spin of the e_g electrons, γ is restricted to the e_g sector, J_H ($>$0) is the Hund coupling between localized t_{2g} spins and mobile e_g electrons, and $\sigma = (\sigma_x, \sigma_y, \sigma_z)$ are Pauli spin matrices.[6]

3.4.2 Heisenberg term

In the limit when the all e_g electrons are removed from the system (x=1), the model becomes trivial since the interaction between localized spins is only mediated by the e_g electrons. Without mobile electrons, the localized spins simply become "free" or

noninteracting. But it is well known that manganites have G-type Antiferromagnetic (AF) state at x=1 (as happens in $CaMnO_3$). Then, the localized spins must have an antiferromagnetic coupling among themselves to account for the G-type state. This is expected, since the t_{2g} electrons can induce an AF Heisenberg interaction through virtual hopping between nearest-neighbors, leading to well known super-exchange mechanism. The account for this effect the term

$$H_{AF} = J_{AF} \sum_{i,j} S_i S_j \qquad (3.5)$$

is introduced, where J_{AF} is the AF coupling between nearest neighbor t_{2g} spins. The value of J_{AF} should be small compared with hopping amplitudes of e_g electrons, and the Hund coupling as well.[6]

3.4.3 The electron-phonon coupling

Another important ingredient in manganites is the lattice distortion coupled to the e_g electrons. In particular, the double degeneracy in the e_g orbitals is removed by the Jahn-Teller distortion of the MnO_6 octahedron.[6] The primary formalism for the study of electrons coupled to Jahn-Teller modes has been set up by Kanamori[9] His studies mainly focused on cases where the electronic orbitals are degenerate in the undistorted crystal structure, as in the case of Mn in an octahedron environment of oxygen atoms. As explained by Kanamori, the Jahn-Teller effect in this context can be stated as follows: when a given electronic level of a cluster is degenerate in a structure of high symmetry, this structure is generally unstable, and the clusters will present a distortion towards a lower symmetry ionic layout. In the case of Mn^{+3}, which is doubly degenerate when the oxygen is undistorted, a splitting will occur when the crystal is distorted. The distortion of the MnO_6 octahedron is "cooperative" since once it occurs in a particular octahedron, it will affect the neighbors. The basic Hamiltonian to describe the interaction between electrons and Jahn-Teller modes was written by Kanamori and it is of the form

$$H_i^{JT} = g(Q_{2\mathbf{i}}T_i^x + Q_{3\mathbf{i}}T_i^z) + (k_{JT}/2)(Q_{2\mathbf{i}}^2 + Q_{3\mathbf{i}}^2) \tag{3.6}$$

where g is the coupling constant between the e_g electrons and distortions of the MnO_6 octahedron. $Q_{2\mathbf{i}}$ and $Q_{3\mathbf{i}}$ are normal modes of vibration of the oxygen octahedron that remove the degeneracy between the electronic levels, and k_{JT} is the spring constant for the Jahn-Teller mode distortions. The pseudo-spin operators are defined as

$$T_i^x = \sum_\sigma (d_{\mathbf{i}a\sigma}^\dagger d_{\mathbf{i}b\sigma} + d_{\mathbf{i}b\sigma}^\dagger d_{\mathbf{i}a\sigma}), T_i^z = \sum_\sigma (d_{\mathbf{i}a\sigma}^\dagger d_{\mathbf{i}b\sigma} - d_{\mathbf{i}b\sigma}^\dagger d_{\mathbf{i}a\sigma}) \tag{3.7}$$

In the expression of H_i^{JT}, a $T_{\mathbf{i}}^y$ term does not appear for symmetry reasons, since it belongs to the A2u representation. The non-zero terms should correspond to the irreducible representations included in $E_g \times E_g$ namely E_g and A_{1g}. The former representation is described by using the pseudo spin operators $T_{\mathbf{i}}^x$ and $T_{\mathbf{i}}^z$ as discussed here, while the latter, corresponding to the breathing mode, is discussed in detail in review by Dagotto.[6]

Following Kanamori, $Q_{2\mathbf{i}}$ and $Q_{3\mathbf{i}}$ are given by

$$Q_{2\mathbf{i}} = \frac{1}{\sqrt{2}}(X_{1\mathbf{i}} - X_{4\mathbf{i}} - Y_{2\mathbf{i}} + Y_{1\mathbf{i}}) \tag{3.8}$$

and

$$Q_{3\mathbf{i}} = \frac{1}{\sqrt{6}}(2Z_{3\mathbf{i}} - 2Z_{6\mathbf{i}} - X_{1\mathbf{i}} + X_{4\mathbf{i}} - Y_{2\mathbf{i}} + Y_{5\mathbf{i}}) \tag{3.9}$$

where $X_{\mu\mathbf{j}}$, $Y_{\mu\mathbf{j}}$ and $Z_{\mu\mathbf{j}}$ are the displacement of the oxygen ions from the equilibrium positions along the x, y and z direction respectively. The representation for the μ of coordinates is shown in Fig. 3.5.

To solve this Hamiltonian, it is convenient to scale the phononic degrees of freedom as

$$Q_{2\mathbf{i}} = (\frac{g}{k_{JT}})q_{2\mathbf{i}}, Q_{3\mathbf{i}} = (\frac{g}{k_{JT}})q_{3\mathbf{i}} \tag{3.10}$$

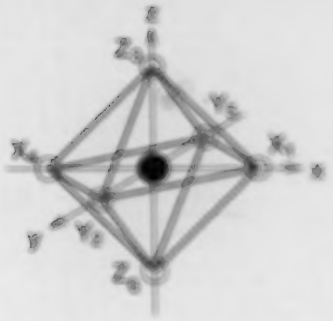

Figure 3.5: MnO_6 octahedron at site i. The labeling for oxygen ions is shown.

where g/k_{JT} is the typical length scale for the Jahn-Teller distortion, which is of the order of 0.1Å (roughly 2.5% of the lattice constant) When the Jahn-Teller distortion is expressed in the polar coordinates as

$$q_{i\xi} = q_\xi \sin(\xi_i), q_{i\theta} = q_\xi \cos(\xi_i) \tag{3.11}$$

the ground state is easily obtained as $(-\sin(\xi_i/2)|d^i_{3z^2}\rangle + \cos(\xi_i/2)|d^i_{3x^2}\rangle)|0\rangle$ with the use of phase ξ_i. The corresponding eigenenergy is given by $-E_{JT}$, where E_{JT} is the static Jahn-Teller energy, defined by

$$E_{JT} = g^2/2k_{JT}. \tag{3.12}$$

Note here that the ground state energy is independent of phase ξ_i. Namely, the shape of the deformed isolated octahedron is not uniquely determined in this discussion. In the Jahn-Teller crystal, the kinetic motion of e_g electrons, as well as the cooperative effect between the adjacent distortions, play a crucial role in lifting the degeneracy and fixing the shape of the local distortion. To complete the electron-phonon coupling term, it is necessary to consider the breathing mode distortion, coupled to the local electron density as

$$H^{ep}_i = gQ_{i\beta}\eta_i + (1/2)k_{br}Q^2_{i\beta} \tag{3.13}$$

where the breathing mode distortion $Q_{i\mathbf{i}}$ is given by

$$Q_{i\mathbf{i}} = \frac{1}{\sqrt{3}}(X_{1\mathbf{i}} - X_{4\mathbf{i}} + Y_{2\mathbf{i}} - Y_{5\mathbf{i}} + Z_{3\mathbf{i}} - Z_{6\mathbf{i}}). \tag{3.14}$$

and k_b is the associated spring constant. Note that, in principle, the coupling constants of the e_g electrons with the Q_1, Q_2 and Q_3 modes could be different from one another. For simplicity, here it is assumed that those coupling constants takes the same value. On the other hand, for the spring constants, a different notation for the breathing mode is introduced, since the frequency for the breathing mode distortion has been found experimentally to be different from that for the Jahn-Teller mode. Note also that the Jahn-Teller and breathing modes are competing with each other. As was shown above, the energy gain due to the Jahn-Teller distortion is maximized when one electron exists per site. On the other hand, the breathing mode distortion energy is proportional to the total number of e_g electrons per site, since this distortion gives rise to an effective on site attraction between electrons. By combining the Jahn-Teller mode and breathing mode distortions, the electron-phonon term is summarized as

$$H_{el-ph} = \sum_{\mathbf{i}} (H_{\mathbf{i}}^{JT} + H_{\mathbf{i}}^{br}) \tag{3.15}$$

Using these terms one can solve the Hamiltonian which describes the fundamental properties of manganites. The most common approaches are summarized below.

3.4.4 One orbital model

A simple model for manganites to illustrate the CMR effect is obtained by neglecting the electron-phonon coupling and the Coulomb interactions as described by Dagotto[6]. Usually, an extra simplification is carried out by neglecting the orbital degrees of freedom, leading to the FM Kondo model or one-orbital double-exchange model, which will be simply referred as the one-orbital model. In this model, generally the Hamiltonian is written as

$$H_{DE} = -t \sum_{\langle \mathbf{i},\mathbf{j} \rangle,\sigma} (a^{\dagger}_{\mathbf{i}\sigma} a_{\mathbf{j}\sigma} + H.c.) - J_H \sum_{\mathbf{i}} s_i S_j + J_{AF} \sum_{\langle \mathbf{i},\mathbf{j} \rangle} S_i S_j \qquad (3.16)$$

where $a_{\mathbf{i}_\sigma}$ is the annihilation operator for an electron with spin σ at site $\mathbf{i}$, but without orbital index. Note that H_{DE} is quadratic in the electron operators, indicating that it is reduced to a one-electron problem on the background of localized t_{2g} spins. As pointed out by Dagotto this is a clear simplification for numerical simulations.[6] Neglecting the orbital degrees of freedom is clearly an oversimplification, and important phenomena such as orbital ordering cannot be obtained in this model. However, one orbital model is still important, since it already includes part of the essence of manganese oxides including metal-insulator competition and phase separation of different phases.

3.4.5 $J_H = \infty$ limit

Another simplification without the loss of essential physics is to take the widely used limit $J_H = \infty$, since in actual material J_H/t is much larger than unity, where t is the hopping amplitude. In such limit, the e_g electron spin perfectly aligns along the t_{2g}-spin direction, reducing the number of degrees of freedom.

3.4.6 Jahn-Teller phononic and Coulombic models (Two-orbital model)

Another possible simplification could have been obtained by neglecting the electron-electron interaction in the full Hamiltonian but keeping the Hund coupling finite, leading to the following purely Jahn-Teller phononic model with active spin degrees of freedom:

$$H_{JT} = H_{kin} + H_{Hund} + H_{AFM} + H_{el-ph} \qquad (3.17)$$

Often this Hamiltonian will be referred to as the "two-orbital model". Dagotto used Monte-Carlo techniques to solve this kind of Hamiltonian numerically. Qual-

itatively, the negligible values of the probability of double occupancy in the strong electron-phonon coupling region with large J_H justifies the neglect of H_{el-el} since the Jahn-Teller energy is maximized when one e_g electron exists at each site. Thus, the JT-phonon-induced interaction will produce physics quite similar to that due to the on-site correlation.

It would be important to verify this last expectation by studying a multi-orbital model with only Coulombic terms, without the extra approximation of using mean-field techniques for its analysis. Of particular relevance is whether phase separation tendencies and charge ordering appear in this case, as they do in the JT-phononic model. This analysis is particularly important since, as explained before, a mixture of phononic and Coulombic interactions is expected to be needed for a proper quantitative description of manganites. For this purpose, yet another simplified model has been analyzed in the literature; $H_C = H_{kin} + H_{el-el}$. Note that the Hund coupling term between e_g electrons and t_{2g} spins is not explicitly included. The reason for this extra simplification is that the numerical complexity in the analysis of the model is drastically reduced by neglecting the localized t_{2g} spins. In the FM phase, this is an excellent approximation, but not necessarily for other magnetic arrangements. Nevertheless, the authors believe that it is important to establish with accurate numerical techniques whether the phase separation tendencies are already present in this simplified two-orbital models with Coulomb interactions, even if not all degrees of freedom are incorporated from the outset. Adding the S=3/2 quantum localized spins to the problem would considerably increase the size of the Hilbert space of the model, making it intractable with current computational techniques.

3.4.7 Main results from theoretical phase separation models of manganites

In the complicated phase diagram for manganites, there are many magnetic phases. A key concept to clarify these phases is the charge and the orbital ordering. Especially, orbital ordering is the remarkable feature, characteristic to manganites with

active e_g orbital. In the coming subsections spin orbital and charge degrees of freedoms for certain doping levels in the phase diagram will be presented. Note that the one-orbital model for manganites contains interesting physics notably a ferromagnetic(FM)-antiferromagnetic(AFM) competition that has similarities with those found in experiments. However, it is clear that to explain the notorious orbital order tendency in Mn-oxides, it is crucial to use a model with two orbitals. Under the assumption that both localized t_{2g}-spins and phonons are classical, the model without Coulombic terms can be studied fairly accurately using numerical and mean field approximations. Results obtained with both approaches will be summarized here.

The first comprehensive computational analysis of the one-orbital model was presented by Yunoki et al. who used classical spins for the t_{2g} electrons and the Monte Carlo (MC) technique.[10] Several unexpected results were found in that study. In particular, when the density of e_g electrons $\langle$ n $\rangle$=(1-x) was being calculated as the chemical potential μ was varied, it was surprising that some densities could not be stabilized; in other words, $\langle$ n $\rangle$ was found to change discontinuously at special values of μ. These densities are referred to as unstable. Alternative calculations in the canonical ensemble[11, 12], where the density is fixed to arbitrary values rather than being regulated by μ, showed that, at unstable densities, the resulting ground state is not homogeneous but is separated into two regions with different densities. The two phases involved correspond to those that bound the unstable range of densities[10, 11, 12]. This phenomenon, which has been named phase separation (PS), appears in many contexts, such as the familiar liquid-vapor coexistence in the phase diagram of water, and it is associated with violation of the stability condition $\kappa^{-1} = \langle$ n$\rangle^2\ \delta^2\ E/\delta\ \langle$ n $\rangle^2 > 0$, where E is the energy of the system per unit volume and κ is the compressibility.

In the realistic limit $J_H/t \gg 1$, PS occurs between hole-undoped $\langle$ n $\rangle$= 1 and hole-rich $\langle$ n $\rangle$ < 1 phases. Although the e_g and t_{2g} spins of the same ion tend to be parallel at large J_H, their relative orientation at one lattice spacing depends on the density. At $\langle$ n $\rangle$= 1, an AF arrangement results because the Pauli principle precludes movement of the electrons if all spins are aligned. However, at stable $\langle$ n $\rangle$ <

1 densities, DE forces the spins to be parallel, as computer studies have indicated.[10] Yunoki and Moreo have shown that if an additional small Heisenberg coupling among the localized spins is introduced, PS occurs also at small $\langle$ n $\rangle$ this time involving FM ($\langle$ n $\rangle > 1$) and electron-undoped AF states.[11] Phase segregation near the hole undoped and fully doped limits implies that a spin-canted state for the one-orbital model is not stable. Others arrived at similar conclusions after observing phase segregation tendencies by several analytical techniques[11, 13]. If a spin-canted state is unequivocally found in experiments, mechanisms other than that of DeGennes[14] may be needed to explain it. Note also that a canted state is difficult to distinguish experimentally from a mixed AF-FM state.

Most of the theoretical studies for manganites have been carried out using the one-orbital model, which certainly provides a useful playground for the test of qualitative ideas. However, quantitative calculations must necessarily include two active e_g orbitals per Mn ion to reproduce the orbital-ordering effects known to occur in these materials.[15]

Yunoki et al. reported the low temperature phase diagram of a two-orbital model with the MC method and they analyzed the results in a manner similar to the one-orbital case.[10] The results are reproduced in Fig. 3.6 for a one-dimensional (1D) system at large Hund coupling. The phase diagram is rich and includes a variety of phases such as metallic and insulating regimes with orbital order. The latter can be uniform, with the same combination of orbitals at every site, or staggered, with combinations alternating between the even and odd sites of the lattice at $\langle$ n $\rangle$= 1. Recently, Dagotto's group observed that the density of states exhibits pseudogap behavior caused by the PS tendencies, in both the one- and two-orbital cases, in agreement with photoemission experiments for layered manganites.[17] Of special importance for the discussion here are the regions of unstable densities. PS appears at small e_g densities between an electron-undoped AF state and a metallic uniform-orbital-ordered FM state. The latter phase itself coexists at larger densities and

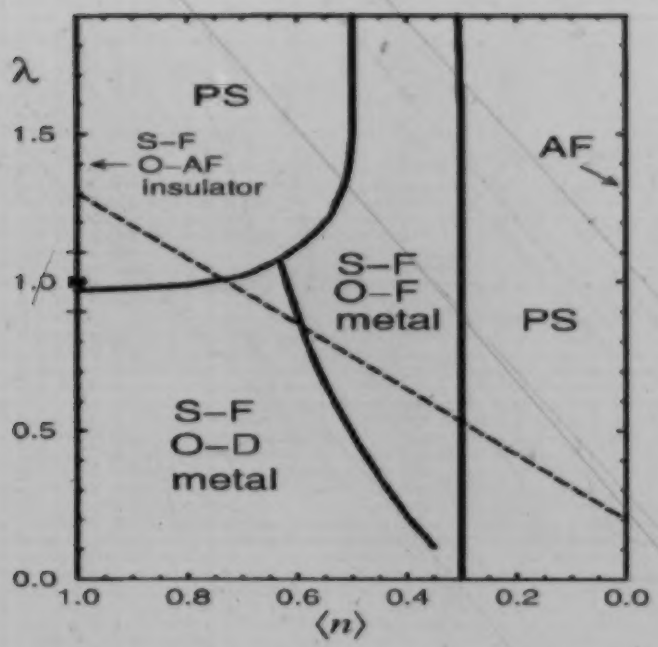

Figure 3.6: Phase diagram of the two-orbital model for manganites in 1D and T=0 including JT phonons, obtained with MC techniques.[10] S-F labels a spin-FM configuration; O-F, O-AF, and O-D denote a state where the orbital degrees of freedom are ordered uniformly, staggered, or disordered, respectively; PS indicates a phase separated state, and AF is an anti-FM state. Hund coupling is J_H=8 and Heisenberg coupling between localized classical spins is J=0.05, both in units of the hopping among the same orbitals. Meaning of the dashed line is a bordering some realistic limit for simulations when compared with the experiments and explained in more detail original citation.[16]

intermediate values of l with an insulating ($\langle$ n $\rangle$= 1) staggered-orbital-ordered FM state in an orbital-induced PS process.[18] The overall results are qualitatively similar to those obtained with other model parameters and in studies of two- and three dimensional (2D and 3D) systems. Overall, PS tendencies are strong in both the one- and two-orbital models and over a wide range of couplings. Similar tendencies have been recently observed including large on-site Hubbard interactions[19], which is reasonable because at intermediate and large electron phonon coupling a negligible probability of on-site double-occupancy was found.[18]

The macroscopic separation of two phases with different densities, and thus different charges, should actually be prevented by long-range Coulombic interactions, which were not incorporated into the one- and two-orbital models discussed thus far. Even including screening and polarization effects, a complete separation leads to a huge energy penalty. This finding immediately suggests that the two large regions involved in the process will break into smaller pieces to spread the charge more uniformly. These pieces are hereafter referred to as polarons if they consist of just one carrier in a local environment that has been distorted by its presence. This distortion can involve nearby spins (magnetic polaron), nearby ions (lattice polaron), or both, in which case this object is simply referred to as a polaron. However, the terms clusters and droplets are reserved for extended versions of the polarons, characteristics of a PS regime, containing several carriers inside a common large magnetic distortion or lattice distortion, or both.

This discussion suggests that in the regime of unstable densities the inclusion of extended Coulomb interactions will lead to a stable state, with clusters of one phase embedded in the other [see also article by Nagaev[20]]. It is expected that the competition between the attractive DE tendencies among carriers and the Coulomb forces will determine the size and shape of the resulting clusters. Either sizable droplets or polarons may arise as the most likely configuration[21] The stable state resulting from the inclusion of extended Coulomb interactions on an otherwise PS unstable regime is referred to as a charge inhomogeneous (CI) state. However, the

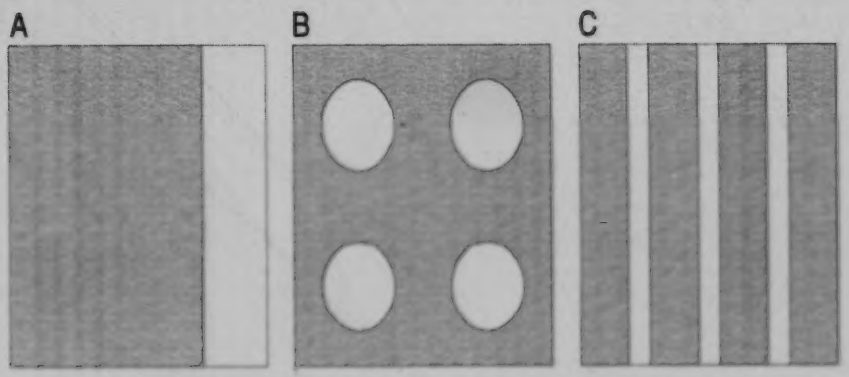

Figure 3.7: Qualitative representation of a macroscopic phase-separated state (A) as well as possible CI states stabilized by extended Coulomb interactions, such as spherical droplets (B) or stripes (C). Diameter of droplets and stripes are expected to be microscopic, but realistic calculations are still lacking.

ideas presented here are still described as the PS scenario, with the understanding that only microscopic phase segregation is the resulting net effect of the DE-Coulomb competition. Related ideas have been discussed in the context of the cuprates, with attractive interactions generated by antiferromagnetism or phonons.[22] An exception to the existence of only purely microscopic effects occurs if the competing phases have about the same density, as observed experimentally at x 5 0.5 (discussed below). In this case, large-scale PS can be expected. Note also that the CI state is certainly different from the meta-stable states that arise in a standard first-order transition. Fig. 3.7 presents a cartoon-like version of possible charge arrangements in the CI state, which are expected to fluctuate in shape, especially at high temperature where the clustering is dynamic. Unfortunately, actual calculations supporting a particular distribution are still lacking. Nevertheless, the currently available results are sufficient to establish dominant trends and to allow a qualitative comparison between theory and experiment.

Independent of the development of theoretical ideas on PS, a large body of exper-

imental evidence has accumulated about the existence of charge inhomogeneities in manganese oxides either in macroscopic form or, more often, through the presence of small clusters of one phase embedded into another. The results have been obtained on several materials, at a variety of temperatures and densities, and using a large array of microscopic and macroscopic experimental techniques. These studies have individually concentrated on particular parameter regions, and the results have rarely been discussed in comparison to similar results obtained in other phase regimes. However, once all these experimental data are combined, it appears that the manganite metallic FM phase is surrounded in both temperature and density by CI regions involving FM clusters coexisting with another phase, which in some cases is AF. It would be unnatural to search for special justifications for each of these experimental results. The most economical hypothesis is to explain the data as arising through a single effect, such as tendencies to PS that compete strongly with ferromagnetism at both large and small x, as well as above T_c.(see review by Dagotto for more detailed comparison of experiment and the phase separation model.[6])

3.4.8 Phase separation caused by the influence of disorder on first-order transitions

The role of quenched disorder appears to be very important for physics of manganites.[23] This type of disorder prevents the system from being totally ferromagnetic or totally CO-AF, as it occurs in the clean limit where a first-order phase transition separates the states. Small amounts of quenched disorder locally favor one phase over the other, leading to the inhomogeneous patterns found in simulations, which are believed to correspond to those in experiments. These predictions were beautifully confirmed by the experimental groups by means of a careful study of a particular Mn oxide (for this case $RE_{0.55}Sr_{0.45}MnO_3$, where RE=La,Nd,Sm,Eu and Gd) that spontaneously forms a structure very close to the clean limit, since all ions order in a regular pattern.[9] This family of compounds presents a bicritical phase diagram, with a first order FM-AF transition in excellent agreement with Monte Carlo simulations. When the material

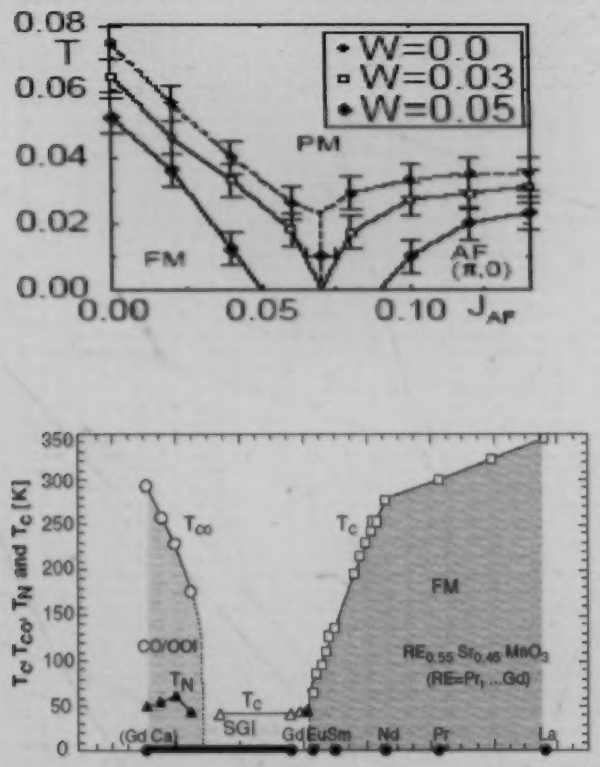

Figure 3.8: Top panel: Phase diagram results for different disorder levels (W) for details see book by Dagotto.[8] Bottom panel: experimental phase diagram for $RE_{0.55}Sr_{0.45}MnO_3$.[9] Note that with the presence of finite disorder simulations will reproduce the experimental data more convincingly.

is rapidly quenched in the growing process, such that the disorder is now incorporated in the distribution of trivalent ions, then a behavior characteristic of many other manganites is recovered. In particular, a large CMR is found in the presence of disorder, a result compatible with the theoretical predictions. The excellent agreement in the experimental phase diagram and simulation result are given in Fig. 3.8.

Recent investigations by Sato, Lynn, and Dabrowski arrived to similar conclusions studying $La_{0.54}Ba_{0.46}MnO_3$.[25] Other recent investigations have shown that the

addition of lattice elastic effects (due to the cooperative nature of the Jahn-Teller distortions) makes the disorder strength needed to induce the CMR phenomenon smaller in magnitude than without elasticity, and avoids limitations in the critical dimension that the naive use of Imry-Ma argumentations would suggest.[26] The relevance of elastic effects has been remarked on extensively in recent literature as well. Other power-law decaying effects, such as unscreened Coulomb interactions, have also been proposed as relevant in this context. In addition, investigations of a variety of models of percolation have shown that correlated disorder to mimic elastic effectscan even change the order of the transition rendering it first order. It may occur that infinitesimal disorder is enough to trigger and stabilize a phase separation process that is intrinsic to systems with first-order phase transitions. Nevertheless, in practice at least small amounts of disorder appear to be crucial to produce the inhomogeneous state that theorists proposed as the key factor to understand the CMR physics.

3.4.9 Resistivity of manganites in the mixed phase regime

Not much work was devoted to the magnitude of the magnetoresistance effect or quantitative description of the resistivity. One of the main lessons learned from the previous analysis of models for manganites is that intrinsic inhomogeneities are very important in this context. It is likely that the real Mn-oxides in the CMR regime are in such a mixed-phase state, a conclusion that appears inevitable based on the huge recent experimental literature. However, note that until recently realistic estimations of the dc resistivity ρ_{dc} in such a mixed-phase regime were not available. This was unfortunate since the interesting form of the ρ_{dc} vs. temperature curves, parametric with magnetic fields, is one of the main motivations for the current huge effort in the manganite context. However, the lack of reliable estimations of ρ_{dc} is not accidental: it is notoriously difficult to calculate transport properties in general, and even more complicated in regions of parameter space that are expected to be microscopically inhomogeneous. Although there have been some attempts in the literature to calculate ρ_{dc} , typically a variety of approximations that are not under

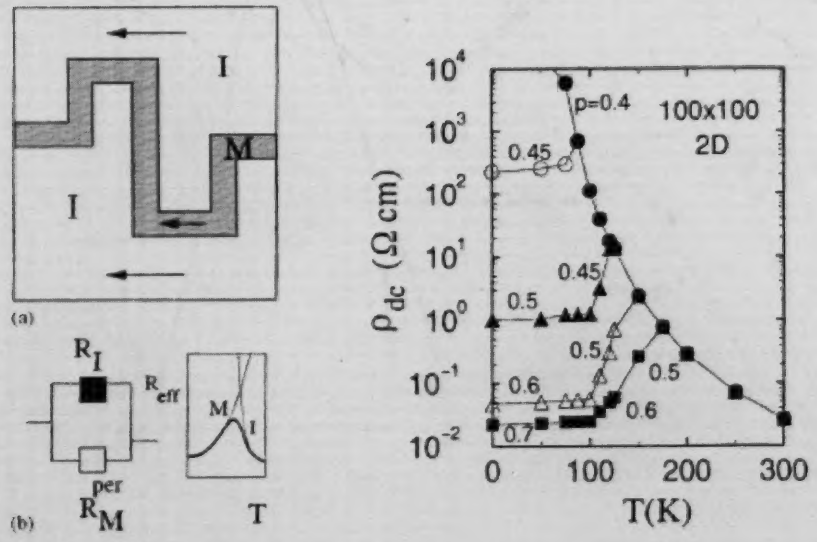

Figure 3.9: (a) Schematic representation of the mixed-phase state near percolation. The arrows indicate conduction either through the insulating or metallic regions depending on temperature. (b) Two resistances in parallel model for Mn-oxides. The (schematic) plot for the effective resistance R_{eff} vs. T arises from the parallel connection of metallic (percolative) R_M^{per} and insulating R_I resistances.[27] Right panel: Net resistivity ρ_{dc} of the 100×100 random resistor network used in the a and b, but with a metallic fraction p changing with temperature. Representative values of p are indicated. Results averaged over 40 resistance configurations are shown.[27]

control have been employed. In fact, the micrometer size of some of the coexisting clusters found in experiments strongly suggest that a fully microscopic approach to the problem will likely fail since, e.g., in a computational analysis it would be very difficult to study sufficiently large clusters to account for such large scale structures. It is clear that a more phenomenological approach is needed in this context.

For all these reasons, recently a two effective resistance picture of the physics of manganites was proposed by Mayr.[27] A sketch of this idea is in Fig. 3.9. Mayr

used random resistor network model to study the ρ_{dc} (see Ref. 106) This model was defined on square and cubic lattices, but with a lattice spacing much larger than the $4\AA$ distance between nearest-neighbor Mn ions. Actually, the new lattice spacing is a fraction of a micrometer, since the random network tries to mimic the complicated fractal like structure found experimentally. At each link in this sort of effective lattice, randomly either a metallic or insulating resistance was located in such a way that the total fraction of metallic component was p, a number between 0 and 1.

The actual values of these resistances as a function of temperature were taken from experiments. Mayr *et al.* used the ρ_{dc}(T) plots obtained by Uehara *et al.* corresponding to $(La_{5/8-y}Pr_y)Ca_{3/8}MnO_3$ (LPCMO), one of the compounds that presents the coexistence of giant FM and CO clusters at intermediate values of the Pr concentration.[27] More specifically, using for the insulating resistances the results of LPCMO at y=0.42 (after the system becomes a CO state with increasing Pr doping) and for the metallic ones the results at y=0.0 (which correspond to a metallic state, at least below its Curie temperature), the results of a numerical study on a 100×100 cluster are shown in Fig. 3.9 (the Kirchhoff equations were solved by a simple iterative procedure). It is interesting to observe that, even using such a simple phenomenological model, the results are already in reasonable agreement with the experiments, namely, (i) at high temperature insulating behavior is observed even for p as large as 0.65; (ii) at low temperature a bad metallic behavior appears; and (iii) a broad peak exists in between. Results in both 2D and 3D lead to similar conclusions. It is clear that the experimental results for manganites can be at least partially accounted for within the mixed-phase scenario.

The results of Fig. 3.9 suggest a simple qualitative picture to visualize why the resistivity in Mn-oxides has the peculiar shape it has. The relevant state in this context should be imagined as percolated, as sketched in Figure Fig. 3.9 (a), as predicted by the analysis of the previous section. Metallic filaments from one side of the sample to the other exist in the system. At low temperature, conduction is through those filaments. Necessarily, ρ_{dc} at T=0 must be large, in such a percolative regime.

As temperature increases, the ρ_{ab} of the filaments grows as in any metal. However, in the other limit of high or room temperature, the resistance of the percolated metallic filament is expected to be much larger than that corresponding to one of the insulating paths. Actually, near room temperature in many experimental graphs, it can be observed that ρ_{ab} in the metallic and insulating regimes are quite similar in value, even comparing results away from the percolative region. Then, at room temperature it is more likely that conduction will occur through the insulating portions of the sample, rather than through the metallic filaments. Thus, near room temperature insulating behavior is expected. In between low and high temperatures, it is natural that ρ_{ab} will present a peak. Then, a simple 'two resistances in parallel' description appears appropriate (see Fig. 3.9 (b)). The insulating resistance behaves like any insulator, while the metallic one starts at T=0 at a high value and then it behaves like any metal. The effective resistance shown in Fig. 3.9 (b) properly reproduces the experiments at least qualitatively (see Fig. 3.9(c)).

The study of effective resistivities and conductances has been also carried out in the presence of magnetic fields. From previous results it is clear that in the percolative regime small changes in the system may lead to large changes in the resistivity. For instance, if p changes by only 5% from 0.45 to 0.5 in Fig. 3.9(c), its magnitude is modified by two orders of magnitude! It is conceivable that small magnetic fields could induce such small changes in p, leading to substantial modifications in the resistivity. Some simulation results on field dependence of resistivity could be found in the book by Dagotto.[8]

3.5 Carrier density collapse and colossal magnetoresistance in doped manganites

Over the past decade, there has been significant interest in the fascinating properties of manganites, such as the metal-insulator transition (MIT) and the colossal magnetoresistance (CMR) effect. According to the double exchange (DE) model, the MIT

and the CMR are a consequence of the DE mechanism combined with the Jahn-Teller electron-phonon interaction with d states, leading to the conclusion that the low and high temperature phases are a spin polarized ferromagnetic metal and a polaronic paramagnetic insulator, respectively.

More recently, the current carrier density collapse model (CCDC), on the other hand, postulates that the MIT and the CMR are caused by a magnetic breakup at T_c of heavy bipolarons which are formed by pairing of oxygen p holes in the paramagnetic phase. Taking into account the tendency of polarons to form local bound pairs (bipolarons) as well as the exchange interaction of p polaronic holes with d electrons, Alexandrov *et. al* find a novel ferromagnetic transition driven by non-degenerate polarons in doped charge-transfer magnetic insulators. The crux of the matter is that in the paramagnetic state above the critical temperature a large fraction of polarons is bound into immobile pairs (bipolarons). As the temperature decreases in the paramagnetic phase ($T > T_c$), so does the density of mobile polarons, and the resistivity quickly increases with the decline of the number of carriers. With the onset of ferromagnetic order at T_c, the situation changes dramatically. As a result of the exchange interaction with the localized Mn spins, the energy of one of the polaron spin subbands sinks abruptly below the energy of the bound pairs. The pairs break up, the density of carriers (mobile polarons) jumps up, and the resistivity suddenly declines, as observed experimentally. The occurrence of the deep minimum in the carrier density close to the transition point, which Alexandrov *et. al* suggest calling a current-carrier-density collapse, allows us to explain the magnetization and temperature/field dependence of the resistivity of $La_{1-x}Ca_xMnO_3$ close to T_c as well as the giant isotope effect, the unusual tunneling gap, and the specific heat anomaly.

3.5.1 Ferromagnetic transitions in doped manganites

The Hamiltonian containing the physics compatible with the experimental observations mentioned above is

$$H = \sum_{k,s} E_k h^\dagger_{ks} h_{ks} - \frac{J_{pd}}{2N} \sum_{kj} m_k S^z_j + H_{sf} + H_{Hund} + \tag{3.18}$$
$$(2N)^{-1/2} \sum_{k,q,s} \hbar\omega_q \gamma_q h^{\dagger}_{l} h_{ks} (b_q - b^\dagger_{-q}) + \sum_q \hbar\omega_q (b_q b^\dagger_q + 1/2)$$

where E_k is the local density approximation (LDA) energy dispersion[7], h_{ks} is the annihilation hole operator of a (degenerate) p oxygen band with spins s= $\uparrow$ and $\downarrow$, J_{pd} is the exchange interaction of p holes with four d electrons of the Mn^{3+} ion at the site j, $m_k = h^\dagger_{k\uparrow} h_{k\uparrow} - h^\dagger_{k\downarrow} h_{k\downarrow}$, S^z_j is the z-component of Mn^{3+} spin, which is S=2 due to the strong Hund coupling, H_{Hund}, of the four d electrons on Mn^{3+} sites,and N is the number of unit cells. The two last terms of the Hamiltonian describe the coupling of p holes with phonons and the phonon energy, respectively. ω_q is the phonon frequency. If the holes were doped into d shell instead of p shell, the Hamiltonian would be similar to the Holstein t-J model with about the same physics of CMR as proposed by Alexandrov.[7, 9] The complete formalism of his approach could be found in the original report by Alexandrov.[9]

The main concept of CCDC is based on the fact that along with the band narrowing effect, the strong electron-phonon interaction binds two holes into a pair (bipolaron). The bipolarons are practically immobile in cubic manganites because the electron-phonon interaction is too strong in contrast with cuprates, where bipolarons are mobile owing to their geometry and a moderate coupling with phonons.

If these bound pairs are extremely local objects, two holes on the same oxygen, then they will form a singlet. If, however, these holes are localized on different oxygens, then they may well form a triplet state. Because of their zero spin, the only role of singlet bipolarons in manganites is to determine the chemical potential μ, which can be found with the use of the total carrier density per cell x as $2\int dE N_{bp}(E) f_{bp}(E) = x-n$, where $N_{bp}(E)$ is the density of bipolaronic states, $f_{bp}(E) = [g^2 \exp[(E-\Delta)/k_B T] - 1]^{-1}$ is the bipolaron distribution function, Δ is the bipolaron binding energy, n is the density of single (unbound) hole polarons, which are the only current carriers in manganites, and x is the doping concentration.

It is the localization of p holes into immobile bound pairs combined with their exchange interaction with the Mn d^4 local moments that are responsible for CMR. The density of these pairs has a sharp peak at a ferromagnetic transition when the system is cooled down through the critical temperature T_c. Below T_c, the binding of polarons into pairs competes with the ferromagnetic exchange which tends to align the polaron moments and, therefore, breaks those pairs apart. These competing interactions lead to unusual behavior of CMR materials and a huge sensitivity of their transport to the external field according to CCDC.

To illustrate the point, Alexandrov *et. al* assume that T_c is comparable with the polaron, W, and bipolaron bandwidths. Then (bi)polarons are not degenerate in the relevant temperature range, $f_p(E)=y\ \exp[-E/k_B]$and $f_{bp}(E)=y^2\ \exp[(E-\Delta)/k_B]$, and we can evaluate integrals reducing the system of mean field equations to,

$$n = 2\nu y cosh[(\sigma + h)/t] \tag{3.19}$$

$$m = n tanh[(\sigma + h)/t] \tag{3.20}$$

$$\sigma = B_2[(m + 4h)/2t] \tag{3.21}$$

$$y^2 = \frac{x - n}{2\nu^2} exp(-2\delta/t) \tag{3.22}$$

Here, t, h and δ corresponds to the dimensionless temperature, magnetic field and the binding energy. Their values are $t = 2k_BT/J_{pd}S$, magnetic field is $h = 2\mu_B H/J_{pd}S$ and binding energy is $\delta = \Delta/J_{pd}S$ while $\nu(=3)$ is the degeneracy of the p band.

The polaron density n is determined by Eq. 3.19 with $\sigma = 0$ above T_c. At the critical temperature, the polaron density has a minimal value $n_c = (2x)^{1/2} exp(-\delta/t_c)$; it then grows exponentially with temperature and saturates at $n = (2x + 1)^{1/2} - 1$. The remarkable observation is that there is a sharp increase of the polaron density at temperatures below T_c. The physical origin of the unusual minimum of the current

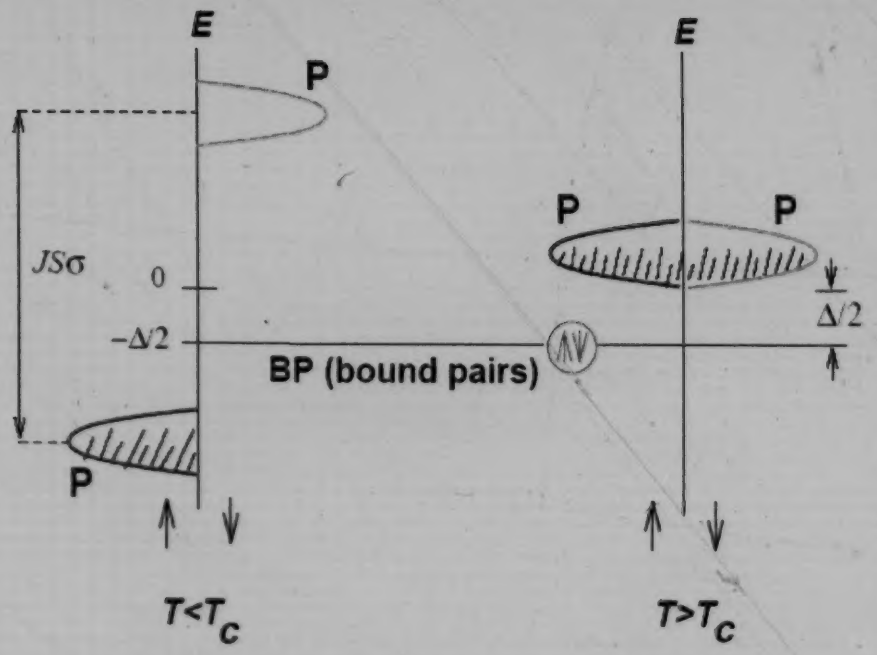

Figure 3.10: A schematic diagram of free-polaron (P) and polaron bound-pair (BP) densities of states at temperatures below and above T_c for up-spin (↑) and down-spin (↓) moments. The pairs (BP) break below T_c if the exchange J_{pd} S between p-hole polarons and Mn d^4 local spins exceeds the pair binding energy Δ, as in the case shown. The exchange interaction of polarons with the localized spins sets in below T_c; the spin-up polaron sub-band sinks abruptly below the bipolaron band, causing the break-up of the immobile bipolarons (left-hand panel). A sudden drop (collapse) of the density of the current carriers (polarons) in the vicinity of the ferromagnetic transition is the cause of a large peak in resistivity and colossal magnetoresistance.

carrier density at T_c lies in the instability of bipolarons below $T_c$due to the exchange interaction of polarons with d electrons. The spin-polarized polaron band falls below the bipolaron band with decreasing temperature, so that all carriers are unpaired at T=0 if $J_{pd}S \geq \Delta$. (See Fig. 3.10)

Linearizing Eq. 3.19 to Eq. 3.21, it is found that the critical temperature in zero magnetic field is $t_c = (n_c/2)^{1/2}$, where the polaron density at the transition nc is determined by

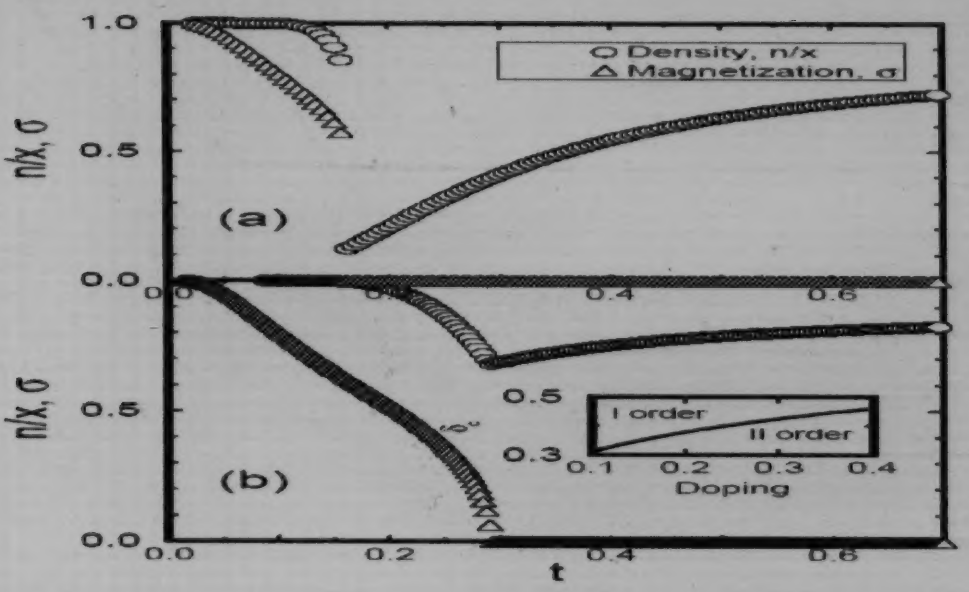

Figure 3.11: Polaron density n/x and magnetization as a function of temperature $t = 2k_BT/J_{pd}S$ in a doped charge-transfer insulator near (a) the first order, $\delta = \Delta/J_{pd}S$=0.5, and (b) second order, δ= 0.25, phase transitions (doping $x = 0.25$). Inset: The critical value of the relative binding energy of polaron pairs δ separating the regions of the first and second order phase transitions.

$$n_c^{1/2} ln \frac{2(x - n_c)}{n_c^2} = 2^{3/2}\delta \tag{3.23}$$

This equation has solutions only for δ below some critical value $\delta(x)$ [Fig. 3.11(b), inset]. The numerical solution of the system Eq. 3.19 to Eq. 3.22 shows that for $\delta > \delta_c(x)$ the ferromagnetic phase transition is first order with jumps of the polaron density and the magnetization, as observed [Fig. 3.11(a)]. The transition is continuous when $\delta < \delta_c(x)$ [Fig. 3.11 (b)].

A relatively weak magnetic field has a drastic effect on the inverse carrier density, near the first order transition, as shown in Fig. 3.12. As a result, the resistivity

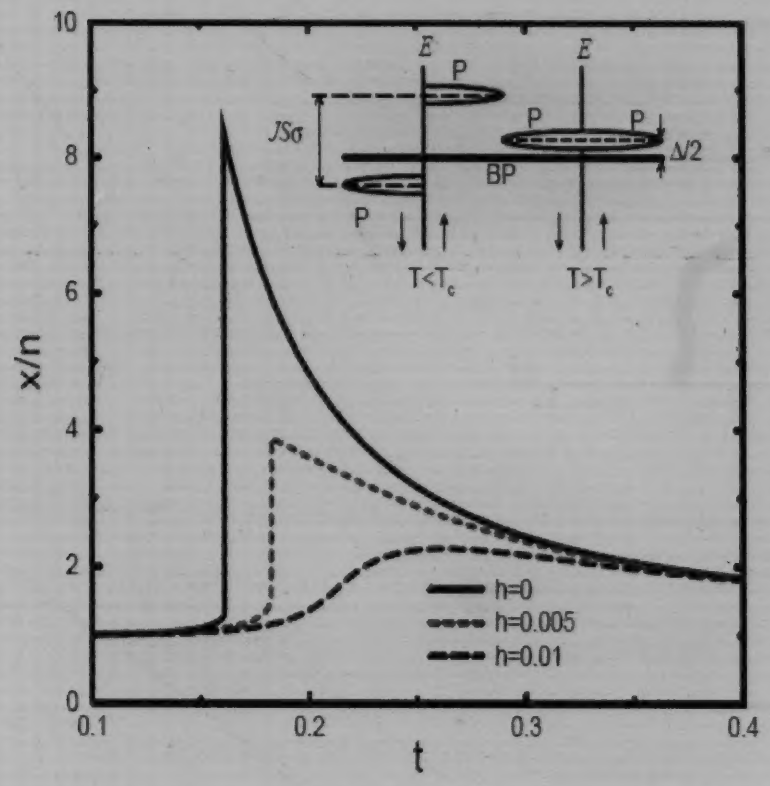

Figure 3.12: Inverse polaron density for different magnetic fields, $\delta = \Delta/J_{pd}S$=0.5, doping x 0.25. Note that the transition is a strong first order, and becomes continuous only when the external magnetic field exceeds some critical value. Inset: Schematic of polaron (P) and bipolaron (BP) densities of states at temperatures below and above T_c for up ($\uparrow$) and down ($\downarrow$) spin moments. The pairs (BP) break below Tc if exchange $J_{pd}S$ exceeds the pair binding energy Δ.

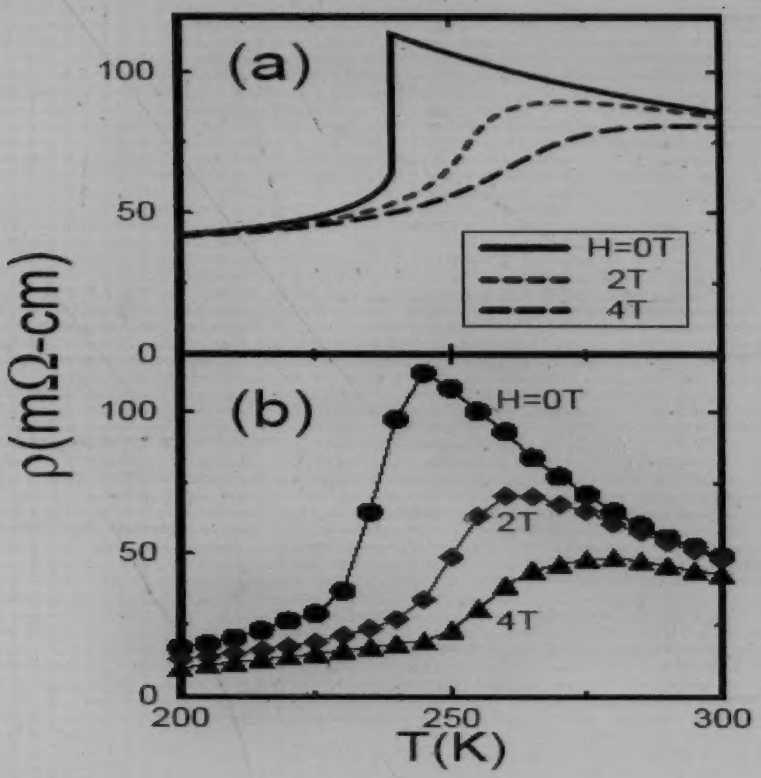

Figure 3.13: Resistivity of $La_{0.75}Ca_{0.25}MnO_3$ calculated within the present theory for the pair binding energy Δ= 900 K, and polaron exchange with the localized Mn^{3+} spins $J_{pd}S$= 2250 K (a), compared with experiment [30] on panel (b). Note an extreme sensitivity of the theoretical resistivity to external magnetic field (a), observed experimentally (b) for the doped manganite.

$\rho = 1/en\mu_p$ has a sharp maximum, which is extremely sensitive to the magnetic field in the vicinity of T_c.

CCDC was very successful in explaining the many physical properties of manganites including the CMR effect (see Fig. 3.13 for comparison with the experimental resistivity data) and specific heat anomaly and more interestingly the giant oxygen isotope effect which cannot be explained with any other existing theory so far. For details of this powerful model we suggest the reader to see relevant publications by

Alexandrov.[7, 9]

Most of the experimental resistivity data measured during the course of this dissertation ($Sm_{1-x}Sr_xMnO_3$, $La_{1-x}Ca_xMnO_3$ and $Nd_{1-x}Sr_xMnO_3$ systems) could be well described by CCDC theory. In fact in a the recent work of Alexandrov *et al.* the phase co-existence is included into the CCDC theory.[3] This excellent work is the basis of the Chapter 12 (percolative model of the resistive peak broadening in $La_{1-x}Ca_xMnO_3$) of the dissertation. Moreover, we would like to also mention that our oxygen isotope exchange experiments on $(SmGd)_{1-x}Sr_xMnO_3$ system (not included to the dissertation see the original publication by Egilmez *et al.*[31]) supports the findings of this theory.

Bibliography

[1] J. H. Van Santen and G. H. Jonker, *Phyica*, **16**, 599 (1950). G. H. Jonker and J. H. Van Santen, *Phyica*, **16**, 337 (1950).

[2] E. O. Wollan and W. C. Koehler, *Phys. Rev.*, **100**, 545 (1955).

[3] Y. Tokura, *Colossal magneto-resistive oxides*, 1st ed. (Gordon and Breach, Amsterdam, 2000).

[4] C. Zener, *Phys. Rev.* , **82**, 403 (1951).

[5] P.W. Anderson, H.Hasegawa, *Phys. Rev.* , **100**, 67 (1955).

[6] E. Dagotto, T. Hotta, A. Moreo, *Phys. Rep.* **344**, 1 (2001).

[7] A. S. Alexandrov and A. M. Bratkovsky, *Phys. Rev. Lett.*, **82**, 141 (1999).

[8] E. Dagotto, *Nanoscale Phase separation and Colossal Magneto-resistance*, 1st ed. (Springer, Berlin, 2002).

[9] J. Kanamori, *Prog. Theor. Phys.*, **30**, 275 (1963).

[10] S. Yunoki *et al.*, Phys. Rev. Lett., **80**, 845 (1998).

[11] S. Yunoki *et. al*, *Phys. Rev. B*, **58**, 6403 (1998).

[12] E. Dagotto *et. al*, *Phys. Rev. B*, **58**, 6414 (1998).

[13] D. Arovas and F. Guinea, *Phys. Rev. B*, **58**, 9150 (1998).

[14] P. G. de Gennes, *Phys. Rev.* , **118**, 141 (1960).

[15] Y. Murakami *et al.*, *Phys. Rev. Lett.*, **80**, 1932 (1998);Y. Murakami *et al.*, *Phys. Rev. Lett.*, **81**, 582 (1998).

[16] A. Moreo *et al.*, *Science* **283**, 2034 (1999).

[17] D. S. Dessau *et al.*, *Phys. Rev. Lett.*, **81**, 192 (1998).

[18] S. Yunoki, A. Moreo, E. Dagotto, *Phys. Rev. Lett.*, **81**, 5612 (1998).

[19] K. Kubo, D.M. Edwards, A.C.M. Green, T. Momoi, H. Sakamoto, *Physics of Manganites*, edited by T.A. Kaplan and S.D. Mahanti 1st ed. (Plenum Publishers, Berlin, 2002) p 71.

[20] E. L. Nagaev, *Phys. Status Solidi B*, **186**, 9 (1994).

[21] A. Malvezzi, S. Yunoki, E. Dagotto, *Phys. Rev. B*, **59**, 7033 (1999).

[22] C. Castellani, C. Di Castro, M. Grilli, *Phys. Rev. Lett.*, **75**, 4650 (1995).

[23] C. Sen, G.Alvarez, H. Alliaga, E. Dagotto, *Phys. Rev. B*, **73**, 224441 (2006).

[24] Y. Tomioka and Y. Tokura, *Phys. Rev. B.* **70**, 014432 (2004);Y. Tomioka, Y. Okimoto, J. H. Jung, R. Kumai, and Y. Tokura, *Phys. Rev. B.* **68**, 094417 (2003) and references therein.

[25] T. J. Sato, J. W. Lynn, and B. Dabrowski, *Phys. Rev. Lett.*, **93**, 267204 (2004).

[26] Y. Imry and S. K. Ma, *Phys. Rev. Lett.*, **35**, 1399 (1975).

[27] M. Mayr *et al.*, *Phys. Rev. Lett.*, **85**, 26 (2000).

[28] A. S. Alexandrov and A. M. Bratkovsky, *J. Phys: Condens. Matter* **11**, 1989 (1999).

[29] A. S. Alexandrov, A. M. Bratkovsky, and V. V. Kabanov, *Phys. Rev. Lett.*, **96**, 117003 (2006).

[30] P. Schiffer *et al.*, *Phys. Rev. Lett.*, **75**, 3336 (1995).

[31] M.Egilmez *et al.*, *Journal of materials chemistry*, **18**, 5796 (2008).

Chapter 4

Experimental set-up and procedure

4.1 Sample preparation

The doped perovskite manganites studied in this dissertation are all home made and could be categorized in two main groups: i) bulk (polycrystalline) materials ii) epitaxial thin films. We will describe the sample preparation characterization methods for these two categories in the next section.

4.1.1 Polycrystalline (Bulk) samples

Polycrystalline samples in this study were prepared using the high temperature solid state reaction method.[1] For instance, to prepare stoichiometric $Sm_{0.55}Sr_{0.45}MnO_3$: A prescribed ratio of Sm_2O_3, $SrCO_3$ and MnO_2 powders were mixed and reacted at 1200 °C for 24 hours in air. The resulting samples were pulverized and sintered twice using the same conditions and subsequently quenched in order to obtain the nominal oxygen content. Notice that in order to obtain a variation in grain size of the sintered samples we modified the last sintering temperature, for example, sintering at 1500 °C for the last step of the sample preparation will result in a larger grain size manganite sample. The sintered samples were in pellet shape of different diameters. We have cut rectangular shaped bars from these pellets for resistivity measurements and magnetization measurements. The remaining part of the pellet was pulverized

and used in powder X-Ray diffraction analysis. X=Ray analysis were carried out on a Rikagu X-Ray diffractometer and all samples studied in this thesis were single phase. In addition, samples with 1 inch diameter were produced as a target material for thin film preparation.

4.1.2 Oxygen stoichiometry in bulk samples

The oxygen stoichiometry has a significant impact on physical properties in manganites. Therefore reliable data can only be obtained from stoichiometric samples where oxygen content is nominal (3±0.01).[2] Franck et al. reported extensive work on effects of oxygen stoichiometry and sintering conditions. In his studies it was shown that at lower sintering temperatures (temperatures substantially lower than 1200°C) oxygen excess always exists. They have optimized the sintering and oxygen exchange conditions to obtain samples with negligible oxygen excess or deficiency. Our sample preparation conditions are identical to that described by Franck where an oxygen content close to 3.0 is expected.[2] In order to further clarify the oxygen stoichiometry and content in our samples, we have carried out iodometric titration on our samples. The iodometry method used in this study is based on that described by Vazquez.[3] Around 30 mg of $(Sm)^{III}_{0.55}Sr^{II}_{0.45}Mn^{III}_{1-p}Mn^{IV}_{p}O_{3\pm\delta}$ is weighed with a microbalance and dissolved in a mixture of 10 mL 2M KI solution, 10 mL 2M HCl and 4mL freshly boiled distilled water. The following reactions occur:

$$2Mn^{III} + 2Cl^- \rightarrow Cl_2 + 2Mn^{II} \tag{4.1}$$

$$2Mn^{IV} + 6Cl^- \rightarrow 2Cl_2 + 2Mn^{II} \tag{4.2}$$

$$Cl_2 + 2I^- \rightarrow 2Cl^- + I_2 \tag{4.3}$$

The resulted iodine is titrated with a standard volumetric solution of sodium thiosulfate (0.02N) until a clear and colorless solution is obtained. Close to the end

point of the titration a 1 % mass excess in solution is added in to see the color change better. The titration process leads to the following reaction:

$$Sr_xBi_yO_z^{n+} + I_2 \rightarrow Sr^{2+} + Bi^{3+} + Sr_xBi_yO_z^{n+} \quad (6.6)$$

From the charge balance for $(Sr_x)^{(2x)}_{x=0}Bi^{(3)}_{x=0}Sr^{(2)}_{x=2}Bi^{(3)}_{x=2}O^{(2)}_{x=0}$ it can be shown that $3.6n = (9.33n-\beta)/2$. Then we can use the volume of the added 0.05 N thiosulfate (V), to calculate the volume of the iodine released from in grams of manganite sample and, therefore, the value of δ. For $(Sr_x)^{(2x)}_{x=0}Bi^{(3)}_{x=0}Sr^{(2)}_{x=2}Bi^{(3)}_{x=2}O^{(2)}_{x=0}$ it can be shown that $\beta = (n-22).8(VV')/(8VV'-m)$, where $V = 0.05$. Using steps described above we have carefully calculated the oxygen contents in our samples and it was found that our sample preparation method allowed us to have an oxygen content of 3.0 (±0.005) for all samples. These results rule out the possibility of oxygen excess or deficiency in our samples.

6.1.2 Thin film growth

Since the discovery of high temperature superconductivity, several methods have been employed to prepare high quality high T_c thin films. The developments in high T_c thin film growth immediately have been applied to manganite thin film deposition techniques. Most of the films are deposited onto lattice substrates of $SrTiO_3$ (a=3.905Å), MgO or sapphire using laser ablation of stoichiometric ceramic targets, rf and dc sputtering of ceramic targets, a reactive co-evaporation technique, and deposition of cations in an oxygen atmosphere. Among these methods, off-axis magnetron sputtering is considered one of the most successful because it allows a slow growth of films and deposition over large areas.

In this dissertation, we have used the DC magnetron sputtering technique to prepare epitaxial thin films on (100) oriented $SrTiO_3$ (a=3.905Å) substrates. This method allowed us to grow films with different thicknesses and resistivity/conductivity through changing the sputtering conditions.

The sputtering deposition system that we used to prepare manganite thin films

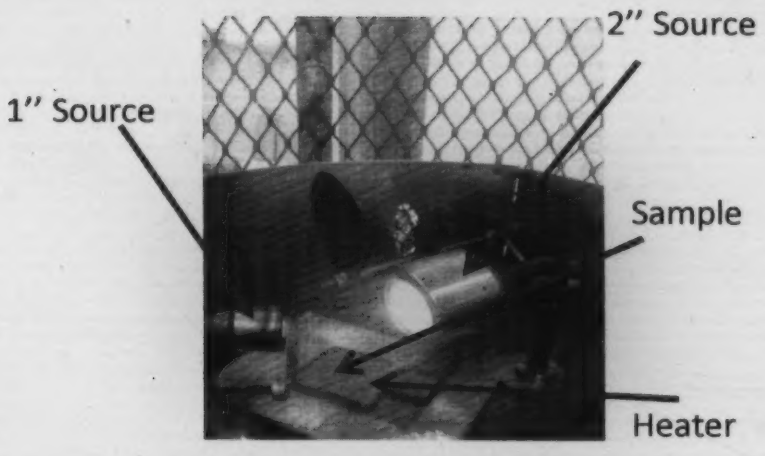

Figure 4.1: A picture from sputtering system during an epitaxial manganite film deposition

consists of a vacuum chamber with a base pressure of $1 \times 10{-}7$ torr produced by a cryopump, an dc magnetron sputter gun and a heater with a nickel plate and a chromel-alumel thermocouple. A temperature controller was used to control the substrate temperature with a stability of $\pm 1^{o}C$. A picture from the deposition system is given in Fig.4.1.

It is known that the growth of epitaxial thin films depends on the deposition conditions and the substrates. For a sputtering deposition technique, these conditions include: the substrate temperature, the O_2/Ar gas pressure ratio, the total gas pressure, the substrate-target distance, the sputtering configuration (on-axis or off-axis) and the sputtering power which controls the deposition rate. Manganite thin films were deposited on (100) oriented $SrTiO_3$, $LaAlO_3$ substrates of different dimensions using the off-axis configuration. The substrates were attached to the heater plate using a silver paint in order to achieve uniform heating. All the targets used in the dissertation were home made and prepared by the standard solid state reaction method described in the first section. The sputtering was performed using a dc power between 30 to 70 W at a total pressure of 120 mtorr in 5:1 oxygen-argon gas mix-

tures. During sputtering the substrate temperature was kept at 750C for both kinds of substrates. The deposition temperatures correspond to those which are required to achieve a high crystalline quality. The deposition time ranges from 6 minutes to 5 hours. After deposition, the chamber was filled with oxygen at a pressure slightly less than 1 atmosphere and the films were subsequently quenched to 650 ^oC and kept at this temperature for 2 hours and then cooled to room temperature with rate of 20 ^oC per minute.

The samples were patterned into strips for resistivity measurements using ion milling etching along with photolithography techniques or simply films were grown on substrates which have smaller dimensions required for measurements (10× 1-2 mm). Large area contacts on the film were deposited by silver-sputtering in order to minimize Joule heating effects. The silver-sputtering was performed using an rf power between 30 to 40 W at an Ar pressure of 20 mtorr for about 2-5 minutes. Copper leads were attached to silver contacts using mechanically pressed indium. A typical distance between voltage probes was 0.5 mm.

4.2 Sample characterization

We used several techniques to characterize our samples including resistivity measurements as function of temperature, angle and magnetic field and magnetization measurements as a function of temperature and magnetic field. Specific heat was measured on some of the samples. Powder X-ray diffraction and scanning electron microscopy (SEM) techniques were used for structural characterization.

The setup that we used to perform the resistive measurements consists of four major parts: cryogenic apparatus, non-superconducting electromagnets, sample holder and the angle controller system. The cryogenic apparatus cons of a narrow tailed stainless steel dewar capable of holding LN_2 for a period between 48 to 72 hours. The narrow tail is to allow the magnet pole separation as small as 10 cm in order to attain greater magnetic fields in the sample region. The cryostat consists of a two

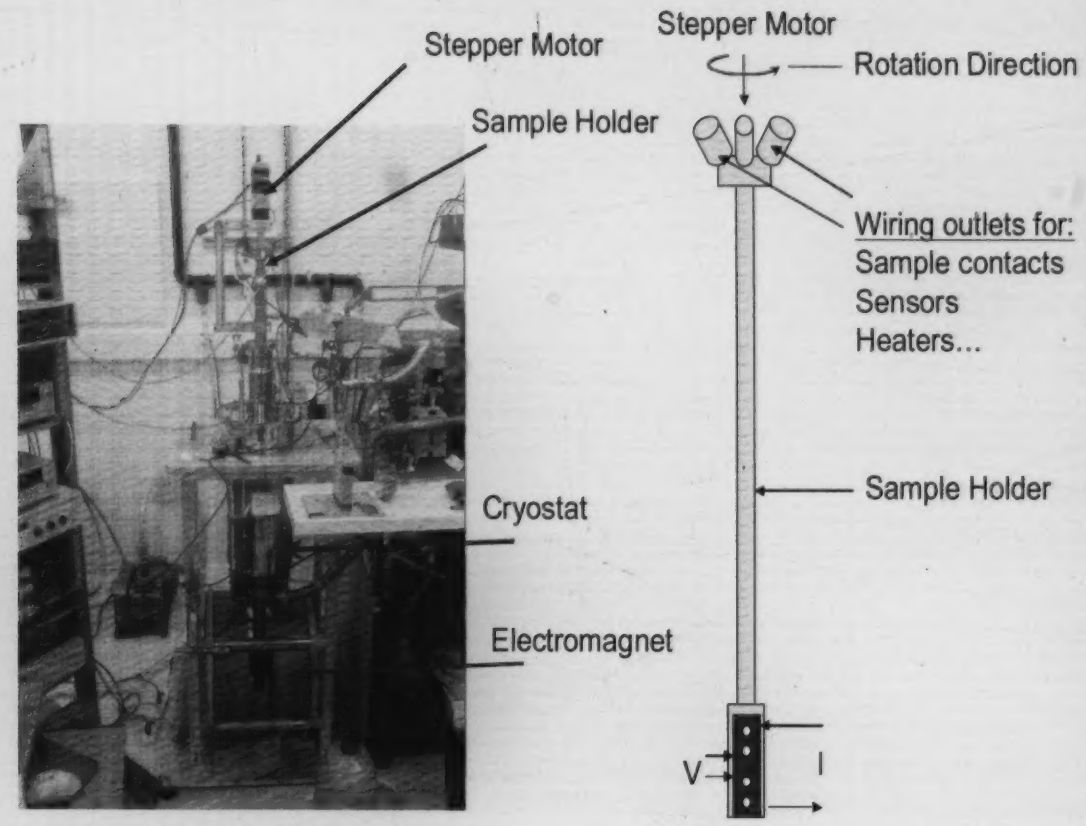

Figure 4.2: A picture of resistivity measurement unit

vacuum-can system. The outer can was evacuated to a pressure of 10^{-7} torr and the inner one was filled with helium gas to a pressure of less than one atmosphere.

The magnetic field was applied using a horizontal two copper-wound coils magnet. The magnet had an iron core that yielded a large field strength. The magnet is powered by a Sorensen DC S20-150SE power supply. The magnet provided a maximum field of 0.8 T at a current of 91 A and voltage of 13 V. The temperature of the magnet coils was kept almost constant by flowing water through them. The magnetic field at the sample was monitored using an ATT hall probe located directly behind the sample. This consistently showed that the applied field did not change by more than

0.1%.

The sample holder is made of a poor thermal conductor of a stainless steel hollow cylinder of 10 mm outer diameter and 1 m long. One end of the cylinder hosted all the electrical connections and was connected to the angle-controller system through a flexible coupling. The other end is fitted with a V-shaped copper block which hosts a carbon-glass resistance thermometer embedded at its center. Attached to the copper block is an inductanceless heater and a hall probe device to monitor the field at the sample position. The sample is placed on the flat side of the V-shape copper block after putting a thin layer of "apiezon" grease on the sample. This type of grease provides a good thermal contact between the copper block and the sample. The sample is attached to the holder by a clip. A picture of the resistivity system could be seen in Fig. 4.2.

The computer-controlled angle-controller system is composed of a 200-step stepping motor, an IMS Micro-LYNX-4 integrated micro-stepping controller, a 100-1 CGI Paragon Planetary Gear-head reducer and a US Digital 3-channel (index) 2000-line optical encoder. The Micro-LYNX-4 is a programmable integrated micro-stepping motor drive and high-performance controller which provides microstep resolution up to 51200 steps per revolution. This allows one to obtain an angular resolution of 0.007^o. However, in general the microstepping devices are not linear which results in nonuniform microsteps. In order to eliminate this nonuniform microstepping, we have used a backlash-free 100-1 gear reducer combination. The optical encoder was attached directly to the sample holder by means of flexible coupling from one side, and the other side was connected to the gear head. The flexible coupling helps to get rid of any misalignments between the sample holder and the angle controller system. The three-channel 2000-line optical encoder imposed an upper limit on the angular resolution that can be accurately monitored. Although the microstepping device can reach an angular resolution down to 0.007^o, the maximum resolution the encoder can read is $360^o/8000(\text{lines}) = 0.045^o$ which is good enough for all of our angular measurements.[4]

The use of the normal stepping motors or the commercial micro-stepping systems to reach small angular resolution (less than 0.1^o) without using a sensor(optical encoder) to read the exact position of the sample, may lead to a substantial ambiguity especially if we add to that the error due to the backlash of the motor. Stepping motors backlashes can be minimized or eliminated by using a high ratio gear reducer combination between the sample and the stepping motor.

The other important issue, which also requires a special attention in the measurement of $\rho(\theta)$, is the precise temperature control. When the sample is being rotated in a magnetic field this produces an induced emf in the heater and in the leads of the thermal sensors attached to the sample holder. If the rotation speed is large this will disturb the heater current and consequently causes large temperature fluctuations during the measurement. To reduce these effects very slow rotation speeds are essential.

In the design of our experimental setup used to measure the angular dependence of resistivity, we have used a combination of a stepping motor and a 100-1 planetary gear reducer to eliminate the backlash and to provide reliable fine rotations. Also we have used an optical encoder attached directly to the sample to read the exact position of the sample. The angular rotations were done at very low speeds to minimize the temperature fluctuations and obtain a very stable temperature.[4]

4.2.1 Resistivity measurement

We performed the measurements of the resistivity as a function of temperature $\rho(T)$ between 80 K and 300 K in zero magnetic field and in a constant magnetic field up to 0.7 Tesla. The measurement of the temperature dependence of resistivity in a constant magnetic field were carried out for three different orientations of the field **B** relative to current **J**. $\rho(T)$ measurements for the range of temperatures between 80 K and 300 K were performed on heating from 80 K to room temperature. We also measured the resistivity as a function of the angle θ between the ab-plane of

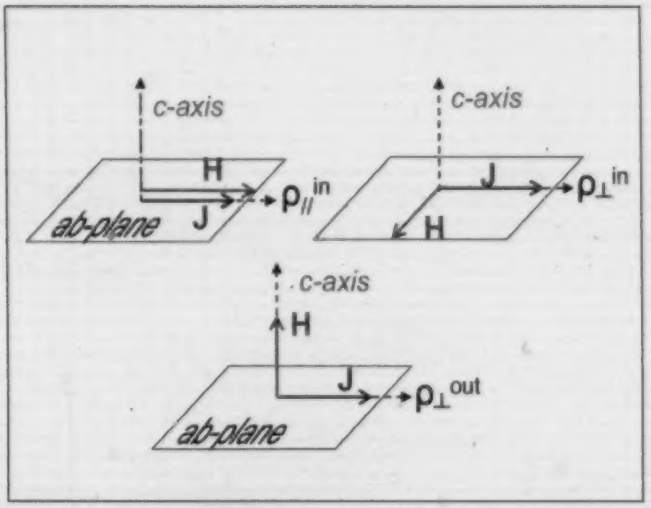

Figure 4.3: Magnetic field and current configurations applied during the measurements of resistivity of manganite thin films.

the film and the direction of the magnetic field B. These angular studies were done over a temperature range of 80 K to 300 K, as a function of the magnitude of the magnetic field. The angular measurements were carried out by rotating the copper sample holder about its vertical axis in a horizontal magnetic field up to 0.7 Tesla. The "in-plane" and the "out-of-plane" resistivity measurements can be used to define fully all types of magneto-resistive anisotropy, i.e. the "in-plane" and the "out-of-plane" AMRs. The AMRs are used to characterize the changes in the resistivity as the direction between the applied magnetic field **H** and the direction of the current **J** changes. In this thesis, the "in-plane" AMR is defined as $\mathrm{AMR}^{in} = (\rho_{\parallel}^{in} - \rho_{\perp}^{in})/\rho_o$, where $\rho_{\parallel}^{in}$ and $\rho_{\perp}^{in}$ are the resistivities of the film for **H** that is located in the plane of the film and is oriented parallel and perpendicular to the current, respectively (see Fig. 4.3), and ρ_o is the resistivity in zero applied field. Notice that the superscript on ρ labels that **H** is in the plane of the film (i.e. *ab*-plane), while the subscript indicates the direction of **H** with respect to **J**. The "out-of-plane" anisotropies are defined as $\mathrm{AMR}_{\parallel}^{out} = (\rho_{\parallel}^{in} - \rho_{\perp}^{out})/\rho_o$ and $\mathrm{AMR}_{\perp}^{out} = (\rho_{\perp}^{in} - \rho_{\perp}^{out})/\rho_o$. The symbol $\rho_{\perp}^{out}$

denotes the resistivity measured when **H** is applied perpendicular to both the film's plane (i.e. out of plane) and the direction of the transport current (see Fig. 4.3). Consequently the "in-plane" AMR^{in} is also the difference between these two "out-of-plane" anisotropies, i.e. $AMR^{in} = AMR_{\parallel}^{out} - AMR_{\perp}^{out}$. Note that sometimes it is desirable to use different definitions for AMR in magnetic materials (see Chapter 10).

Resistivity was measured using a standard DC four-probe method. The current was applied to the sample in the form of short pulses (of duration less than 200 ms) in both directions, in order to eliminate the background noise and charge accumulation as well as to reduce Joule heating. The voltage was measured using a Keithley 2182 nanovoltmeter in synchronization with a Keithley 236 current source, where the nanovoltmeter was used as the triggering unit. The nanovoltmeter was operated in a delta mode. This mode allowed the measurement and the calculation of the voltage for the DC current-reversal technique to eliminate the effects of thermal emf's in the leads. Each Delta reading is calculated from two voltage measurements of the sample for two opposite directions of the current. In this mode, the basic Delta voltage calculation is given by:

$$V_{Delta} = \frac{V_1 - V_2}{2} \tag{4.5}$$

where: V_1 and V_2 are the voltage measurements on the positive and negative phases of the current source. This 2182 nanovoltmeter is optimized to provide low-noise readings when the measurement speed (the applied current reversal speed) is set between 100 msec and 333 msec . At these reading rates, noise induced by the power line should be insignificant. Each Delta mode measurements was repeated ten times and then the results of the ten measurement were stored in the buffer of the nanovoltmeter. Only the average value of the ten measurements, the maximum and the minimum values were transferred to the computer. In most cases the variation between the average and the corresponding maximum and minimum values is less than 0.1%.

Our measurements require precise temperature control. Temperature was monitored by a carbon-glass resistance thermometer and an inductionless heater and

controlled to better than 10mK for each single angular sweep. For the angular measurement this was achieved by rotating the sample very slowly in the magnetic field in order to reduce variations in the emf in the heater which could disturb the temperature stability. In order have better temperature control especially at higher temperatures (above 200 K) we installed a platinum temperature sensor and manganin wire heater.

The whole experimental setup (except the electromagnet) was completely computerized using a GBIB IEEE-488 interface card for all electronics except the Micro-LYNX angle-controller which was remotely controlled by an RS-232 interface port. The program code was written previously in Microsoft Visual Basic language. The experimental setup with the remote control is capable of measuring voltage (1nV-100V) as a function of current (10 pA-100mA), temperature (65-300 K), and angle ($0.045^o - 360^o$) unattended.

4.2.2 Magnetization measurements

The magnetization measurements and magnetic hysteresis loops were done using a SQUID magnetometer (MPMS, Quantum Design). Both zero field cooled (ZFC) and field cooled (FC) magnetization curves were measured as follows: the sample is initially cooled in zero field down to 6 K, then the field is applied at this temperature and the magnetization is measured while warming up to 300 K (ZFC magnetization), followed by cooling back again to 6 K (FC magnetization) without changing the magnetic field. Specific heat measurements on some of the samples were done using a Quantum design physical property measurement system (PPMS).

4.2.3 Structural characterizations

Phase purity and phase identification measurements were done using a RIKAGU 12 kW rotating anode X-Ray diffractometer. A JEOL Scanning electron microscope (SEM) was used for microstructural characterization.

Bibliography

[1] M. Egilmez, *et al.*, *J. Mater. Chem.*, **18** 5796, (2008).

[2] J. P. Franck, *et al.*, *Phys. Rev. B*, **64**, 214412 (2001).

[3] C. V. Vazquez, *et al.*, *J. Mater. Chem.*, **15** 1542, (2005).

[4] Maher Abdelhadi, *intrinsic properties of YBCO thin films*, University of Alberta Thesis, (2002).

Chapter 5

Oxygen redistribution induced disorder and magneto-transport properties of $Sm_{0.55}Sr_{0.45}MnO_3$ manganites

5.1 Introduction

Manganites, $R_{1-x}A_xMnO_{3-\delta}$ (where R and A are trivalent rare earth and divalent alkaline earth ions, respectively) continue to attract considerable scientific and technological attention, primarily because many of them exhibit colossal magnetoresistance (CMR). The manganites are good candidates for applications such as magnetic sensors[1], magnetic read heads, resistance switches[2], magnetostrictive devices[3] or infrared bolometers [1]. $R_{1-x}A_xMnO_3$ compounds exhibit a rich phase diagram whose transport and magnetic properties are strongly affected by a variety of physical factors. These factors include the value of x (e.g. the ratio between Mn^{+4} and Mn^{+3} ions) and hence the hole concentration, the average size of the ion A and the resulting cationic size mismatch, the Mn-O distances and the Mn-O-Mn bond angles[4], etc. A good scientific understanding of the magnetotransport properties, and consequently

how they can be manipulated, is clearly very important if reliable and efficient CMR-based devices are to be fabricated.

Recent experimental and theoretical work suggest that the CMR manganites are intrinsically inhomogenous[5]. Phase separation between metallic (ferromagnetic) and insulating clusters has been proposed to explain these inhomogeneities [6]. For example the temperature dependence of the resistivity $\rho(T)$ of manganites at the metal-insulator transition (MIT) has been studied by Mayr et al [7] using a random resistor network based on this phase separation scenario. In their model, resistivity in the CMR regime is governed by the existence of percolating conduction paths with ferromagnetic metallic filaments extended across the sample. At low temperatures the ferromagnetic clusters are connected, leading to metallic behavior. At higher temperatures these domains become disconnected and the conduction occurs preferentially through the insulator. Burgy et al. [8] theoretically studied the effect of a quenched long-range correlated disorder (through the elastic lattice distortions) on $\rho(T)$ in CMR materials. Monte Carlo methods were used to simulate the behavior of the peak in ρ(T) near the MIT. The magnitude of this peak was found to increase sharply and the corresponding peak width to decrease with an increasing disorder (a decreasing size of ferromagnetic clusters). Nagaev[41] suggested that magnetoresistive state of manganites (such as $La_{1-x}Ca_xMnO_3$) is a result of a non-uniform oxygen distribution. For example, doping of $LaMnO_3$ with Ca could lead to disorder due to oxygen phase separation, i.e. formation of oxygen vacancies and interstitial oxygen atoms clustered in different parts of the crystal. According to this model regions of the crystal containing interstitial oxygen atoms (acceptors) have enhanced hole density. Since holes are responsible for establishing the ferromagnetic ordering, these parts are ferromagnetic. On the other hand, regions containing oxygen vacancies (donors) behave like compensated semiconductors and are characterized by low conductivity and antiferromagnetic ordering. Lattice distortions (strain) can be produced by oxygen vacancies that form insulating clusters[10]. Assuming that only the insulating phase is strained, recent theoretical work by Ahn *et al.*[11] suggests that the metal-insulator

phase coexistence in manganites is strain-induced.

Experimental studies of the role of disorder on ρ(T) is crucial for the basic understanding of magneto-transport properties of manganites as well as for engineering applications. Nevertheless, despite the importance of this issue, such measurements have not yet been reported extensively because it is very difficult to control disorder in actual experimental situations. Such a study is reported in the present section of the dissertation for the $Sm_{1-x}Sr_xMnO_3$ manganite.

5.2 The resistivity of $Sm_{1-x}Sr_xMnO_3$ system

We have prepared $Sm_{1-x}Sr_xMnO_3$ (SSMO) bulk samples with the composition 0.40< x <0.50 with standard solid state reactions (For details of solid state reaction see Chapter 4). All the samples prepared were single phase according to X-ray diffraction analysis. The temperature dependence of resistivities for different compositions of SSMO is shown in Fig. 5.1.

As can be seen from Fig. 5.1, below 0.48 doping level SSMO shows a metal insulator transition and above 0.48 doping level it is insulating. The x=0.44 and 0.45 samples have similar magnetotransport properties and metal insulator transition temperature. It is shown theoretically that for manganites in the vicinity of half doping(x=0.45-0.50), ground state is very sensitive to any kind of perturbation namely temperature, X-Rays, etc. Therefore, for further studies we mainly focused on the x=0.45 doping level which can be considered as a composition bordering the charge orbital instability in SSMO and the composition which exhibits the highest metal insulator transition temperature.

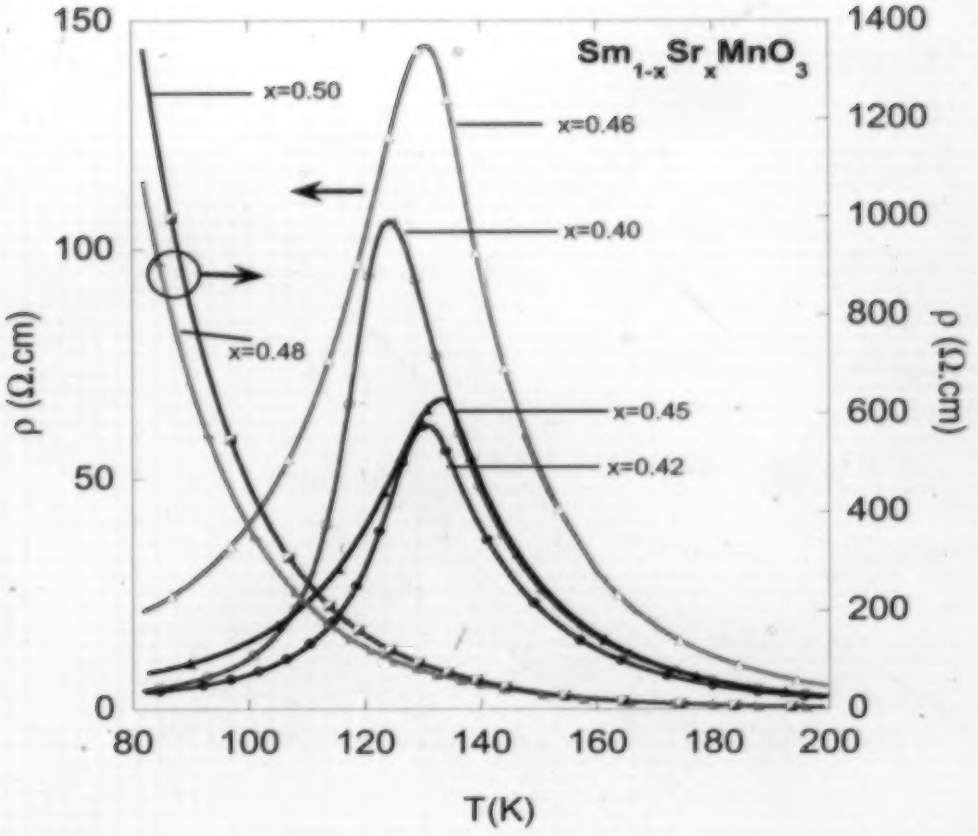

Figure 5.1: Temperature dependence of resistivity of SSMO for $0.40 < x < 0.50$.

5.3 Vacuum annealing induced Oxygen disorder in $Sm_{0.55}Sr_{0.45}MnO_3$

Disorder can be introduced into a manganite using a variety of methods. For example, one can substitute different quantities of ions onto R, A, or Mn sites. This approach is however very inconvenient since it requires preparation of many samples with different concentration of those ions. In this case the resultant disorder may depend strongly on slight variations of the sample preparation conditions and on the amount of oxygen introduced into each sample. Another approach, that we adopted here, is to produce disorder through a careful redistribution of oxygen atoms within a single sample. Quenched disorder is obtained by first annealing the manganite sample at a relatively "low" temperatures in vacuum and then cooling it rapidly. As we shall discuss below, this procedure does not change the overall oxygen content of the system. However one might expect off-center distortions in the positions of oxygen atoms, and oxygen diffusion into interstitial sites. These effects are likely to create lattice strain, changes in Mn^{3+} and Mn^{4+} fractions (i.e. carrier concentration), and hence disorder. Using this procedure, the amount of disorder is expected to increase with an increasing annealing time.

Although, in principle, disorder can be created in many types of manganites using the thermal treatment described above, we chose to investigate the effects of disorder on the magneto-transport properties of bulk $Sm_{1-x}Sr_xMnO_{3-\delta}$ close to half-doping (i.e. $x \approx 0.5$). These compounds are of particular interest since they are characterized by a charge ordered phase[4] and by a ground state that is very sensitive to perturbation [13]. Our growth conditions are such that in our samples, a particularly narrow peak in the resistivity at the MIT is observed (at about $\approx$ 135 K). Hence, this is an ideal material for investigating small changes in the shape of the resistivity peak due to disorder.

As a starting point we vacuum annealed a $Sm_{0.55}Sr_{0.45}MnO_3$ bulk sample for different temperatures for 30 minutes and fast cooled to room temperature with a

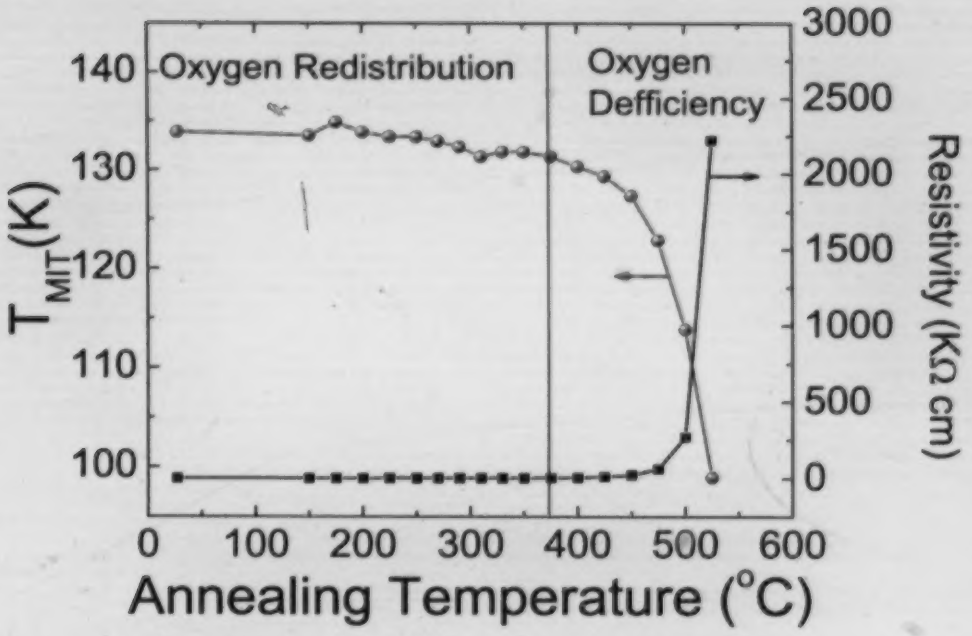

Figure 5.2: The resistivity at the Metal insulator transition temperature and the metal insulator transition temperature for SSMO for different vacuum anneal conditions. The lines are guide for eye.

rate of 21°C/min. After each temperature we measured the temperature dependence of resistivity and mass with a microbalance to quantify the oxygen deficiency. The resulting measurements are shown Fig. 5.2. As it is evidenced in weight analysis the mass change up to $375 - 400$°C is negligible. The sudden change of the peak resistivity at these annealing temperatures supports the idea of fast oxygen loss above these temperatures. We attributed the region up to $375 - 400$°C vacuum annealing temperature as an oxygen redistribution region. Note that there is always an oxygen loss in a high temperature vacuum anneal processes but in this region it is negligible. Annealing above this temperature will cause a relatively large oxygen deficiency.

In order to study the effects of vacuum annealing in the oxygen redistribution region we annealed the samples in vacuum at 325°C for a specific amount of time (e.g. initially 30 minutes) to produce the oxygen motion, and the disorder subsequently

frozen in by a relatively fast cooling (at a rate of 21°C per minute) to room temperature in vacuum. The temperature dependence of resistivity was then measured using the standard four-probe technique and $1\mu A$ current pulses (pulse duration $\approx$ 200 ms with current reversal) between 80 and 200 K. The magnetoresistivity MR = $[\rho(H) - \rho(0)]/\rho(0)$ (where $\rho(H)$ and $\rho(0)$ are resistivities in a magnetic field H and in a zero field, respectively) was also measured in a field H of 0.68 T. After these measurements, the annealing, rapid cool down, and resistivity measurement procedures were again repeated. Throughout this process, a weight analysis using a microbalance did not detect any change (within the sensitivity of the measurement $\delta = 5 \times 10^{-5}$) in the overall oxygen content, i.e. $3 - \delta$, of the samples. Hence, the oxygen loss δ was less than 5×10^{-5} after the whole annealing process.

Vacuum annealing has a dramatic effect on the transport properties of the $Sm_{0.55}Sr_{0.45}MnO_3$ manganite. Fig. 5.3 shows that an initial 0.5 hour annealing increases the resistivity of the sample by roughly an order of magnitude. This is accompanied by only a 1.5 K decrease in T_p (see Fig. 5.4). After subsequent annealings the resistivity continues to increase but T_p remains almost constant. The initial annealing also reduces the width of the resistive peak significantly. This is especially evident in Fig. 5.5, which shows the resistivity normalized to the maximum value at T_p. The change in the peak's width (FWHM: full width at half maximum) with an increasing annealing time is shown in the inset. The FWHM decreases significantly, i.e. by about 8 K, in the first hour of annealing but remains essentially constant afterwards. Fig. 5.6 presents corresponding changes in the magnitudes of both the resistive peak ρ_{max} and the magnitude of the magnetoresistance peak MR_{max}. During the first hour of annealing, a sharp increase of MR_{max} is observed. (The data presented in Figures 1-4 are typical of all our $Sm_{0.55}Sr_{0.45}MnO_3$ samples studied.)

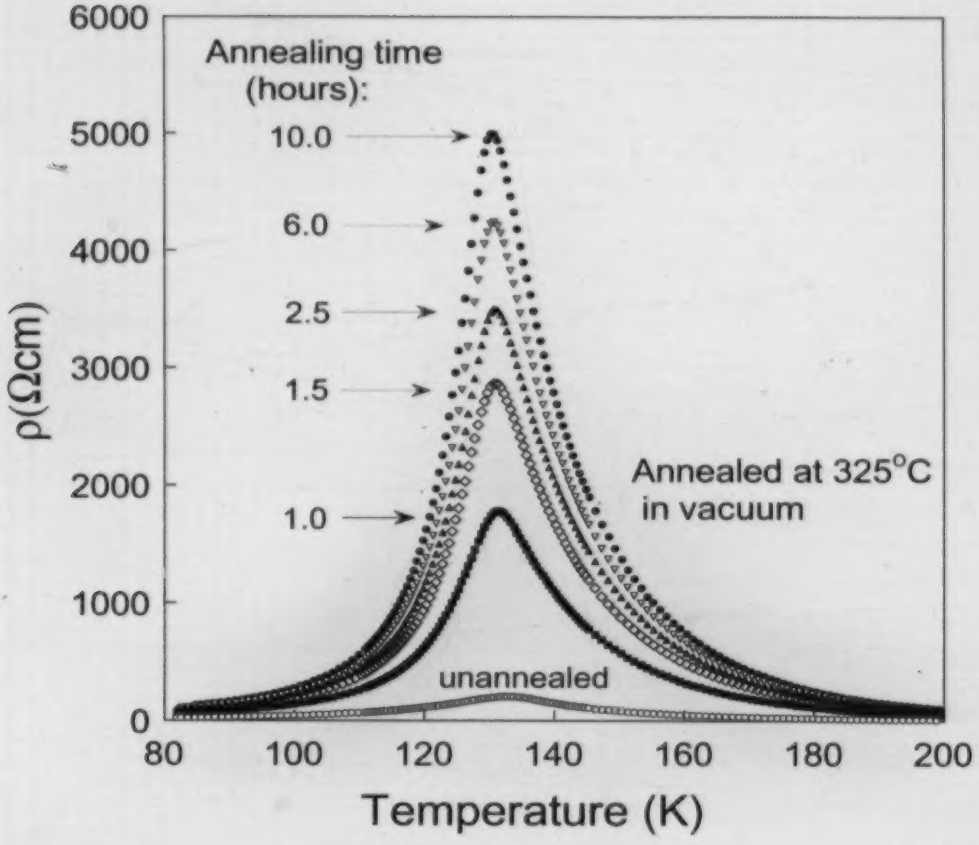

Figure 5.3: Temperature dependence of resistivity of $Sm_{0.55}Sr_{0.45}MnO_3$ for different annealing times at 325°C in vacuum.

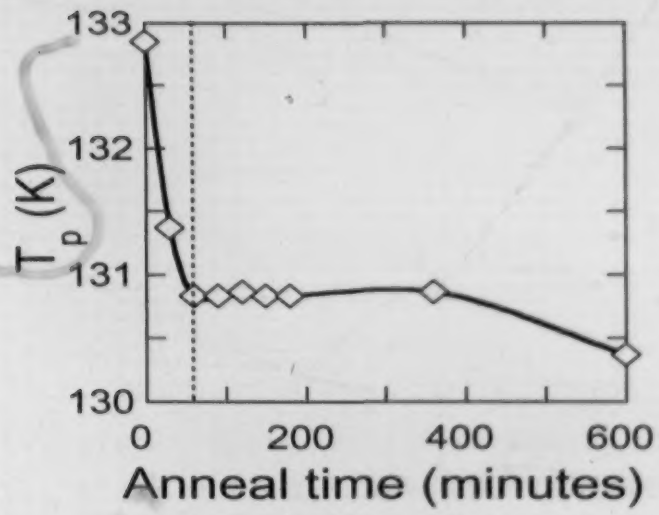

Figure 5.4: The change in T_p (metal insulator transition temperature) with an increasing annealing time. The line is a guide to the eye.

5.4 Discussion and summary

We now discuss some mechanisms that could be responsible for the observed changes in resistivity due to vacuum annealing. Applying the non-uniform oxygen distribution scenario proposed by Nagaev[41] to unannealed as-grown samples, doping of $SmMnO_3$ with Sr should already cause disorder in the oxygen distribution and lead to formation of oxygen rich and oxygen poor clusters. Oxygen-rich clusters contain interstitial oxygen atoms and are ferromagnetic conductors. On the other hand, oxygen-poor clusters contain oxygen vacancies and are antiferromagnetic insulators. Although possibly only one contribution to the magnetotransport of an as-grown sample, this type of oxygen-related disorder will certainly affect the resistivity and magnetoresitivity at the MIT[41].

During thermal treatment of the manganite samples at $325°C$ in vacuum the free energy has to be minimized. This will eventually lead to the production of an equilibrium concentration of intrinsic oxygen defects, i.e. oxygen vacancies and oxygen

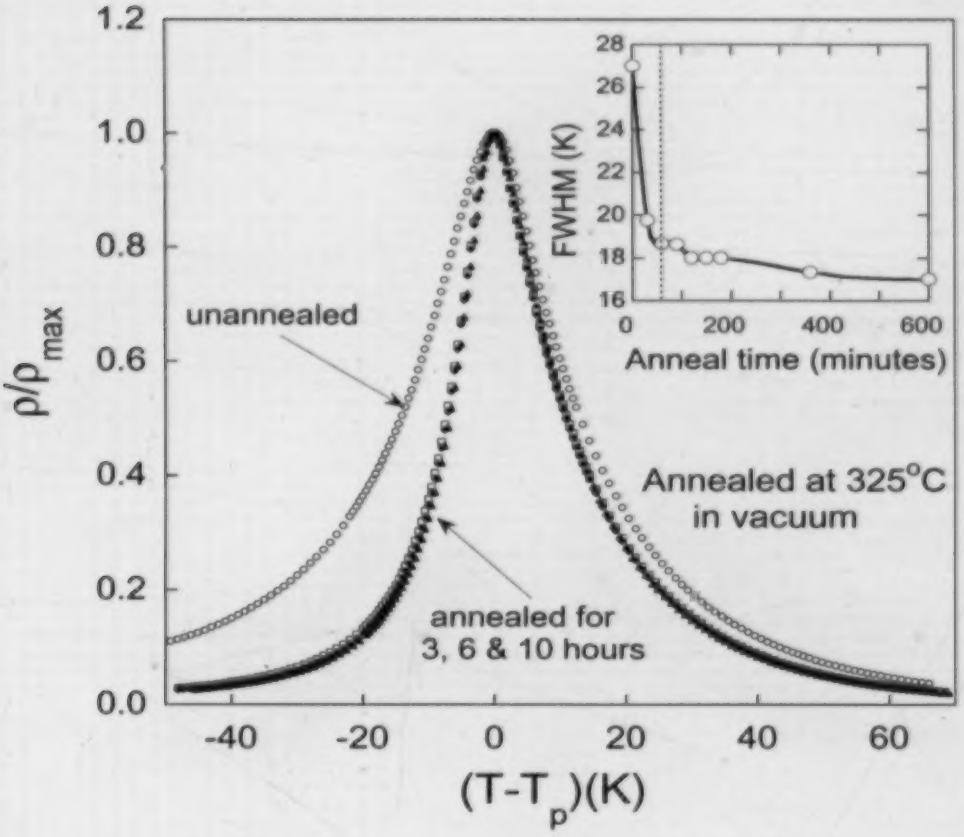

Figure 5.5: Temperature dependence of resistivity ρ/ρ_{max} of $Sm_{0.55}Sr_{0.45}MnO_3$ normalized to the maximum magnitude of resistivity ρ_{max} and to T_p. The curves are plotted for different annealing times at 325°C in vacuum. The inset shows the change in FWHM (full width at half maximum) of the resistive peak with an increasing annealing time. The line is a guide to the eye.

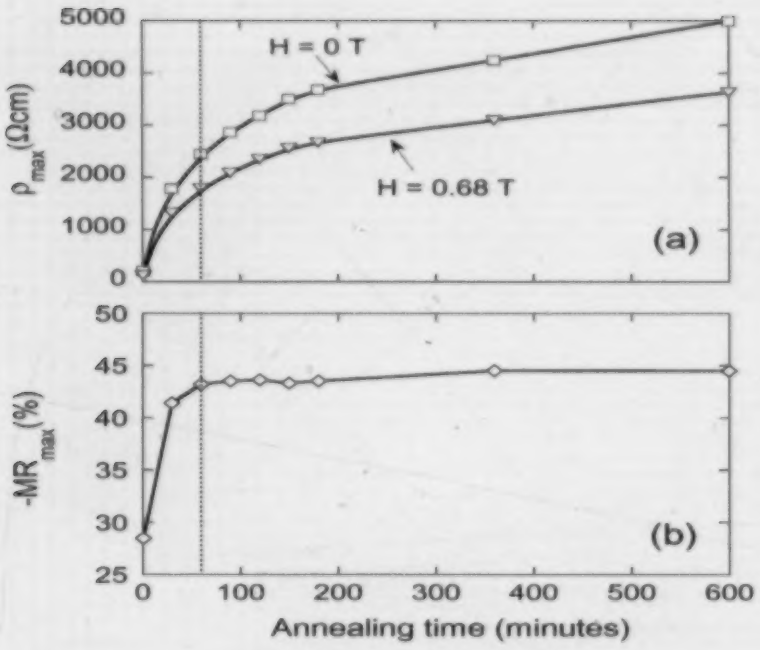

Figure 5.6: Dependence of (a) the magnitude of resistivity at the maximum ρ_{max} measured in a field of 0 T and 0.68 T, and (b) the magnitude of magnetoresistance at the maximum, MR_{max}, measured in a magnetic field of 0.68 T, on the annealing time at 325°C in vacuum. The lines are guides to the eye.

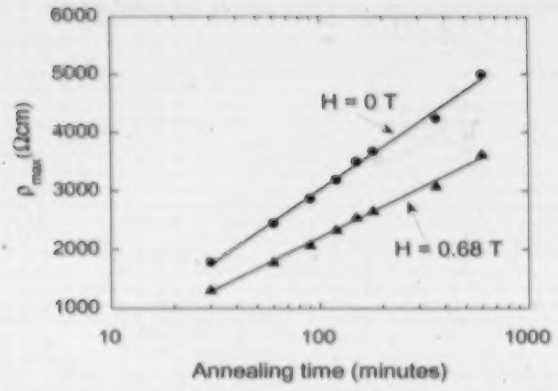

Figure 5.7: Dependence of the magnitude of resistivity at the maximum ρ_{max} measured in a field of 0 T and 0.68 T on the annealing time at 325^oC in vacuum. In both 0 T and 0.68 T, ρ_{max} shows logarithmic dependence on the annealing time. The lines are the fits to the data. Similar behavior was observed in all $Sm_{0.55}Sr_{0.45}MnO_3$ samples studied.

interstitial atoms, that is different from what was originally present in the sample. These defects can diffuse randomly into different parts of the sample, forming *additional* clusters. We assume that this disorder remains frozen inside the sample after subsequent quenching down to room temperature. An increased volume of conductive ferromagnetic clusters generated by the first one-hour annealing produces three effects: (a) The asymmetry in the shape of the resistive peak about T_p (see Fig. 5.5), (b) The sharp reduction in the resistive peak width (FWHM) by 8K, as seen in the inset of Fig. 5.5, and (c) The sharp increase in MR_{max} seen in Fig. 5.6(b) from 28% before annealing to 43% after one-hour annealing. Since the weight analysis revealed that the oxygen loss δ over the entire ten-hour annealing period is less than 5×10^{-5} (very small), it is likely that these changes are due solely to oxygen redistributing within the sample. The asymmetry, FWHM, MR_{max} and T_p are almost independent of subsequent annealings (see insets in Fig. 5.3 and 5.5, and Fig. 5.6(b)), suggesting that the volume of the ferromagnetic phase no longer changes, i.e. the equilibrium value has been reached. On the other hand, the resistivity continues to increase significantly with increasing annealing time (see Fig. 5.6(a)). This could be due to changes

in oxygen distribution (changes in the relative size of ferromagnetic clusters) resulting in a continuous increase of the lattice strain. The dependence of ρ_{max} on the annealing time, measured with both H=0 T and 0.68 T, is well-described as being logarithmic, i.e. $\rho_{max} = -a + b \ln t$, where a and b are constants (see Fig. 5.7). This type of time dependence could indicate that strain-induced motion of ferroelastic domain walls in the annealed manganite is occuring[15, 16]. Consequently, there is a reduction of the conducting paths across the sample (reduction of percolation conductivity) with an increasing annealing time, i.e. a transition to a more homogeneous mixture of smaller conducting (ferromagnetic) and insulating clusters.

Hence, our experiments on the resistivity and the magnetoresistivity near the metal-insulator transition in vacuum annealed $Sm_{0.55}Sr_{0.45}MnO_3$ revealed a number of phenomena that can be compared with the available models (presented in the introduction) of the magneto-transport of CMR manganites. We believe that a combination of these models provides a good explanation of the observed behavior. Our observation that the annealing causes changes in the magneto-transport properties due to oxygen distribution is consistent with Nagaev's model[41] and his assumption that a non-uniform oxygen distribution is an important contributor to the magneto-transport properties of CMR manganites at the MIT. It is also reasonable to assume that oxygen distribution also causes a large strain build-up in the insulating phase through generation of large concentrations of oxygen vacancies. Such a lattice strain could be also responsible for the phase separation at temperatures near the MIT according to the model of Ahn et al[11]. Our observation that the annealing causes a *reduction* in the resistive peak width and an increase of resistivity with the annealing time is in agreement with the results of the random-resistor-network model of Burgy et al[8]. Our measurements also suggest that the annealing process could be responsible for a transformation of a heterogenous distribution of conducting and insulating clusters into a more homogeneous one. Recently, a model by Alexandrov et al[2] has been proposed that can be applied to describe homogeneous phase-separated mixtures away from the percolation limit. This model might be adopted to explain our

experiments, but probably only after long-term annealing when the samples become more homogeneous.

Bibliography

[1] A. Lisauskas, J. Back, I. Khartsev, and A. M. Grishin, *J. Appl. Phys.* **89**, 6961 (2001).

[2] H. Oshima, K. Miyano, Y. Konishi, M. Kawasaki, and Y. Tokura, *Appl. Phys. Lett.* **75**, 1473 (1999).

[3] A. I. Abramovich, L. I. Koreleva, A. V. Michurin, O. Y. Gorbenko, and A. R. Kaul, *Physica B* **293**, 38 (2000).

[4] C. Martin, A. Maignan, M. Hervieu, and B. Raveau, *Phys. Rev. B* **60**, 12191 (1999).

[5] A. Moreo, S. Yunoki, E. Dagotto, *Science* **283**, 2034 (1999).

[6] E. Dagotto, T. Hotta, and A. Moreo, *Physics Reports* **344**, 1 (2001).

[7] M. Mayr, A. Moreo, J. A. Vergs, J. Arispe, A. Feiguin, and E. Dagotto, *Phys. Rev. Lett.* **86**, 135 (2001).

[8] J. Burgy, A. Moreo, and E.Dagotto, *Phys. Rev. Lett.* **92**, 97202 (2004).

[9] E. L. Nagaev, *Phys. Lett. A* **218**, 367 (1996).

[10] J. R. Sun, C. F. Yeung, K. Zhao, L. Z. Zhou, C. H. Leung, H. K. Wong, and B. G. Shen, *Appl. Phys. Lett.* **76**, 1164 (2000).

[11] K.H. Ahn, T. Lookman, A.R. Bishop, *Nature* **428** 6981 (2004).

[12] A. S. Alexandrov, A. M. Bratkovsky, and V. V. Kabanov, *Phys. Rev. Lett.*, **96**, 117003 (2006)

[13] G. C. Milward, M. J. Calderon, and P. B. Littlewood, *Nature* **433**, 607 (2005).

[14] I. Isaac, J. Jung, J. P. Franck, and M. Abdelhadi, *Phys. Rev. B* **70**, 212410 (2004).

[15] J. C. Phillips, Rutgers University, private communication.

[16] N. Farag, M. Bobeth, W. Pompe, A. E. Romanov, and J. S. Speck, *Phys. Stat. Solidi A* **202**, R44 (2005).

Chapter 6

Disorder induced softening of the first-order magnetic phase transition and grain size dependent properties of $Sm_{0.55}Sr_{0.45}MnO_3$ manganite

6.1 Introduction

Over the last decade, there has been significant progress made in understanding the fascinating properties of manganites $RE_{1-x}A_xMnO_3$ (where RE and A are the rare earth and the alkaline elements, respectively).[1, 2, 3, 4] One widely accepted view of manganites is that the colossal magneto-resistance (CMR) effects that are observed in these materials are a consequence of competition of phases, supplemented by disorder that may be introduced via chemical doping, strain fields, etc.[4, 5, 6, 7, 8]. These theories predict the coexistence of ferromagnetic metal (FM) and antiferromagnetic insulator (AFI) phases, neither of which dominates in the region of the metal-insulator transition (MIT), hence causing a competition between different possible orderings.

The competition between metal and insulator leads to phase separation, inhomogeneity, and percolative transport[9, 10], and becomes more pronounced close to the half-doping level ($x = 0.5$) in all manganites. The commensurate nature of orbital, charge, and spin ordered phases occurring at this doping level has been investigated both experimentally[4, 5] and theoretically.[13, 14] A strong competition between different ordering tendencies results in a fragile phase diagram[4], implying that in addition to magnetic fields, perturbations in the form of pressure, strain and electric field can induce dramatic changes in the physical properties of manganites. This high tunability can be very useful for applications based on manganites.

The competition between FM and charge/orbital ordered anti-ferromagnetic insulator phases in $RE_{1-x}Sr_xMnO_3$ (where RE = La, Pr, Nd, Sm or Eu, and $x = 0.45$ or 0.50) crystals has been described comprehensively.[15] It has been established that the Y shaped bi-critical feature of the phase diagram is modified by variations in the cation disorder (due to the difference in ionic radii of different RE elements). In particular, it was found that this type of disorder causes "smearing" of the phase diagram. When $x = 0.45$ and RE = Sm or Eu (which have smaller ionic radii in comparison with other rare earth ions) the Curie temperature T_c is strongly suppressed and the CMR effect is enhanced dramatically. This makes the $Sm_{0.55}Sr_{0.45}MnO_3$ (SSMO) manganite near the half-doping level particularly interesting.[16, 17, 18] SSMO exhibits a number of intriguing physical properties. For example, the inverse magnetization of this compound shows a clear deviation from the Curie-Weiss law.[19] Its paramagnetic region above T_c is magnetically heterogeneous, as indicated by neutron diffraction and the μSR experiments.[20, 21] The magnetostriction measurements revealed that the magneto-transport properties of SSMO, compared to the other manganites, are extremely strain sensitive.[19] These properties suggest that the SSMO is very susceptible to the presence of structural disorder. There are many different sources of disorder that could occur in SSMO: examples include chemical doping on Mn sites, grain boundaries, lattice imperfections, local lattice strains, oxygen redistribution, etc.

It is widely accepted that the magnetic transition between the ferromagnetic and paramagnetic phases is first order.[4] However, some theories predict that the second order magnetic phase transitions in manganites, eg. continuous magnetic transitions could be induced by disorder.[22] Although extensive experimental studies of the magneto-transport have been performed in manganites so far, the effects of the order of the phase transition on the magneto-transport have not been fully investigated. In this paper we present studies of the magneto-transport in SSMO at the MIT where the first-order phase transition has been gradually replaced with the second-order one by an increasing structural disorder. An increasing density of grain boundaries has been used as the measure of an increasing structural disorder. We have investigated the low-field magnetization and the magneto-transport in SSMO at the MIT for the second-order and the first-order magnetic phase transitions.

6.2 Sample preparation and structural properties

The $Sm_{0.55}Sr_{0.45}MnO_3$ (SSMO) compound was prepared using a standard solid state reaction method.[13] A prescribed ratio of Sm_2O_3, $SrCO_3$ and MnO_2 powders was mixed and calcined at 1200°C for 24 hours in air. The resulting sample was crushed and sintered again using the same conditions. Four identical pellets were prepared from the powder and sintered at temperatures T_a = 1200°C, 1300°C, 1400°C and 1500°C for 24 hours in air. The pellets were then cooled quickly from T_a down to room temperature at a rate of about 30°C/minute. For clarity, we will refer to these samples using the notation SSMO(T_a), where T_a corresponds to the sintering temperature used for the corresponding sample. X-ray diffraction (XRD) peaks and the corresponding Miller's indices of the SSMO(T_a) samples are shown in Fig.6.1.

The XRD patterns show that all samples are single phase. The microstructure of the samples and the lattice strain were investigated using a scanning electron microscope (SEM) and the Williamson-Hall (W-H) analysis of the XRD lines/profiles. The SEM micrographs (see Fig.6.2) show the granular structure of the SSMO sam-

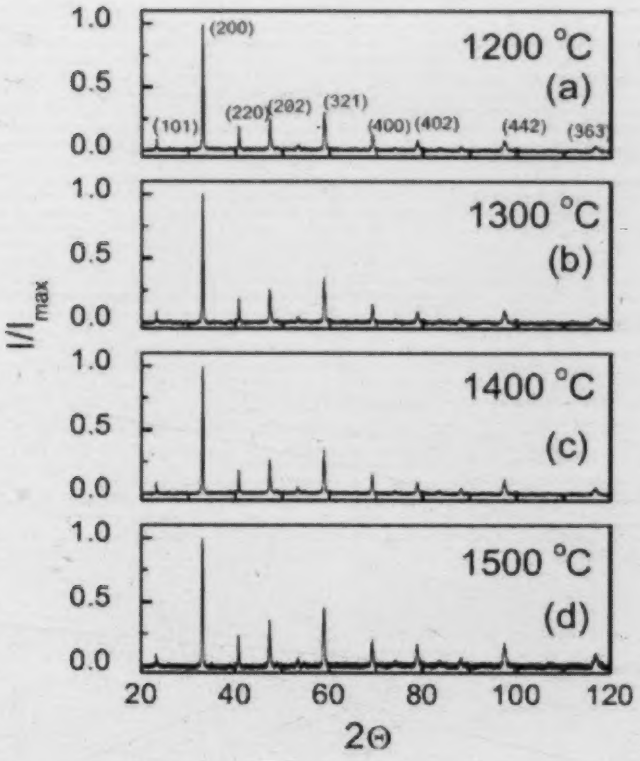

Figure 6.1: X-ray diffraction patterns of SSMO(T_a): (a) SSMO(1200) (b) SSMO(1300) (c) SSMO(1400) (d) SSMO(1500). The intensity of each pattern was normalized to the (200) peak intensity.

ples with the grain size ranging from ≈ 0.8 μm in the SSMO(1200) up to ≈ 20 μm in the SSMO(1500). The W-H analysis of the measured broadening of the XRD lines/profiles[24, 25] revealed however the presence of smaller grains at the sub-micrometer level which are not apparent in the SEM micrographs. The W-H analysis is based on the relationship between β, the full width at half maximum of the x-ray peak, and ϵ, the lattice strain.These two quantities are related by the following equation:[26]

$$(\beta/\lambda)cos\theta = 4(\epsilon/\lambda)sin\theta + 1/D \tag{6.1}$$

where λ is the X-ray radiation wavelength, D is the average grain size and θ is the diffraction angle. In a typical W-H plot $\beta^*=(\beta/\lambda)\cos\theta$ increases linearly with an increasing $d^*=4\sin\theta/\lambda$. The W-H plots for all samples are shown in Fig.6.3. The average grain size D of the sample has been evaluated from the intercept of the straight line with the β^* axis. The slope of this line gives the lattice strain. The estimated value of D is 66 nm in the SSMO(1200) sample and increases with T_a, reaching 227 nm in the SSMO(1500) sample. Therefore, the SSMO(1200) sample contains the largest density of grain boundaries and thus it is the most disordered. The average lattice strain in these samples ranges from 0.21% up to 0.35%. The smaller D in the SSMO(1200) and SSMO(1300) samples compared to those in the SSMO(1400) and SSMO(1500)samples are probably caused by the smaller sintering temperatures. On the other hand, an increase of the lattice strain at higher annealing temperatures could be associated with thermal quenching. The summary of physical properties of samples are given in Table 6.1 and Table 6.2.

The magnetization measurements were done using a SQUID magnetometer (MPMS, Quantum Design). Both zero field cooled (ZFC) and field cooled (FC) magnetization curves were measured as follows: the sample is initially cooled in zero field down to 6 K, then the field is applied at this temperature and the magnetization is measured while warming up to 300 K (ZFC magnetization), followed by cooling back again to 6

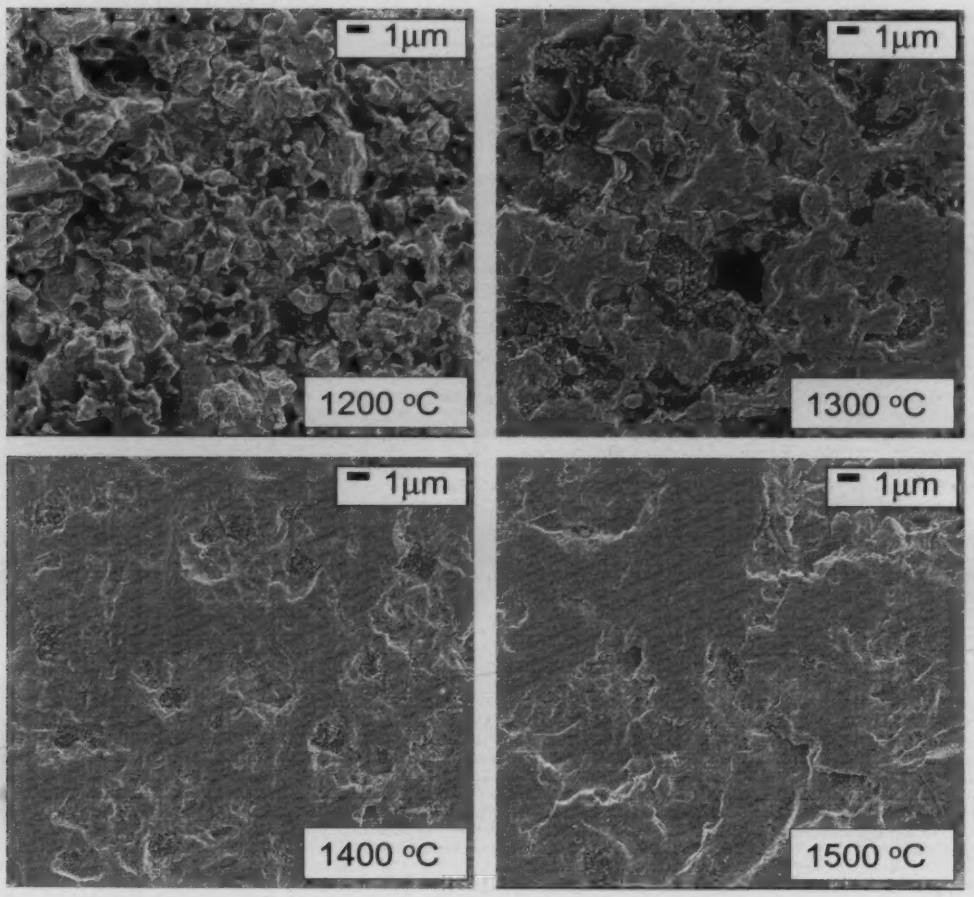

Figure 6.2: SEM surface micrographs of SSMO annealed at different temperatures T_a.

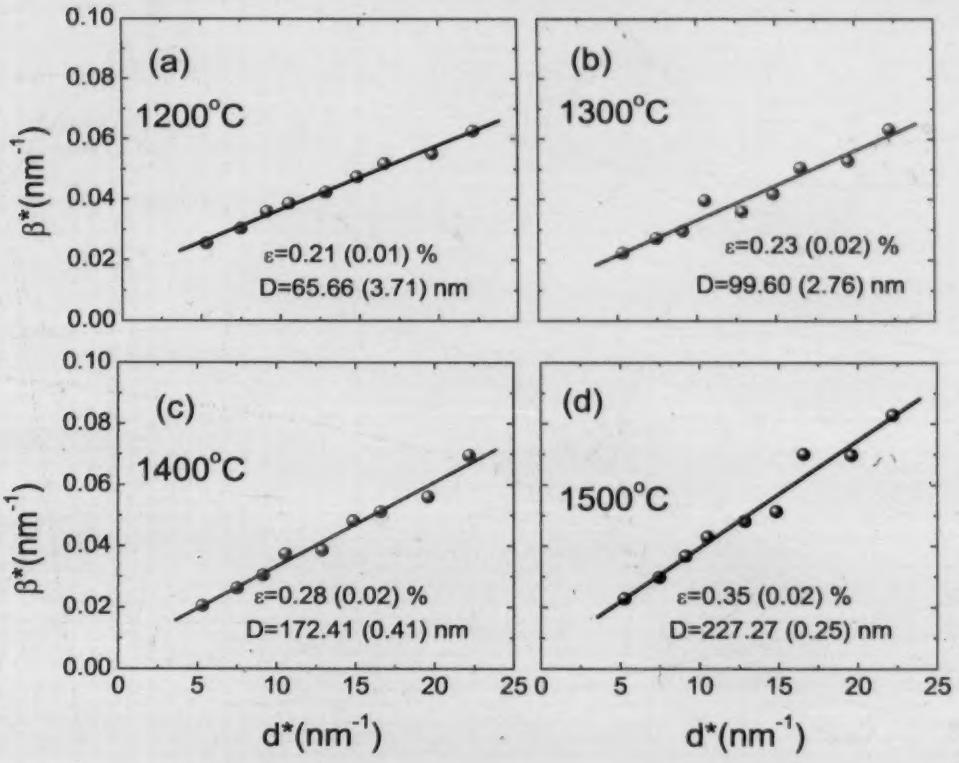

Figure 6.3: Williamson-Hall plots of SSMO(T_a) for different annealing temperatures.

Table 6.1: Parameters that describe SSMO(T_a): ϵ is the magnitude of the micro-strain obtained from a W-H analysis, GS1 and GS2 corresponds to the grain size obtained from SEM and W-H analysis, T_{MIT} is the metal-insulator transition temperature, T_c is the Curie temperature.

T_a (°C)	GS1(SEM) (μm)	GS2(W-H) (nm)	ϵ (%)	T_{MIT} (K)	T_c (K)
1200	0.8	66	0.21	133	133
1300	3.5	99	0.23	132	131
1400	15.0	172	0.28	130	129
1500	20.0	227	0.35	129	125

Table 6.2: Parameters that describe SSMO(T_a): T_{MIT} is the metal-insulator transition temperature, T_c is the Curie temperature, ρ_0 is the residual resistivity, ρ_2 is the electron-electron scattering coefficient, ρ_5 is the electron-phonon scattering coefficient, b is the polaronic coefficient, Δ is the bipolaron binding energy, and δC_p is the full width at half maximum of the specific heat peak.

T_a	T_{MIT}	T_c	ρ_0	ρ_2	ρ_5	b	Δ	δC_p
(°C)	(K)	(K)	(Ωcm)	$(\Omega cm K^{-2})$	$(\Omega cm K^{-5})$	$(\Omega cm K^{-1})$	(meV)	(K)
1200	133	133	2.63	$19.0\ 10^{-5}$	$7.30\ 10^{-10}$	$10.0\ 10^{-6}$	243	5.3
1300	132	131	0.69	$6.00\ 10^{-5}$	$2.10\ 10^{-10}$	$6.05\ 10^{-6}$	240	4.1
1400	130	129	0.08	$0.75\ 10^{-5}$	$0.28\ 10^{-10}$	$2.71\ 10^{-6}$	238	3.0
1500	129	125	0.01	$0.08\ 10^{-5}$	$0.04\ 10^{-10}$	$1.66\ 10^{-6}$	238	3.0

K (FC magnetization) without changing the magnetic field. The magnetic hysteresis loops were measured at different temperatures using 500 G intervals starting at the largest negative magnetic field. In order to measure the temperature dependence of the resistivity (during the warming cycle) over a temperature range of $80 - 200$ K, we used a standard four probe technique with 1 μA current pulses. The magnetoresistivity $-MR = [\rho(H) - \rho(0)/\rho(0)]$, where $\rho(H)$ and $\rho(0)$ are the resistivities in an applied field H and in zero field, respectively, was also measured for different fields up to $H = 0.75$ Tesla.

6.3 Magnetic properties

The magnetization for all samples of SSMO(T_a) was measured as a function of temperature in two different magnetic fields, 0.025 and 0.75 Tesla. The temperature dependence of the ZFC magnetization in 0.025 T is qualitatively similar in all samples (see Fig. 6.4). Starting at low temperatures the magnetization increases almost linearly with temperature, peaks at about 36 K followed by a plateau, before decreasing sharply at T_c near 130 K. The behavior below $T_s \sim 36$ K (value inde-

pendent of the grain size) could be related to the onset of the antiferromagnetic order and/or spin-reorientation of the spontaneous magnetization[8], while the sharp decrease at $T_c \sim 130$ K is due to the transition from the ferromagnetic to the paramagnetic regime. Note that in this small magnetic field the magnetization is largest for SSMO(1200) and decreases monotonically with an increasing T_a. We correlate this behavior with the different sizes of the grains in the four samples. The temperature dependence of the magnetization in a higher field of 0.75 T is dramatically different, ie. it is much less dependent on the grain size (see Fig. 6.4 (e)-(h)).

In a ferromagnetic material one expects magnetic domains to be formed, with the local magnetization being saturated in each domain. The domain walls allow different orientations of magnetization to be present in different domains.[27] The effect of the grain size on the formation of domains in a ferromagnet was studied by Dunlop.[28] It was found that small grains are most likely occupied by a single domain which is uniformly magnetized to its saturation magnetization. In contrast, larger grains are more likely to contain multiple domains, each magnetized with a different orientation. These effects may explain our observations. As shown in Fig.6.4 (a) - (d), in a low magnetic field, the net magnetization is higher in samples with smaller grains. One could expect a reduced density of domain walls in samples with smaller grains. The magnetic domains in these samples can be easily aligned using a small applied field, while an alignment of domains in samples with larger grains requires larger magnetic fields. Therefore in a low field the overall magnetization for samples with smaller grains (and hence with smaller domain wall density) is higher than that measured in samples with larger grains (and hence with larger domain wall density). On the other hand, in a high magnetic field all domain walls are suppressed within the grains of all sizes, leading to the larger magnetization (see Fig.6.4(e)-(h)).

The region between T_c and T_s in the temperature dependence of the magnetization measured in 0.025 T is very sensitive to the variations in T_a, ie. higher T_a produces a flatter magnetization plateau which can be seen in Fig.6.5 (a)-(d). Note that the peak

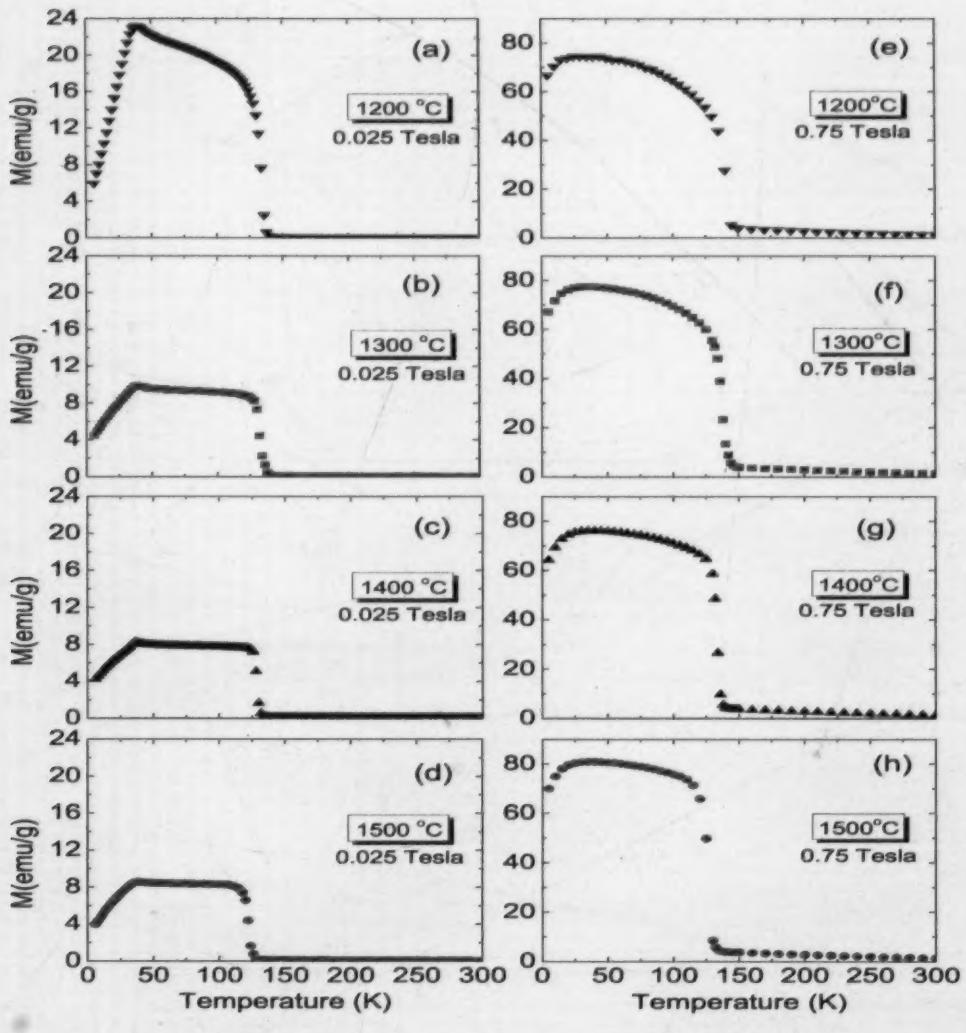

Figure 6.4: Temperature dependence of the ZFC magnetization for SSMO(T_a) samples measured in a field of 0.025 T (figures (a)-(d)), and in a field of 0.75 T (figures (e)-(h)).

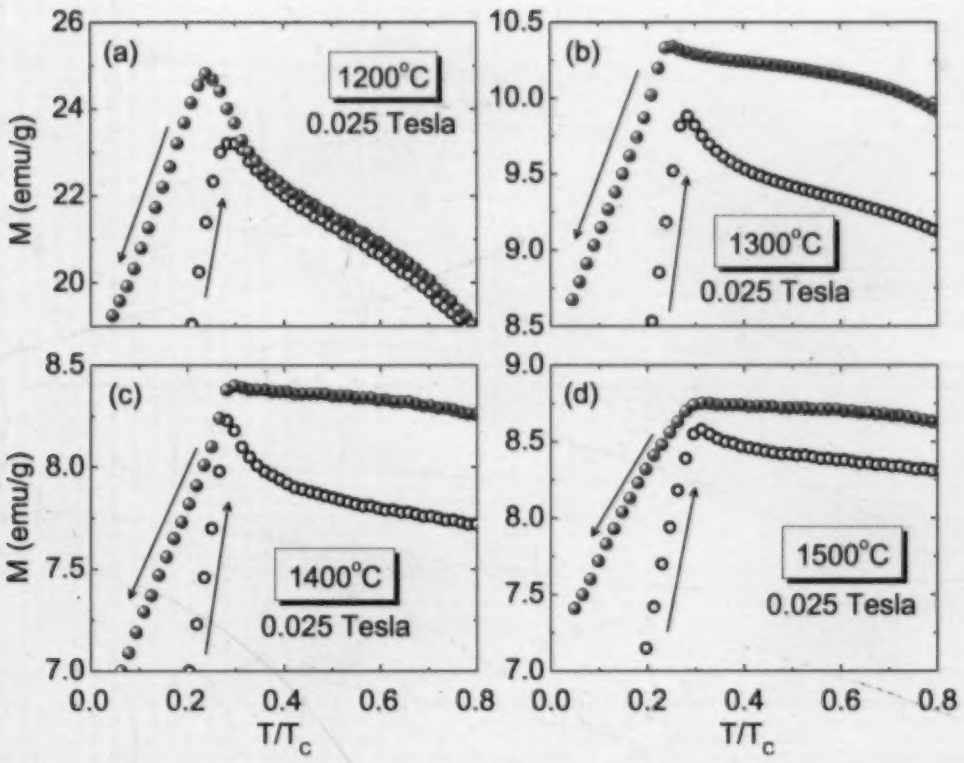

Figure 6.5: Temperature dependence of the ZFC (solid symbols) and FC (open symbols) magnetization measured in a field of 0.025 T for (a) SSMO(1200) (b) SSMO(1300) (c) SSMO(1400) (d) SSMO(1500). Temperature is normalized to T_c obtained from the minimum of the temperature dependence of dM/dT, which corresponds very closely to the onset of the increase in magnetization M. The arrows indicate the warming and cooling cycles.

at T_s "flattens", i.e., becomes less prominent, as T_a is increased. There is noticeable amount of thermal hysteresis in SSMO(1300), SSMO(1400) and SSMO(1500) samples, while it is almost absent in the SSMO(1200) sample. In particular, in the SSMO(1200) sample, the magnetization upon cooling and warming for T $\approx$ 0.3 T_c is very nearly identical. Similar thermal hysteresis was also observed in $La_{1-x}Sr_xMnO_3$ ($x = 0.5$ and 0.6) compounds by Dho *et al.*[29] which was attributed to the competition between the A-type antiferromagnetic and ferromagnetic phases. Such competition is likely to be responsible for the thermal hysteresis effects that are observed in our samples.

Magnetic field dependence of the magnetization (magnetic hysteresis) is shown in Fig.6.6 for all four samples of SSMO(T_a). The magnetization saturation field and the hysteresis width at a particular measurement temperature increase monotonically with an increasing T_a. This is attributed to the larger grain size in the sample and therefore multi-domain structure in the grain and larger density of domains walls.[28] This is because small grains are most likely occupied by a single domain which is uniformly magnetized to its saturation magnetization. In contrast, larger grains are more likely to contain multiple domains, each magnetized with a different orientation.

Theoretical studies of the influence of disorder on the phase transitions, including magnetic transitions, show that the quenched disorder causes a softening of the first order transition into a second order one.[22, 30] Banerjee suggested a method to distinguish between the first order and second order magnetic phase transitions[31] using the generalized thermodynamic theory of the second order phase transitions developed by Landau[32] and Lifshitz[33] and the approach for the first order magnetic phase transitions proposed by Bean and Rodbell.[34] In this model the nature of the magnetic phase transition could be analyzed from the isotherms of H/M versus M^2 in the vicinity of T_c. The negative and positive signs of the derivative of $d(H/M)/d(M^2)$ correspond to the first order and the second order magnetic phase transitions, respectively.

We used the positive branch of the magnetic hysteresis loops measured from +0.1 up to +1.0 Tesla and close to the transition temperature at 130 K (Fig.6.6) to plot

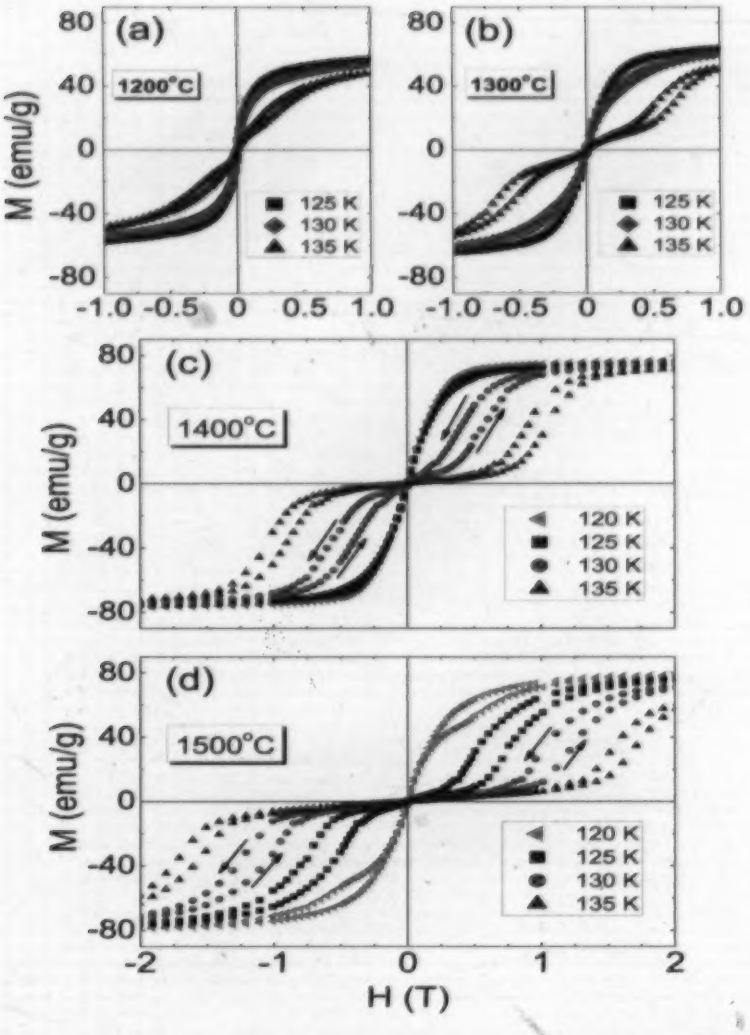

Figure 6.6: Magnetic field dependence of magnetization of SSMO(T_a) for different annealing temperatures T_a: (a) SSMO(1200) (b) SSMO(1300) (c) SSMO(1400) (d) SSMO(1500). Arrows indicate an increasing or a decreasing applied field.

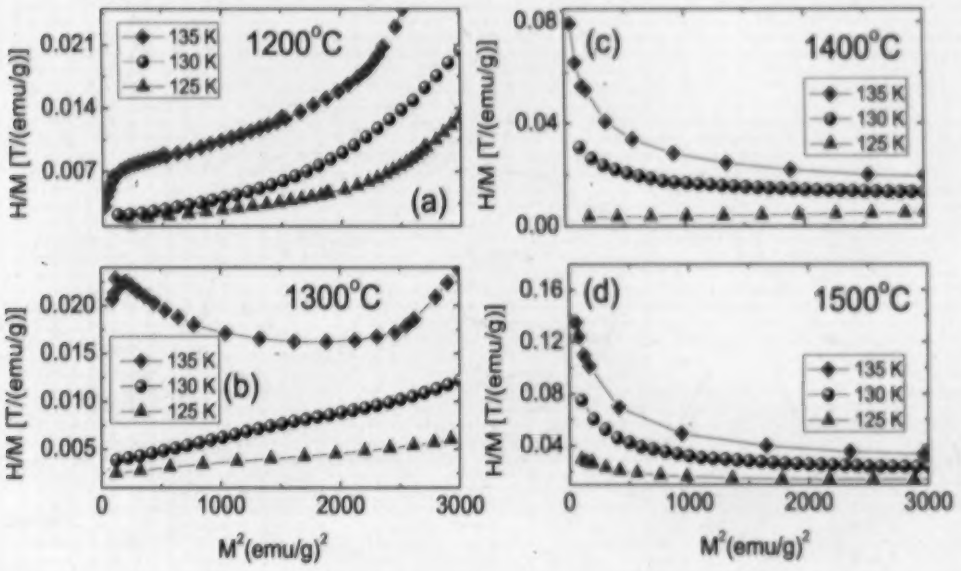

Figure 6.7: (a)-(d) H/M versus M^2 plotted for SSMO(T_a) samples for temperatures close to 130 K. The data were obtained from the field dependence of the magnetization. Note the positive sign of the slope d(H/M)/d(M^2) for SSMO(1200) and SSMO(1300) samples (the second-order phase transition) and the negative one for SSMO(1500) and SSMO(1400) samples (the first-order magnetic phase transition).

H/M versus M^2 for the SSMO(T_a) samples (see Fig.6.7). According to the Banerjee's criterion, the SSMO(1500) and SSMO(1400) samples exhibit the first order magnetic phase transition. The SSMO(1200) and SSMO(1300) samples, on the other hand, display the second order magnetic phase transition. The change of the type of the magnetic phase transition from the first order to the second order as the disorder (the density of grain boundaries) is increased may be attributed to a distribution of the transition temperatures.

As discussed by the Mercaldo *et al.*[22] when quenched disorder is introduced into the system the temperature dependence of magnetization also broadens, which is also evidence of the softening of the first-order phase transition into a second-order one. The broadening of the temperature dependence of the normalized magnetization with an increasing disorder (an increasing grain boundary density) in SSMO(1200) and

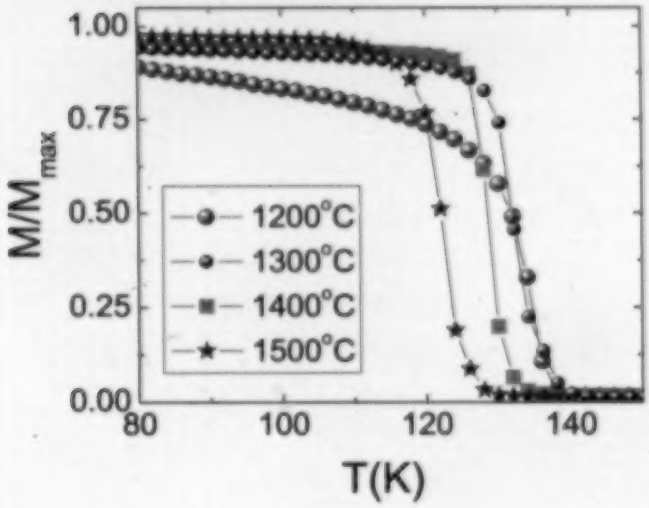

Figure 6.8: Temperature dependence of reduced magnetization(Magnetization normalized to its maximum in the M(T) curves) for all SSMO(T_a) samples.

SSMO(1300) samples characterized by the second-order magnetic phase transition, supports this conclusion (see Fig.6.8).

6.4 Specific heat and entropy

The nature of magnetic phase transitions has been revealed by measurements of the dependence of the specific heat C_p on temperature near the MIT (see Fig. 6.9). The specific heat jump ΔC_p at the transition was obtained by subtracting a smooth lattice background (see the solid curve in Fig. 6.10). ΔC_p is the smallest in SSMO(1200) sample. The dependence of ΔC_p on temperature in SSMO(1500) and SSMO(1400) samples shows much sharper maxima then SSMO(1200) and SSMO(1300) samples. This suggests that in highly disordered samples there is a large distribution of transition temperatures, which cause a broadening of both the resistive and the specific heat peaks. Broad specific heat peaks observed in some manganites have been associated with the second order magnetic phase transitions.[35] The disorder induced

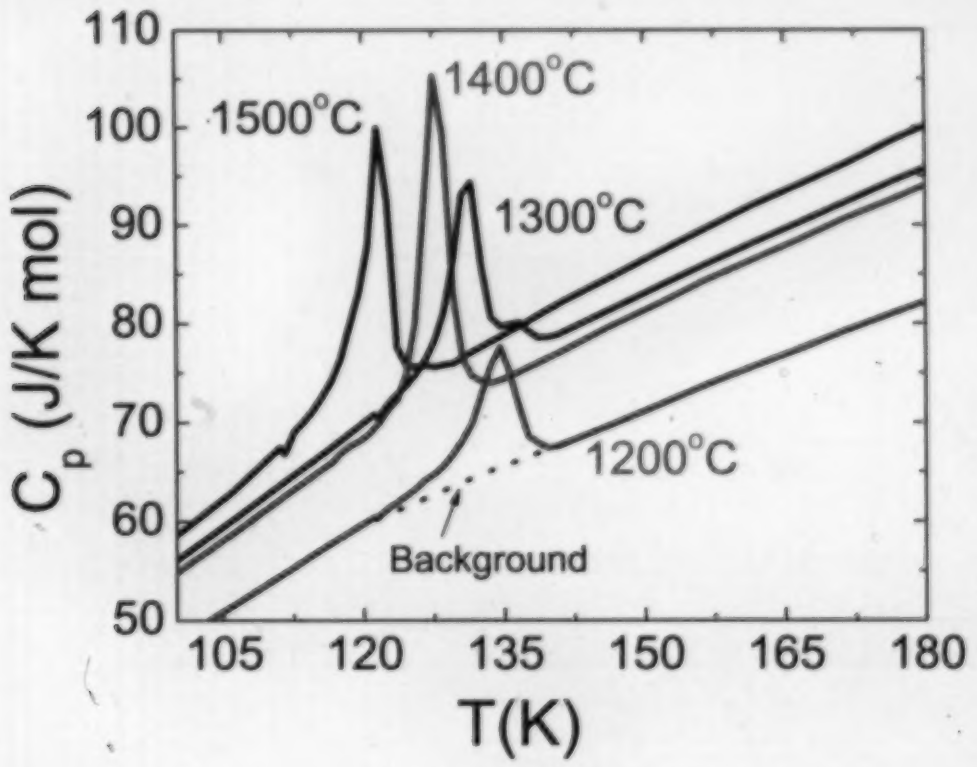

Figure 6.9: Temperature dependence of the specific heat (C_p) for SSMO(T_a) samples.

static deformation of the lattice was found to cause a broadening of the temperature dependence of the specific heat peak near the second-order phase transition temperature.[36] Note that the conversion of the type of the magnetic phase transition from the first to the second order should not be attributed to the size effect because of the relatively large size of the grains (66-227 nm) in SSMO samples.

The temperature dependence of the entropy of the samples was evaluated from the equation $S = \int(\Delta C_p/T)dT$. The entropy was calculated relative to its value at 95 K (see Fig. 6.11). The disorder reduces ΔS from $0.15R$ in SSMO(1500) sample to $0.06R$ in the SSMO(1200) sample (where is R is the ideal-gas constant). These values are much smaller than those predicted for Ising ($Rln2$) and Heisenberg ($Rln4$)

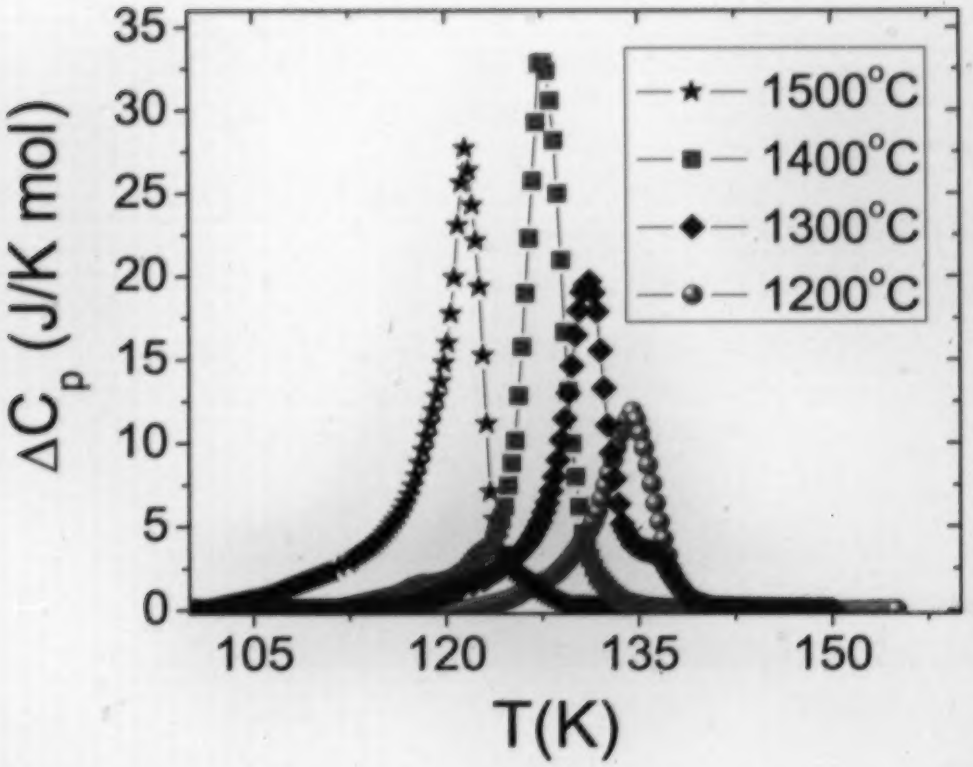

Figure 6.10: Temperature dependence of the specific heat jump (ΔC_p) at the transition for SSMO(T_a) samples.

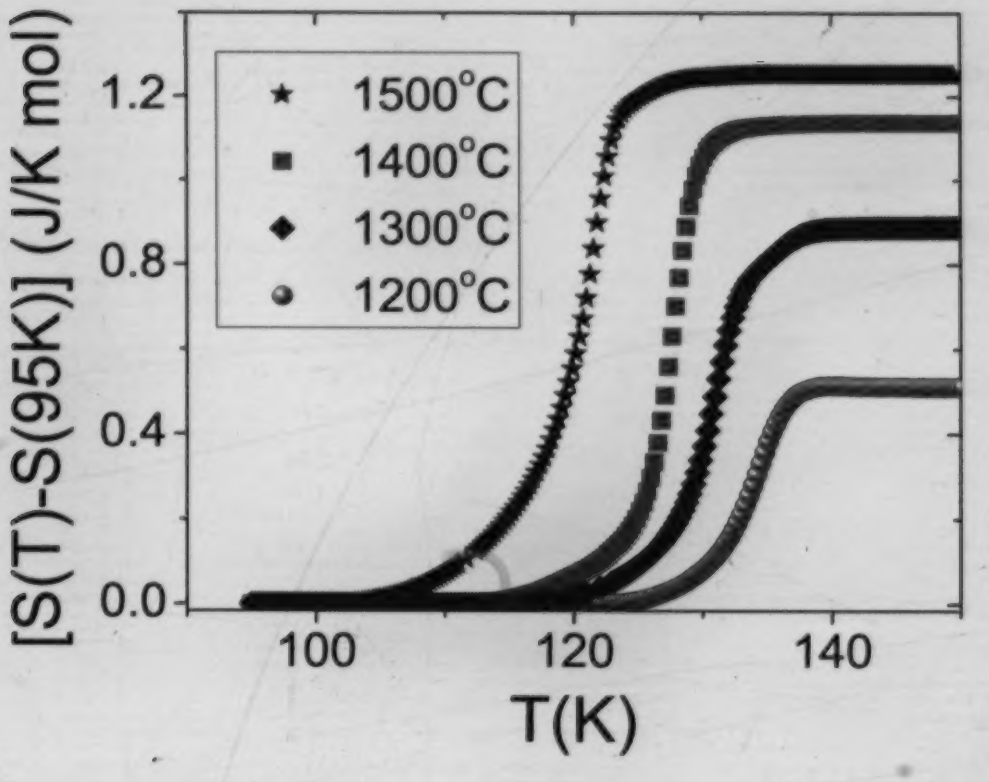

Figure 6.11: Temperature dependence of the entropy change (Δ S) at the vicinity of metal insulator transition.

magnets.[37] The missing entropy could be caused by the short range correlations in SSMO samples as suggested by a deviation of the inverse magnetization versus temperature from the Curie-Weiss law (see Fig. 6.12).[38]

An important aspect of the phase transitions in disordered systems is the spatial fluctuations of the transition temperatures especially around a defect.[39] The resulting Gaussian distribution of the transition temperatures eventually "smears" the magnetic transition.[40] The softening of the phase transition by disorder causes a shift of the onset of the deviation from the Curie-Weiss law (seen in the temperature dependence of the inverse magnetization at temperatures above T_c) to lower temper-

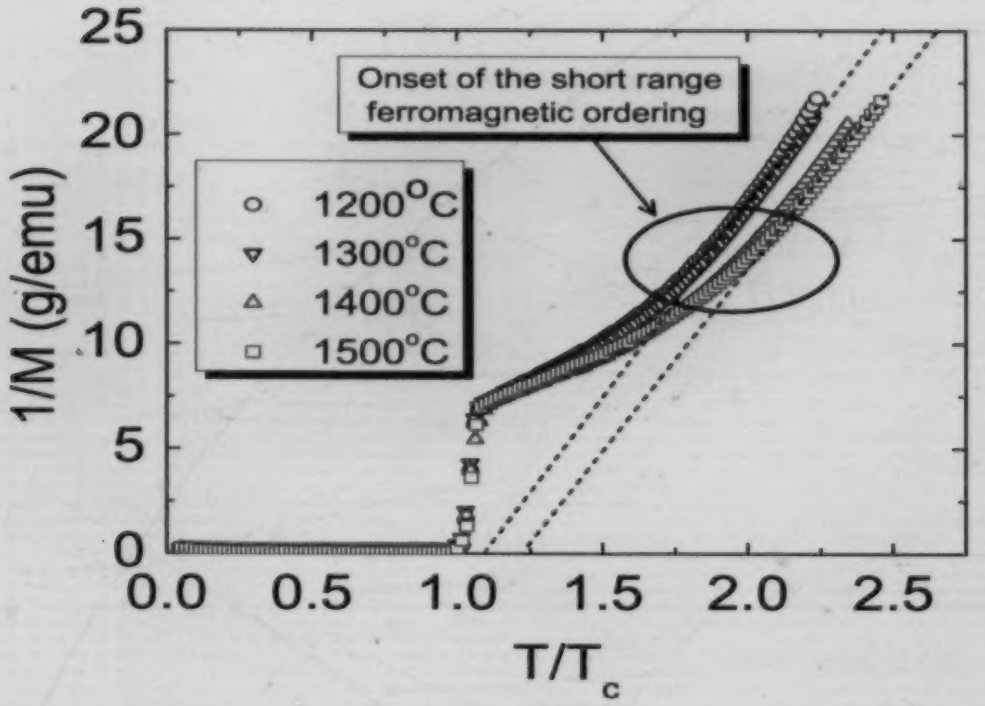

Figure 6.12: Temperature dependence of the inverse magnetization measured in a field of 0.025 T for SSMO(T_a) samples. The straight dashed lines are the fits of the theoretical Curie-Weiss law to the high temperature data with the Curie constants of 2.49 and 2.57 (emu K)/T for SSMO(1200-1300) and SSMO(1400-1500) samples, respectively.

atures as the disorder is increased (Fig. 6.12). In manganites[41] this deviation is believed to be due to the partial short range ferromagnetic ordering at temperatures higher than the metal-insulator transition temperature and T_c. This suggests that the larger grain size in the SSMO(1500) enables formation of metallic short range ferromagnetic regions at higher temperatures compared to more disordered samples with smaller grain size, such as the SSMO(1200). The SSMO(1200) and SSMO(1300) samples show similar behavior. The same is true for the SSMO(1400) and SSMO(1500) samples, indicating that these two groups have similar microstructure.

6.5 Electrical transport

Resistivity measurements, in zero applied field, appear to be more sensitive than the magnetic measurements to the microstructural properties and the order of the magnetic transition. The temperature dependence of the resistivity $\rho(T)$, measured in zero applied magnetic field is shown in Fig. 6.13. The shape of the resistive peak for SSMO(1500) sample is almost identical to that of a SSMO single crystal[19]. Dramatic changes in $\rho(T)$ of SSMO(T_a) samples occur with an increasing density of grain boundaries. An increase in the magnitude of ρ is consistent with an increase in the scattering rate due to a higher density of grain boundaries and a reduction of the mean free path of the carriers in samples with a smaller T_a. The solid curves in the figure describes the fits which we will describe as follows.

At temperatures higher than the MIT where SSMO is a paramagnetic insulator the temperature dependence of the resistivity can be described by Eq. 6.2.[3]

$$\rho_i(T) = bT \exp(\Delta/2k_BT) \tag{6.2}$$

where k_B is Boltzmanns constant and Δ is the bipolaron binding energy. Note that $b = 2k_B/(3na^2e^2\nu)$ is a constant[48] that depends on the charge concentration n, the longitudinal optical phonon frequency ν, the hopping distance a and the electron charge e. The bipolaron binding energy is about 240 meV (see Table 6.2) and seems

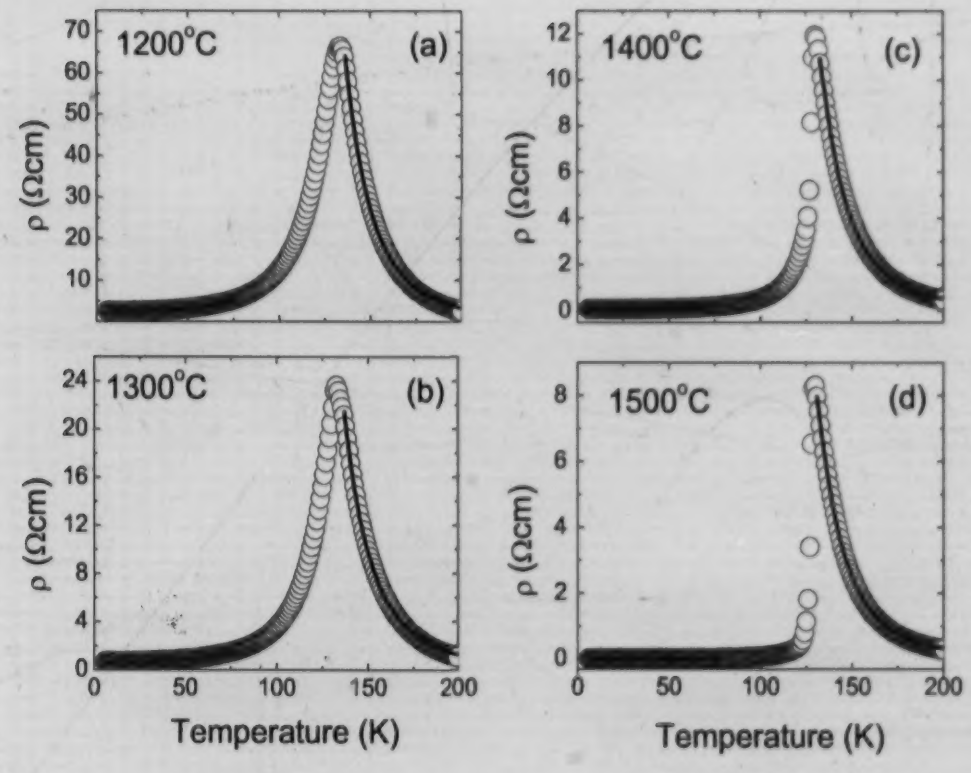

Figure 6.13: Temperature dependence of resistivity ρ measured in zero magnetic field for al samples. Solid lines are fits (see text).

to depend only slightly on the lattice disorder. The magnitude of b and that of the maximum resistivity at the MIT in SSMO(1200) is about six to eight times larger than in the SSMO(1500) sample. An increase of b with an increasing disorder could be caused by a reduction of the effective hopping distance of bipolarons.

The resistivity data far below the MIT (i.e. at temperatures below 75 K) is well-described by Eq. 6.3.

$$\rho_m(T) = \rho_0 + \rho_2 T^2 + \rho_5 T^5 \tag{6.3}$$

where ρ_0 is the residual resistivity, and ρ_2 and ρ_5 are the electron-electron and the electron-phonon scattering coefficients, respectively.[3] In this temperature range the disorder does not affect the temperature dependence of ρ_m, however it causes an increase of the coefficients ρ_0, ρ_2 and ρ_5 by almost two orders of magnitude (see Table 6.2). The fits could be seen in Fig. 6.14.

A theory of the electron-electron scattering resistivity[46] shows that the presence of the anisotropic scattering centers such as those caused by dislocations, grain boundaries etc. in a metal leads to an anisotropic electron scattering relaxation time, which in turn, results in an increase of ρ_2. Furthermore, a theory of the electron-phonon scattering rate in impure polycrystalline metals found that this rate is enhanced by the disorder due to impurities and random lattice shift of grains.[47] This may explain the increase of ρ_5 with an increasing grain-boundary-induced disorder in our samples (see Table 6.2).

An increase in the resistive peak width is apparent from the plot of the temperature coefficient of resistivity TCR $= (1/\rho)(d\rho/dT)$ as a function of temperature (see Fig. 6.15). In contrast to the SSMO(1200) and SSMO(1300) samples, the TCR(T) exhibits a very sharp maximum in the SSMO(1400) and SSMO(1500) samples, suggesting a change of the order of the phase transition from the first to the second order with an increasing disorder consistent with specific heat and magnetization measurements.

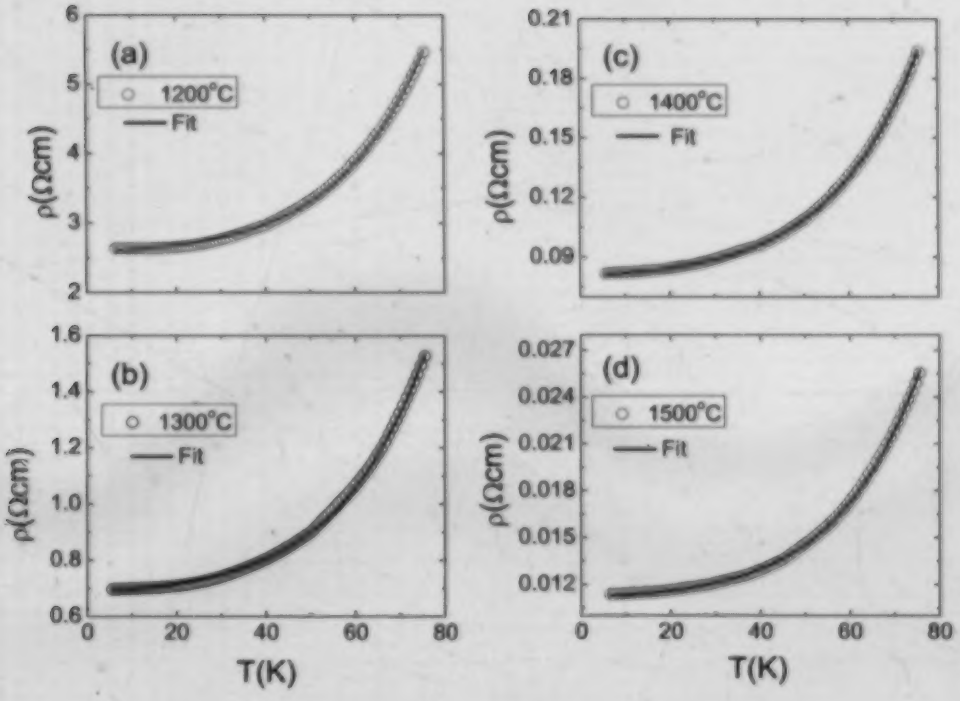

Figure 6.14: Temperature dependence of resistivity ρ data far below the MIT. Solid lines are fits (see text).

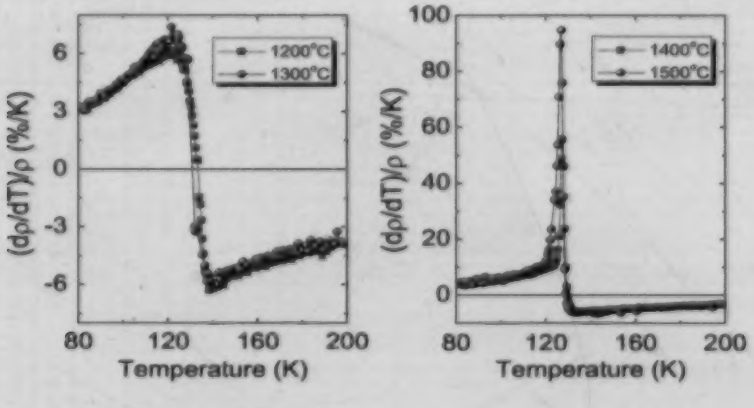

Figure 6.15: Temperature dependence of the TCR measured at zero field for SSMO(T_a) samples.

The dependence of the MR on temperature, shown in Fig. 6.16, exhibits a sharp peak in the vicinity of the MIT for SSMO(1500) and SSMO(1400) samples.Note that we have plotted the temperature dependence of resistivity again in these plots in order to compare the peak position in MR data, A large magneto-resistance is expected in phase separation theories when the competition between the ferromagnetic and antiferromagnetic phases is very strong.[3] In contrast, the MR is suppressed in the more disordered SSMO(1200) and SSMO(1300) samples. This appears to be consistent with the observation that in the SSMO(1400) and SSMO(1500) samples the onset of the short range ferromagnetic ordering starts at higher temperatures than in SSMO(1200) and SSMO(1300) samples (see Fig. 6.12). A more electronically phase separated structure and therefore, a strong competition between different magnetic and electronic phases is expected.

The field dependence of resistivity near the MIT for SSMO(T_a) samples is displayed in Fig. 6.17. At higher fields, starting at about 0.4-0.5 T, $\rho(H)$ of the SSMO(1400) and SSMO(1500) samples decreases much more dramatically than that of SSMO(1200) and SSMO(1300). A sharp decrease of $\rho(H)$ was observed at the MIT and a field of about 0.25-0.30 T in SSMO single crystals of the same composition.[19, 51] This was attributed to a field-induced non-metal to metal phase transition accompanied by a sharp increase of the magnetostriction above this field. In contrast, these studies also report that a $Nd_{0.55}Sr_{0.45}MnO_3$ (NSMO) single crystal, i.e. of the same composition as SSMO, shows neither a sharp decrease of $\rho(H)$ nor a corresponding increase in the magnetostriction.[19] The field-induced transition in $\rho(H)$ can be seen clearly at temperatures near the MIT in SSMO(1400) and SSMO(1500) samples only. It is clearly smeared out in more disordered SSMO(1200) and SSMO(1300) samples.

6.6 Summary and conclusions

In summary, we investigated the effects of the lattice disorder-induced softening of the first-order magnetic phase transition on the magneto-transport properties and

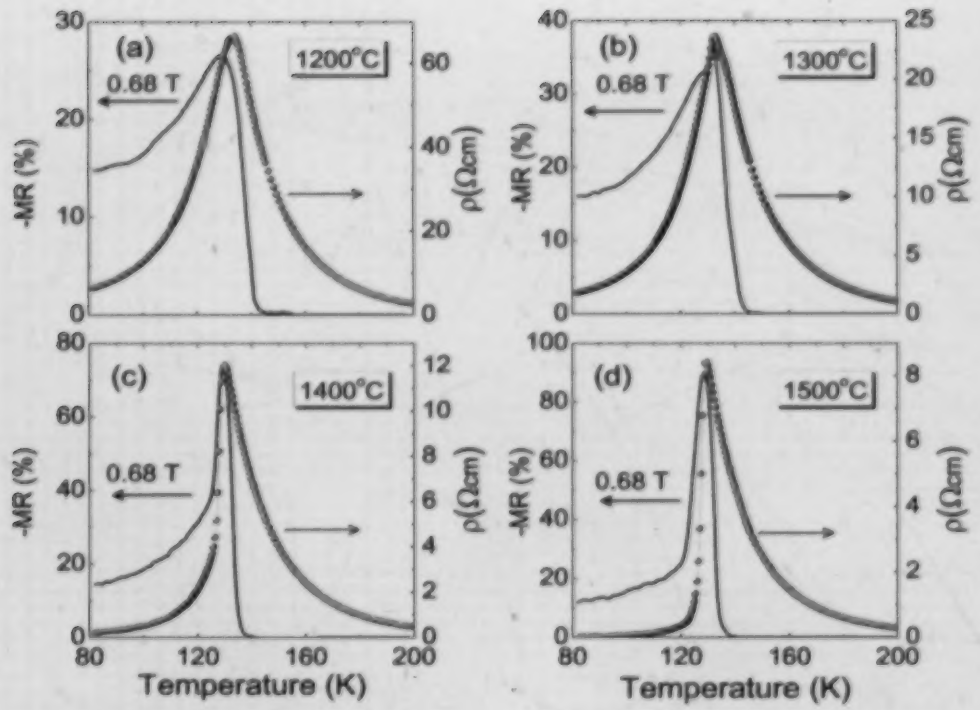

Figure 6.16: Temperature dependence of resistivity ρ measured in zero magnetic field for SSMO(T_a) samples and temperature dependence of the magneto-resistivity MR measured in a field of 0.68 T for SSMO(T_a) samples.

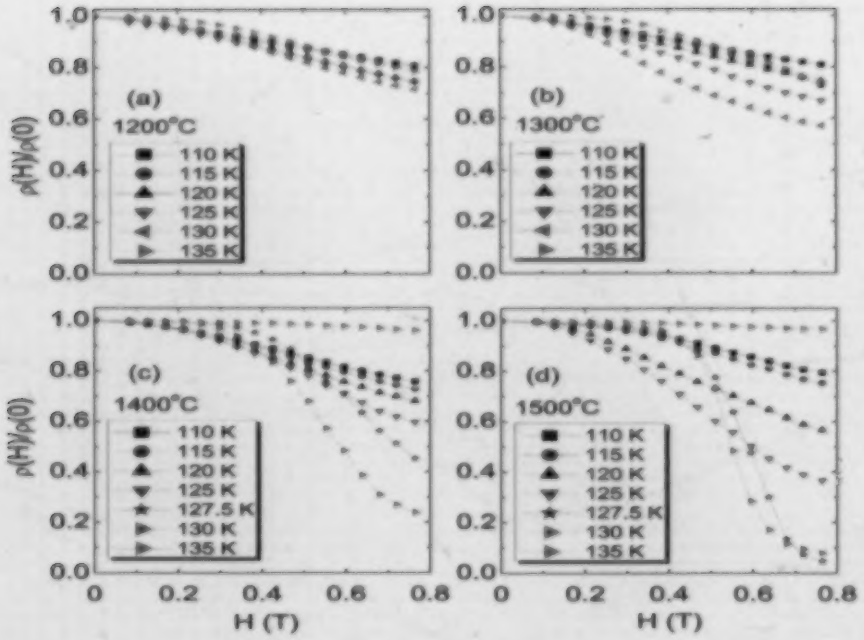

Figure 6.17: Dependence of resistivity on magnetic field measured at different temperatures for SSMO(T_a) samples. The resistivities are normalized to the value of zero field resistivity. The lines are guides to the eye.

the specific heat of a prototypical $Sm_{0.45}Sr_{0.55}MnO_3$ CMR manganite near the MIT. The lattice disorder (induced by the grain boundaries) causes a conversion of the order of the magnetic phase transition from the first to the second order, leading to a continuous metal-insulator transition. According to Evetts *et al.* [52] T_c could vary strongly over distances of several nanometers on each side of the grain boundary. Taking this into account, the spatial variation of the transition temperatures in our samples could lead to a broadening of the peaks in the temperature dependence of the resistivity, the TCR and the specific heat. The magneto-resistance (MR) at the MIT in the SSMO samples that exhibit first-order transition is much larger than the corresponding one in the SSMO samples that exhibit second-order like transitions. This is interesting since it suggests that the large MR in SSMO(1500) is caused by the greater amount of electronic disorder compared to SSMO(1200) which contains more structural disorder. However the deviation from the Curie-Weiss law implies that SSMO(1500) has higher propensity toward short range ferromagnetic correlations than SSMO(1200).

The studies presented above should be of particular interest to researchers who study the theoretical aspects of the effects of disorder on the softening of the first-order magnetic phase transitions.

Bibliography

[1] A. J. Millis, P. B. Littlewood and B. I. Shraiman, *Phys. Rev. Lett.*, **74**, 5144 (1995).

[2] A. S. Alexandrov and A. M. Bratkovsky, *Phys. Rev. Lett.*, **82**, 141 (1999).

[3] A. S. Alexandrov, A. M. Bratkovsky, and V. V. Kabanov, *Phys. Rev. Lett.*, **96**, 117003 (2006).

[4] E. Dagotto, *Science* **309**, 257 (2005).

[5] C. Sen, G.Alvarez, H. Alliaga, E. Dagotto, *Phys. Rev. B*, **73**, 224441 (2006).

[6] C. Sen, G.Alvarez, and E. Dagotto, *Phys. Rev. Lett.*, **98**, 127202 (2007).

[7] L. M. Rodriguez-Martinez and J. P. Attfield, *Phys. Rev. B*, **54**, R15622 (1998).

[8] M. Egilmez, R. Patterson, K. H. Chow, and J. Jung, *Appl. Phys. Lett.* **90**, 232506 (2007).

[9] G. C. Milward, M. T. Calderon, and P. B. Littlewood, *Nature* **433**, 607 (2005).

[10] M. Egilmez, K. H. Chow, and J. Jung, *Appl. Phys. Lett.* **92**, 162515 (2008).

[11] M. Zimmermann, C. S. Nelson, J. P. Hill, D. Gibbs, M. Blume, D. Casa, B. Keimer, Y. Murakami, C. C. Kao, C. Venkataraman, T. Bog, Y. Tomioka, and Y. Tokura , *Phys. Rev. B* **64**, 195133 (2001).

[12] S. Larochelle, A. Mehta, N. Kaneko, P. K. Mang, A. F. Panchula, L. Zhou, J. Arthur, and M. Greven, *Phys. Rev. Lett.* **87**, 095502 (2001).

[13] L. Brey, *Phys. Rev. Lett.* **92**, 127202 (2004).

[14] E. Dagotto, *Nanoscale phase separation and colossal magnetoresistance* 1st ed. (Springer, Berlin, 2003), pp. 193-208.

[15] Y. Tomioka and Y. Tokura, *Phys. Rev. B.* **70**, 014432 (2004).

[16] M. Egilmez, K. H. Chow, and J. Jung, *Appl. Phys. Lett.* **89**, 062511 (2006).

[17] M. Egilmez, K. H. Chow, J. Jung, and Z. Salman, *Appl. Phys. Lett.* **90**, 162508 (2007).

[18] Y. Tomioka, H. Hiraka, Y. Endoh, and Y. Tokura, Phys. Rev. B. **74**, 104420 (2006).

[19] Y. Tomioka, H. Kuwahara, A. Asamitsu, M. Kasai, and Y. Tokura, *Appl. Phys. Lett.* **70**, 3609 (1997).

[20] Y. Endoh, H. Hiraka, Y. Tomioka, Y. Tokura, N. Nagaosa, and T. Fujiwara, *Phys. Rev. Lett.* **94**, 017206 (2005).

[21] J. M. Teresa, M. R. Ibarra, P. Algarabel, L. Morellan, B. Garacia-Landa, C. Marquina, C. Ritter, A. Maignan, C. Martin, B. Raveau, A. Kurbakov, and V. Trounov, *Phys. Rev. B* **65**, 100403 (2002).

[22] M. T. Mercaldo, J-C. Angles d'Auriac, and F. Igloi, *Europhys. Letters*, **70**, 733 (2005).

[23] I. Isaac, J. Jung, J. P. Franck, and M. Abdelhadi, *Phys. Rev. B*, **70**, 212410 (2004).

[24] W. H. Hall and G. K. Williamson, *Proc. Phys. Soc.* , **64B**, 937 (1951).

[25] G. K. Williamson and W. H. Hall, *Acta. Metall.* , **1**, 22 (1953).

[26] A. Taylor, *X-Ray metallography* 1st ed. (John Wiley and Sons, Inc.., New York, 1961), pp. 656 and 787

[27] S. Blundell, *Magnetism in condensed matter* 1st ed. (Oxford University Press, New York, 2001), pp. 127-136.

[28] D. J. Dunlop, *Rep. Prog. Phys.* **53**, 707 (1990).

[29] J. Dho, W. S. Kim, and N. H. Hur, *Phys. Rev. Lett.* **87**, 187201 (2001).

[30] C. Chatelain, B. Berche, W. Janke, and P. E. Berche, *Phys. Rev E* **64**, 036120 (2001).

[31] S. K. Banerjee, *Phys. Lett.* **12**, 16 (1964).

[32] L. D. Landau, *Zh. Eksp. Fiz.* **7**, 19 (1937).

[33] E. M Lifshitz, *Zh. Eksp. Fiz.* **11**, 269 (1941).

[34] C. P. Bean and D. S. Rodbell, *Phys. Rev.* **126**, 104 (1962).

[35] D. Kim, B. Revaz, B. L. Zink, and F. Hellman, J. J. Rhyne, J. F. Mitchell, *Phys. Rev. Lett.* **89**, 227202 (2002).

[36] A. P. Levanyuk, V. V. Osipov, A. S. Sigov, and A. A. Sobyanin, *Sov. Phys. JETP* **49**, 176 (1979).

[37] Y. Moritomo, A. Machida, E. Nishibori, M. Takata, and M. Sakata *Phys. Rev. B* **64** 214409 (2001).

[38] J. Y. Gu, S. D. Bader, H. Zheng, J. F. Mitchell, J. E. Gordon *Phys. Rev. B* **70** 054418 (2004).

[39] T. Vojta, *Phys. Rev. Lett.* **90**, 107202 (2003).

[40] T. Mercaldo, J-Ch. Angles dAuriac,F. Igloi, Phys. Rev E **69**, 056112 (2004), M. T. Mercaldo, J-Ch. Angles dAuriac,F. Igloi, *Phys. Rev E* **73**, 026126 (2006)

[41] E. L. Nagaev, *Colossal magnetoresistance and phase separation in manganites*(Imperial College Press, London, 2002), pp. 317- 318.

[42] C.N.R. Rao and B. Raveau, *Colossal magnetoresistance, charge ordering and related properties of manganese oxides* 2nd ed. (World Scientific, Singapore, 2004), pp. 190-193.

[43] A. Moreo, S. Yunoki, and E. Dagotto, *Science* **283**, 2034 (1999).

[44] H. Y. Hwang, S. W. Cheong, N. P. Ong and B. Batlogg, *Phys. Rev. Lett.* **77**, 2041 (1996).

[45] J. Z. Sun and A. Gupta, *Annu. Rev. Mater. Sci.* **28**, 45-78 (1998).

[46] M. Kaveh, N. Wiser, *J. Phys. F: Met. Phys.*, **12**, 935 (1982).

[47] W. Jan, G. Y. Wu, and H. S. Wei, *Phys. Rev. B*, **64**, 165101 (2001).

[48] D. Emin and T. Holstein, *Ann. Phys.*, **53**, 439 (1969).

[49] R. Mahesh, R. Mahendiran, A. K. Raychaudhuri and C. N. R. Rao, *Appl. Phys. Lett.* **68**, 2291 (1996).

[50] D. D. Sarma, Sugata Ray, K. Tanaka, M. Kobayashi, A. Fujimori, P. Sanyal, H. R. Krishnamurthy, and C. Dasgupta, *Phys. Rev. Lett.* **98**, 157205 (2007).

[51] Y. Tokura, *Colossal magneto-resistive oxides* 1st ed. (Gordon and Breach, Amsterdam, 2000), pp. 35-37.

[52] J. E. Evetts, M. G. Blamire, N. D. Mathur, S. P. Isaac, B.-S. Teo, L. F. Cohen, J. L. Macmanus-Driscoll, P. B. Littlewood, G. A. Gehring, T. Venkatesan, M. Rzchoswki, R. Stroud and A. J. Millis, *Philosophical Transactions: Mathematical, Physical and Engineering Sciences*, **356**, 1593 (1998)

Chapter 7

Grain size dependence of the magnetoresistive anisotropy in polycrystalline $Sm_{0.55}Sr_{0.45}MnO_3$

7.1 Introduction

Colossal magnetoresistance (CMR) in manganites has been studied during the last decade not only for a better understanding of these metallic oxides but also to explore the possibility for various novel magnetic devices.[1] However, the requirement of a large applied magnetic field for a sizeable magnetoresistance (MR) value in such systems has been one of the main drawbacks to their applicabilities. One way to reduce the field scale where sizeable MR exist is controlling the crystallinity and defect constitution in these materials. Introduction of grain boundaries has been used as the main routine for controlling the crystallinity and defect structure. The spin polarized transport of the charge carriers across the grain boundary is accepted to be the main factor which reduces the field scale of sizeable magnetoresistance in manganites.[10]

Whilst, the colossal magnetoresistance effect and its understanding are the main motivations of the manganite studies, in practice manganites exhibit many other

functionalities such as anisotropic magnetoresistance (AMR).[8] AMR is a property of ferromagnetic materials and originates from the response of the charge carriers to the change in orientation of the magnetization with respect to the direction of the current.[7] AMR in manganites is of particular interest since AMR in these materials could reach much higher values than conventional ferromagnetic alloys and metals.[6] This is because of the strong coupling between the spin-orbital-charge degrees of freedom in manganites[4, 2] However, the microscopic physics of the AMR in manganites is complex and not completely understood. AMR has been observed in both epitaxial thin films[6, 8] and in bulk granular polycrystalline samples.[8] Nevertheless so far there is no study dedicated to the grain boundary induced structural disorder dependence of anisotropic transport in manganites. In particular a few important questions need to be addressed: Does the low field and low temperature AMR improve with increasing density of the grain boundaries as in the case of colossal magnetoresistance? Does the spin polarized tunneling of the charge carriers depend on the direction of the applied field?

In order to address these issues, in this chapter we present studies of the structural disorder dependence of the AMR in $Sm_{0.55}Sr_{0.45}MnO_3$, a composition known to be very susceptible to structural disorder.[16] An increasing density of grain boundaries has been used as the measure of an increasing structural disorder. Our results suggest that the well established spin polarized transport model for understanding of the low temperature and the low field CMR in manganites is essentially anisotropic and the AMR in manganite samples could be tuned for large temperature ranges at low magnetic fields by controlling the crystallinity and defect structure.

Polycrystalline samples of $Sm_{0.55}Sr_{0.45}MnO_3$ were prepared using the standard solid state reaction method.[9] A prescribed ratio of Sm_2O_3, $SrCO_3$ and MnO_2 powders was mixed and calcined at 1200°C for 24 h in air. The resulting sample was crushed and sintered again using the same conditions. Four identical pellets were prepared from the powder and sintered/annealed at temperatures T_a=1200, 1300, and 1400°C for 24 h in air. The pellets were then cooled from T_a down to room tem-

perature at a relatively rapid rate of about 30 C/min in order to have the optimum oxygen content.[9] We refer to these samples using the notation SSMO(T_a), where T_a corresponds to the annealing temperature used for the corresponding sample. All samples are single phase, as confirmed by X-ray diffraction (XRD). Scanning electron microscope (SEM) analysis shows that increasing T_a increases the grain size (D) and, hence, decreases the density of grain boundaries. The Williamson/Hall (WH) analysis of the measured broadening of the XRD lines/profiles revealed, however, the presence of much smaller grains at the sub-micrometer level which are not visible in the SEM micrographs (see Table 7.1).[10]

7.2 Results and discussion

The temperature dependence of the resistivity in zero magnetic field (ρ(H=0)) and a field of 6.8 kG are shown in the left panel of the Fig. 7.1. In this figure there are two configurations for resistivity measured in a magnetic field: $\rho_\perp$ corresponds to measured resistivity when applied magnetic field, **H** is perpendicular to the applied current **J** in the four probe measurement configuration, $\rho_\parallel$ corresponds to the measured resistivity when the applied magnetic field, **H** is parallel to the applied current **J**. Dramatic changes in $\rho(T)$ of SSMO(T_a) samples occur with an increasing density of grain boundaries. The resistive transition is more abrupt when the amount of the structural disorder is reduced (increasing T_a). An increase in the magnitude of ρ is consistent with an increase in the scattering rate due to a higher density of grain boundaries and a reduction of the mean free path of the carriers in samples with a smaller T_a. Increase in the grain size is evident in the SEM micrographs shown in the insets of Figure 7.1. Right panel of the Fig. 7.1 expresses the dramatic increase in the MR values when the density of grain boundaries is reduced; MR for SSMO(1400) is about one order of magnitude higher than that for SSMO(1200). The MR peak in SSMO(1400) sample is also very sharp while the peak in SSMO(1200) is much more broader and displays a prominent shoulder that extents down to low

temperatures as expected in highly disordered manganite samples.[5] The effect of the directional dependence of the applied field with respect to current density **J** is clarified in Fig. 7.1 (see left panel) by plotting the magneto-resistance of all samples for the resistivity configurations described above. Here magneto-resistivities are defined as $MR_{\perp}$= [ρ(0)-$\rho_{\perp}$]/$\rho_{\perp}$ and $MR_{\parallel}$= [ρ(0)-$\rho_{\parallel}$]/$\rho_{\parallel}$. As seen from right panel of Figure 7.1 the magneto-resistive anisotropy increases dramatically when the grain boundary induced disorder is reduced in the samples. Notice that since the low temperature part of the magneto-resistivity is governed by the presence of grain boundaries the magnitude of the $MR_{\perp}$ and $MR_{\parallel}$ have similar values which indicates that magneto-transport is mainly governed by intergrain effects. However, close to metal insulator transition the magnetotransport is governed by intragrain effects and subsequently Both $MR_{\perp}$ and $MR_{\parallel}$ exhibited dramatic changes as a function of grain boundary density.

The resistivity of all the samples was measured as a function of the angle θ between applied field (**H**) and the current (**J**) direction with a resolution of 0.04°. This allowed us to determine the temperature and the magnetic field dependence of the anisotropic magneto-resistance. The AMR is defined as AMR= $(\rho_{\parallel} - \rho_{\perp})/\rho_{av}$, where $\rho_{\parallel}$ is the resistivity of the film for a magnetic field **H** that is parallel to the current, and $\rho_{\perp}$ denotes the resistivity measured when **H** is perpendicular to the direction of the transport current. ρ_{av} is the average resistivity ρ_{av} =$(1/3)\rho_{\parallel}$+$(2/3)\rho_{\perp}$.[7] The dependence of resistivity on the angle θ follows a $cos(\theta)^2$ dependence for all the films and over the whole temperature range studied, where $\theta = 0^o$ corresponds to the configuration where **H** is perpendicular to the direction of **J**. Left panel of Fig. 7.2 shows a typical angular dependence of the resistivity for all samples at a temperature of 127 K and in fields of 0.85, 2.10 and 6.80 kG. The solid lines in these figures are the fits to the theoretical expression derived for the angular dependence of the resistivity in ferromagnetic metals $\rho(\theta)$= A+[$\rho_{\parallel}$-$\rho_{\perp}$]$cos^2(\theta)$.[7] Here $\rho(\theta)$ is the resistivity normalized to its value at $\theta = 0^o$.

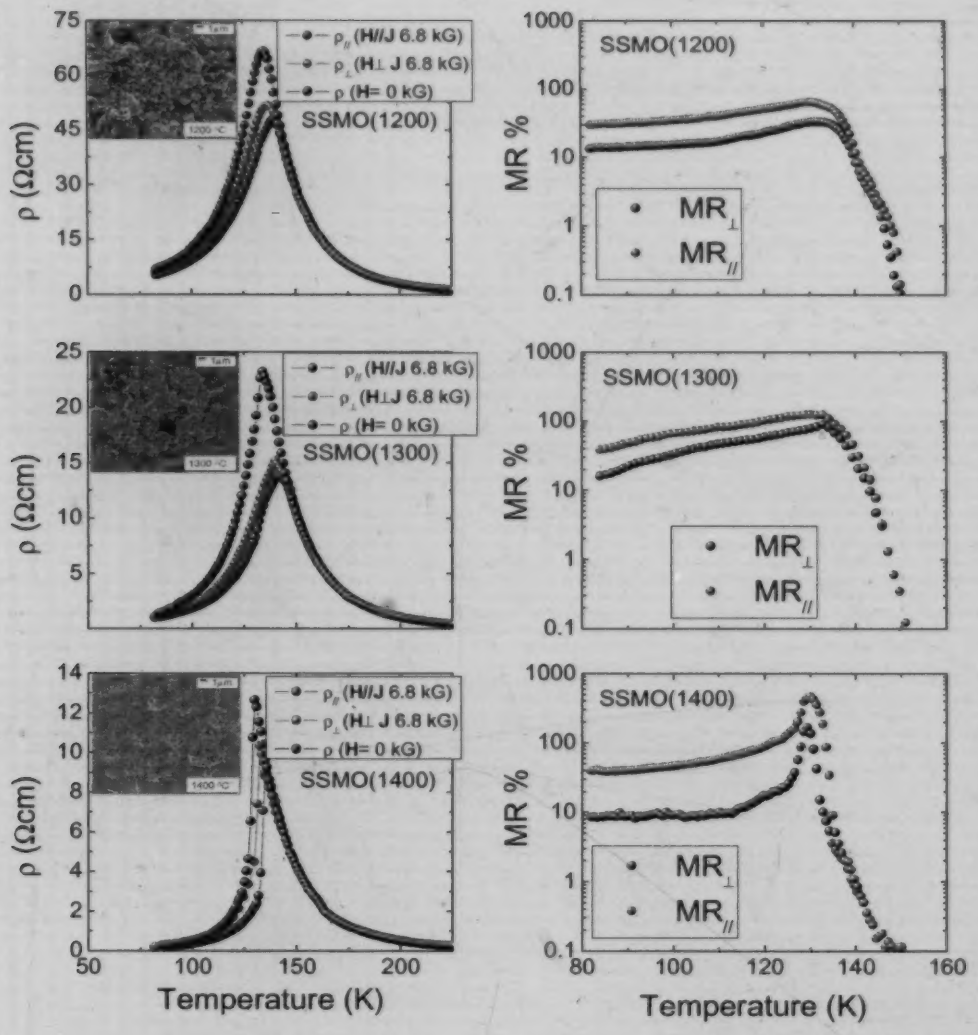

Figure 7.1: [Left panel] Temperature dependence of the resistivity for SSMO(T_a). For definitions of $\rho_\perp$ and $\rho_\parallel$ see text. Insets are SEM pictures for corresponding samples. [Right panel] The temperature dependence of magnetoresistance measured in a field of 6.8 kG for two different resistivity measurement configuration. For definitions of $MR_\perp$ and $MR_\parallel$ see text.

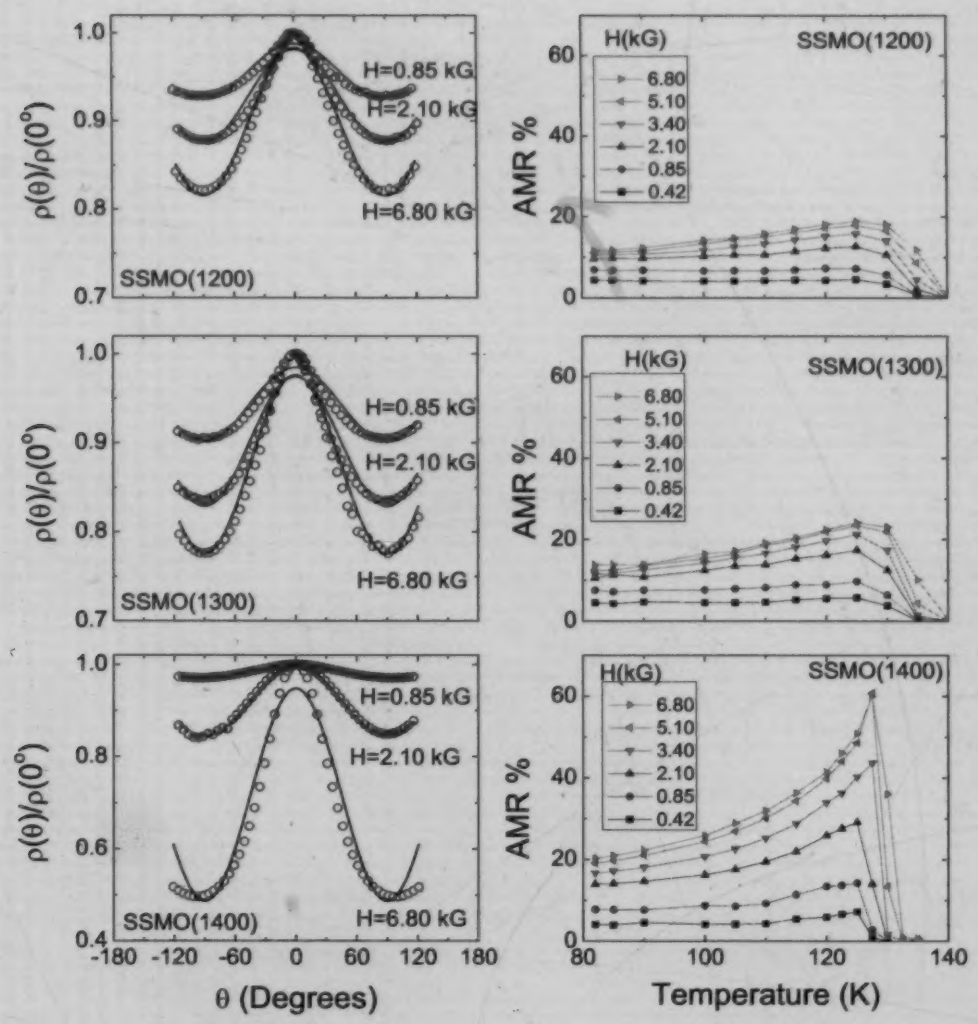

Figure 7.2: [Left panel] (Color online) Angular dependence of resistivity measured at 127 K in fields of 0.85, 2.10 and 6.80 kG for SSMO(T_a). The lines are fits to the theoretical expression (see text). [Right panel] Temperature dependence of the AMR measured in fields of 0.42, 0.85, 2.1, 3.4, 5.1 and 6.8 kG for SSMO(T_a). The lines are guides for the eye.

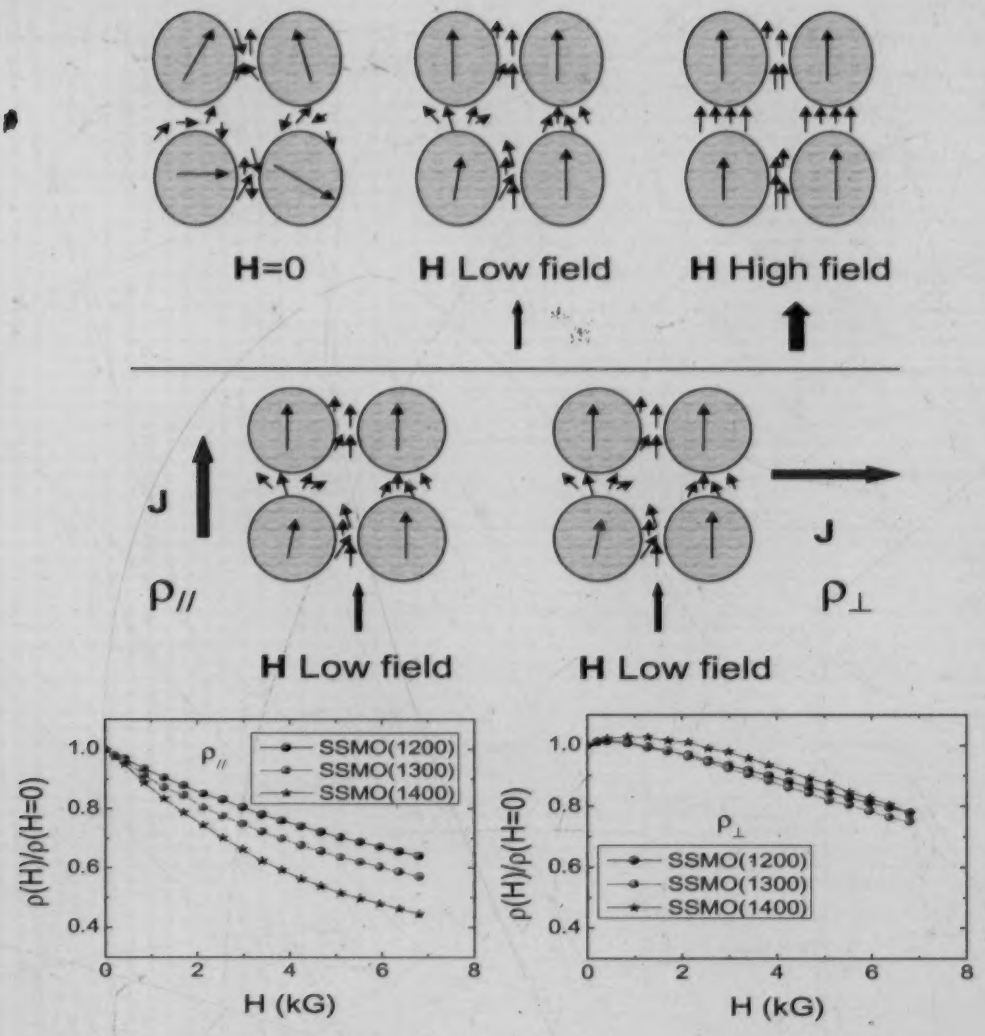

Figure 7.3: [Top panel] A schematic representation for the magnetotransport behavior of the manganite samples with grains. Here, circles represents individual grains, large arrow inside the circles corresponds to the internal magnetization direction within the grain. The region with small arrows around the individual grains stand for the grain-boundary (small arrows indicates the magnetization direction within the grain-boundary region). [Bottom panels] A schematic representation for the anisotropic magnetotransport behavior of the manganite samples with grains. Graphs represent the field dependence of the resistivity of SSMO(T_a) for $\rho_\perp$ and $\rho_\parallel$ configuration at 125 K.

Table 7.1: Parameters that describe the properties of the SSMO samples: T_p is the metal insulator transition temperature (MIT), ρ_p is the resistivity at the MIT, D is the grain size

Sample	T_p (K)	ρ_p (Ωcm)	D(SEM) (μm)	D(WH) (nm)
SSMO(1200)	133	66	0.8	66
SSMO(1300)	132	23	3.5	99
SSMO(1400)	130	12	15	172

The temperature dependence of the AMR for all samples is shown in the right panel of the Fig. 7.2 for magnetic fields of 0.42, 0.85, 2.1, 3.4, 5.1 and 6.8 kG. In samples which contain large density of grain boundaries (SSMO(1200-1300)) the AMR exhibits a very broad peak extending to low temperatures with prominent shoulder. On the other hand, the AMR of the SSMO(1400) is showing a pronounced peak at around MIT and the AMR is almost as twice as high as that of the (SSMO(1200-1300)) samples. Note that all samples exhibit a sizeable AMR at temperatures far more below the metal insulator transition temperature. This is in contrast to single crystal and epitaxial samples of manganites where AMR diminishes at lower temperatures.[5] It is also interesting that the temperature dependence of the AMR for all samples follows that of the MR (see Fig. 7.1).

The main contribution to the AMR, especially in the polycrystalline samples, appears to be Lorentz-force driven since there is no preferred crystallographic direction. Note that the rotation of the applied field **H** from the perpendicular to the parallel configuration with respect to the applied current **J** changes the magnitude of the Lorentz force on the charge carries from the maximum to zero. In the $\mathbf{H} \perp \mathbf{J}$ configuration (see Fig. 7.2) the Lorentz force hinders the conductivity by bending the trajectories of the charge carriers. However, this effect is not the only source of the AMR in manganites. Interestingly, the results obtained on the epitaxial films revealed that the influence of the Lorentz force is negligible.[6, 8] It has

been suggested that spin-orbit coupling, magneto-crystalline anisotropy and orbital deformation contribute to the AMR in these materials.[6] The understanding of the origin of the AMR in manganites is complicated and to our knowledge a theoretical understanding is missing.

The most important result of the current paper is the presence of strong magnetoresistive anisotropy in polycrystalline manganite samples. This anisotropy could be tuned for a large range of temperatures in polycrystalline samples using relatively small magnetic fields. It is widely accepted that the low field and low temperature MR observed in polycrystalline samples of manganites originates from the spin polarized transport across the grain boundaries.[10]. In Fig. 7.3 (the top panel) one can see a sketch of this phenomenon. Without any external magnetic field, the magnetization direction of the each grain is randomly oriented even if it is ferromagnetic within the grain (circles represents the grains, large arrow indicates the internal magnetization direction of the grain) as shown in Fig. 7.3 (top panel). Also, the individual magnetic spins in the grain boundary region (small arrows in between the grains) are randomly oriented. By applying a low magnetic field (up to 1 Tesla), the magnetization of each grain starts to align toward the direction of the external magnetic field as shown in Fig. 7.3. At relatively low field it is believed that the magnetoresistance in bulk manganites is governed by the tunneling of the charge carriers from one grain to a neighboring grain. On the other hand, a larger magnetic field is necessary to align the spins of the grain boundary region to the external magnetic field direction and it is found that at higher fields resistance of the material slightly changes once all the spins are aligned. Presence of large low field and low temperature AMR in our samples suggests that the spin-polarized tunneling of the carriers between the grains is directional, i.e., it depends on the direction of **H** with respect to **J**. We suggest the following model, based on the mechanism reported by Xu *et al.*[8], to explain the presence of large low field AMR at low temperatures in polycrystalline SSMO; When the current flows parallel to **H**, the carriers must tunnel through the grain boundaries between the north pole of a grain and south pole of its neighbor. In this configuration,

the resistance ($\rho_{\parallel}$)is strongly field dependent[10, 8] and hence there is significant MR. On the other hand, if the current is perpendicular to **H**, the carriers flow between the side walls of the grains. In this configuration, the resistance ($\rho_{\perp}$) is less sensitive to the applied field, and hence a weak MR is expected. The AMR arises because the MR for the **H** $\parallel$ **J** and **H** $\perp$ **J** configurations are different. The proposed differences in the field sensitivity of the resistance in the two directions can be understood by keeping in mind that the transport is governed by the tunneling of the carriers across the grain boundaries and is hence very sensitive to the degree of spin alignment in these regions. In the absence of an external magnetic field, the magnetization direction of each grain is arbitrarily oriented even if it is ferromagnetic within the grain due to the polycrystalline nature of the sample; the magnetic spins in the grain boundary regions are randomly oriented. When an external field is applied, it preferentially aligns the magnetization of the grains. The resulting local field between the north pole of one grain and the south pole of the other assists the external field to align the spins in the boundary regions between these two poles. This boundary alignment depends strongly on the degree of alignment of the grains, which, in turn, depends strongly on the strength of the **H**; hence the significant field dependence of the boundary spin alignment and consequently the resistance in this direction. On the other hand, the local fields induced by the aligned grains partially compensate the external field at the sidewalls of neighboring grains. These boundary spins thus remain essentially unaffected (i.e. still random) by changes in **H**. Consequently, the resistance in this direction does not change much with **H**. The magnetic correlation between the grains is expected to be larger when the grain size is increased or the density of the grain-boundaries is reduced; therefore, one can expect a large increase in the magnetic field sensitivity of the $\rho_{\parallel}$. However, in low magnetic fields since sidewall grain-boundary region spins are still random magnetic field sensitivity of the $\rho_{\parallel}$ is expected to give weaker response to the external magnetic fields. This behavior is evidenced in the field dependence of $\rho_{\parallel}$ and $\rho_{\perp}$ as shown in Fig. 7.3 (the $\rho_{\perp}$ is less sensitive to applied fields than the $\rho_{\parallel}$). This observation supports our qualitative explanation for the

increase in the magneto-resistive anisotropy at low fields in samples with larger grain size. Therefore in grained samples we believe in addition to Lorentz Force effects, spin-orbit coupling, the defect structure is important for understanding the magneto-resistive anisotropy.

7.3 Summary and conclusions

In summary we have shown that polycrystalline SSMO samples exhibit large magneto-resistive anisotropy. The magnitude of the AMR strongly depends on the grain size of the samples. The AMR in polycrystalline samples exhibit sizeable low field and low temperature AMR which is in contrast to single crystal samples and epitaxial films.[5] This suggests that the well established spin polarized transport model for understanding low temperature and low field MR in manganites is essentially directional. Our results indicate that AMR in manganite samples could be tuned for large temperature ranges at low fields by controlling the defect structure.

Bibliography

[1] C. Israel, M. J. Calderon, and N. D. Mathur, *Materials Today*, **10**, 24 (2007).

[2] S. M. Thompson, *J. Phys. D: Appl. Phys.* **41**, 093001 (2008).

[3] A. S. Alexandrov and A. M. Bratkovsky, *Phys. Rev. Lett.*, **82**, 141 (1999).

[4] E. Dagotto, *Science* **309**, 257 (2005).

[5] J. O. Donnell, J. N. Eckstein, and M. S. Rzchowski, *Appl. Phys. Lett.* **76**, 218 (2000); J. N. Eckstein, I. Bozovic, J. O. Donnell, M. Onellion, and M. S. Rzchowski, *Appl. Phys. Lett.* **69**, 1312 (1996); M. Ziese, *Phys. Rev. B*, **62**, 1044 (2000).

[6] M. Egilmez, R. Patterson, K.H. Chow, and J. Jung, *Appl. Phys. Lett.* **90**, 232506 (2007); M. Egilmez, M.M. Saber, A. I. Mansour, Rongchao Ma, K. H. Chow, and J. Jung, *Appl. Phys. Lett.* **93**,182505(2008).

[7] Y. Tokura, N. Nagaosa, *Science* **288**, 462 (2000).

[8] Yunhui Xu, V. Dworak, A. Drechsler, and U. Hartmann, *Appl. Phys. Lett.***74**, 2513 (1999).

[9] M. Egilmez, I. Isaac, D.D. Lawrie, K.H. Chow, and J. Jung, *Journal of Materials Chemistry* **18**, 5796 (2008).

[10] W. H. Hall and G. K. Williamson, *Proc. Phys. Soc.* , **64B**, 937 (1951).

[11] M. Egilmez, A.I. Mansour, M.M. Saber, K.H. Chow, and J. Jung, *Appl. Phys. Lett.* **92**,022501 (2008).

[12] T. R. McGuire and A. R. I. Potter, *IEEE Transactions on on magnetics* **MAG-11**, 1018 (1975)

[13] H. Y. Hwang, S. W. Cheong, N. P. Ong and B. Batlogg, *Phys. Rev. Lett.* **77**, 2041 (1996).

Chapter 8

Magnetotransport and magnetoresistive anisotropy in $Sm_{0.55}Sr_{0.45}MnO_3/Nd_{0.55}Sr_{0.45}MnO_3$ bilayers

8.1 Introduction

$Sm_{0.55}Sr_{0.45}MnO_3$ (SSMO) is a member of the family of $Re_{1-x}A_xMnO_3$ manganites (where Re = rare earth, A = alkaline earth) near the half-doping level (with composition $x \approx 0.5$). SSMO is particularly interesting for applications since thin films and single crystals of this material exhibit resistive switching behavior (induced by magnetic or electric fields, or laser light irradiation), giant magnetostriction, or large magneto-caloric effect that could be applied in magnetic refrigeration.[1, 16, 3] From the physics point of view, on the other hand, these materials have attracted more attention due to the commensurate nature of orbital, charge, and spin ordered phases occurring at this doping level. Their phase diagram is therefore very fragile, suggesting that any small external stimulus such as pressure, electric field or magnetic field could dramatically modify their magneto-transport properties.[4, 5]

SSMO single crystal has the metal-insulator transition (MIT) at around 130 K.[6] A number of studies dedicated to single crystals, thin films and polycrystalline samples of this composition have been reported. Regarding SSMO thin films, Tokura's group[1] reported difficulties with the growth of 100 nm thick $Sm_{1-x}Sr_xMnO_3$ films of compositions x between 0.4 and 0.6 on $SrTiO_3$ (100) substrates by the pulsed laser deposition. Strangely none of these films revealed the presence of the metal-insulator transition in magnetic fields up to 7 Tesla. An insulating behavior of SSMO films has been attributed to the large lattice mismatch between the substrate and the film. The deposition of SSMO films which show bulk (single-crystal) like properties with the MIT close to 130 K has not been reported so far.

We have deposited SSMO films of thickness between 60 and 1000 nm on $SrTiO_3$ (STO), $LaAlO_3$ (LAO), MgO and YSZ (100) substrates in order to test the effect of the lattice mismatch on the properties of these films. The lattice mismatch between the SSMO films and the STO, LaO, MgO and YSZ substrates at room temperature is +1.0%, -1.6%, +9.3% and +35.3 %, respectively.[7] None of these films showed the MIT at 130 K. They were insulators down to 80 K with a negligible CMR effect at low magnetic fields. Even the thickest films in which a strong strain relaxation is expected, exhibited similar transport properties below 130 K.Post-annealing of the thickest films at 850 ^oC in air produced the MIT but at temperatures not higher than 80-90 K, implying that the lattice strain has been only partly removed. These properties are much different from those of the bulk (single crystal) SSMO, suggesting that in addition to the lattice mismatch, other factors such as the mismatch in thermal expansion coefficients or a chemical reaction between the substrate and the film could be responsible for the insulating behavior. Notice also that the magnetostriction values reported for SSMO is more than one order of magnitude larger than those of the same composition of $Nd_{0.55}Sr_{0.45}MnO_3$ (NSMO) manganite. This suggest that in SSMO the lattice is extra strongly coupled to the magneto-transport.[8] Therefore, in order to prepare SSMO films with bulk like properties, one has to find a way to fine control the strain in the SSMO lattice.

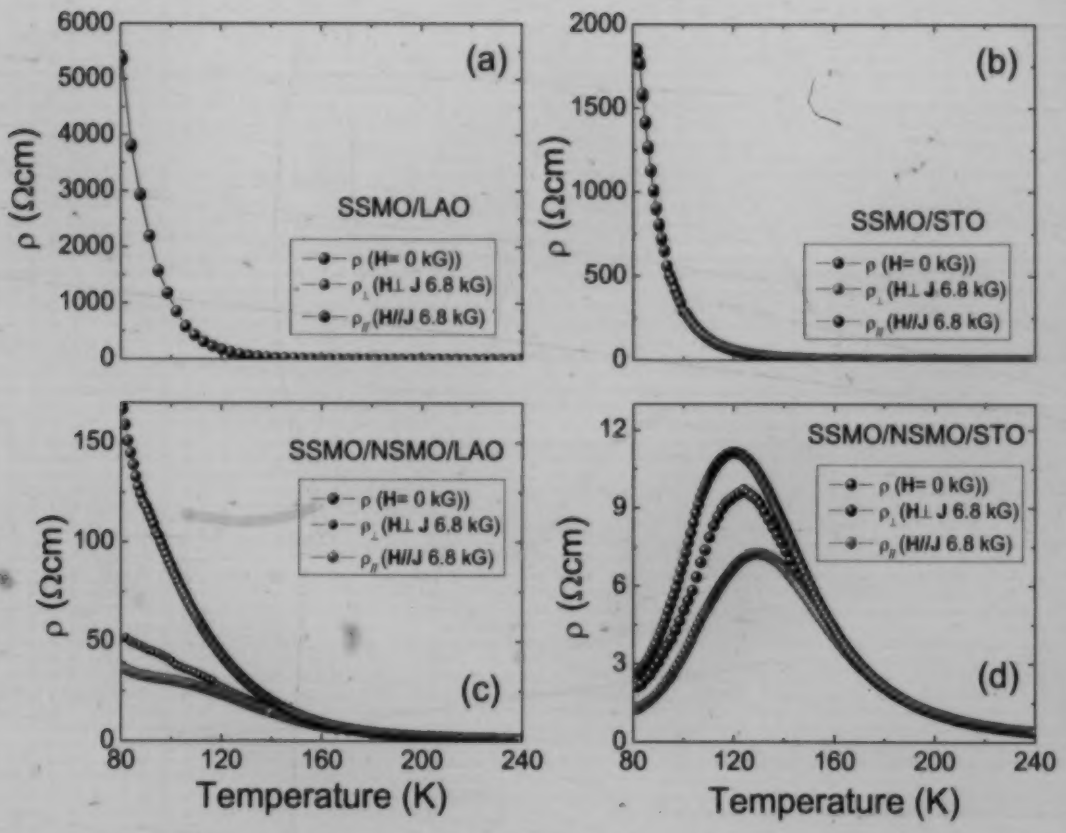

Figure 8.1: [Top panel] Temperature dependence of the resistivity for SSMO grown on LAO and STO. [Bottom panel] Temperature dependence of the resistivity for NSMO buffered SSMO grown on LAO and STO. For definitions of $\rho_\perp$ and $\rho_\parallel$ see text.

In order to solve this problem we deposited $Nd_{0.55}Sr_{0.45}MnO_3$ (NSMO) as a thin buffer layer between the substrate and the SSMO film. The lattice mismatch between the SSMO and NSMO is very small (+0.1%) allowing an epitaxial growth.[7, 9] This process produced SSMO films of single-crystal-like properties with a giant response to the relatively small magnetic fields.

8.2 Results and discussion

Thin film bilayers were grown using dc magnetron sputtering at 750°C (50 W power, in an argon-oxygen mixture of partial pressures: 100 mTorr of oxygen and 20 mTorr of argon) on $LaAlO_3$ and $SrTiO_3$ substrates. A 18 nm thick layer of NSMO followed by a 450 nm thick SSMO film have been grown on both substrates using the same deposition conditions. A small thickness of the NSMO film allowed us to avoid an overlap of the magneto-transport properties of the NSMO with those of the SSMO. After deposition the chamber was filled with oxygen at atmospheric pressure in order to ensure that the samples gained the optimum content of oxygen. The films were cooled down from 750°C to 650°C with a rate of 20°C/min, followed by annealing at 650°C for 3 h and subsequent cooling down to room temperature with a rate of about 20°C/min.

The temperature dependence of the resistivity ρ was measured with a four-probe method in a zero magnetic field and in a field of 6.8 kG (see Fig. 8.1). The dependence of ρ on the magnetic field was measured for two different configurations: i) with an applied magnetic field **H** perpendicular to the applied current density **J** (out of plane resistivity $\rho_\perp$), and ii) with **H** parallel to **J** (in plane resistivity $\rho_\parallel$). As seen in Fig. 8.1 a and 1b there is no change resistivity when the magnetic field is applied in samples which were directly deposited on LAO and STO substrates respectively. The SSMO films deposited on a 18 nm thick NSMO buffer layer exhibit a dramatic change in the transport properties, in contrast to the SSMO films deposited without the buffer layer. The SSMO/NSMO/LAO films do not display any metallic-like resistivity, however,

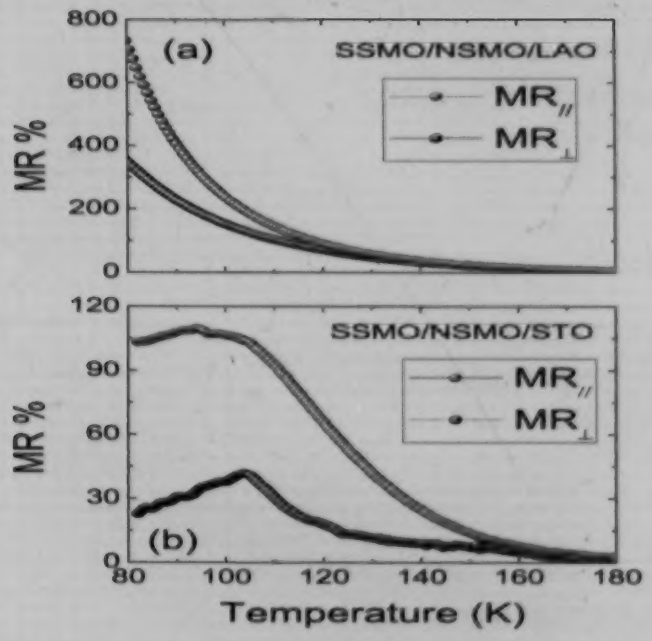

Figure 8.2: The temperature dependence of magnetoresistance measured in a field of 6.8 kG for two different resistivity measurement configuration. For definitions of $MR_{\perp}$ and $MR_{\parallel}$ see text.

their resistivity is strongly suppressed by a magnetic field. On the other hand, even in the absence of any applied field, the SSMO/NSMO/STO films show the MIT with the peak's temperature around 120 K which is close to that of 130 K seen in single crystals. The response of the SSMO/NSMO/STO films to a magnetic field is weaker than that of the SSMO/NSMO/LAO films.

Fig. 8.2 presents the temperature dependence of the magneto-resistivity $MR_{\perp}$= $[\rho(0)\text{-}\rho_{\perp}]/\rho_{\perp}$ and $MR_{\parallel}$= $[\rho(0)\text{-}\rho_{\parallel}]/\rho_{\parallel}$ of SSMO/NSMO/LAO and SSMO/NSMO/STO films for the two **H-J** configurations described above. The ratio of the $MR_{\parallel}/MR_{\perp}$ is higher for the STO/NSMO/SSMO, suggesting higher magneto-resistive anisotropy. The magneto-resistive anisotropy in these films was obtained from the measurements of the resistivity as a function of the angle θ between **H** and **J** directions ($\theta = 0^o$ for **H** parallel to **J**, and $\theta = 90^o$ for **H** perpendicular to **J** and the plane of the film).

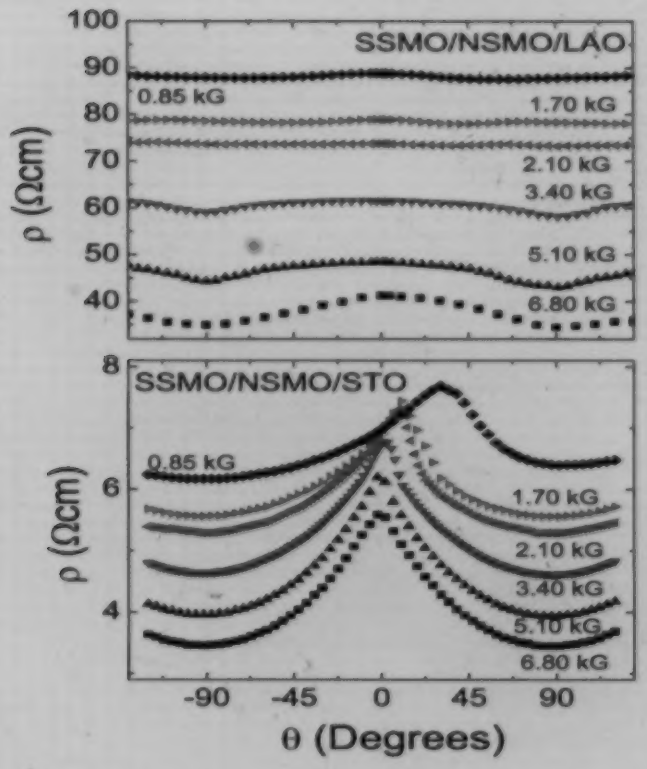

Figure 8.3: [Top panel] Angular dependence of resistivity measured at 100 K in different magnetic fields for NSMO buffered SSMO films.

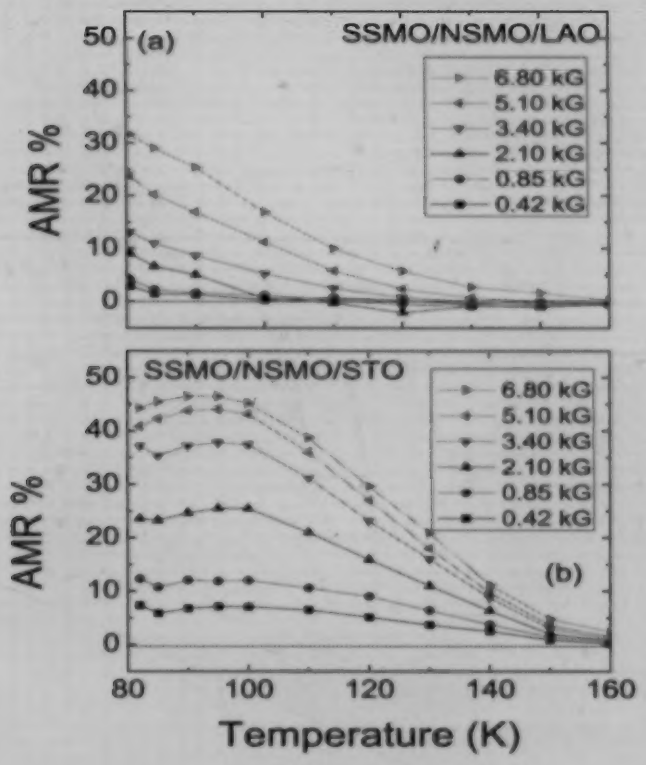

Figure 8.4: Temperature dependence of the AMR measured in different fields for NSMO buffered SSMO films. The lines are guides for the eye.

Fig. 8.3 shows an angular dependence of the resistivity $\rho(\theta)$ for both samples measured at 100 K in fields up to 6.80 kG. The $\rho(\theta)$ of SSMO/NSMO/STO film is noticeably different from that of SSMO/NSMO/LAO film. Magneto-resistive anisotropy is suppressed in the SSMO/NSMO/LAO film especially in fields lower than a few kG. The low field resistivity of SSMO/NSMO/STO film peaks at angles larger than 0^o in contrast to that at higher fields. The films with the in-plane compressive strain (eg. films grown on LAO) favor the out-of-plane easy axis magnetization direction, whereas those with the in-plane tensile strain (eg. films grown on STO) favor the in-plane easy axis magnetization.[8, 9] In SSMO/NSMO/STO film the easy axis of the magnetization does not match the direction of the applied field at low fields. For

any given angle θ and intensity **H** of the applied field, the equilibrium direction of the magnetization is $\phi^* \approx \theta$-ϕ, where ϕ is the angle between the current density and magnetization of the sample. ϕ^* which could be found by the minimization of free energy of the system, is slightly different from θ at lower fields.A deviation from the $cos^2(\theta)$ dependence in SSMO/NSMO/STO film is due to higher anisotropy energy, with the magnetization pinned in the plane of the film at fields lower than a few kG. [12] On the other hand, a deviation from the $cos^2(\theta)$ dependence has not been seen in SSMO/NSMO/LAO film in the same magnetic field range. This could be due to the lower anisotropy energy of this film.

The resistivity of the film could be calculated from the formula $\rho(\phi^*) = \rho_\perp - \Delta\rho cos^2(\phi^*)$, where $\rho_\perp$ is the resistivity when the magnetization is perpendicular to the current and $\Delta\rho$ is the maximum change of the resistivity, i.e. $\Delta\rho = \rho_\perp - \rho_\parallel$. This expression could be used to fit the data at all temperature and field ranges.

Fig. 8.4 shows the temperature dependence of the anisotropic magneto-resistivity AMR for both films in different magnetic fields. Here the AMR is defined as $(\rho_\parallel - \rho_\perp)/\rho_{av}$, where ρ_{av} is the average resistivity $\rho_{av} = (1/3)\rho_\parallel + (2/3)\rho_\perp$.[7] The AMR of SSMO/NSMO/LAO film increases monotonically with a decreasing temperature, which is similar to the behavior of the MR. On the other hand the temperature dependence of the AMR in SSMO/NSMO/STO films exhibits a peak at around 100 K. The resistivity peak in SSMO/NSMO/STO films is broader than that in a bulk SSMO, suggesting that some disorder at the interface of SSMO and NSMO favors a spin polarized transport. A broad magneto-resistance and an AMR peak is expected in this case according to the studies of MR and AMR in disordered CMR oxides.[15]

Our results suggest that the mismatch between the properties of the substrate and SSMO is minimized by the buffer layer. Dramatically different behavior in the magneto-transport properties of bi-layers grown on LAO and STO substrates may indicate, however, two different strain states. The strain state due to the mismatch of the lattice constants between the film and the substrate plays a dominant role in the electronic phase separation, modifying the charged/orbital ordered state and hence

the phase competition in CMR materials. We believe that the large difference between the strain states and hence the magneto-transport properties of films grown on LAO and STO substrates are the result of these different phase separation tendencies. For instance, the SSMO/NSMO/LAO film appears to exhibit a meta-stable behavior: the resistivity of the sample below 150 K displays a strong time dependence in a magnetic field, i.e. it decreases with an increasing time. This suggests a glassy behavior due to the melting of a charge/orbital ordered insulating antiferromagnetic phase into a ferromagnetic metallic phase.[16] For this film the phase diagram is very fragile as evidenced by a strong low field CMR and glassy behavior.[17] On the other hand the resistivity of the STO/NSMO/SSMO film does not exhibit any time dependence in a field and at any temperature, suggesting that the charge ordered phases are stable due the strong strain relaxation in this sample. Whereas the SSMO/NSMO/LAO films have the largest MR, the AMR is the largest in the SSMO/NSMO/STO films, which should be expected since the AMR reaches a maximum close to MIT. The absence of the metallic behavior in the SSMO/NSMO/LAO film in our measurement range implies a relatively small AMR.[5]

8.3 Summary and conclusions

In summary we have shown that the SSMO films grown on LAO and STO substrates exhibit insulating behavior with a negligible magneto-resistance effect. On the other hand, when SSMO/STO films are buffered with a thin layer of NSMO a large low field magneto-resistance behavior along with the single-crystal-like properties are observed. These results are reproducible and suggest that the low field magneto-resistance and magneto-resistive anisotropy could be enhanced dramatically in multilayered manganite films.

Bibliography

[1] H. Oshimaa, K. Miyano, Y. Konishi, M. Kawasaki, and Y Tokura, *Appl. Phys. Lett.* **75**, 1473 (1999); M. Kasai, H. Kuwahara, Y. Tomioka, and Y. Tokura, *J. Appl. Phys.*, **80**, 6894 (1996).

[2] Y. Tomioka, H. Kuwahara, A. Asamitsu, M. Kasai, and Y. Tokura, *Appl. Phys. Lett.* **70**, 3609 (1997).

[3] A. Rebello and R. Mahendiran, *Appl. Phys. Lett.* **93**, 232501 (2008).

[4] M. Zimmermann, C. S. Nelson, J. P. Hill, D. Gibbs, M. Blume, D. Casa, B. Keimer, Y. Murakami, C. C. Kao, C. Venkataraman, T. Bog, Y. Tomioka, and Y. Tokura , *Phys. Rev. B* **64**, 195133 (2001).

[5] S. Larochelle, A. Mehta, N. Kaneko, P. K. Mang, A. F. Panchula, L. Zhou, J. Arthur, and M. Greven, *Phys. Rev. Lett.* **87**, 095502 (2001).

[6] M. Egilmez, K. H. Chow, and J. Jung, *Appl. Phys. Lett.* **89**, 062511 (2006); M. Egilmez, K. H. Chow, J. Jung, and Z. Salman, Appl. Phys. Lett. **90**, 162508 (2007).

[7] Y. Tomioka, H. Hiraka, Y. Endoh, and Y. Tokura, *Phys. Rev. B* **74**, 104420 (2006). The lattice constants of STO, LAO, MgO and YSZ are 3.790, 3.905, 4.21 and 5. 21 $\AA$ respectively.

[8] . Tomioka, H. Kuwahara, A. Asamitsu, M. Kasai and Y. Tokura *Appl. Phys. Lett.* **70**, 3609 (1997)

[9] F. Millange, C. V. Caignaert, G. Matter, E. Suard, and B. Raveau, *J. Solid State Chem.* **127**, 131 (1996).

[10] J. O. Donnell, J. N. Eckstein, and M. S. Rzchowski, *Appl. Phys. Lett.* **76**, 218 (2000); J. N. Eckstein, I. Bozovic, J. O. Donnell, M. Onellion, and M. S. Rzchowski, *Appl. Phys. Lett.* **69**, 1312 (1996).

[11] B. I. Belevtsev, V. B. Krasovitsky, D. G. Naugle, K. D. D. Rathnayaka, A. Parasiris, S. R. Surthi, R. K. Pandey, and M. A. Rom, *Phys. Stat. Sol.a*, **188**, 1187 (2001).

[12] S. Mandal, RC Budhani, *Journal of magnetism and magnetic materials* **320**, 3323 (2008).

[13] I. Pallecchi, A. Gadaleta, L. Pellegrino, G. C. Gazzadi, E. Bellingeri, A. S. Siri, and D. Marr, *Phys. Rev. B* **76**, 174401 (2007).

[14] T. R. McGuire and A. R. I. Potter, *IEEE Transactions on on Magnetics* **MAG-11**, 1018 (1975)

[15] M. Egilmez, A. I. Mansour, M. M. Saber, K. H. Chow, and J. Jung, *Appl. Phys. Lett.* **92**, 022501 (2008)

[16] V. Markovich, G. Jung, Y. Yuzhelevski, and G. Gorodetsky, A. Szewczyk, M. Gutowska, D. A. Shulyatev and Ya. M. Mukovskii, *Phys. Rev. B* **70**, 064414 (2004).

[17] D. N. H. Nam, N. V. Khien, N. V. Dai, L. V. Hong, and N. X. Phuc, *Phys. Rev. B* **77**, 214406 (2008).

[18] M. Egilmez, R. Patterson, K. H. Chow, and J. Jung, *Appl. Phys. Lett.* **90**, 232506 (2007); M. Egilmez, M. M. Saber, A. I. Mansour, R. Ma, K. H. Chow, and J. Jung, *Appl. Phys. Lett.* **93**,182505(2008).

Chapter 9

Magnetoresistive anisotropy and magneto-resistivity in strained $La_{0.65}Ca_{0.35}MnO_3$ films near the metal-insulator transition

9.1 Introduction

A number of theories attempt to explain the resistivity and magneto-resistivity in materials that exhibit colossal magneto-resistance (CMR), such as the manganites, at temperatures near the metal-insulator transition (MIT) using phase separation scenarios. These models rely predominantly on two very different mechanisms to explain inhomogeneities in manganites: electronic phase separation for nanometer-scale inhomogeneities, and the effects of disorder for micrometer-scale inhomogeneities.[1, 2, 3] In both cases one expects the transport current to flow along some filamentary paths which "dodge" the insulating clusters by zigzagging between them. A recent theoretical calculation suggests that the metal-insulator phase coexistence in manganites is strain induced[4]. In this model only the insulating phase (which is embedded into a metallic one) is strained. An increasing lattice strain should result in the break

up of large insulating clusters into progressively smaller ones. It is known that both the lattice strain and the magneto-crystalline anisotropy contribute to the magneto-resistive anisotropy (AMR) of manganites.[5] The AMR is important for a number of applications that utilize films of CMR materials, such as magneto-resistive read heads or nonvolatile magnetic random access memory devices. Previous measurements of the magnitude of the "in-plane" resistivity ρ^{in} at the MIT, i.e. when a magnetic field is applied in the plane of very thin c-axis oriented films and the resistivity also measured in the same plane, showed that it is highly anisotropic. It is largest when the magnetic field is perpendicular to the current and smallest when the field is parallel to the current[6]. The magnitude of the "in-plane" resistivity ρ^{in} was also found to be different from that of the "out-of-plane" resistivity ρ^{out} measured for the magnetic field perpendicular to the plane of a film [7].

The "in-plane" and the "out-of-plane" resistivity measurements can be used to define fully all types of magneto-resistive anisotropy, i.e., the "in-plane" and the "out-of-plane" AMRs. The AMRs are used to characterize the changes in the resistivity as the direction between the applied magnetic field **H** and the direction of the current **J** changes. In this paper, the "in-plane" AMR is defined as $\mathrm{AMR}^{in} = (\rho_{\parallel}^{in} - \rho_{\perp}^{in})/\rho_o$, where $\rho_{\parallel}^{in}$ and $\rho_{\perp}^{in}$ are the resistivities of the film for **H** that is located in the plane of the film and is oriented parallel and perpendicular to the current, respectively (see Fig. 9.1), and ρ_o is the resistivity in zero applied field. Note that the superscript on ρ labels that **H** is in the plane of the film (i.e. ab-plane), while the subscript indicates the direction of **H** with respect to **J**. The "out-of-plane" anisotropies are defined as $\mathrm{AMR}_{\parallel}^{out} = (\rho_{\parallel}^{in} - \rho_{\perp}^{out})/\rho_o$ and $\mathrm{AMR}_{\perp}^{out} = (\rho_{\perp}^{in} - \rho_{\perp}^{out})/\rho_o$. The symbol $\rho_{\perp}^{out}$ denotes the resistivity measured when **H** is applied perpendicular to both the film's plane (i.e. out of plane) and the direction of the transport current (see Fig. 9.1). Consequently the "in-plane" AMR^{in} is also the difference between these two "out-of-plane" anisotropies, i.e. $\mathrm{AMR}^{in} = \mathrm{AMR}_{\parallel}^{out} - \mathrm{AMR}_{\perp}^{out}$.

Recent studies of thin films of the well-known CMR manganite $La_{1-x}Ca_xMnO_3$ with compositions within the range $x = 0.30 - 0.35$ revealed that both the "in-plane"

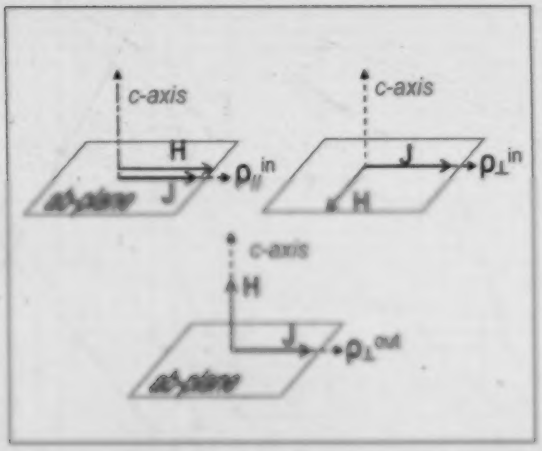

Figure 9.1: Magnetic field and current configurations applied during the measurements of resistivity of LCMO thin films.

and the "out-of-plane" AMRs are present and are anomalous near the Curie temperature T_c, when compared to metallic ferromagnetic alloys. In particular, LCMO films exhibit a peak at temperatures near the metal-insulator transition[6, 7, 8, 9, 10] while the AMR in ferromagnetic alloys decreases monotonically with increasing temperature. Furthermore, it is known experimentally that deposition of thin films on a substrate leads to strain in the film because of the lattice mismatch[11]. The strain state of the films evolves from coherently strained at a small thickness to (partially) strain relaxed at larger thicknesses.

9.2 Results and discussion

The studies of the magneto-resistivity (MR) and the AMR in strained $La_{0.65}Ca_{0.35}MnO_3$ (LCMO) films, described in this chapter, were designed to answer the following question: What is the dependence of both the AMR and the MR close to the MIT on the film thickness and the external magnetic field in strained LCMO films? Answers to this question are interesting from a scientific point of view, and would also give re-

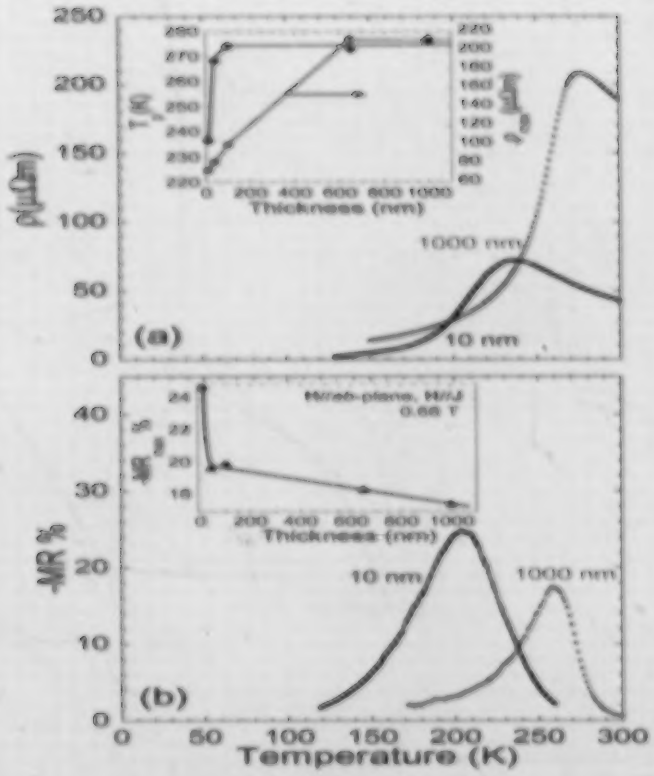

Figure 9.2: (a) Temperature dependence of the resistivity measured in a zero magnetic field for 10 nm and 1000 nm thick samples. Inset: Thickness dependences of the value of the peak resistivity and the temperature at which the peak resistivity occurs T_p. (b) Temperature dependence of the magneto-resistivity MR measured in a magnetic field of 0.68 T for 10 nm and 1000 nm samples. Inset: Thickness dependence of the MR.

searchers important clues on manipulating the magneto-resistive anisotropy of LCMO and other CMR materials.

Our magneto-transport measurements were carried out on a set of LCMO films with thickness varying from 1000 nm down to 10 nm. The temperature and magnetic field dependence of the magneto-resistivity and the "in-plane" and "out-of-plane" magnetic anisotropies were systematically studied at the MIT. The samples were epitaxial strained films of c-axis oriented $La_{0.65}Ca_{0.35}MnO_3$ which were deposited by dc magnetron sputtering (using 50-70W power) in an argon-oxygen mixture (of partial pressures: 100 mTorr of oxygen and 20 mTorr of argon) at 750°C on $LaAlO_3$ substrates. The lattice mismatch between LCMO and the $LaAlO_3$ substrate is rather large with a compressive strain of - 1.7%.[12] Deposition time varied from 0.5 hour for a 10 nm thick film up to 4.5 hours for a 1000 nm thick film. After deposition the chamber was filled with oxygen at atmospheric pressure in order to ensure that the samples gained the optimum oxygen content and hence the maximum T_c. The films were cooled down from 750°C to 650°C with a rate of 10°C/minute, followed by annealing at 650°C for two hours and subsequent cooling down to room temperature with a rate of about 15°C/minute. It is known that post-annealing at elevated temperatures, such as 950°C in an atmospheric pressure of oxygen, reduces the internal lattice strain in the films.[12] We deliberately eliminated this step in order to maintain the lattice strain in our samples. Since the $LaAlO_3$ substrates are twinned, during the growth of LCMO films twinned domains (islands) are formed. This makes the film isotropic in the ab-planes, leading to the suppression of of the effect of the in-plane magneto-crystalline anisotropy on the measured magneto-resistivity.

The temperature dependence of the resistivity ρ and the MR= $[\rho(0) - \rho(H)]/\rho(0)$ for the 10 nm and 1000 nm LCMO films are plotted in Fig. 9.2. Both the resistivity and the metal-insulator transition temperature T_p of the films were found to decrease with a decreasing film thickness (see Fig. 9.2(a)). On the other hand, a reduction in film thickness increases the MR of these films (see Fig. 9.2(b)).

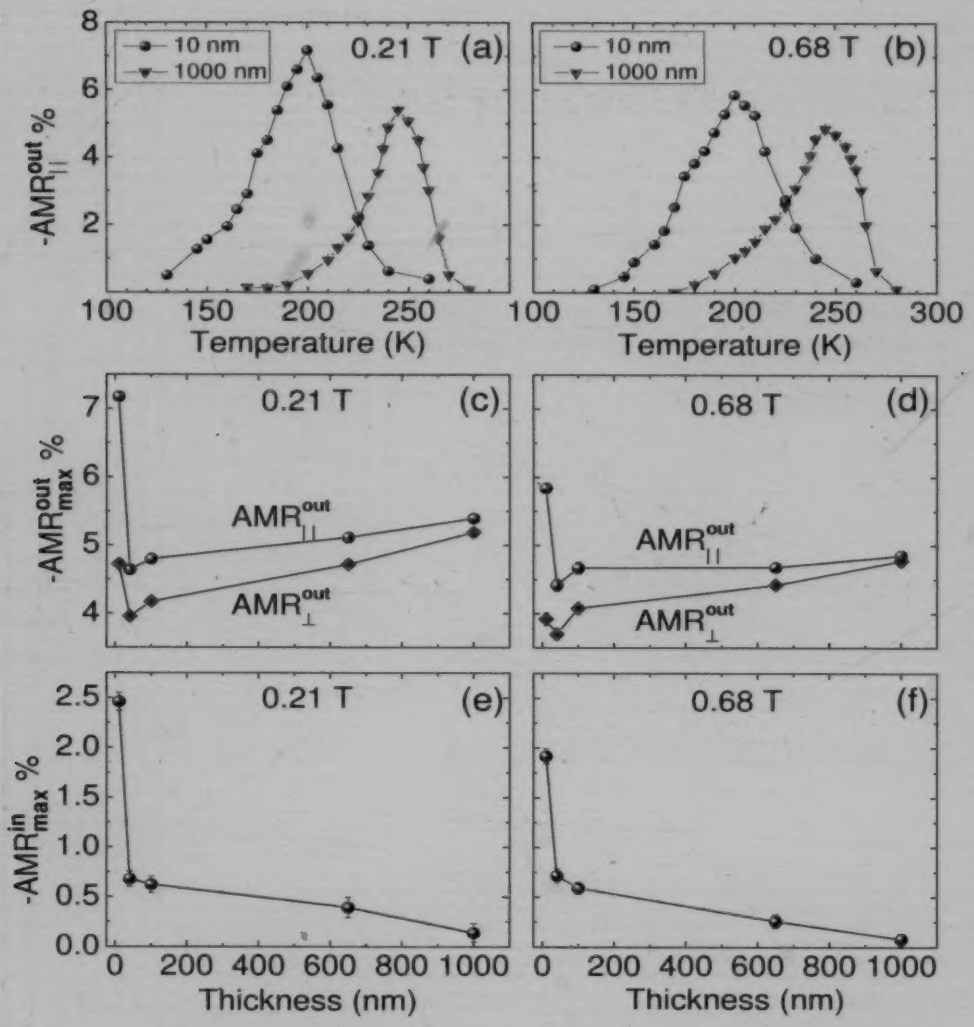

Figure 9.3: (a) and (b) Temperature dependence of the magneto-resistive anisotropy AMR_1^{out} measured for 10 nm and 1000 nm thick LCMO films in a field of 0.21 T and 0.68 T, respectively. (c) and (d) Thickness dependence of the maximum values of the "out-of-plane" AMR_1^{out} and AMR_2^{out} for a field of 0.21 T and 0.68 T, respectively. (e) and (f) Thickness dependence of the maximum values of the "in-plane" AMR^{in} for a field of 0.21 T and 0.68 T, respectively. The lines are guides for the eye.

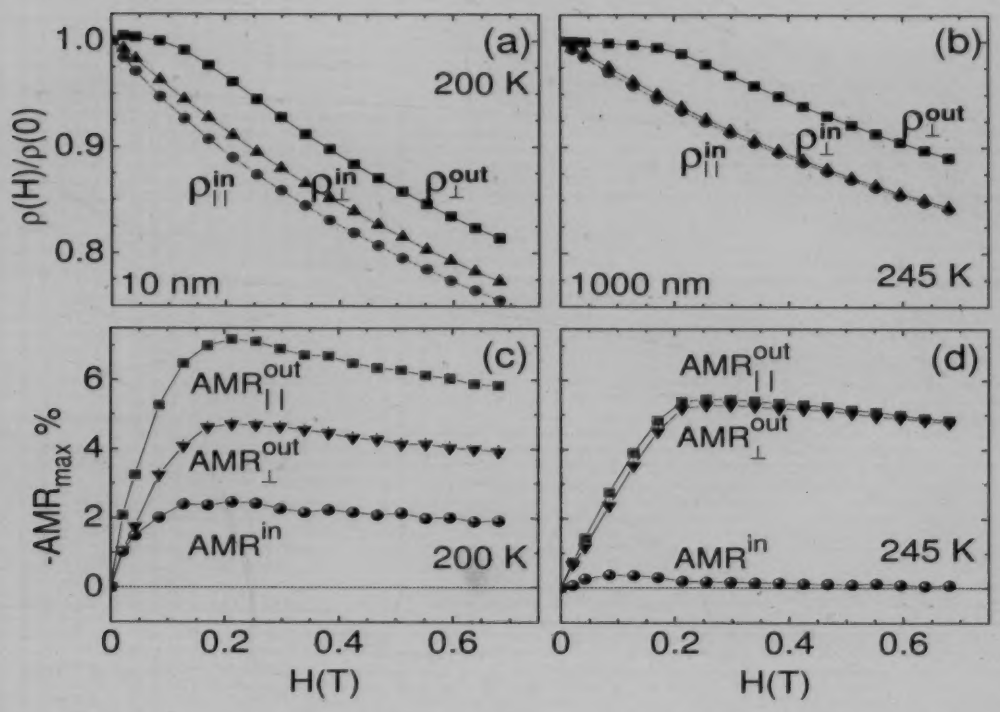

Figure 9.4: (a) and (b) Magnetic field dependence of the resistivity measured for 10 nm and 1000 nm thick LCMO films, respectively, for different magnetic field-current configurations (see Fig. 9.1). The resistivities were measured at a temperature corresponding to the maximum AMR. They were normalized to the value of the zero-field resistivity. An increase followed by a decrease of the magnetic field shows negligible hysteretic effects. (c) and (d) The field dependence of the maximum values of the "out-of-plane" and the "in-plane" AMRs for 10 nm and 1000 nm thick films, respectively. The lines are guides for the eye.

The resistivity of the LCMO films was also measured as a function of the magnetic field **H**; the angle θ between **H** and the c-axis direction (with a resolution of 0.04°); and the angle ϕ between **H** and the direction of the current **J** while **H** is rotated in the plane of the film. The dependence of resistivity ρ on the angles θ and ϕ follows $\sin^2\theta$ and $\sin^2\phi$ dependences, respectively over the whole temperature range studied. For the $\sin^2\theta$ dependence the maximum and the minimum resistivity occurs for **H** parallel to the c-axis, and for **H** perpendicular to both the c-axis and the current, respectively. On the other hand, for $\sin^2\phi$ dependence the maximum of the resistivity occurs for **H** perpendicular to the c-axis and the current, while the minimum occurs for **H** parallel to the current. This is similar to $\rho(\phi)$ measured previously by O'Donnell et al[6] for a magnetic field rotated in the plane of the film. The $\sin^2\theta$ or $\sin^2\phi$ dependences were found to be independent of the thickness of the film.

In addition, we determined the temperature and the magnetic field dependences of the "in-plane" and the "out-of-plane" magnetic anisotropies. As mentioned earlier, the experimental configurations relevant to measurements of AMR are shown in Fig. 9.1. The temperature dependence of the "out-of-plane" $\mathrm{AMR}_{\parallel}^{out}$ for 1000 nm and 10 nm samples close to the MIT is shown in Fig. 9.3 for two different magnetic fields of 0.21 and 0.68 T. All AMRs, the "in-plane" and the "out-of-plane" ones, exhibit a peak close the metal-insulator transition for all the films studied. The thickness dependence of the maximum value of these AMRs is plotted for 0.21 T and 0.68 T in Fig. 9.3 (c)-(f). In a field of 0.21 T the "out-of-plane" AMRs decrease slightly with a decreasing thickness, however, they increase suddenly when the film thickness becomes less than 10 nm. The "in-plane" AMR shows a steady increase with a decreasing thickness, with a sudden jump to a higher value for 10 nm thick film.

Magnetic field dependence of both the "in-plane" and the "out-of-plane" resistivities is plotted for the 10 nm and 1000 nm films in Fig. 9.4 (a) - (b). The "in-plane" resistivities are almost isotropic, i.e. $\rho_{\parallel}^{in} \approx \rho_{\perp}^{in}$, for the 1000 nm thick film. This is not the case for the 10 nm thick film whose "in-plane" resistivities are clearly different. This is also seen in the magnetic field dependence of the "in-plane" anisotropy AMR^{in}

shown in Fig. 9.4(c) - (d) for both films. Consequently the field dependence of the "out-of-plane" anisotropies $AMR_{\parallel}^{out}$ and $AMR_{\perp}^{out}$ are identical for the 1000 nm thick film, in contrast with the field dependence of the 10 nm thick films.

We now discuss possible explanations for our observations. Keeping in mind that the lattice strain decreases with an increasing thickness[12], we believe that our 1000 nm thick film of $La_{0.65}Ca_{0.35}MnO_3$ is thick enough for the internal strain to be substantially reduced. We observed that the temperature and magnetic field dependences of the "out-of-plane" $AMR_{\parallel}^{out}$ and $AMR_{\perp}^{out}$ are very similar and consequently the "in-plane" AMR^{in} is almost zero (see Fig. 9.4). On the other hand, a strained 10 nm thick film exhibits different behavior with the non-zero "in-plane" AMR^{in}. As discussed in the introduction, one might expect that the presence of insulating and metallic clusters in an LCMO film at the metal-insulator transition would force the transport current to percolate across the film. Monte-Carlo calculations by Burgy et al.[?] suggest that if a reasonable amount of disorder already exists in the sample, then increasing the disorder further leads to a decrease in the magnitude of the peak resistivity ρ_{max}. This is because an increasing quenched disorder (eg. an increasing lattice strain) would reduce the size of the insulating and metallic clusters; this enhances the percolation of the transport current across the sample resulting in a decrease of the resistivity. The observed reduction of the LCMO film resistivity (as well as a decreasing metal-insulator transition temperature T_p) with a decreasing thickness of the film (see Fig. 9.2(a)) supports this model. To our knowledge, no computational studies of the dependence of the magneto-resistive anisotropy AMR at the MIT on the lattice strain have been undertaken. Therefore, one has to rely on the experimental data to explain the dependence of the AMR at the MIT on a decreasing film thickness (an increasing lattice strain). The data show that at the MIT the "in-plane" $\rho(H)$ of the 1000 nm thick film is almost isotropic in the *ab*-plane, ie. the resistivity is almost independent of the direction of **H** in this plane. In contrast to this, the "in-plane" $\rho(H)$ of the 10 nm thick film is anisotropic in the *ab*-plane. The amount of this anisotropy increases with a decreasing thickness of the LCMO

film. The angular dependence of the in-plane magneto-resistivity $\rho(\phi)$ (where ϕ is the angle between the directions of the current and the field) in our twinned LCMO films is independent of the crystallographic direction of the flow of the current. This suggests that the changes in the in-plane anisotropy of $\rho(\phi)$ observed near the MIT only are caused by the Lorentz force which is present when the magnetic field is perpendicular to the current. Near the MIT the epitaxial lattice strain-induced phase separation into metallic ferromagnetic and insulating clusters forces the current to percolate. In very thin films strain-induced percolation causes the resistivity to drop (see Fig. 9.2(a)). The Lorentz force may hinder this percolation (i.e. increase the resistivity) by bending the trajectories of the charge carriers.

9.3 Summary and conclusions

In summary, we investigated the magneto-transport properties (in particular the MR and the AMR) at the MIT in strained films of $La_{0.65}Ca_{0.35}MnO_3$ as a function of the film thickness. The data suggests that an increasing epitaxial lattice strain that develops as the film thickness is decreased is responsible for an increase of both the MR and the "in-plane" AMR. This is consistent with the observation of an increasing in-plane strain-state with a decreasing thickness of LCMO films deposited on $LaAlO_3$ substrates.[6]

Bibliography

[1] A. Moreo, S. Yunoki, and E. Dagotto, *Science* **283**, 2034 (1999).

[2] E. Dagotto, T. Hotta, and A. Moreo, *Phys. Rep.* **344**, 1 (2001).

[3] J. Burgy, A. Moreo, and E. Dagotto, *Phys. Rev. Lett.* **92**, 097202 (2004).

[4] K. H. Ahn, T. Lookman, and A. R. Bishop, *Nature* **428**, 401 (2004).

[5] Y. Suzuki, H. Y. Hwang, S.W. Cheong, and R. B. van Dover, *Appl. Phys. Lett.* **71**, 140 (1997).

[6] J. O'Donnell, J. N. Eckstein, and M. S. Rzchowski, *Appl. Phys. Lett.***76**, 218 (2000).

[7] M. Ziese, *Phys. Rev. B* **62**, 1044 (2000).

[8] M. Ziese and S. P. Sena, *J. Phys.:Condens. Matter* **10**, 2727 (1998).

[9] V. S. Amaral, A. A. C. S. Lourenco, J. P. Araujo, A. M. Pereira, J. B. Sousa, P. B. Tavares, J. M. Vieira, E. Alves, M. F. da Silva, and J. C. Soares, *J. Appl. Phys.* **87**, 5570 (2000).

[10] B. I. Belevtsev, V. B. Krasovitsky, D. G. Naugle, K. D. D. Rathnayaka, A. Parasiris, S. R. Surthi, R. K. Pandey, and M. A. Rom, *Phys. Stat. Sol.(a)* **188**, 1187 (2001).

[11] T. Y. Koo, S. H. Park, K. B. Lee, and Y. H. Jeong, *Appl. Phys. Lett.* **71**, 977 (1997).

[12] M. Ziese, H. C. Semmelhack, K. H. Han, S. P. Sena, and H. J. Blythe, *J. Appl. Phys.* **91**, 9930 (2002).

[13] R. A. Rao, D. Lavric, T. K. Nath, C. B. Eom, L. Wu and F. Tsui, *Appl. Phys. Lett.* **73**, 3294 (1998).

Chapter 10

Dramatic strain induced modification of the low field anisotropic magneto-resistance in ultra-thin manganite films

10.1 Introduction

Early commercial magneto-resistive random access memory (MRAM) computer chips were based on an effect called the anisotropic magneto-resistance (AMR) which occurs in ferromagnetic metals and alloys.[1, 2] The AMR defines the response of charge carriers in ferromagnetic materials to changes of the orientation of the magnetization with respect to the direction of the current. Since in ferromagnetic metals and alloys the AMR is very small, i.e. only of the order of a few percent, these devices suffered from a relatively long read-access-time. The discovery of the giant magnetoresistance (GMR) led to a reduction of the read-access-time and was responsible for an enormous acceleration of MRAM's technology.[3] Colossal magneto-resistance manganite films might be good candidates for the next generation of AMR devices due to the many functional magnetic properties resulted from the strong coupling between the

charge, orbital, spin and lattice degrees of freedom.[3, 2, 16] The magnetotransport properties of the manganite films are generally extremely sensitive to the epitaxial strain, implying that the AMR may also be significantly affected. However, the effects of lattice strain on the AMR of ultra thin manganite films have never been carefully investigated.

In this chapter, we show studies of highly strained ultra-thin La based manganite films, and found that the AMR in some of these systems can reach very high values, exceeding 100%. These values are much higher than those previously reported for ferromagnetic metals, alloys and thicker manganite films.[8] Furthermore, if the epitaxial strain is compressive, the AMR can even undergo a field-induced sign-flip. The observation that the AMR in manganite films can be modified to such a dramatic extent is relevant for the development of manganite-film based devices.

The majority of the measurements reported in this chapter were carried out on $La_{0.65}Ca_{0.35}MnO_3$ (LCMO) grown on $LaAlO_3$ (LAO) and $SrTiO_3$ (STO) substrates. Since LCMO has an an in-plane lattice constant a = 3.863 Å, films that are grown on LAO and STO substrates have an epitaxial strain of -1.7% and +0.9%, respectively, in the plane of the film. This enables the effects of tensile and compressive strain on the AMR, as well as their dependence on film thickness, to be investigated. The LCMO films had thicknesses varying from 7 nm to 150 nm and were grown via magnetron sputtering following the approach described elsewhere.[5] The LCMO/STO and LCMO/LAO samples which had the same thickness of LCMO were grown simultaneously in order to avoid any differences in the deposition conditions, enabling a more reliable comparison of the substrate effects. The resistivity of the LCMO films were measured as a function of the angle θ between H and the direction of the current J, allowing us to determine the temperature and the magnetic field dependencies of the AMR. The AMR measured on the LCMO films is defined as AMR= $(\rho_{\parallel}^{in} - \rho_{\perp}^{out})/\rho_{av}$, where $\rho_{\parallel}^{in}$ is the resistivity of the film for a magnetic field **H** that is located in the plane of the film and is oriented parallel to the current, and $\rho_{\perp}^{out}$ denotes the resistivity measured when **H** is applied perpendicular to both the film's

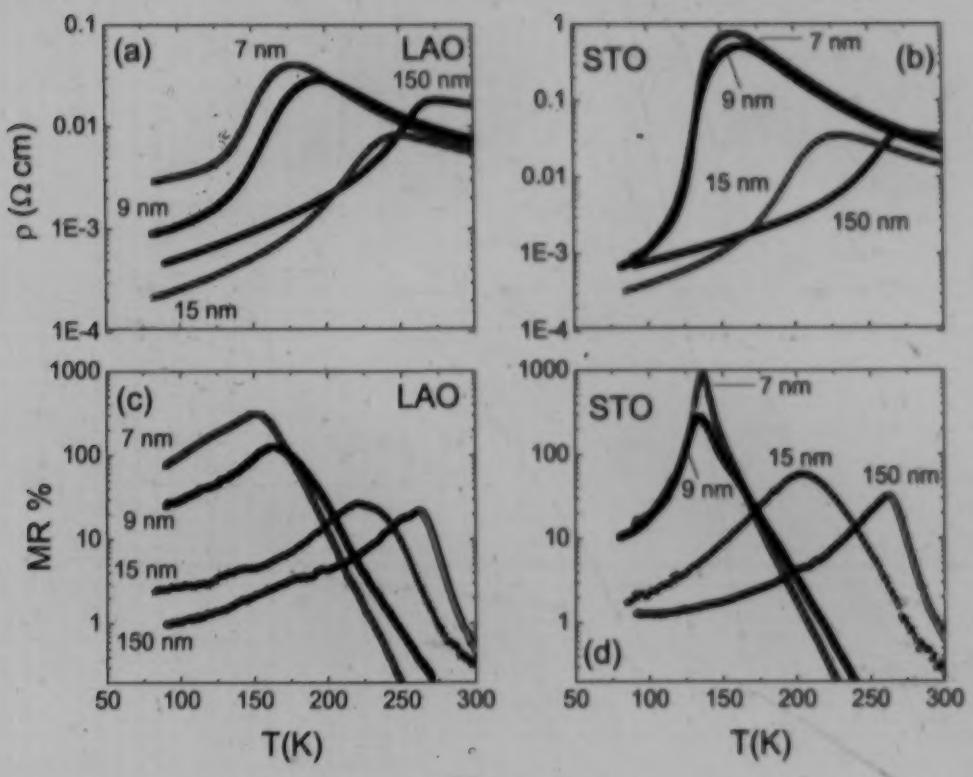

Figure 10.1: Temperature dependence of the (a)-(b) Resistivity in zero field and temperature dependence of (c)-(d) Magnetoresistivity of LCMO/STO and LCMO/LAO samples in a field of 6800 Gauss.

plane and the direction of the transport current. The average resistivity is defined to be $\rho_{av} = (1/3)\rho_{\parallel}^{in}+(2/3)\rho_{\perp}^{out}$.[7] The AMR was measured in magnetic fields up to 0.7 T. This field is larger than that required to saturate the magnetization in LCMO thin films.[8, 9]

10.2 Results and discussion

Temperature dependence of resistivities and magnetoresistivities ,MR =[ρ(0)-$\rho(H)/\rho(H)$] are shown in Fig. 10.1. As the thickness of film decreased the metal insulator tran-

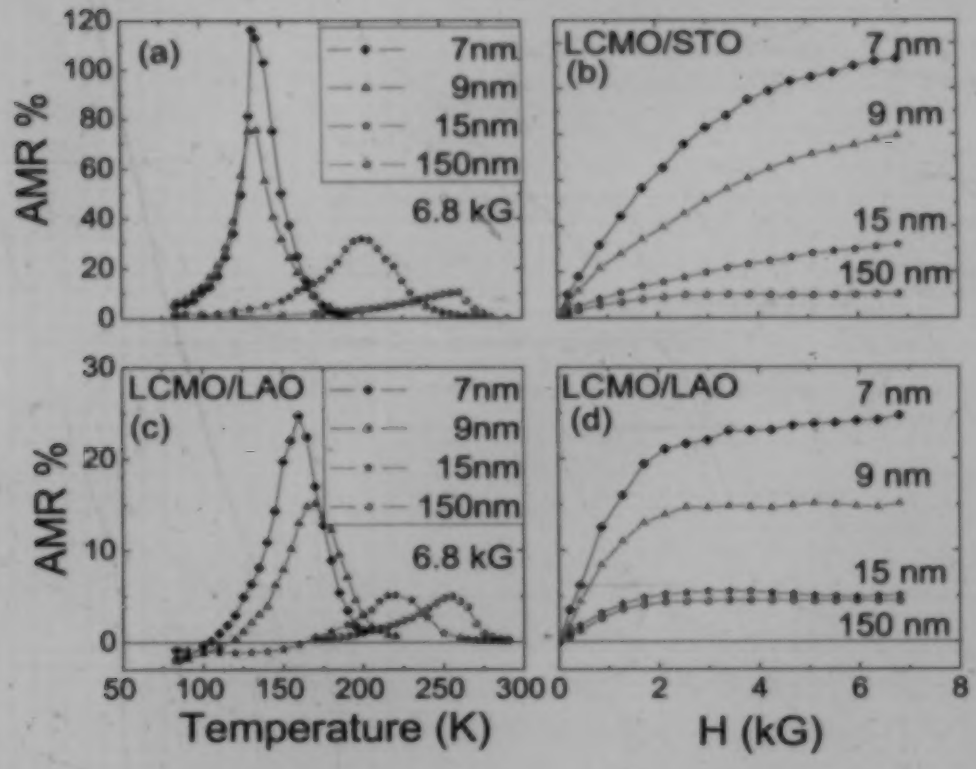

Figure 10.2: (a)-(b) The angular dependence of the normalized resistivity at the AMR peak's maximum temperature measured in the 7 and 150 nm thick films. The solid lines are the fits to the data (see text); The corresponding polar plots of the angular dependence of the normalized resistivity at the AMR peak's maximum temperature, measured for different applied fields.

sition temperatures decreases noticeably in both sets of samples grown on LAO and STO due to the increased strain. The MR magnitude increases dramatically as the thickness of the films are reduced. The MR of the LCMO/STO reaches 800% at a field of 0.68 T and is very different from those of the LCMO/LAO, in particular the MR ratio is a few times less in LCMO/LAO samples.

The temperature dependence of the AMR for the LCMO/STO and LCMO/LAO films is shown in Fig. 10.2 (a) and (c). For all samples the AMR shows a peak in the vicinity of the metal-insulator transition (MIT) temperature. For the LCMO films

grown on STO substrates the AMR increases with a decreasing thickness of the film, i.e. it is around 120% in 7 nm thick films but has dropped to around 10% in 150 nm thick films. A similar dependence of the AMR on thickness has been observed also in the LCMO/LAO films (see Fig. 10.2). An increase of the epitaxial strain with a decreasing thickness of the film could account for the observed behavior. The field dependence of the AMR was measured at the temperature corresponding to the peak's maximum (see Fig. 10.2 (b) and (d)). The AMR shows a tendency to saturate at higher magnetic fields. For 150 nm thick films the AMR is fully saturated above 3-4 kG. However these fields are too small to saturate the AMR of thinner films. It is remarkable that at temperatures far below the MIT temperature, the AMR for the LCMO/LAO films undergoes a change in sign (see Fig. 10.2 (c)). In contrast, the temperature dependence of the AMR in the LCMO/STO films does not display this effect.

The angular dependences of the resistivity at the AMR peak's temperature are plotted in Fig. 10.3 (a) and (b) for the 7 nm and 150 nm thick films of LCMO/LAO and LCMO/STO. The solid lines in these two figures represent the fits to the theoretical expression $\rho(\theta) = A + [\rho_{\parallel}^{in} - \rho_{\perp}^{out}]\cos^2(\theta)$ for the angular dependence of resistivity in ferromagnetic metals.[13] The resistivity $\rho(\theta)$ was normalized to its value at $\theta = 0°$ which corresponds to the configuration where **H** is both parallel to the c-axis of the film and perpendicular to the direction of **J**. It is interesting that $\rho(\theta)$ shows two different behaviors when the lattice strain is being increased in the LCMO/LAO and LCMO/STO films. The fits to the data for all the LCMO/LAO films and the 150 nm thick LCMO/STO film are in a very good agreement with the theoretical expression. However, this expression fails to describe the data when the thickness of the LCMO/STO films is reduced to below 15 nm. The angular dependence of the resistivity at the AMR peak's temperature measured in different applied fields can be seen clearly in the polar plot in Fig. 10.3. The response of the ultra thin LCMO/STO film to the direction of the applied field corresponds to the largest value of the AMR ever reported in the literature for any ferromagnetic material, including manganites.

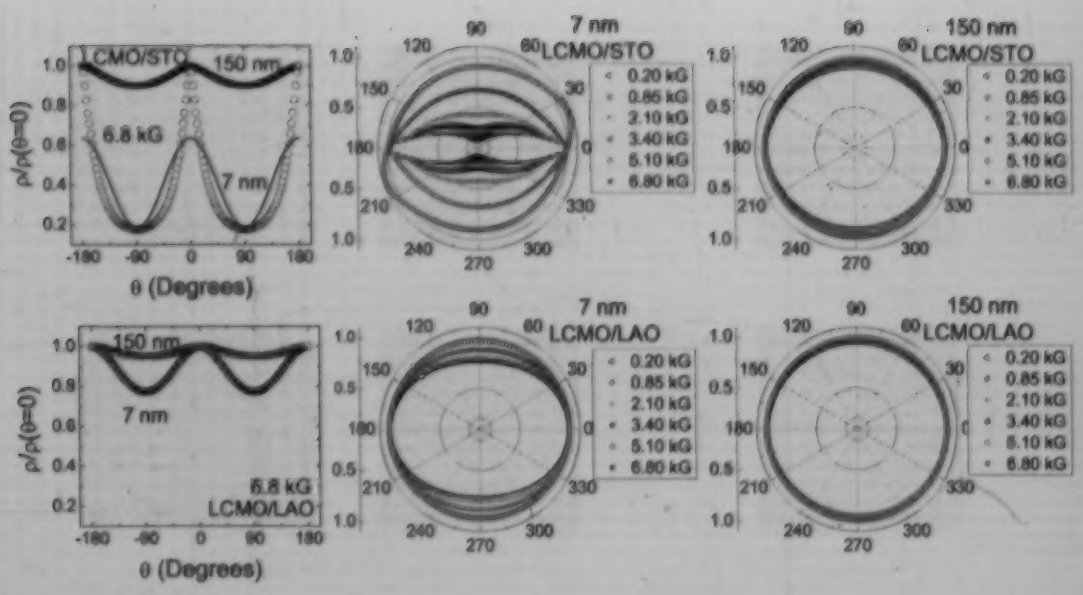

Figure 10.3: The angular dependence of the normalized resistivity at the AMR peak's maximum temperature measured in the 7 and 150 nm thick films. The solid lines are the fits to the data (see text); The corresponding polar plots of the angular dependence of the normalized resistivity at the AMR peak's maximum temperature, measured for different applied fields.

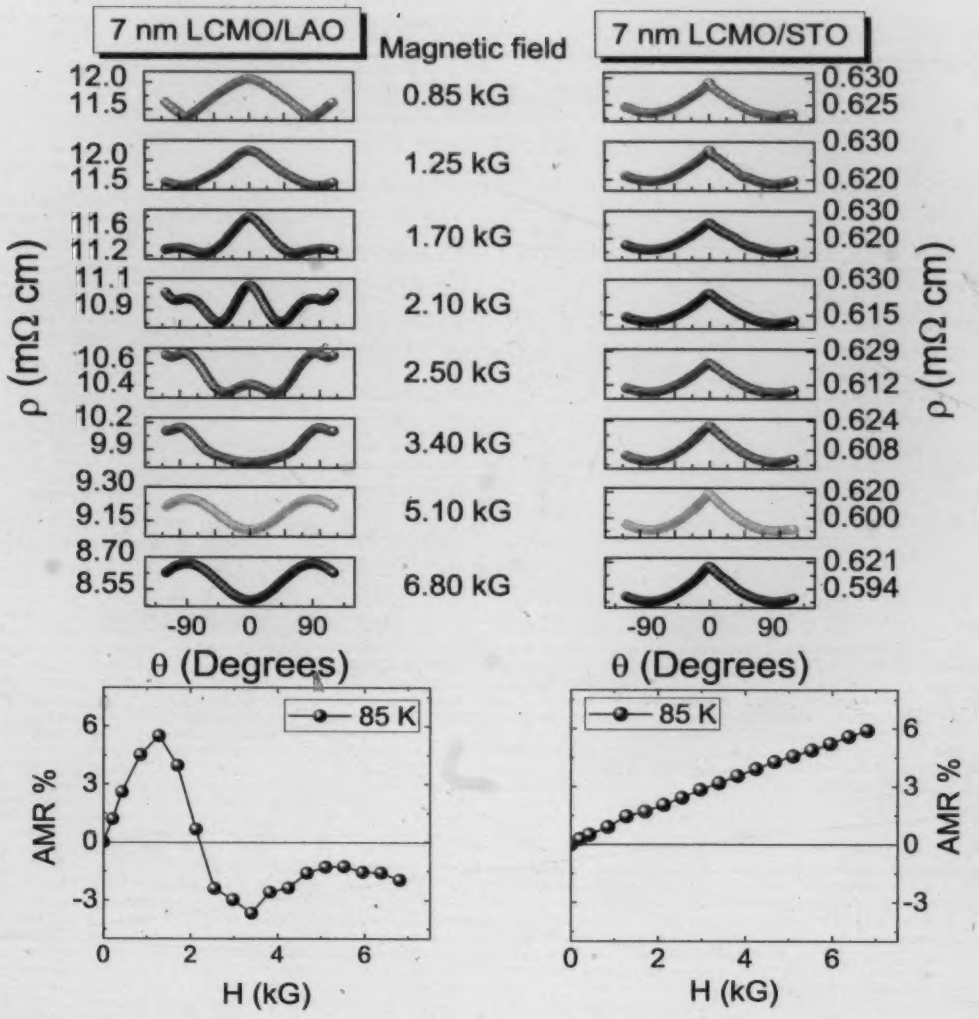

Figure 10.4: The angular dependence of the resistivity measured at 85 K in the 7 nm thick LCMO/LAO and LCMO/STO films; The corresponding dependence of the AMR on the applied field.

At relatively low temperatures, well below that of the MIT, the AMR was found to exhibit an unusual behavior. The low field AMR of the ultra thin films of LCMO/STO and LCMO/LAO increases in comparison to that of the thicker films. But most interestingly, when a magnetic field is increased, the AMR flips and changes sign in the ultra thin films of LCMO/LAO (see Fig. 10.4 (a)), while in the ultra thin films of LCMO/STO only a monotonic increase of the AMR with an increasing field is observed (see Fig. 10.4 (b)). The flip of the anisotropy was observed in all LCMO/LAO films with thickness less than 15 nm. This phenomenon is found to be temperature and field induced; the flip occurs when the temperature is reduced to that well below the MIT and the applied field exceeds 2 kG (see Fig. 10.4 (c)). The process of the change of sign occurs gradually, i.e. the $\cos^2(\theta)$ dependence is slowly transformed into the $\sin^2(\theta)$ one as the field is increased.

We now discuss the mechanism responsible for the dramatic effects of lattice strain on the AMR: A recent study explains an increase of the AMR with a decreasing thickness in terms of the Lorentz force-induced reduction of conductivity in the LCMO/LAO films.[5] An increased epitaxial strain in ultra thin films is expected to modify the electronic phase separation between the metallic and insulating phases in the film. Since the Lorentz force is expected to bend the trajectories of the charge carriers this should lower the conductivity and increase the AMR. In order to test this hypothesis, we measured the AMR for a different configuration where the field **H** is always perpendicular to the direction of the current **J**. In this case the Lorentz force is always acting on the charge carriers and is independent of the direction of **H** which is applied parallel and perpendicular to the c-axis. The AMR reported in these studies has been measured for a configuration with the field applied parallel to the current (no Lorentz force) and perpendicular to the current (the maximum Lorentz force). We have found that the magnitudes of both AMR's are very close to each other, which suggests that the Lorentz force by itself is not sufficient to explain the origin of the AMR in these films.

The most traditional explanation of AMR in ferromagnetic metals considers the

spin-orbit coupling and the anisotropic scattering rate of the charge carriers.[11, 12] According to these theories the magnitude of the AMR is proportional to the magnetization. Therefore the AMR is zero above the Curie temperature (T_c), but increases linearly with a decreasing temperature below T_c. This is not the case in manganites where the AMR has a peak in the vicinity of the MIT and T_c and persists even in the paramagnetic region (see Fig. 10.2). According to some theories of the spin-orbit interaction in ferromagnetic metals, the angular dependence of resistivity should follow the $\cos^2(\theta)$ dependence.[7] This is however not the case for some films, such as the biaxially tensile (extrinsically) strained LCMO/STO manganite films (see Fig. 10.2 (a) and (b)). The very large AMR values observed in these films could also be obtained intrinsically in a layered manganite of composition $La_{1.2}Sr_{1.8}Mn_2O_7$, where the AMR is of the order of 140%. We attribute this AMR to the similar orbital state in both materials.[16]

The observed change in sign of the AMR in the ultra thin LCMO/LAO samples (which exhibit a compressive negative strain in the film's plane) at low temperatures is another unexpected effect of the lattice strain. Surprisingly this phenomena only shows up in films grown on LAO substrates. We also observe this phenomena for $La_{0.8}Sr_{0.2}MnO_3$, a manganite which has a similar lattice constant to LCMO. However, the AMR does not change sign in films grown on STO, MgO and YSZ substrates, where a tensile in-plane strain (a positive strain in the film's plane) is expected. This suggests that the observation or non-observation of the sign-effect is associated with the strain state of the film. The θ=90^o shift in the angular dependence of the resistivity in the film could be attributed to a strain-induced rotation of the direction of the easy axis magnetization.

10.3 Summary and conclusions

In summary we have shown that depending on the strain-driven orbital state, the AMR in manganites could be enhanced dramatically. This AMR is much larger than

in ferromagnetic metals, where its magnitude is only of the order of a few percent. Surprisingly, at temperatures far below the MIT, the AMR in LCMO/LAO also flips and changes sign in contrast to LCMO/STO films. Current theories of AMR in ferromagnetic materials cannot explain the origin of the AMR in manganites. These results may be of interest to researchers developing manganite-film based magnetic devices and those working on theories of the AMR.

The work was supported by the Natural Sciences and Engineering Research Council.

Bibliography

[1] T. Jungwirth, J. Sinova, J. Masek, J. Kuera, A. H. MacDonald, *Reviews of Modern Physics*, **78**, 809 (2006).

[2] S. M. Thompson, *J. Phys. D: Appl. Phys.* **41**, 093001 (2008).

[3] E. Gerstner, *Nature Physics*, **3**, 754 (2007).

[4] E. Dagotto, *Science* **309**, 257 (2005).

[5] A. S. Alexandrov and A. M. Bratkovsky, *Phys. Rev. Lett.*, **82**, 141 (1999).

[6] Y. Tokura, N. Nagaosa, Science **288**, 462 (2000); Y. Okimoto, Y. Konishi, M. Izumi, T. Manako, M. Kawasaki and Y. Tokura, *Journal of the Physical Society of Japan*, **71**, 613 (2002).

[7] T. R. McGuire and A. R. I. Potter, *IEEE Transactions on on magnetics* **MAG-11**, 1018 (1975)

[8] J. O. Donnell, J. N. Eckstein, and M. S. Rzchowski, *Appl. Phys. Lett.* **76**, 218 (2000); J. N. Eckstein, I. Bozovic, J. O. Donnell, M. Onellion, and M. S. Rzchowski, *Appl. Phys. Lett.* **69**, 1312 (1996); H. S. Wang, Qi Li, Kai Liu, and C. L. Chien, *Appl. Phys. Lett.* **74**, 2212 (1999); I. C. Infante, V. Laukhin, F. Sanchez, J. Fontcuberta, O. Melnikov, O. Yu Gorbenko, and A. R. Kaul, *J. Appl. Phys.* **99**, 08C502 (2006);M. Ziese, *Phys. Rev. B*, **62**, 1044 (2000).

[9] B. I Belevtsev, V. B. Krasovitsky, D. G. Naugle, K. D. D. Rathnayaka, A. Parasiris, S. R. Surthi, R. K. Pandey, M. A. Rom, *Phys. Stat. Sol. (a)* **188**, 1187 (2001).

[10] M. Egilmez, R. Patterson, K.H. Chow, and J. Jung, Appl. Phys. Lett. **90**, 232506 (2007).

[11] P. A. Stampe, H. P. Kunkel, Z. Wang, and G. Williams, *Phys. Rev. B*, **52**, 335 (1995).

[12] A. P Malozemoff, *Phys. Rev. B*, **34**, 1853 (1986).

[13] J. ODonnell, M. Onellion, and M. S. Rzchowski, J. N. Eckstein and I. Bozovic, *Phys. Rev. B*, **55**, 5873 (1997).

Chapter 11

Lattice-strain control of magneto-resistivity and magneto-resistive anisotropy induced by ion-beam-milling in $La_{0.65}Ca_{0.35}MnO_3$ films near the metal-insulator transition

11.1 Introduction

The hole doped perovskite manganites are of great interest due to the wide range of different electronic, magnetic and structural properties that determine their applicability as magnetic devices.[1] Many of the remarkable properties of manganites such as the colossal magneto-resistance (CMR) effect arise from strong electron correlations.[2, 3] The existence of a variety of competing interactions creates a subtle equilibrium which defines the ground state of these materials. The lattice strain and disorder may drastically affect the balance of the competing energies, which conse-

quently leads to a significant change in the bulk properties of manganites.[4, 5, 6] In particular, this is true for the highly strained ultra thin oxygen-annealed manganite films of thickness less than 20 nm, where both the magneto-resistivity (MR) and the magneto-resistive anisotropy (AMR) are much higher than those of partially relaxed or fully relaxed thick films.[4, 7] This suggests that the enhancement of both the MR and AMR in these films is being caused by the same mechanism, namely the lattice strain induced by the elastic misfit between the film and the substrate (the epitaxial strain). The lattice strain could be responsible for the electronic phase separation occurring near the substrate-film interface as detected by NMR experiments[7]. The lattice strain could be changed by a controlled introduction of defects, which would allow for a better understanding of the nature of the MR and the AMR in these films and how these properties can be modified. This is important from both basic and applied science perspectives.

In this chapter we report studies of the changes in the low-field magneto-transport properties of the thin manganite films that were induced by ion-beam-milling. This technique introduces large concentrations of point defects (including oxygen vacancies) into the film[9] and also cause crystal deformation and lattice strain.The magneto-transport properties of the ion-milled films were then compared to those measured in the as-grown oxygen-annealed thin films that have never been subjected to the ion-beam-milling process. The investigations suggest that in contrast to the ultra-thin (of thickness less than 20 nm) as-grown films where an increase of both the MR and the AMR is determined by the epitaxial strain, the ion-beam-milling of the ultra-thin films causes point-defect-induced deformation leading to an increase of the MR and a reduction of the AMR. This implies that the ion-beam-milling could be effectively used to modify the MR and the AMR in the manganite films of thickness less than 20 nm.

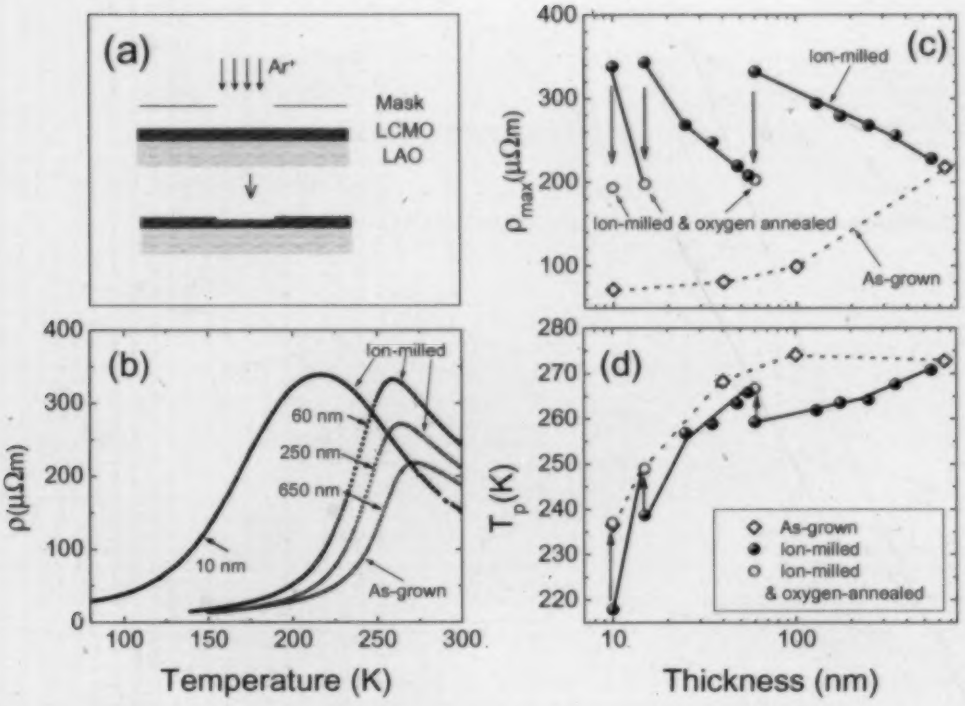

Figure 11.1: (a) Ion-beam-milling experimental set-up; (b) Temperature dependence of the resistivity in a zero magnetic field for the ion-beam-milled $La_{0.65}Ca_{0.35}MnO_3$ films of thicknesses between 10 and 650 nm; (c) Thickness dependence of the resistivity at the resistive peak; (d) Thickness dependence of the metal-insulator transition temperature (T_p). The lines are guides for the eye.

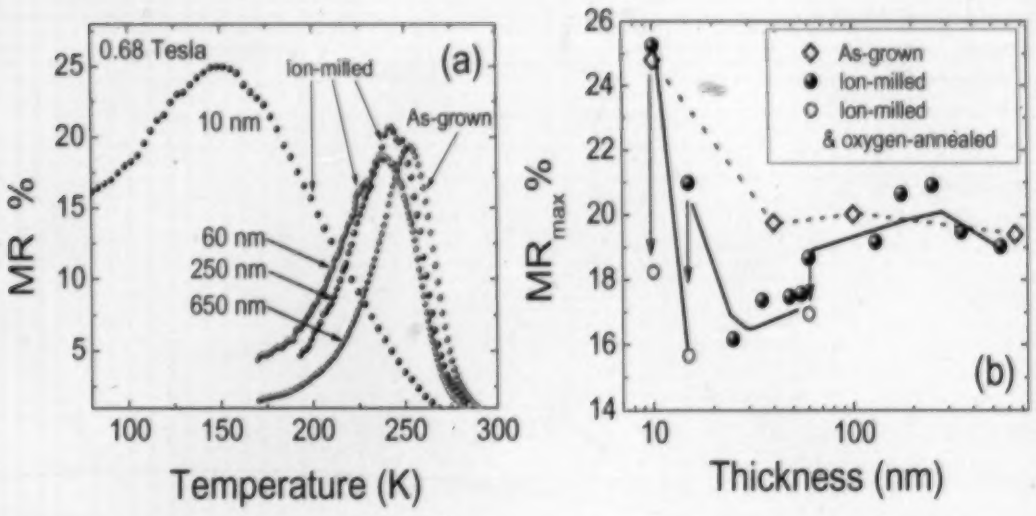

Figure 11.2: Magneto-resistivity (MR) measured in a magnetic field of 0.68 T for the ion-beam-milled films. (b) Thickness dependence of the maximum values of the MR. The lines are guides for-the eye.

11.2 Results and discussion

Studies of the low-field magneto-transport properties were carried out on an ion-beam milled epitaxial $La_{0.65}Ca_{0.35}MnO_3$ (LCMO) film grown on a $LaAlO_3$ substrate using dc-magnetron sputtering.[4] The $LaAlO_3$ substrates are twinned, and hence twinned domains (islands) are also formed in the LCMO films during the growth process. This suppresses the net effect of the in-plane magneto-crystalline anisotropy on the measured magneto-resistivity. The magneto-resistivity measurements were carried out on a strip about 5 mm long and 1 mm wide. Four silver contacts were deposited on the film using an rf-magnetron sputtering technique. The distance between the voltage contacts was 1 mm. The area of the film between the voltage contacts was bombarded with 2.5 keV Ar ions at a constant power of 5 W (see Fig. 11.1(a)). The film's temperature during the ion-beam-milling did not exceed 60^oC.

The ion-beam-milling was performed several times, starting with an as-grown

film with a thickness of 650 nm. After each ion-beam-milling step, the temperature dependence of the fundamental transport parameters associated with CMR materials, ie. the magneto-resistivity and the magneto-resistive anisotropy, were measured at temperatures near the metal-insulator transition (MIT). The properties of the ion-beam-milled film were compared to those of the as-grown oxygen-annealed films of $La_{0.65}Ca_{0.35}MnO_3$ with the same thickness. In order to investigate the oxygen related changes that arise from ion bombardment, the film, after being subjected to several steps of ion-beam-milling, was annealed at 650^oC in pure oxygen for several hours.

Fig. 11.1(b) shows the temperature dependence of the resistivity near the MIT for the as-grown 650 nm thick film and the 250, 60 and 10 nm thick films thinned down by the ion-beam-milling process. As the film is made progressively t nner, we observe a monotonic increase of the magnitude (ρ_{max}) and the width of the resistive peak (see Figs. 11.1(b) and (c)) This is also accompanied by a steady decrease of the metal-insulator transition temperature (T_p) (see Fig. 11.1(d)). As shown in Figs. 11.1(c) and (d), it was found that the resistivity of the ion-beam-milled film decreased and T_p increased, after each annealing step in oxygen.

The temperature dependence of the magneto-resistivity MR=[(ρ(0)-$\rho(H)$)/ρ(0)], where ρ(0) and $\rho(H)$ are resistivities in a zero field and in a finite field **H** applied parallel to the current, respectively, is shown in Fig. 11.2 for the ion-beam-milled film at 0.68 T. Reduction of the thickness of the film by the ion-beam-milling from 25 nm down to 10 nm leads to an increase of the MR from 16 to 25%. In general, oxygen annealing causes a decrease of the MR in the ion-beam-milled films.

The anisotropic magneto-resistance (AMR) appears to be an excellent probe of the crystallographic quality of the epitaxial films, since this property is absent in poly-crystalline or amorphous manganite samples. We performed the measurements of the in-plane and the out-of-plane AMR on all ion-milled films and as-grown films of the same thickness. The AMR indicates the relative changes in the resistivity as the direction between the applied magnetic field **H** and the direction of the current **J** changes. The in-plane AMR is defined as $AMR^{in}=(\rho_{\parallel}^{in} - \rho_{\perp}^{in})/\rho_o$, where $\rho_{\parallel}^{in}$ and $\rho_{\perp}^{in}$

are the resistivities of the film for a magnetic field **H** that is located in the plane of the film and is oriented parallel and perpendicular to the current, respectively, and ρ_o is the resistivity in zero applied field. Note that the superscript "in" indicates that **H** is in the plane of the film i.e., *ab* plane, while the subscript indicates the direction of **H** with respect to **J**. The out-of-plane AMR is defined as $AMR^{out}=(\rho_{\parallel}^{in} - \rho_{\perp}^{out})/\rho_o$. The $\rho_{\perp}^{out}$ denotes the resistivity measured when **H** is applied perpendicular to both the films plane and the direction of the transport current. The temperature dependence of the AMR^{out} at 0.21 T and 0.68 T is plotted in Fig. 11.3. For thicknesses smaller than 50 nm, both AMR^{out} and AMR^{in} decrease with a decreasing thickness of the ion-beam-milled film. This is opposite to the behavior of the as-grown oxygen-annealed films where both AMR^{out} and AMR^{in} increase with a decreasing thickness. Annealing of the ion-beam-milled film in oxygen does not change its anisotropy.

The differences between the transport properties of the ion-beam-milled and the as-grown oxygen-annealed films are more evident if the film thickness is below 60 nm (see Fig. 11.3). The temperature dependence of the resistivity, the magneto-resistivity and the magneto-resistive anisotropy of the as-grown and both the un-annealed and oxygen-annealed ion-beam milled films is shown in Fig. 11.4 for the 10 and 60 nm thick films.

According to the studies of metal-oxide substrates such as $LaAlO_3$, a bombardment with 0.5 keV Ar ions produces a deformed surface layer a few nanometers thick.[9] The effect of the damaged surface layer on the physical properties of the material should be more pronounced if the thickness of the film is very small. The comparison of the magneto-transport properties of the ion-beam-milled LCMO films with those of the as-grown oxygen-annealed LCMO films, reveals that the MR of the 10 nm thick ion-beam-milled films at the MIT is the same or higher than the MR of the as-grown fully oxygenated films of the same thickness, which is thought to originate from the elastic misfit between the film and the substrate (see Fig. 11.2 (b)).[4] Annealing of the 10 nm thick ion-beam-milled film in oxygen leads to a suppression of

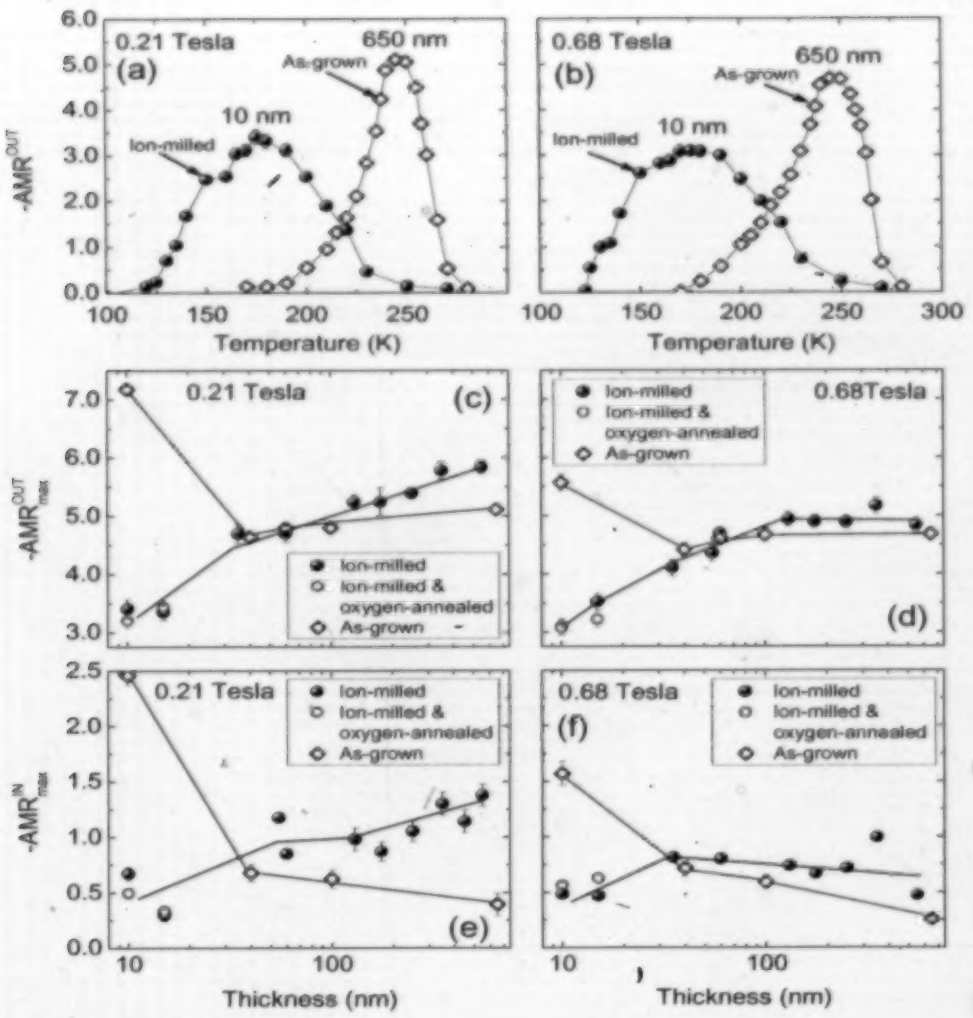

Figure 11.3: [(a)-(b)] Temperature dependence of the magneto-resistive anisotropy AMR^{out} for the ion-beam-milled films in a field of 0.21 and 0.68 T, respectively. Thickness dependence of the maximum value of the AMR^{out} [(c)-(d)], and the AMR^{in} [(e)-(f)] for the ion-beam-milled (both un-annealed and oxygen-annealed) films and the as-grown films in a field of 0.21 and 0.68 T, respectively. The lines are guides for the eye.

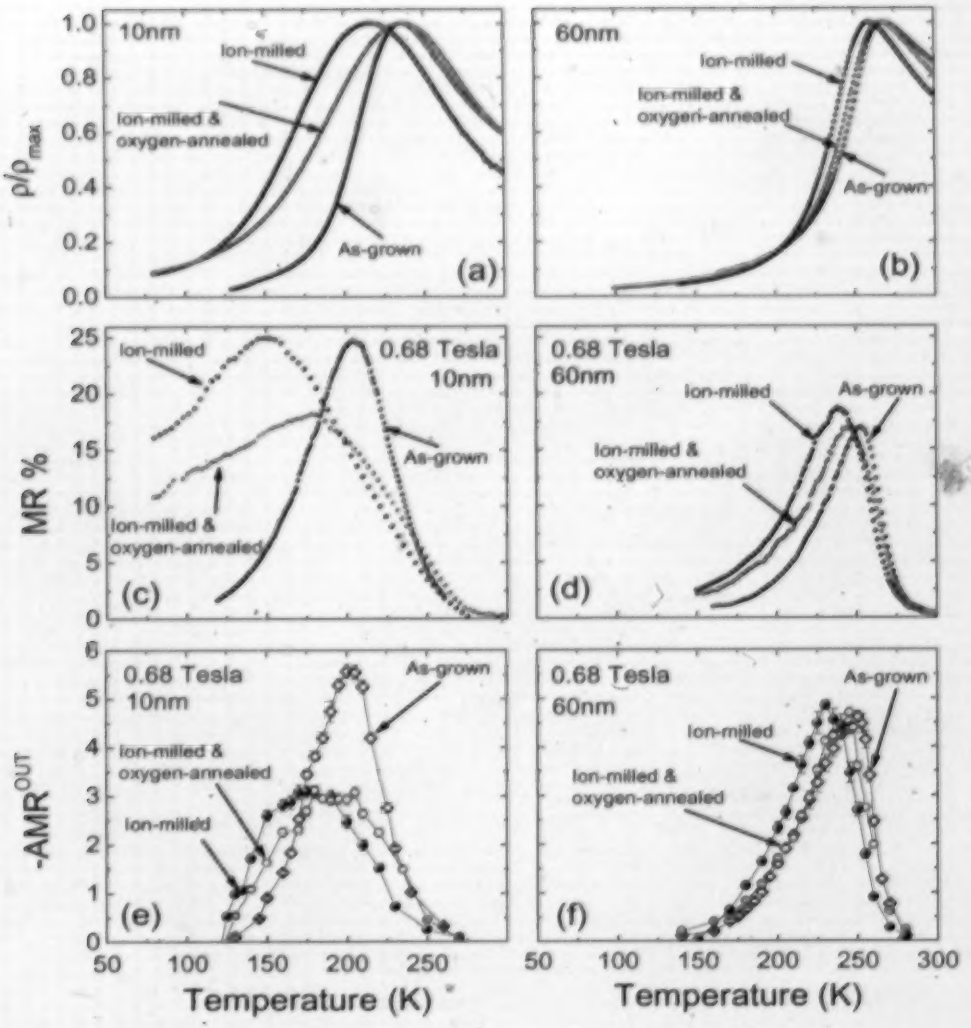

Figure 11.4: Temperature dependence of the normalized resistivity [(a)-(b)], in a zero field measured for the 10 and 60 nm thick ion-beam-milled (both un-annealed and oxygen-annealed) films and the as-grown films. Temperature dependence of the magneto-resistivity (MR) [(c)-(d)] and the the magneto-resistive anisotropy AMR^{out} [(e)-(f)] of the 10 and 60 nm thick ion-beam-milled (both un-annealed and oxygen-annealed) films and the as-grown films in a field of 0.68 T.

the MR peak at the MIT. This suggests that the increase of the MR in the films upon ion milling is via a mechanism that is different from that in the as-grown material, i.e. not due to elastic misfit. Instead, we believe it originates from the large concentration of point defects, including oxygen vacancies, that are introduced into the film when it is being ion-milled. Evidence for this is as follows: the peak in the temperature dependence of the MR of the 10 nm thick ion-beam-milled film is much broader than that in the as-grown film. It also displays a prominent "shoulder" that extends down to low temperatures (see Fig. 11.4). Such asymmetric MR peaks have been observed in bulk disordered samples[10, 11, 12] indicating that the 10 nm thick film is highly disordered. It has been well established that there is a local spin disorder around lattice defects in manganites and a ferromagnetic alignment of these spins by a very small magnetic field could give rise to an enhanced spin polarized transport across the defects.[10] This mechanism has been thought to be responsible for the enhancement of the low field and low temperature MR in the disordered manganite samples and it is, therefore, likely to explain the behavior of the MR in our ion-beam-milled films. Since the annealing in oxygen reduces the magnitude of the MR also at temperatures well below the MIT, oxygen vacancies are likely to be at least partially responsible for the formation of the low temperature "shoulder" in the MR.

It is interesting that in spite of the presence of lattice disorder in the 10 nm thick ion-milled films, as documented by the behavior of the MR, these films still exhibit both the out-of-plane and in-plane AMR peaks at the MIT. However, the magnitudes are smaller than the corresponding ones for the as-grown 10 nm thick oxygen-annealed films (whose large AMR has been interpreted as due to epitaxial strain[4](see Fig. 11.3)). Oxygen annealing has very little effect on the AMR in the ion-beam-milled films. This suggests that the ion-beam-milling produces a mosaic-type deformation which does not completely crystal structure of the film, and hence the AMR is partially reduced.

11.3 Summary and conclusions

In summary, we have studied the magneto-transport properties of the ion-beam-milled high quality epitaxial $La_{0.65}Ca_{0.35}MnO_3$ film grown on $LaAlO_3$ substrate. The film thickness has been reduced gradually down to 10 nm with 2.5 keV Ar ion-beam-milling. The low field properties of the ion-beam-milled film have been compared to those of the as-grown $La_{0.65}Ca_{0.35}MnO_3$ films of the same thickness. The thickness dependence of the magneto-transport properties of the ion-beam-milled films is dramatically different from those of the as-grown oxygen-annealed films especially for films of thickness less than 20 nm. In contrast to the as-grown films, where an increase of both the MR and the AMR appears to be the result of the epitaxial strain, in the ion-beam-milled films point-defect-induced deformation seems to be responsible for both an increase of the MR and a decrease of the AMR. This should allow one to exhibit more control of the MR and the AMR of LCMO films by the ion-beam-milling.

Bibliography

[1] M. B. Salamon and M. Jaime, *Rev. Mod. Phys.* **73**, 583 (2001).

[2] A. S. Alexandrov and A. M. Bratkovsky, *Phys. Rev. Lett.* **82**, 141 (1999).

[3] E. Dagotto, *Science* **309**, 257 (2005).

[4] M. Egilmez, R. Patterson, K. H. Chow, and J. Jung, *Appl. Phys. Lett.* **90**, 232506 (2007).

[5] M. Ziese, *Phys. Rev. B* **62**, 1044 (2000).

[6] R. A. Rao, D. Lavric, T. K. Nath, C. B. Eom, L. Wu, and F. Tsui, *Appl. Phys. Lett.* **73**, 3294 (1998).

[7] J. Fontcuberta, I. C. Infante, V. Laukhin, F. Sanchez, M. Wojcik and E. Jedryka, *J. Appl. Phys.* **99**, 08A701 (2006).

[8] M. Bibes, L. Balcells, S. Valencia, J. Fontcuberta, M. Wojcik, E. Jedryka and S. Nadolski, *Phys. Rev. Lett.* **87**, 067210 (2001).

[9] I. Takeuchi, R. P. Sharma, S. Choopun, C. J. Lobb and T. Venkatesan, *Appl. Phys. Lett.* **70**, 3098 (1997).

[10] H. Y. Hwang, S. W. Cheong, N. P. Ong and B. Batlogg, *Phys. Rev. Lett.* **77**, 2041 (1996).

[11] M. Egilmez, K. H. Chow, J. Jung, Z. Salman, *Appl. Phys. Lett.* **90**, 162508 (2007).

[12] P. Dey, T. K. Nath, *Phys. Rev. B* **73**, 214425 (2006).

[13] R. Patterson, C. Ozeroff, K. H. Chow, and J. Jung, *Appl. Phys. Lett.* **88**, 172509 (2006)..

Chapter 12

Percolative model of the effect of disorder on the resistive peak broadening in $La_{2/3}Ca_{1/3}MnO_3$ near the metal-insulator transition

12.1 Introduction

Manganites such as $RE_{1-x}A_xMnO_3$ (where RE and A are the rare earth and the alkaline elements, respectively) are members of complex materials where the electron correlations play a crucial role; they exhibit metal-insulator transitions (MIT)[1, 3] and phase separation.[3] Tunneling experiments[4] and Monte-Carlo[5] simulations suggest that the ground state of manganites is intrinsically inhomogeneous due to the strong tendencies toward phase separation, typically involving ferromagnetic metallic and antiferromagnetic charge and orbital ordered insulating domains. Disorder is an important inherent element of the colossal magneto-resistance (CMR) effect. It could be introduced into the manganite system either intrinsically or extrinsically. The former is introduced by chemical substitution and is often referred to as an "unavoidable disorder". The latter is realized by introducing the lattice defects such

Table 12.1: Parameters that describe LCMO crystal and films: t is the film thickness, T_p is the metal-insulator transition temperature, ρ_0 is the residual resistivity, ρ_2 and ρ_5 are the electron-electron scattering and the electron-phonon scattering coefficients, respectively, b is the polaronic coefficient, Δ is the bipolaron binding energy, and Γ is the width of the Gaussian distribution. The fitting parameters errors are around 1%. IM corresponds to ion milled.

Sample	T_p	ρ_0	ρ_2	ρ_5	b	Δ	Γ
	(K)	(Ωcm)	$(\Omega cm K^{-2})$	$(\Omega cm K^{-5})$	$(\Omega cm K^{-1})$	(meV)	(K)
Sing. crys.	242	0.0011	$5.7\ 10^{-9}$	$1.4\ 10^{-16}$	$2.0\ 10^{-6}$	188	5±1
Film-650nm	273	0.0010	$5.9\ 10^{-9}$	$5.4\ 10^{-15}$	$4.8\ 10^{-6}$	135	20±3
Film-10nm	236	0.0001	$8.5\ 10^{-9}$	$2.3\ 10^{-15}$	$0.5\ 10^{-6}$	170	30±4
IM film-10nm	235	0.0012	$7.3\ 10^{-8}$	$3.5\ 10^{-14}$	$1.2\ 10^{-6}$	182	80±10

as grain boundaries or point defects, or lattice strain into the manganite system.

Experiments[6] and theoretical models[5, 6, 9] have established that the disorder causes dramatic changes of the physical properties of manganites. For example the sharpness of the resistivity peak is significantly affected by the lattice disorder. In particular, the metal-insulator transition is very sharp in disorder-free single crystals of manganites, but becomes very broad in disordered samples. [5] Although extensive experimental studies of the broadening of the resistive peak at the MIT due to disorder have been performed in manganites, the origin and the modeling of the broadening have not been fully investigated. Recent models suggest that the resistive peak and its broadening at the metal-insulator transition is a result of the phase co-existence and the competition between insulating and metallic phases with different magnetic properties.[2]

12.2 Results and discussion

In this chapter, we report studies of the nature of the resistive peak broadening in disordered manganites using a simple percolation model based on Alexandrov *et al.*.[9] The disorder is assumed to induce a large variation of phases where each phase has a different transition temperature. In the percolation model we assume that the distribution of transition temperatures is Gaussian and that its width, which increases with increasing disorder, determines the broadening of the resistive peak. The assumption of a Gaussian distribution of the transition temperatures allows one to estimate fractions (ν) and (1-ν) of the metallic and the insulating phases in the material, respectively. The total resistivity of the system could then be calculated from the harmonic average $\rho = \rho_i^{1-\nu}\rho_m^{\nu}$ using a simple percolation model[12] of a manganite, where metallic clusters with resistivity ρ_m are embedded in an insulating matrix of resistivity ρ_i. We applied this model to compute resistivities at the metal insulator transition of a clean single crystal (where only "unavoidable disorder" is assumed to be present) and disordered thin films of $La_{1-x}Ca_xMnO_3$ (LCMO) near $x = 1/3$.

The temperature dependence of the resistivity ρ(T) of a typical LCMO film (Fig. 12.1 (a)) shows that close to the MIT ρ(T) deviates from that of a metal and an insulator at low and high temperatures, respectively. In the transition region the metal and the insulator co-exist. The temperature dependence of the resistivity and that of the temperature coefficient of resistivity TCR = $(1/\rho)(d\rho/dT)$ for a LCMO single crystal and LCMO films are shown in Fig. 12.1 (b)-(e). An increase of the width of the resistive peak and TCR is caused by strain or disorder in the system. The boundaries of the mixed metal-insulator regions mark temperatures at which the temperature dependence of the resistivity deviates from that of a metal or that of an insulator at temperatures below or above the peak, respectively. An increase in the width of the mixed region is attributed to an increase of the lattice strain or disorder in the system.

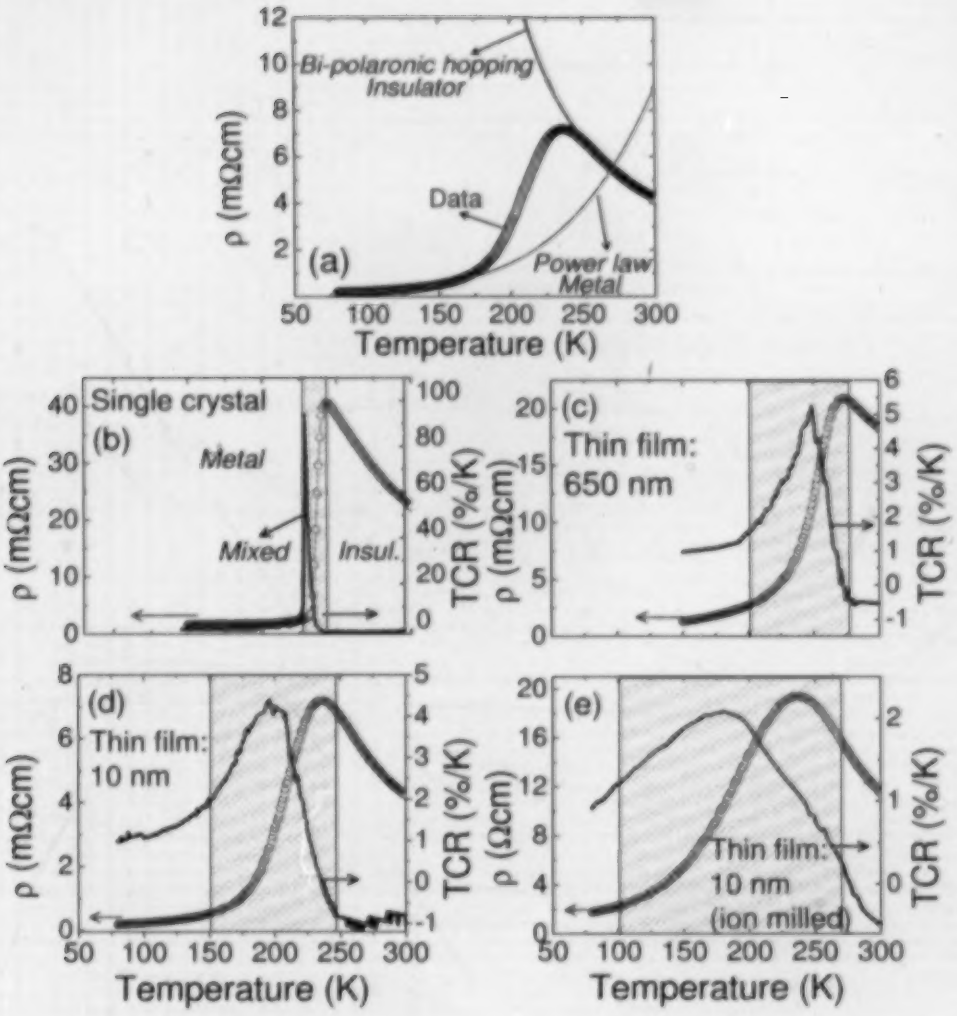

Figure 12.1: (a) Temperature dependence of generic LCMO data. Solid lines indicate the extrapolated fits at low temperatures to a power law and at high temperatures to bi-polaronic hopping model. (b)-(e) Temperature dependence of resistivity ρ measured in zero magnetic field, and the temperature coefficient of resistance (TCR) for LCMO crystal and films. The resistivity data of single crystal sample was taken from the Tokura.[16] The shaded area marks the mixed metal-insulator state.

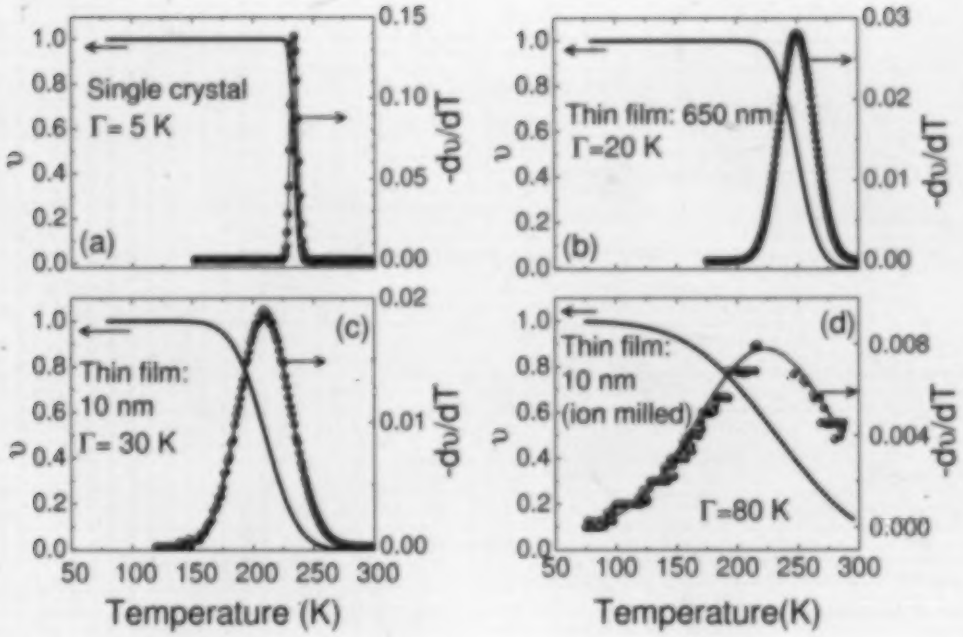

Figure 12.2: Temperature dependence of the fraction ν of the metallic phase and the corresponding Gaussian distribution of transition temperatures in LCMO crystal and films.

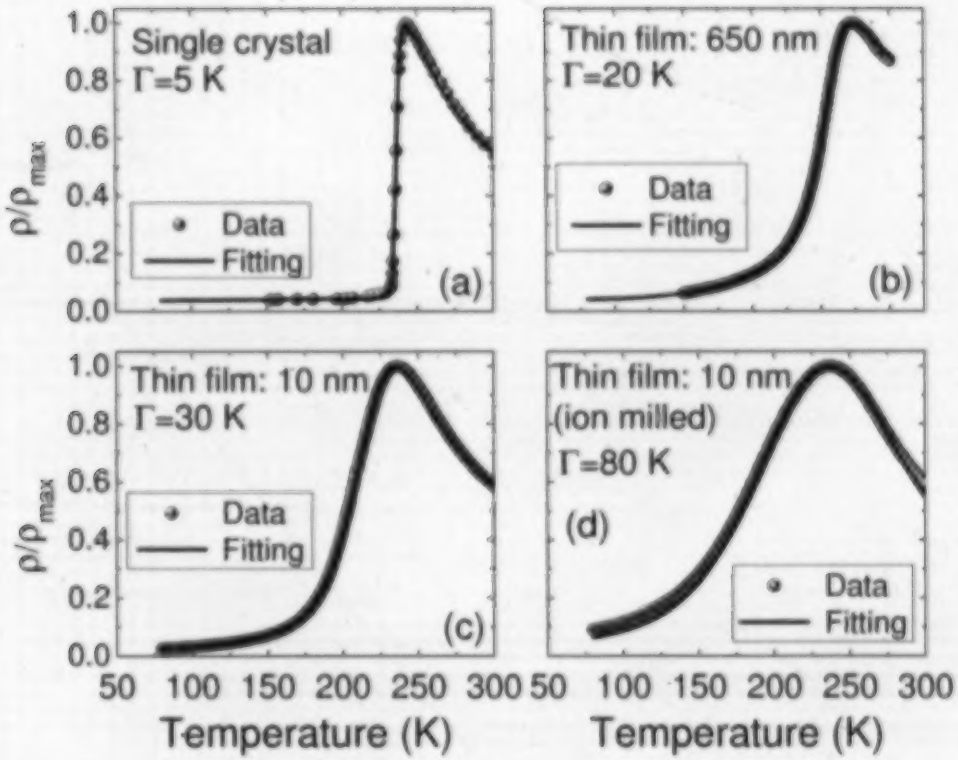

Figure 12.3: Temperature dependence of resistivity ρ measured in zero magnetic field. The resistivity was normalized to that at the peak's maximum. The solid lines represent the fits to the data.

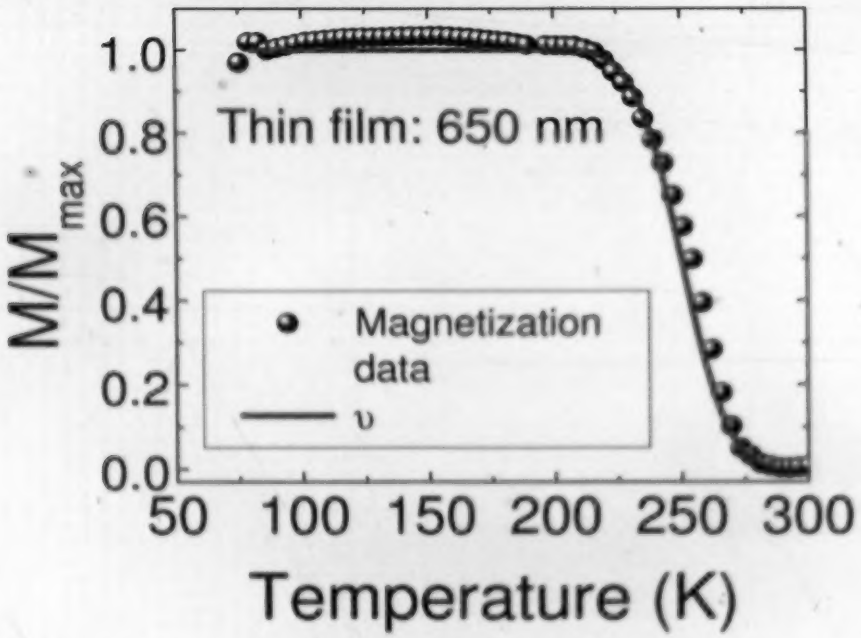

Figure 12.4: Temperature dependence of the reduced magnetization M(T)/M_{max} and of the fraction ν of the metallic phase in a 650 nm thick film.

The observed changes in the width are attributed to a distribution of transition temperatures induced by the lattice disorder. Making the reasonable assumption that this distribution of temperatures around the peak temperature T_p is Gaussian allows one to estimate the change of the relative fraction of the metallic phase near the metal-insulator transition(see Eq. 12.1).[9, 13]

$$\nu(T) = (1/2)erfc[(T - T_p)/\Gamma] \tag{12.1}$$

Eq. 12.1 is a cumulative Gaussian distribution function where

$$erfc(y) = \sqrt{1/2\pi} \int_0^\infty exp(-y^2)dy \tag{12.2}$$

and Γ is the width of the Gaussian distribution.[14] Notice that this assumption is valid if at temperatures below T_p - Γ (the low temperature side of the Gaussian

distribution) the manganite is fully metallic (i.e. $\nu(T) = 1$), and above $T_p + \Gamma$ (the high temperature side of the Gaussian distribution) it is fully insulating (i.e. $\nu(T) = 0$). The mixed region over a temperature range of T_p - $\Gamma \leq T \leq T_p + \Gamma$ defines the sharpness of the metal- insulator transition. The estimated temperature dependence of the metallic fractions is plotted in Fig 12.2. Increasing disorder or strain increases the width of the Gaussian/normal distribution. This is in agreement with recent Monte-Carlo simulations[15] which revealed that in a percolative system the distribution of transition temperatures is Gaussian, and its width increases with an increasing disorder.

Kabanov et al.[12] developed a model of the resistivity of a regular inhomogeneous two component isotropic medium in which the droplets of phase (a) with resistivity ρ_a are embedded in phase (b) of resistivity ρ_b. The resultant resistivity is given by $\rho = \rho_b^{1-\nu}\,\rho_a^{\nu}$, where ν is the fraction of phase (a). This expression could be also used if the ratio of phases (a) and (b) is temperature-dependent. The change of the resistivity due to the phase separation at the MIT in manganites could therefore be described by the equation $\rho(T) = \rho_i(T)^{1-\nu(T)}\rho_m(T)^{\nu(T)}$, where ν is the fraction of the metallic phase.

The results indicate that the temperature dependence of the metallic resistivity well below the MIT could be fit to: $\rho_m(T) = \rho_0 + \rho_2 T^2 + \rho_5 T^5$, where ρ_2 and ρ_5 are the electron-electron and the electron-phonon scattering coefficients, respectively, and ρ_0 is the residual resistivity.[9, 17] In this temperature range the disorder does not affect the temperature dependence of ρ_m, however it is responsible for the changes of coefficients ρ_0, ρ_2 and ρ_5 (see Table 12.1). At temperatures higher than the MIT where LCMO is a paramagnetic insulator the temperature dependence of the resistivity could be expressed as $\rho_i(T) = bT\exp(\Delta/2kT)$, where Δ is the bipolaron binding energy, b is a resistivity constant, and k is the Boltzmann's constant.[9] The values of the fitting parameters such as the bipolaron binding energies and the resistivity constant b are given in Table 12.1. Since the interpretation of the effect of disorder on parameters ρ_0, ρ_2, ρ_5, and b has been given in our previous report[18] (see Chapter

7), we will not discuss them again here.

We assume that the temperature dependence of the resistivity $\rho(T)$ is given by $\rho(T) = \rho_i(T)^{1-\nu(T)}\rho_m(T)^{\nu(T)}$ where the values of $\rho_i(T)$ and $\rho_m(T)$ at all temperatures, including the mixed region, are described by the parameters (ρ_0, ρ_2, ρ_5, b, and Δ) in Table 12.1. This enables us to fit the experimental data of each sample with Γ as the free parameter, i.e. via $\nu(T)$. Table I lists the fitted values of Γ. Note, as indicated in Figure 12.3, the simple percolation model produces generally good fits of the data. In a highly disordered sample (eg. 10 nm thick ion-milled LCMO film) the fits to the resistivity (see Fig 12.3 (d)) are poorer. A likely explanation is that the vast amount of disorder in the sample is changing the scattering mechanism. This could be possible because insulating clusters in this sample coexist even at temperatures far below the MIT (see Fig 12.2 (d)).

Regarding the value of Γ, the single crystal has a relatively small Γ of 5 K. Its value increases to 20 K in the 650 nm thick film and to 30 K in the 10 nm thick film. The epitaxial strain between the substrate and the film causes the broadening of the resistive peak[11, 20]. The epitaxial strain and correspondingly the broadening is very large in thin films of thickness $\ll$ 10 nm. Ion milling introduces additional disorder, such as point defects into thin films, causing very large broadening of the resistive peak and Γ of 80 K (see Fig 12.3 (d)). Such a large distribution of transition temperatures implies that over a very large temperature range the ion-milled film is in the mixed state formed by the co-existence of the metallic and insulating phases.

The temperature dependence of the fraction of the metallic phase in LCMO scales well with the measured temperature dependence of the reduced magnetization $M(T)/M_{max}$ (see Fig 12.4), indicating that our estimate of $\nu(T)$ is correct since the metallic and insulating resistivities correspond to those of the ferromagnetic metallic and paramagnetic insulating states of LCMO.

12.3 Summary and conclusions

In summary, we analyzed the origin of the disorder-induced resistive peak broadening in LCMO manganites at the MIT using a simple percolation model. The resisitivity around T_p in the LCMO crystal and films can be described by a Gaussian distribution of transition temperatures. The width of the Gaussian distribution, which defines the temperature range where the metallic and insulating clusters simultaneously exist, increases with an increasing lattice disorder. We calculated the temperature dependence of resistivity using the temperature dependence of the fraction of the metallic phase obtained from the Gaussian distribution. The results show a very good agreement with the experimental data for LCMO crystal and films, suggesting that the disorder induced multi-phase coexistence and the large distribution of transition temperatures contributes significantly to the resistive peak broadening in manganites.

Bibliography

[1] J. H. Van Santen and G. H. Jonker, *Physica*, **16**, 599 (1950); G. H. Jonker and J. H. Van Santen, *Physica*, **16**, 337 (1950).

[2] A. S. Alexandrov and A. M. Bratkovsky, *Phys. Rev. Lett.*, **82**, 141 (1999).

[3] E. O. Wollan and W. C. Koehler, *Phys. Rev.*, **100**, 545 (1955).

[4] M. Uehara, S. Mori, C. H. Chen, and S.W. Cheong, *Nature* **399**, 560 (1999).

[5] E. Dagotto, T. Hotta, A. Moreo, *Phys. Rep.* **344**, 1 (2001).

[6] D. Akahoshi, M. Uchida, Y. Tomioka, T. Arima, Y. Matsui, and Y. Tokura, *Phys. Rev. Lett.*, **90**, 177203 (2003).

[7] C. Sen, G. Alvarez, H. Alliaga, E. Dagotto, *Phys. Rev. B*, **73**, 224441 (2006).

[8] C. Sen, G. Alvarez, and E. Dagotto, *Phys. Rev. Lett.*, **98**, 127202 (2007).

[9] A. S. Alexandrov, A. M. Bratkovsky, and V. V. Kabanov, *Phys. Rev. Lett.*, **96**, 117003 (2006).

[10] M. Egilmez, K. H. Chow, J. Jung, and Z. Salman, *Appl. Phys. Lett.* **90**, 162508 (2007).

[11] E. Dagotto, *Science* **309**, 257 (2005).

[12] V. V. Kabanov, K. Zagar, and D. Mihailovic, *JETP* **100**, 715 (2005).

[13] For the samples which have large amount of disorder this expression could give the distribution around a temperature which turns out to be larger several degrees of Kelvin than experimental T_p. For accurate fits, the distribution should be adjusted around T_p.

[14] J. R. Taylor, *An introduction to error analysis*, 2nd ed. (University Science Books, Sausalito, California 1997), pp. 135-136.

[15] M. T. Mercaldo, J-Ch. Angles dAuriac, F. Igloi, *Phys. Rev. E* **73**, 026126 (2006)

[16] Y. Tokura, *Colossal magneto-resistive oxides*, 1st ed. (Gordon and Breach, Amsterdam, 2000), pp. 2-3.

[17] A. A. Abrikosov, *Fundamentals of the theory of metals* (North-Holland, Amsterdam, 1988), pp. 62.

[18] M. Egilmez, K. H. Chow, J. Jung, I. Fan, A. I. Mansour, and Z. Salman, *Appl. Phys. Lett.* **92**, 132505 (2008).

[19] M. Egilmez, R. Patterson, K. H. Chow, and J. Jung, *Appl. Phys. Lett.* **90**, 232506 (2007).

[20] M. Egilmez, A. I. Mansour, M. M. Saber, K. H. Chow, and J. Jung, *Appl. Phys. Lett.* **92**, 022501 (2008).

Chapter 13

Strain induced meta stable phases in $La_{0.65}Ca_{0.35}MnO_3$ films

13.1 Introduction

Manganites $R_{1-x}A_xMnO_{3-\delta}$ (where R and A are trivalent rare earth and divalent alkaline earth ions, respectively) continue to attract considerable scientific and technological attention, primarily because many of them exhibit colossal magnetoresistance (CMR). The manganites are good candidates for applications such as magnetic sensors[1], magnetic read heads, resistance switches[2], magnetostrictive devices[3] or infrared bolometers [1]. $R_{1-x}A_xMnO_3$ compounds exhibit a rich phase diagram whose transport and magnetic properties are strongly affected by a variety of physical factors. One of the most important of such factors is the lattice strain; experimentally it is evidenced that there is a strong interplay between lattice degrees of freedom and the electronic properties.[11] In this context thin films serve as an excellent playground for studies aimed at understanding the relation between the physical properties and the lattice distortions since in a film lattice distortion could be fine tuned with choice of substrate or film thickness.[5] In this chapter we show that strain associated with a lattice mismatched substrate can cause new electronic behavior, not found in bulk materials of the same chemical composition.

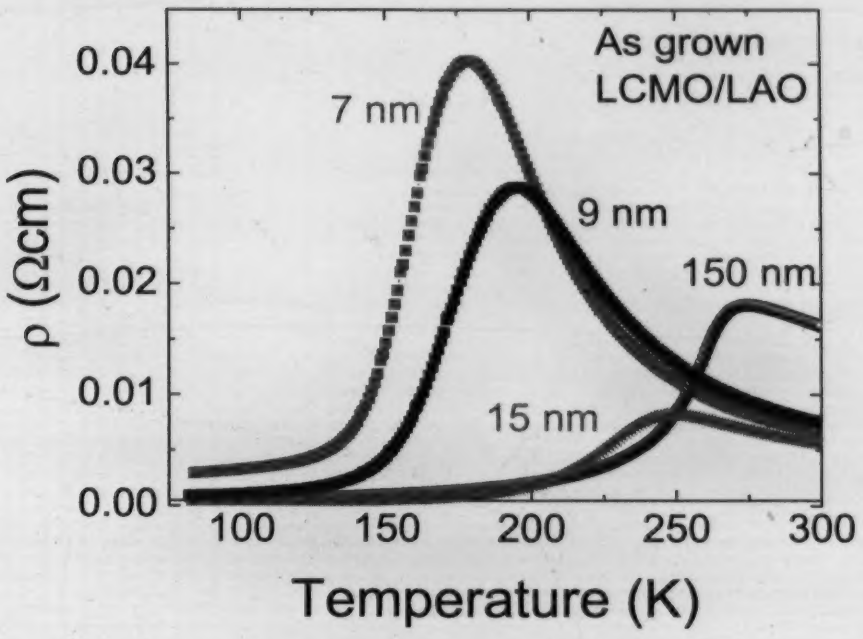

Figure 13.1: Temperature dependence of resistivity of LCMO/LAO for 7 nm, 9 nm, 15 nm and 150 nm samples.

13.2 Results and discussions

In our investigations we have used films of $La_{0.65}Ca_{0.35}MnO_3$ with several different thicknesses. The studied epitaxial films were grown on $LaAlO_3$ substrates using dc-magnetron sputtering.[11] It is known experimentally that deposition of thin films on a substrate leads to strain in the film because of lattice mismatch. The strain state of the films evolves from coherently strained at a small thickness to (partially) strain relaxed at larger thicknesses. Therefore, we tune the strain in our samples by simply changing the thickness of the film.

The temperature dependence of the resistivity ρ for 7 nm, 9 nm, 15 nm and 1000 nm LCMO films is plotted in Fig. 13.1. The metal-insulator transition temperature T_p of the films was found to decrease with a decreasing film thickness (see Fig. 13.1).

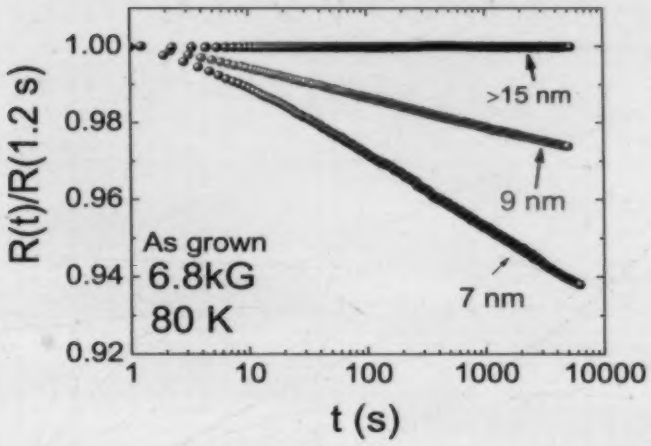

Figure 13.2: The time dependence of resistivity measured in a constant field 0f 6.8 kG at 80 K for films of different thicknesses.

Beyond the pure phase behavior, the observation of electronic phase separation in manganites has generated considerable interest. It has been shown that for a wide range of temperatures, there is a coexistence of ferromagnetic metallic (FM) and charge-ordered insulating (COI) antiferromagnetic phases in La based manganites and several others especially when hole doping takes a commensurate value(x=0.5).[6] On the other hand, it has been shown that the strain also could lead to electronic phase separation even if the hole doping value is not $x\approx0.5$. The lattice strain induced reconstruction of the orbital structure is believed to be responsible for the electronic phase separation occurring near the substrate-film interface as detected by the NMR experiments and linear dichroism in x-ray absorption experiments.[7, 8]

An interesting result of such kind of strain induced electronic phase separation is given in Fig. 13.2. As seen from Fig. 13.2 when the film thickness is less than 15 nm resistivity of the sample in a magnetic field has a noticeable time dependence i.e., the resistivity of the 7 nm film changes around 6-7 % in a field of 6.8 kG in less than an hour. This kind of relaxing behavior results from the strain induced instability of the charge ordered insulating phases towards the ferromagnetic metallic phases on

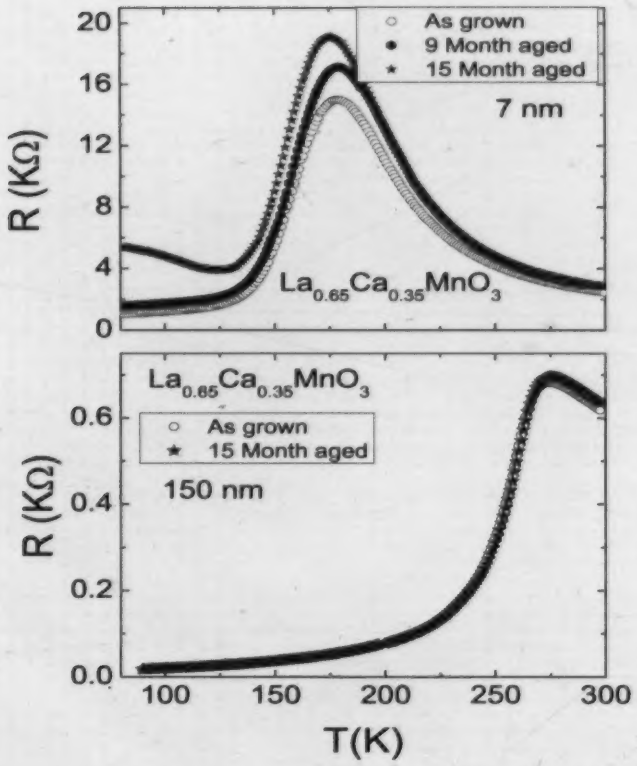

Figure 13.3: Aging effect for 7 nm and 150 nm LCMO/LAO films.

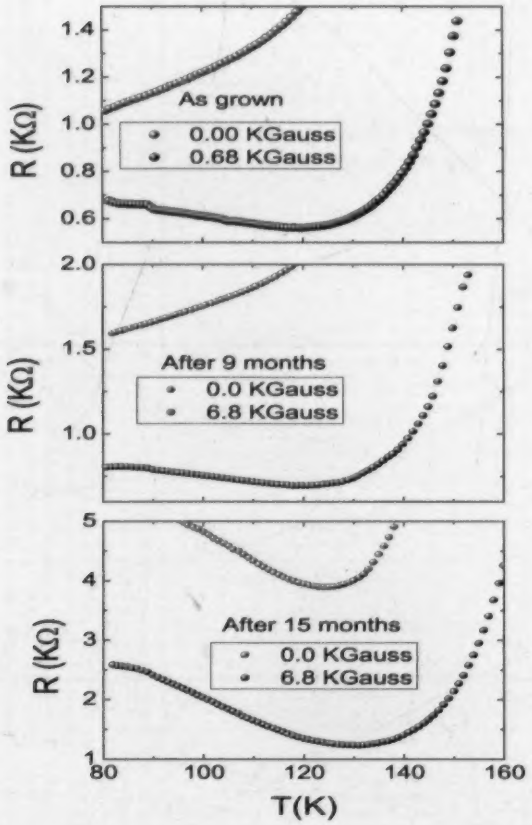

Figure 13.4: The temperature dependence of resistivity of 7 nm LCMO/LAO sample measured in zero field and field of 6.8 kG for different aging conditions.

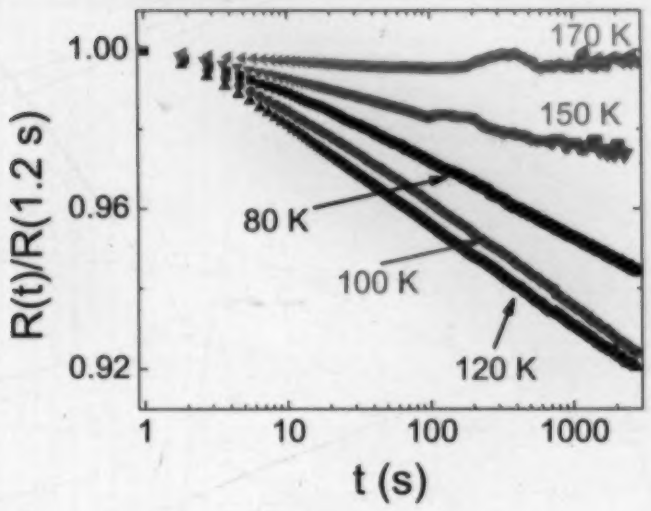

Figure 13.5: Time dependence of resistivity measured in a constant field of 6.8 kG at different temperatures.

the application of perturbation, such as a magnetic field, external or internal strain, etc.[9, 10]

More interestingly the charge/orbital ordered insulating phases are also metastable against time in zero external magnetic field. In other words highly strained ultra thin films exhibits anomalous aging effects. A representation of this effect is shown in Fig. 13.3. As seen from the figure the effect is strongly correlated to the strain state of the sample since the aging effects are negligible in partially relaxed films such as 150 nm. The absence of relaxation effects in the 150 nm sample suggests that the electronic phase in this sample is mainly dominated by the ferromagnetic metallic phase below the metal insulator transition temperature. On the other hand, strong relaxation effects in the 7 nm sample suggests a highly phase separated state (between the FM and COI phases) below the metal insulator transition temperature.[9, 10] Since the aging effect is minor in a strain relaxed sample (150 nm) it appears that oxygen at sites of the charge ordered phase is the main reason for the aging effects.

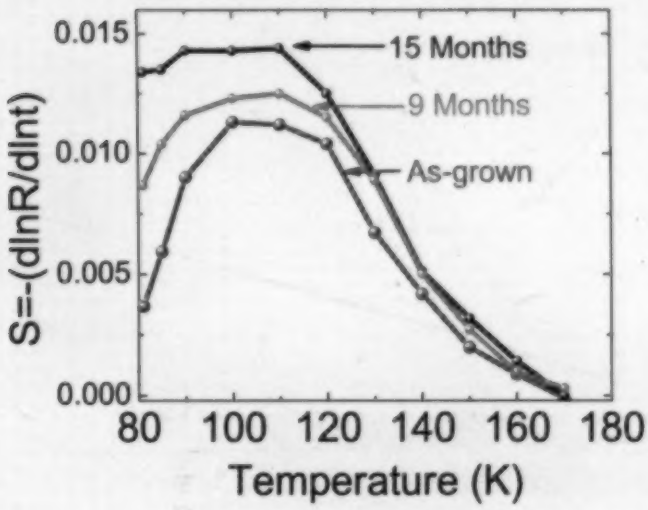

Figure 13.6: Temperature dependence of relaxation rate for all samples. The lines are guides for the eye.

Aging also has dramatic effects on the temperature dependence of the resistivity measured in a constant magnetic field of 6.8 kG (see Fig. 13.4). Resistivity up turn in the temperature dependence of resistivity of manganites has been previously interpreted as quantum interference effects or Kondo like transport previously.[11, 12] However, in both cases the upturn was occurring at very low temperature (well below the metal insulator transition temperature) in contrast to our case. In fact in our case the upturn happens 110-120 K (around 20-30 K below the MIT) likely to be caused by the multi-phase coexistence. We believe that below the metal insulator transition temperature our sample contains a low field sensitive the FM phase and a low field less sensitive COI phase. When a field is applied FM phase exhibits a large response to the magnetic field and ρ of the sample drops, however, the COI phase still remains insulating at the low temperatures and causing resistivity minima in the overall ρ(T).

Evolution of the phase separation of COI and FM phases at different temperatures evidences itself in the time dependence of resistivity data of as grown 7 nm LCMO measured in a constant field (see Fig. 13.5). From the data one can obtain the

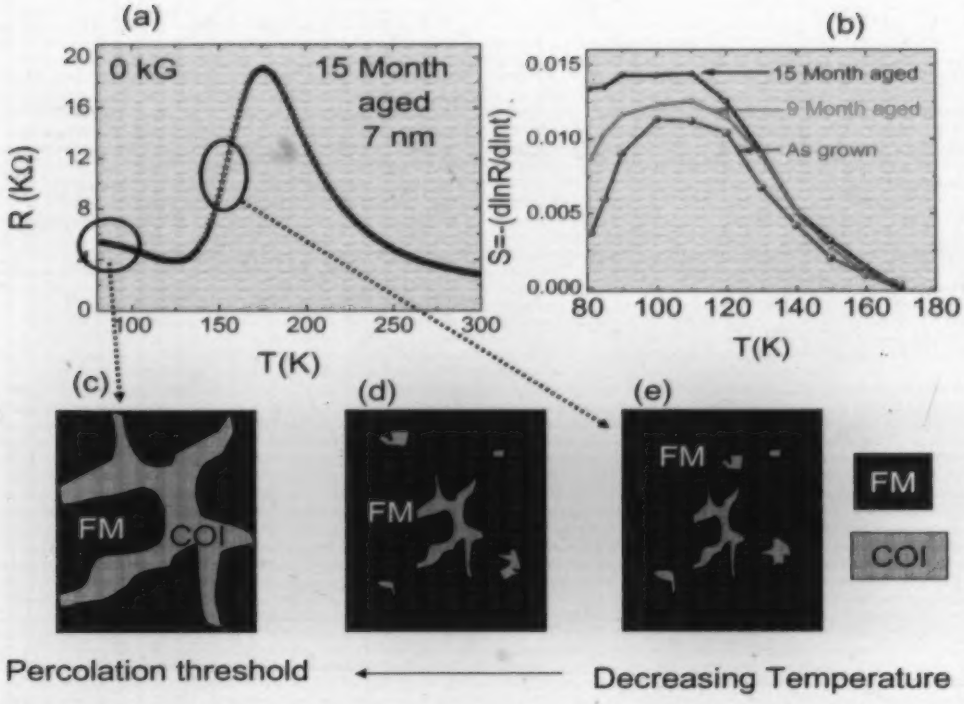

Figure 13.7: (a) Temperature dependence of resistivity of 15 months aged $La_{0.65}Ca_{0.35}MnO_3$ sample, (b) temperature dependence of relaxation rate for all samples, (c)-(e) A qualitative description of the electronic phase separation in our samples.

decay rate S=d(lnρ)/d(ln$t$), which is a measure of the strength of meta-stability in our samples. The result is plotted in Fig. 13.6 as a function of temperature for as grown and the aged samples. The upturn in the temperature dependence of zero field resistivity of aged samples (see Fig. 13.3) reflects itself in an increase of S. This suggests that the relative fraction of the COI phase is increasing with aging. Notice that the peak in the temperature dependence of S of the as grown sample almost disappears in the 15 month aged sample which suggests that meta stable phases firstly form at low temperatures when a sample is aged.

Fig. 13.7 illustrates a qualitative picture for our observations. If one assigns the relaxation effects to the presence of a COI phase, the finite relaxation rates will be a qualitative measure of the electronic phase separation in our sample. In this sense as seen from Fig. 13.7 (b) in our samples the COI phase starts to show up in the resistivity data below 170 K and the relative ratio of the COI phase to the FM phase increases with decreasing temperature in the 15 month aged sample (see Fig. 13.7 (a)-(b)) A cartoon like illustration is given in Fig. 13.7 (c)-(e). Notice that when the COI phase reaches the percolation threshold, the sample's overall resistance will exhibit insulating like behavior as shown in Fig. 13.7 (c).

13.3 Summary and conclusions

In summary we have shown that strain associated with a lattice mismatched substrate in ultra thin films can cause new electronic behavior, not found in bulk materials or thicker films of the same chemical composition of LCMO. Resistivity of the ultra thin films exhibits strong relaxation effects when measured as a function of time in a constant magnetic field. Moreover, ultrathin films age dramatically faster than the thicker counterparts causing a upturn in the temperature dependence of the resistivity at lower temperatures where material is supposed to be ferromagnetic.

Bibliography

[1] A. Lisauskas, J. Back, I. Khartsev, and A. M. Grishin, *J. Appl. Phys.* **89**, 6961 (2001).

[2] H. Oshima, K. Miyano, Y. Konishi, M. Kawasaki, and Y. Tokura, *Appl. Phys. Lett.* **75**, 1473 (1999).

[3] A. I. Abramovich, L. I. Koreleva, A. V. Michurin, O. Y. Gorbenko, and A. R. Kaul, *Physica B* **293**, 38 (2000).

[4] M. Egilmez, R. Patterson, K. H. Chow, and J. Jung, *Appl. Phys. Lett.* **90**, 232506 (2007).

[5] M. Egilmez, M. Saber, A. Mansour, Rongchao Ma, K. H. Chow, and J. Jung, *Appl. Phys. Lett.* **93**, 182505 (2008).

[6] A. Moreo, S. Yunoki, E. Dagotto, *Science* **283**, 2034 (1999); E. Dagotto, T. Hotta, and A. Moreo, *Physics Reports* **344**, 1 (2001).

[7] M. Bibes, L. Balcells, S. Valencia, J. Fontcuberta, M. Wojcik, E. Jedryka and S. Nadolski, *Phys. Rev. Lett.* **87**, 067210 (2001).

[8] A. Tebano, C. Aruta, S. Sanna, P. G. Medaglia, and G. Balestrino, A. A. Sidorenko and R. De Renzi, G. Ghiringhelli and L. Braicovich, *Phys. Rev. Lett.* **100**, 137401 (2008).

[9] V. Markovic, G Jung, Y Yuzhelevskii, G Gorodetsky, F X Hu, J Gao *Europhysics Letters* **52**, 674 (2000).

[10] M Uehara, S W Cheong *Phys. Rev. B* **75**, 104419(2007).

[11] M. Ziese, *Phys. Rev. B* **100**, 137401 (2008).

[12] Jincang Zhang, Yan Xu, Shixun Cao, Guixin Cao, Yufeng Zhang, and Chao Jing, *Phys. Rev. B* **68**, 134411 (2003).

Chapter 14

Summary and future work on manganites

We have studied several topics in the area of manganites during the course of this dissertation. In a rough categorization we can divide the topics in two main groups namely bulk and epitaxial thin films. The studies included the low-field magnetoresistance effect and magnetoresistive anisotropy of the strained manganite thin films, and granular manganite samples which have grain sizes from a few tens of nanometer to micrometer scale. We attempt to explain our experimental data with help of the three main theoretical contribution to the physics of manganites: According to the double-exchange (DE) model, the MIT and the CMR are a consequence of the DE mechanism combined with the Jahn-Teller electron-phonon interaction with d states, leading to the conclusion that the low and high temperature phases are a spin polarized ferromagnetic metal and a polaronic paramagnetic insulator, respectively.[1, 3, 4] Tunneling experiments and Monte Carlo simulations suggest that the ground states of manganites tend to be intrinsically inhomogeneous due to strong tendencies toward phase separation, typically involving ferromagnetic metallic and antiferromagnetic charge and orbital ordered insulating domains.[2] This implies that disorder is an important inherent element of the CMR effect.[5, 6] Indeed, it has been demonstrated in various experimental studies that lattice disorder introduced into manganites through

chemical substitutions, pressure, strain, and electric field induces dramatic changes in their ground state properties. More recently, the current carrier density collapse theory (CCDC), on the other hand, postulates that the MIT and the CMR are caused by a magnetic breakup at T_c of heavy bi-polarons (which are formed by pairing of oxygen p holes in the paramagnetic phase).[3, 4] Among these models and theories CCDC has special importance since it is the only one that allows us to analyze our data quantitatively. Also we should mention the success of the phase separation scenario from the Monte Carlo simulations especially in their explanations of multiphase coexistence for a wide temperature range.

Besides the hole doping level x, the disorder due to the ionic size mismatch of the A-site cations (RE and AE) is also an important factor that controls the electronic phase of the doped manganites $RE_{1-x}AE_xMnO_3$. The magnitude of the quenched disorder/the local structural size mismatch could be evaluated using the variance of the ionic radii, defined as $\sigma^2=\Sigma(x_i r_i^2 - r_A^2)$, where $r_A=(0.55)r_{RE}+(0.45)r_{AE}$ and x_i and r_i denote the fractional occupancies and the effective ionic radii of the cations.[7, 8] The significant role of disorder has been pointed out in conjunction with the nature of the CO/OO structure and magnetic structure. A large disorder decreases the electronic correlation length and induces spatial phase fluctuation and hence shortrange CO/OO and phase separation. Such a short-range structure or phase separation would play an important role in the physical properties. In $Sm_{0.55}Sr_{45}MnO_3$ that has a larger quenched disorder, the electronic phase fluctuation should dominate and induce complex electronic properties.[9] According to Tomioka *et al.* the magnetic and electronic properties at $x\approx0.5$ are strongly related to the competition among the CO/OO, FM, and A-type AFM phases. Unfortunately, there were few studies on this important composition in the literature especially on the effects of different types of disorder.[10]

In the first part of the dissertation we aimed to study the effects of different types of disorder in the $Sm_{1-x}Sr_xMnO_3$ system close to $x\approx0.5$ hole doping level. In order to study oxygen disorder, we vacuum annealed the $Sm_{0.55}Sr_{45}MnO_3$ at temperatures up

to 700 ° C. Our temperature dependence of the resistivity results supported with the weight analysis showed that up to 375 °C annealing temperature oxygen redistribution is the main source of the disorder and above this temperature oxygen deficiency is the main source of the disorder in our samples. We have shown that oxygen redistribution induced disorder could be studied in the sample by annealing at 325° C in vacuum for different annealing times. The temperature dependencies of resistivity and magnetoresistance were measured as a function of the vacuum annealing time. We observed a dramatic increase in the magnitude of the resistivity peak at the metal-insulator transition and a reduction of its width after an initial short-time annealing, followed by a logarithmic increase of the resistivity with annealing time.

We also studied grain boundary disorder, another important type of disorder in $Sm_{0.55}Sr_{45}MnO_3$. We have shown the an increasing lattice disorder softens the magnetic phase transition from a first order phase transition into a second order transition. Furthermore, the peaks in the resistivity and specific heat are broadened and there is an increase in the charge-carrier scattering rates in the metallic and insulating states. The origin of these phenomena is discussed in the dissertation.

One of the most functional properties of ferromagnetic materials is anisotropic magneto-resistance (AMR). This effect was the basis of the first non volatile random access memories. However, recently AMR based technology replaced in the market by giant magnetoresistance (GMR) based devices. This is because the magnitude of the effect in ferromagnetic metal and alloys is very small, on the order of a few percent. Due to the strong coupling between the spin-orbital-charge degrees of freedom in manganites, the AMR in these materials could reach the much higher values desired for the new generation of spin and charge based devices.We have shown that polycrystalline $Sm_{0.55}Sr_{0.45}MnO_3$ samples exhibit large anisotropic magnetoresistance (AMR). The magnitude of the AMR strongly depends on the grain size of the samples. The AMR in poly samples exhibits sizeable low field and low temperature AMR which is in contrast to single crystal samples and epitaxial films.[11] This suggests that the well established spin polarized transport model for understanding low temperature and

low field MR in manganites is essentially anisotropic. Our results indicate that AMR in manganite samples could be tuned for large temperature ranges at low magnetic fields by controlling the crystallinity and defect structure.

Up to date, no report has been published on SSMO films which shows bulk like properties. In early reports by Tokura's group SSMO films with compositions from x=0.4 to 0.6 were grown (thickness of the films were around 100 nm) by pulse laser deposition (PLD) on $SrTiO_3$ (100) substrates. None of the films with composition of $x \sim 0.5$ exhibited metal insulator transition at fields up to 7 Tesla.[1] The main reason for insulating behavior in as grown films was attributed to the lattice mismatch between the substrate and SSMO. Our group attempted to make $Sm_{0.55}Sr_{0.45}MnO_3$ films using various substrates. Our films grown on $SrTiO_3$, $LaAlO_3$, MgO and YSZ (100) substrates showed insulating behavior down to 80 K with negligible CMR effect at low magnetic fields consistent with the previous reports on SSMO films and properties of the films were far from the bulk SSMO. Our film thicknesses ranged from 60 nm to 1000 nm. At these thicknesses one can expect a strong relaxation of the strain due to the lattice mismatch between the film and substrate. This suggests in addition to the mismatch between the lattice parameters, mismatch in thermal expansion coefficient and the chemical reaction between the substrate and the film could be the reason for insulating behavior in $Sm_{0.55}Sr_{0.45}MnO_3$ films. In order to circumvent these problems we used a different approach in this study: We have used another type of manganite ($Nd_{0.55}Sr_{0.45}MnO_3$) as a thin buffer layer between the substrate and the $Sm_{0.55}Sr_{0.45}MnO_3$ film. In the resulting films we have obtained bulk like properties and a giant response to the relatively small magnetic fields.

$La_{1-x}Ca_xMnO_3$ is the most studied manganite in the scientific community due to its tunability to a wide range Curie temperatures (100-270 K), and its rich phase diagram as a function of hole doping x. Although a vast amount of literature is dedicated on this type of manganite, there are only a few studies to the magneto-resistivity of epitaxial thin films of $La_{1-x}Ca_xMnO_3$, During the course of the thesis we have made a comprehensive study on the anisotropic properties of this compound. The magneto-

transport properties of strained $La_{0.65}Ca_{0.35}MnO_3$ thin films with thickness between 10 and 1000 nm were investigated at temperatures near the metal-insulator transition and in magnetic fields up to 0.7 Tesla. The reduction of the thin film thickness which, in turn, produces an increasing epitaxial lattice strain dramatically increases the in-plane magnetic anisotropy and the magnetoresistivity. Furthermore, we investigated the anisotropic magnetoresistance (AMR) in ultrathin La-based manganite films grown on various substrates. It was found that depending on the strain state, the AMR in some of these systems exceeds 100% and can even change sign. These changes are very dramatic when compared to the few percent change in AMR in conventional ferromagnets. The mechanism behind these large changes in the AMR is discussed

We also investigated the effect of lattice disorder in $La_{0.65}Ca_{0.35}MnO_3$ (LCMO) thin films. We formed the disorder with low power ion bombardment of the film. In addition to the ion bombardment induced point defect type disorder formation, we also reduced the thickness of the film. Therefore we were able to study the effects of point defect type disorder on the magnetotransport properties of disordered films and as grown (point defect disorder free) films as a function of thickness. The results suggest that, for films less than 20 nm thick, an increase of the magnetoresistivity and a reduction in the magnetoresistive anisotropy of the ion-beam-milled films are governed mostly by point-defect-induced deformation, in contrast to the as-grown films where an increase of both the magnetoresistivity and the magnetoresistive anisotropy are determined by the epitaxial strain.

We analyzed the origin of the disorder-induced resistive peak broadening in LCMO manganites at the MIT using a simple percolation model based on the theory of Alexandrov.[9] The resistivity around the metal insulator transition temperature in the $La_{2/3}Ca_{1/3}MnO_3$ single crystal and films can be described by a Gaussian distribution of transition temperatures. The width of the Gaussian distribution, which defines the temperature range where the metallic and insulating clusters simultaneously exist, increases with an increasing lattice disorder. We calculated the tempera-

ture dependence of resistivity using the temperature dependence of the fraction of the metallic phase obtained from the Gaussian distribution. The results show a very good agreement with the experimental data for $La_{2/3}Ca_{1/3}MnO_3$ crystal and films, suggesting that the disorder induced multi-phase coexistence and the large distribution of transition temperatures contributes significantly to the resistive peak broadening in manganites.

We have shown that strain associated with a lattice mismatched substrate in ultra thin films can cause new electronic behavior, not found in bulk materials or thicker films of the same chemical composition of $La_{0.65}Ca_{0.35}MnO_3$. Resistivity of the ultra thin films exhibits strong relaxation effects when measured as a function of time in a constant magnetic field. Moreover, ultrathin films age dramatically faster than the thicker counterparts causing a upturn in the temperature dependence of the resistivity at lower temperatures where material is supposed to be ferromagnetic.

The content of the dissertation has contributed to understanding of the functional magnetic and magnetotransport properties of manganites for further device applications by studying an important issue, namely disorder in the form of oxygen redistribution, grain boundary, point defects or strain in polycrystalline samples and epitaxial thin films of different types of manganites.

Furthermore, the author of the dissertation studied many other topics related to manganites. Some of the results of these topic will be given in the coming section.

14.1 Future work

14.1.1 Correlation between the structural phase transition and the electrical transport properties of manganite films on $SrTiO_3$

Magnetic phase transition in the manganite films has been found to be induced by the structural phase transition of the $SrTiO_3$ substrate at $T_s = 105$ K. However, no

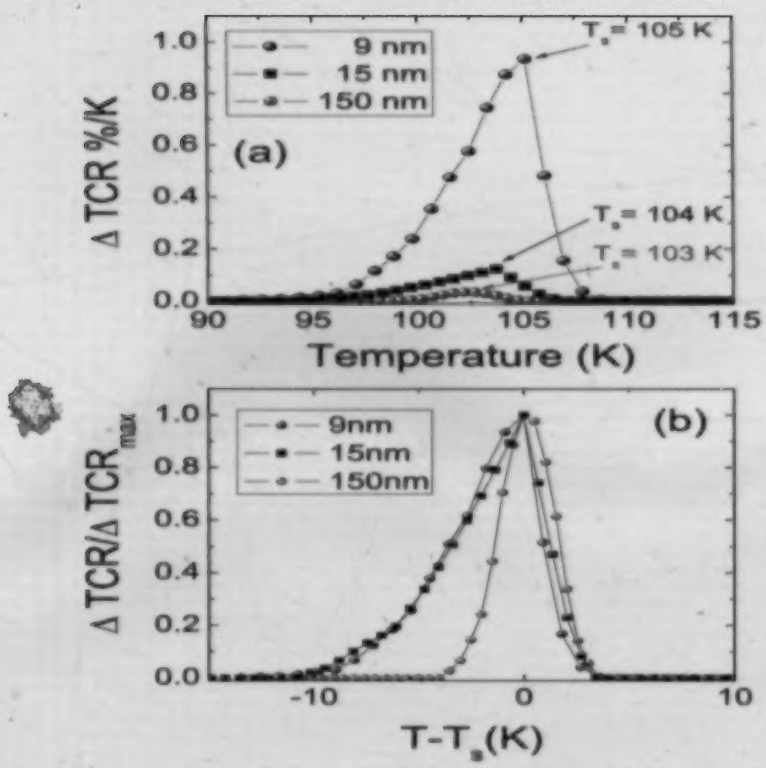

Figure 14.1: (a) Temperature dependence of ΔTCR of LCMO films obtained by subtracting the background from the temperature dependence of TCR shown in Figure 1. (b) Temperature dependence of ΔTCR normalized to its maximum value. The lines are guides for the eye.

change in the electrical transport properties has been detected at this temperature. We for the first time reported the observation of satellite peaks in the temperature dependence of the temperature coefficient of resistivity (TCR) at temperatures around 105 K in ultra-thin manganite films grown on $SrTiO_3$ substrates, triggered by the cubic-to-tetragonal structural phase transition $SrTiO_3$. The TCR peak's magnitude decreases with an increasing thickness of the manganite film and with an increasing applied magnetic field. Our results demonstrate the strong coupling between the structural and transport properties in the manganite films.

In order to detect the very small changes in the resistivity of these films at T_s we calculated the temperature coefficient of resistance TCR = $(1/\rho)(d\rho/dT)$ for the LCMO films. The temperature dependence of the TCR clearly exhibits two peaks, a prominent one at the metal-insulator transition temperature of the LCMO films, and a small sharp peak at T_s a temperature which characterizes the structural phase transition temperature in in $SrTiO_3$. The amplitude of the peak at $T_s \approx$ 102-105 K increases as the LCMO film is made thinner. In Fig 14.1 we have plotted ΔTCR at T_s. ΔTCR was obtained by subtracting the background from the temperature dependence of the TCR. Fig 14.1 (a) shows an increase of the ΔTCR with a decreasing thickness of the film. ΔTCR peaks normalized to their maximum value reveal that the ultra-thin films exhibit a broader transition at T_s (see Fig 14.1 (b)).[12]

14.1.2 Oxygen-isotope exchange and quenched disorder effects on magnetotransport properties of $(Sm_{1-y}Gd_y)_{0.55}Sr_{0.45}MnO_3$

$(Sm_{1-y}Gd_y)_{0.55}Sr_{0.45}MnO_3$ manganites exhibit a transition from a metallic ferromagnet ground state (at $y = 0$) to an insulating spin-glass state (at $y = 1$). We performed detailed systematic studies of the effects of both the quenched disorder and the oxygen isotope exchange $^{16}O \longrightarrow {}^{18}O$ on the magneto-transport properties of this system for y between 0 and 1. The data revealed that for both ^{16}O and ^{18}O samples an increasing quenched disorder converts the ferromagnetic metal state into the charge-ordered antiferromagnetic insulating ground state characterized by a high magneto-resistance and a field-induced ferromagnetism. We observed very pronounced effects of the oxygen isotope substitution on the magneto-transport properties of samples with a high magneto-resistance including the oxygen-isotope exchange induced metal-insulator transition. Very large quenched disorder leads to formation of the insulating spin-glass state in which no colossal magneto-resistance or field-induced ferromagnetism occurs. There is also no significant effect of the oxygen isotope exchange on samples

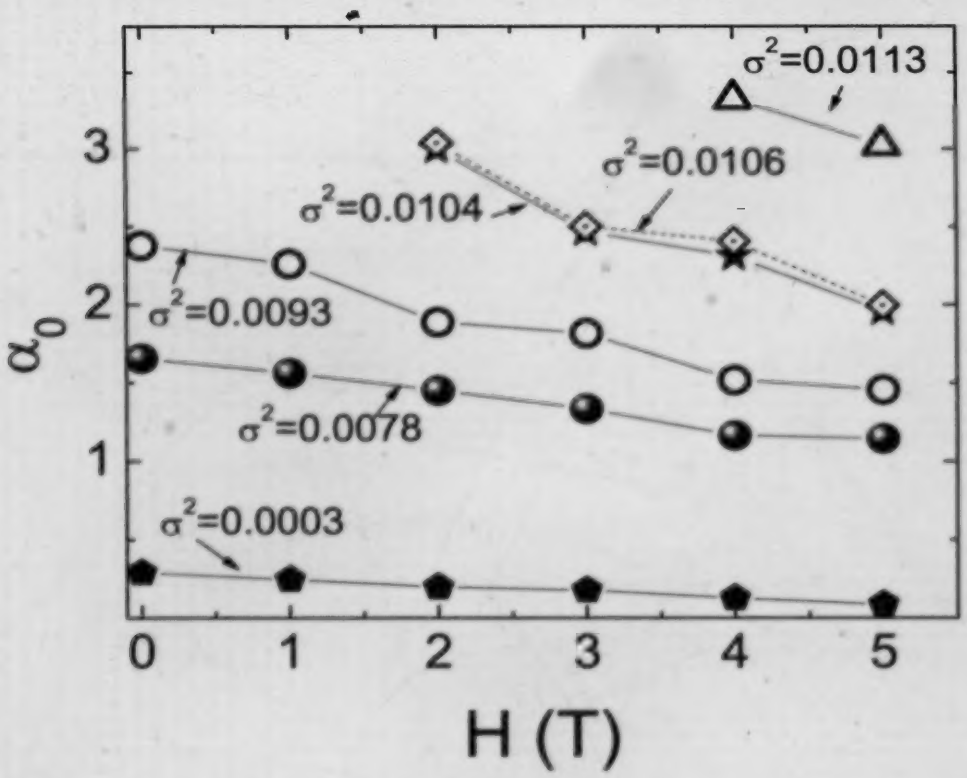

Figure 14.2: The field dependence of the isotope exchange exponent α_0 for different levels of quenched disorder. All σ^2 values (quench disorder) are in units of $\AA^2$. The lines are guides for the eye.

in the spin-glass state.

If a ferromagnetic state appears in the temperature dependence of magnetization graphs, one could estimate the magnitude of the Curie temperature T_c as the temperature at which the derivative of the temperature dependence of the magnetization is minimum. This allowed us to evaluate for all the samples the isotope exponent[13] defined as α_o=-Δln(T_c)/Δln(M) where M is the isotopic mass.[14] The calculated α_o for the ^{16}O and ^{18}O samples in which a ferromagnetic transition takes place are shown in Fig 14.2. Here σ^2 is the measure of the quench disorder in our samples, for details see the original publication.[15] For comparison, we also plotted the data

for $La_{0.65}Ca_{0.35}MnO_3$ with σ^2=0.0003 $\AA^2$ (relatively small quenched disorder) as well as $Eu_{0.55}Sr_{0.45}MnO_3$ with σ^2=0.0104 $\AA^2$ on this graph. These data appear to be consistent with those obtained for our samples.

14.1.3 Magnetotransport in $Nd_{0.55}Sr_{0.45}MnO_3$ films

We also studied a large number of $(Nd)_{0.55}Sr_{0.45}MnO_3$ (NSMO) type manganite films. The large lattice mismatch between these films and the $LaAlO_3$ and $SrTiO_3$ substrates makes it difficult to grow films with bulk like properties. We have optimized the film fabrication after systematic studies of controlled post annealing processes. Fig 14.3 illustrates the temperature dependence of resistance of NSMO/LAO films for different post annealing conditions. As seen from the figure the response of the electrical transport to post annealing at higher temperatures is anomalous. We have obtained bulk like properties in 900°C oxygen annealed films.

We also found very large magnetoresistive anisotropy in NSMO films. Strain relaxed films exhibits metal insulator transition (MIT) around 250 K which is very similar to the metal insulator transition temperature of $La_{0.65}Sr_{0.35}MnO_3$ films. However, we found large differences in AMR values between two different compounds with similar MIT. Fig 14.4 represents a typical angular dependence resistance data for NSMO/STO films.

14.1.4 Magnetic tunnel junctions with MgO tunnel barrier

Magnetic tunnel junctions (MTJ) are of great interest to the data storage based companies such SEAGATE Technologies and IBM duë to their potential in magnetoresistance based devices since their discovery in 1995.[16] The new generation data storage medias recently started to use MTJ read head sensors. A magnetic tunnel junction is generally formed from two ferromagnetic electrodes separated by a thin insulating tunnel barrier. Recently, it has been shown that very high tunnel magnetoresistance values can be achieved if MgO is used as the tunnel barrier. Definition

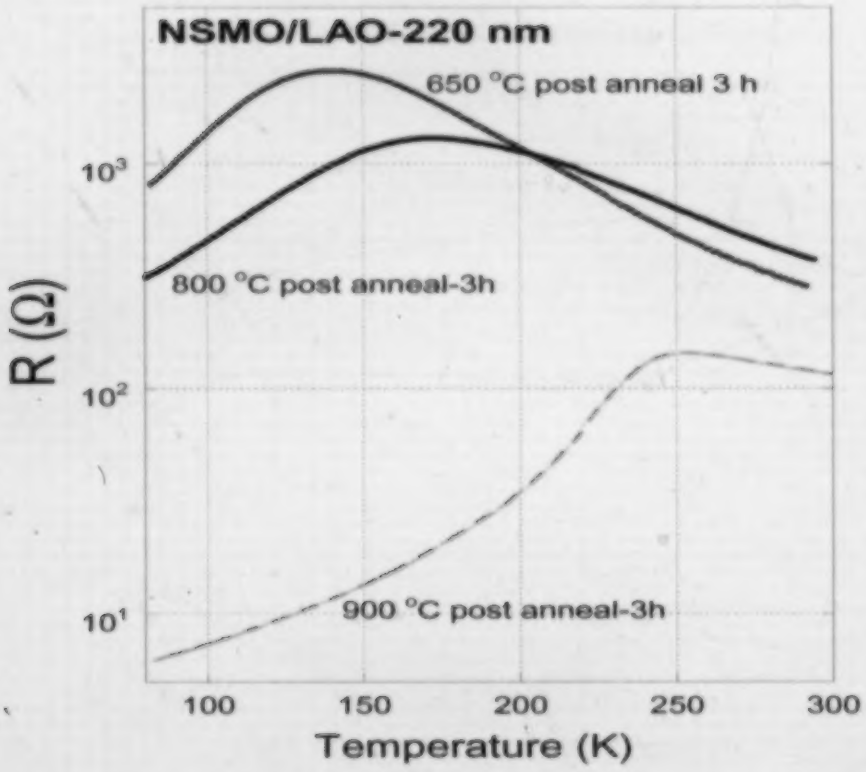

Figure 14.3: Temperature dependence of resistance of NSMO/LAO films for different post annealing conditions.

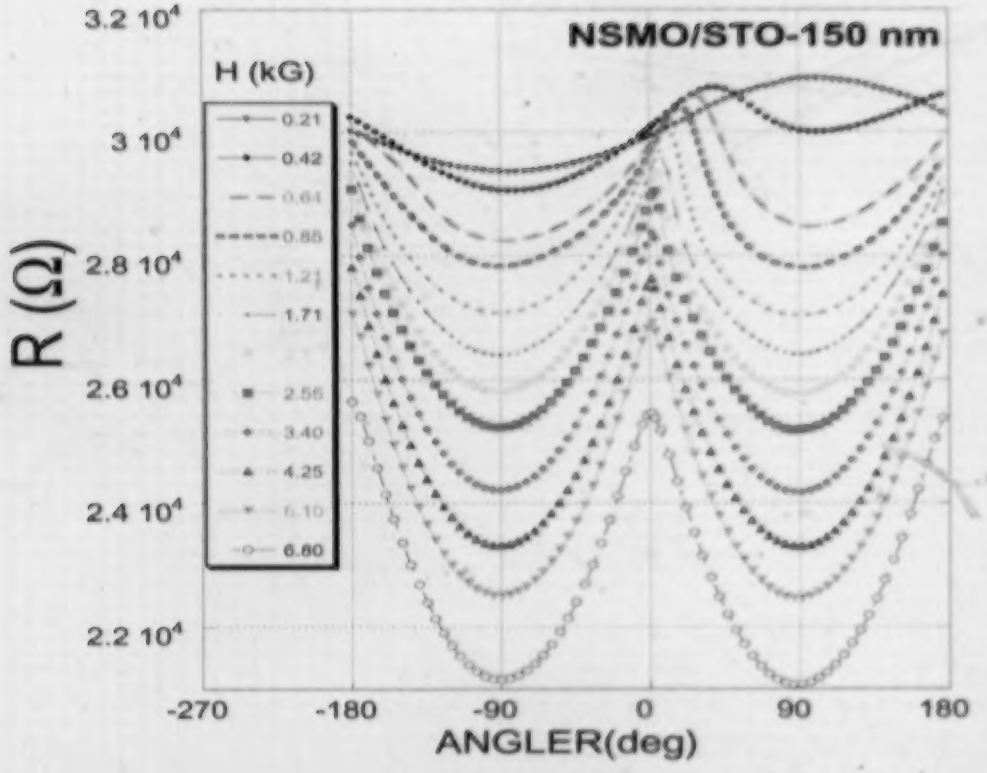

Figure 14.4: Angular dependence of resistance for 250 nm NSMO/STO film measured at 80 K for different magnetic fields.

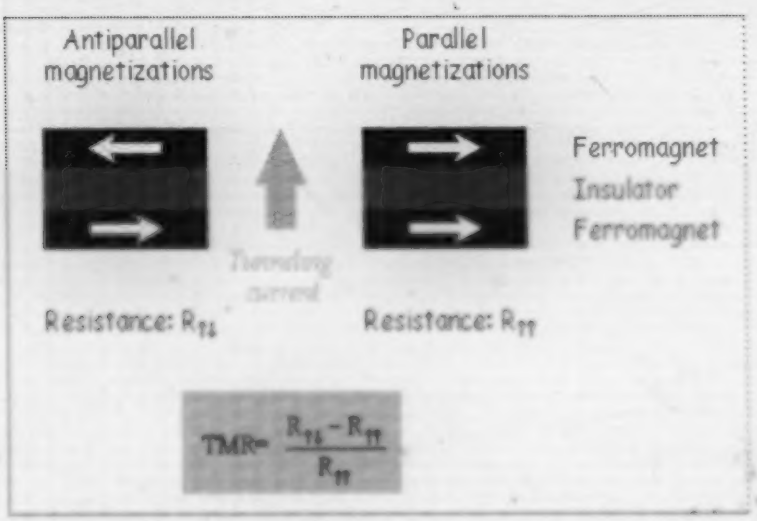

Figure 14.5: Definition of tunnel magnetoresistance.

of the tunnel magnetoresistance is given in Fig 14.5.

As being one of the most interesting family of ferromagnetic materials, manganites attracted great interest as a ferromagnetic electrode in development of new generation magnetic tunnel junctions. Although a number of studies were published on the TMR effect in manganites, there is not many studies dedicated to the tunneling anisotropic magnetoresistance (TAMR) effect in manganites. We fabricated a number of manganite tunnel junctions (similar to the cartoon representation shown in Fig 14.5). Some of the results from $La_{0.65}Sr_{0.35}MnO_3/MgO/La_{0.65}Sr_{0.35}MnO_3$ junctions are given from Fig 14.6-Fig 14.9. We observed multiple discontinuities in the current voltage characteristics of our samples. One such example is given in Fig 14.6 and Fig 14.7; the low voltage and high voltage curves exhibit two clear discontinuity at different voltages. Origin of this behavior is still not fully understood. As seen from Fig 14.8 and Fig 14.9, LCMO/MgO/LCMO junctions exhibit large TAMR and TMR. More interestingly, the angular dependence of the tunneling current in our junctions exhibited a discontinuity at certain angles where several orders of magnitude changes

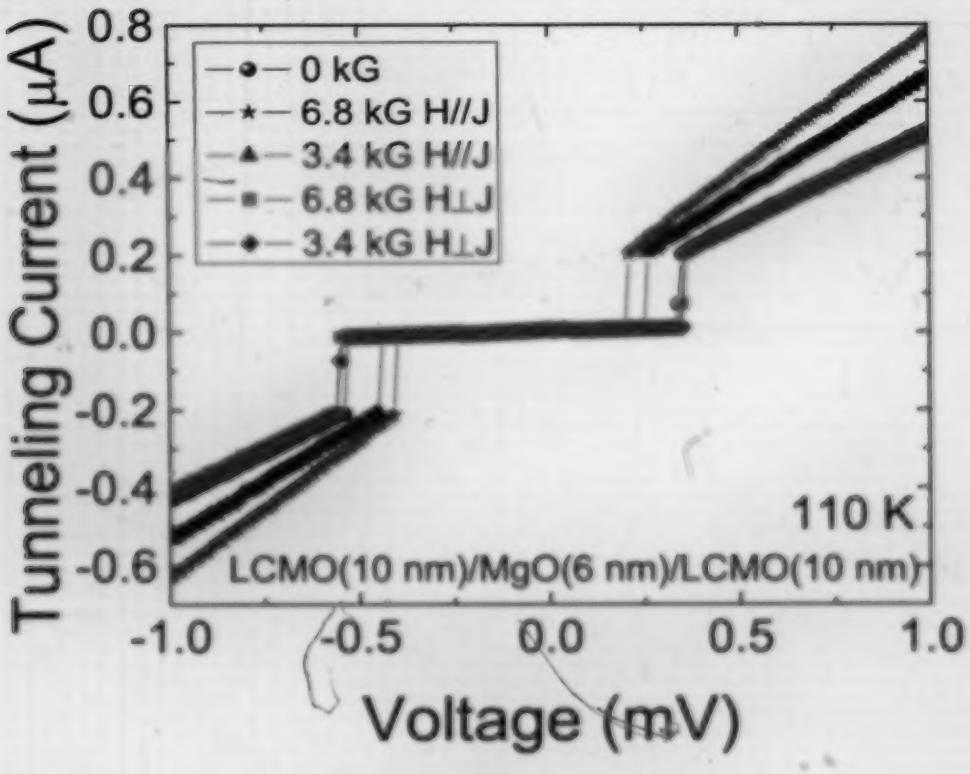

Figure 14.6: Bias voltage dependence of the tunneling current in LCMO/MgO/LCMO junctions for relatively low voltages.

occurred o in low magnetic fields.

We also discovered that in stacks of tunnel junctions such as LCMO / MgO / LCMO / MgO / LCMO.. the TAMR and TMR could be improved when compared to the three layer structures. Due to the over loaded content of the dissertation, we did not find it convenient to include these new results.

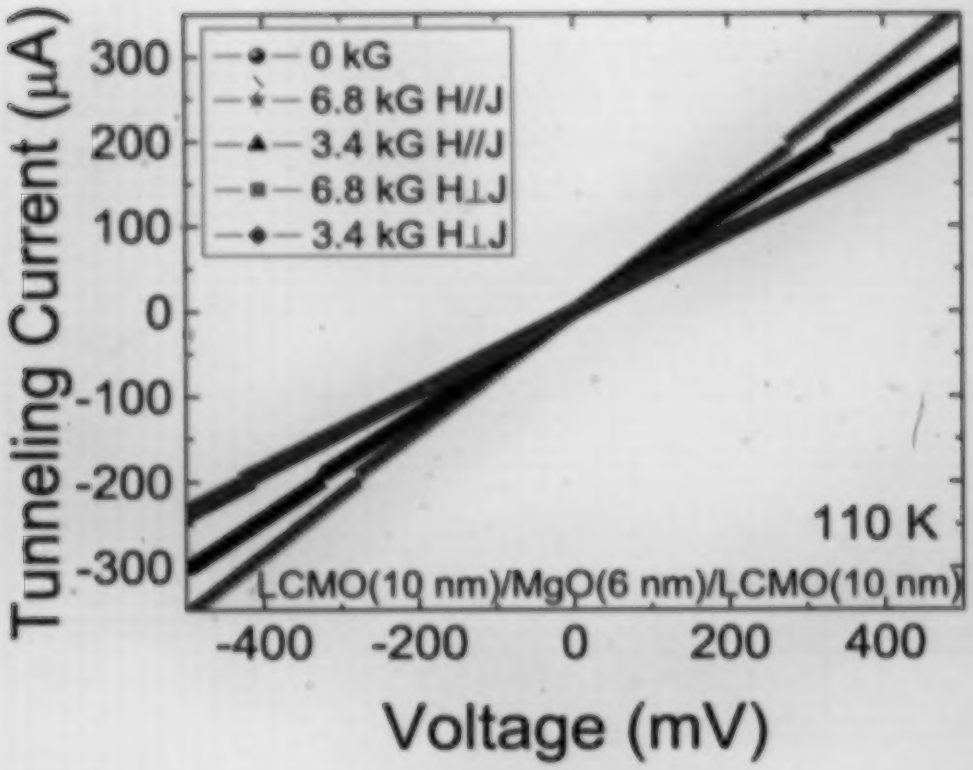

Figure 14.7: Bias voltage dependence of the tunneling current in LCMO/MgO/LCMO junctions for relatively high voltages.

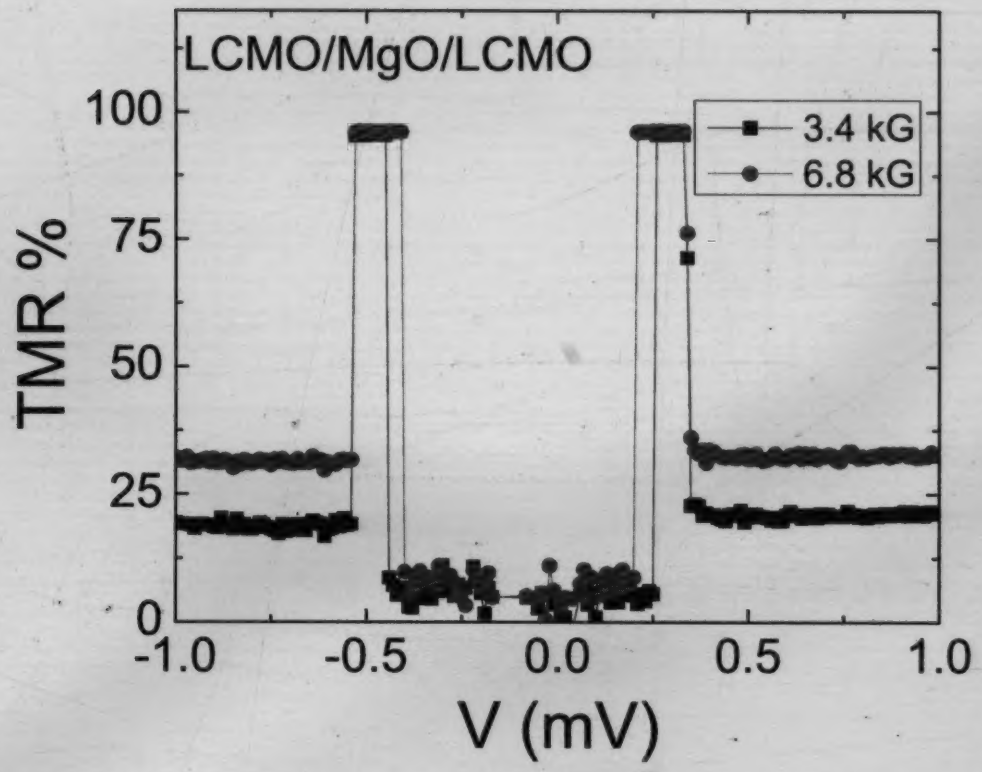

Figure 14.8: Bias voltage dependence of the TMR in LCMO/MgO/LCMO junctions for 3.4 and 6.8 kG.

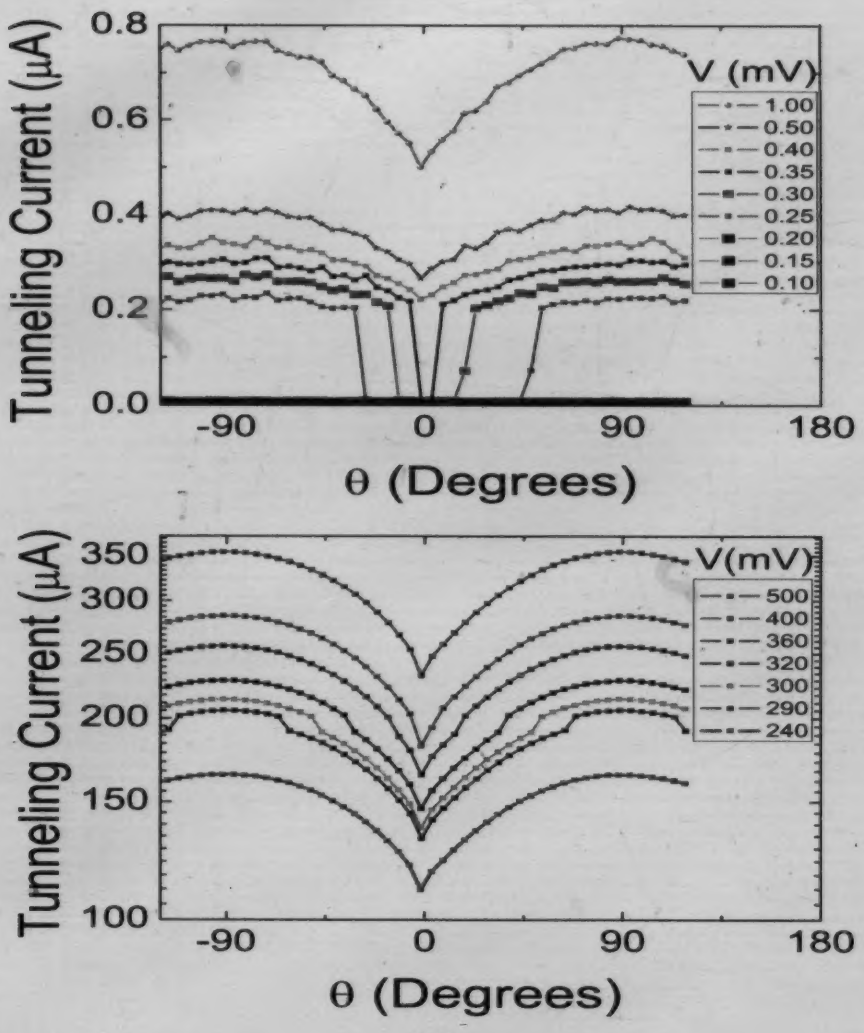

Figure 14.9: Angular dependence of the tunneling current LCMO/MgO/LCMO junctions for different bias voltages in a constant field of 6.8 kG. At some certain angles the carriers starts to tunnel across the junction causing a discontinuities in the data.

Bibliography

[1] A. J. Millis, P. B. Littlewood and B. I. Shraiman, *Phys. Rev. Lett.*, **74**, 5144 (1995).

[2] E. Dagotto, *Science* **309**, 257 (2005).

[3] A. S. Alexandrov and A. M. Bratkovsky, *Phys. Rev. Lett.*, **82**, 141 (1999).

[4] A. S. Alexandrov, A. M. Bratkovsky, and V. V. Kabanov, *Phys. Rev. Lett.*, **96**, 117003 (2006).

[5] C. Sen, G.Alvarez, H. Alliaga, E. Dagotto, *Phys. Rev. B*, **73**, 224441 (2006).

[6] C. Sen, G.Alvarez, and E. Dagotto, *Phys. Rev. Lett.*, **98**, 127202 (2007).

[7] Lide M. Rodriguez-Martinez and J. P. Attfield, Phys. Rev. B, **54**, R15622 (1996).

[8] Lide M. Rodriguez-Martinez and J. P. Attfield, Phys. Rev. B, **63**, 024424 (2000).

[9] Y. Tokura, N. Nagaosa, Nature **288**, 462 (2000).

[10] Y. Tomioka, H. Hiraka, Y. Endoh, and Y. Tokura, Phys. Rev. B. **74**, 104420 (2006).

[11] M. Egilmez, R. Patterson, K. H. Chow, and J. Jung, *Appl. Phys. Lett.* **90**, 232506 (2007).

[12] M. Egilmez, M.M. Saber, I. Fan, K.H. Chow, and J. Jung, *Phys. Rev. B,*. **78**, 172405 (2008).

[13] I. Isaac, J. Jung, J. P. Franck, and M. Abdelhadi, Phys. Rev. B, **70**, 212410 (2004).

[14] G-M. Zhao, K. Conder, H. Keller and K. A. Muller, Nature **381**, 679 (1996).

[15] M. Egilmez, R. Patterson, K. H. Chow, and J. Jung, *Journal of Materials Chemistry.* **18**, 5796 (2008).

[16] T. Miyazaki, N. Tezuka, *Journal of Magnetism and magnetic materials.* **139**, L231 (1995).